Universitat Politècnica de Catalunya

Departament d'Enginyeria Elèctrica

Doctoral Thesis

Energy-based control schemes of Modular Multilevel Converters for HVDC applications

Enric Sánchez-Sánchez

Thesis advisors:
Prof. Oriol Gomis-Bellmunt (UPC, Spain)
Dr. Eduardo Prieto-Araujo (UPC, Spain)

Examination Commitee:
Dr. Florent Morel (École Centrale de Lyon / SuperGrid Institute, France)
Dr. Salvatore D'Arco (SINTEF, Norway)
Prof. Emilio José Bueno Peña (Universidad de Alcalá, Spain)

Barcelona, November 2020

"In times of change,
learners inherit the earth,
while the learned find themselves
beautifully equipped to deal with
a world that no longer exists."

Eric Hoffer

Acknowledgements

Després de més de quatre anys, finalment es tanca un capítol ple d'experiències i de treball intens. Certament ha estat un camí ple de reptes, dificultats i, fins i tot en alguns moments, frustracions. La veritat és que no me n'hagués sortit de la mateixa manera tot sol, i és per això que voldria dedicar un espai d'agraïments a diverses persones.

En primer lloc, als meus directors de tesi. A l'Oriol voldria agrair-li la oportunitat de poder iniciar aquesta aventura a finals del 2015, amb una temàtica engrescadora que em va servir per iniciar-me, i posteriorment aprofundir, en el camp dels sistemes HVDC i, més concretament, d'aquests extranys convertidors anomenats MMC. També agrair-li la capacitat de guiar aquesta recerca en la direcció correcta. A l'Edu, per altra banda, agrair-li la seva proximitat i el seu seguiment constant, especialment en tots els detalls més tècnics de la recerca, així com les constants discussions i la capacitat per donar sempre una volta més quan alguna cosa no sortia. Un famós expert en la matèria deia que sempre se n'aprenia alguna cosa nova, dels MMC, i la veritat és que no li faltava raó.

També voldria donar les gràcies als companys i amics del CITCEA: als que ja hi eren quan vaig començar al 2012, als que es van anar incorporar al llarg d'aquests anys i també als que han marxat. Especialment al nucli dur del grup de xarxes AC/DC: Ricard, Joan, Marc, Carlos, Pepe i Josep, així com als estudiants de nova fornada; als doctorands de l'InnoDC: Saman, Daniel, Luis i Jovana; a l'equip de Mecatrònica: Dani Heredero, Marc Llonch, Cristian, Macià, Tomàs, Carlos Miguel, Gabri, Miquel i Pablo; a la gent d'Enertrònica: Pol, Íngrid, Edu Bullich, Francesc, Sara, Pau i Paco; així com a l'equip de Gestió: Anna, Maria, Jordi i David, i a la resta de professors del centre: Dani Montesinos, Sam, Andi, Roberto i Toni.

I would also like to thank Prof. Florian Dörfler for welcoming and hosting me as a visiting researcher at the Automatic Control Laboratory (ETH Zürich) for five fruitful months, as well as for his guidance during that time. Being surrounded by such nice and smart people and learning many crazy things related to control engineering was truly an invaluable experience. Many thanks to Dominic, Marcello, Saverio, Bala, Paul, Basilio, Dario, Nicolò, Alexandros, Ben, Robin, Jeremy, Catalin, Taouba, Luca, Ilnura and Sabrina, among others.

Thanks also to Dr. Adrià Junyent, who made my second international mobility possible at the Control and Power Research Group (Imperial College

London) for a period of three months. It is undeniable that his knowledge and encouragement were vital to rebuild and test a functional experimental platform that seemed impossible to be set up in such a short period of time. Many thanks to the colleagues in the group who made my stay more than enjoyable, specially to Joan Marc, Nikhil, James, Willem, Jochen, Michael, Caspar, Anastasios, Nico, Carlos and Jelena. Also, to some of the creators of the MMC prototype, Geraint and Paul, for allowing me to bother them several times in the phone with questions about the hardware and the control of the platform.

I would like to drop a few lines for the InnoEnergy PhD school crew, with whom I spent some time throughout the course of my PhD in different courses and workshops around Europe (as well as *extracurricular* activities). A special mention to Konstantinos, Boaz, Tom, Guillaume, Miquel, Dhruv, Amin and Arthur, among many others. It was a pleasure to meet you and I hope we can meet again in the future.

Fora de l'àmbit laboral, donar les gràcies a tots els amics de Premià i rodalies, per la seva amistat i per la infinitat de bones estones compartides, que espero que durin molts més anys. Sense vosaltres tot seria molt més complicat.

També vull agrair a la meva la família, especialment als meus pares, Xavier i Núria, el seu suport, esforç i estima incondicional, en tots els àmbits, així com la seva ajuda sempre que ho he necessitat. Finally, I want to say thanks to Christina, for all the adventures, for being by my side in the distance and for making me lose track of time when we are together.

Abstract

High Voltage Direct Current (HVDC) is a power electronics-based technology that enables the transmission of large amounts of power over long distances, the integration of remote offshore wind power to the main land, and the interconnection of asynchronous AC systems. The Modular Multilevel Converter (MMC) is the state-of-the-art technology for Voltage Source Converter (VSC) based HVDC applications.

As compared to the two-level converter, the MMC presents a more complex control scheme. However, it brings additional flexibility into the system. As a subject of broad and current interest, several works on the MMC have been recently developed in the literature, and actual MMC-based HVDC projects are currently being installed around the world. The present work focuses on the control of the MMC for HVDC applications, aiming to understand the additional degrees of freedom related to the internal energy of the MMC.

First, the DC voltage regulation in HVDC point-to-point links is addressed. Different control structures are analysed and compared through simulations and linear analysis, highlighting the challenges of shorter HVDC links. Moreover, an experimental validation using a scaled MMC-based point-to-point link is carried out, particularly focusing on a novel experimental design of an HVDC cable emulator. With such a laboratory setup, the simulated system dynamics are contrasted with experiments. Furthermore, a generic controller for the same application is presented, and different optimal tuning techniques are investigated. Thus, the most suitable control gains are obtained automatically based on system constraints.

In HVDC applications such as remote offshore wind farm clusters or isolated systems with low or non-existing synchronous generation, the MMC needs to operate as grid-forming. Although grid-forming is well-known in two-level VSCs, the present work explores the role of the internal energy of the MMC through different control structures. Both single and multiple grid-forming scenarios are considered.

Finally, a multi-terminal HVDC grid where some terminals share the regulation of the DC voltage and others operate in grid-forming mode is considered. The distributed DC voltage droop control design methodology of such a grid is addressed, considering converters with different ratings and dealing with power sharing requirements as well as transient limitations.

viii

Resum

L'alta tensió en corrent continu (HVDC) és una tecnologia basada en electrònica de potència que permet la transmissió de gran potència en distàncies llargues, la integració de parcs eòlics marins remots a la xarxa terrestre, i la interconnexió de sistemes asíncrons de corrent altern. El convertidor modular multinivell (MMC) és la tecnologia més recent per aplicacions HVDC basada en convertidors en font de tensió (VSC).

Comparat amb el convertidor de dos nivells, l'MMC presenta un esquema de control més complex, però aporta una major flexibilitat al sistema. Degut a l'interès actual per aquesta tecnologia, se'n poden trobar nombroses investigacions a la literatura. A més, s'ha fet palès un augment del nombre de projectes HVDC basats en MMC arreu del món. Aquest treball es centra en el control dels MMC per aplicacions HVDC, amb l'objectiu d'entendre els graus de llibertat addicionals relacionats amb la seva energia interna.

En primer lloc, aquesta tesi tracta sobre el control de l'MMC per aplicacions de control de tensió contínua en enllaços punt a punt. S'analitzen i es comparen diverses estructures de control, remarcant els reptes dels enllaços curts. A continuació, es realitza una validació experimental mitjançant un enllaç punt a punt a escala basat en MMC, posant l'èmfasi en el disseny d'un emulador de cable HVDC. D'aquesta manera, els resultats de les simulacions es poden contrastar amb els experiments de laboratori. Com a darrer pas en aquesta línia, es presenta una estratègia de control genèrica i el càlcul òptim dels seus paràmetres amb diferents mètodes. Així doncs, els guanys més adequats pels controladors s'obtenen automàticament, basats en un conjunt de restriccions sobre el sistema.

En aplicacions HVDC com els grans parcs eòlics marins o els sistemes aïllats amb poca o cap generació síncrona, un o diversos convertidors han de generar la xarxa d'alterna. Tot i que aquest mode de funcionament és ha estat molt estudiat en el cas de convertidors de dos nivells, en aquest treball s'investiga el rol de l'energia interna de l'MMC, implementant diferents estructures de control en escenaris amb un i diversos convertidors.

Finalment, es considera una xarxa HVDC multiterminal, en la qual un conjunt de convertidors controla la tensió contínua i d'altres formen la xarxa d'alterna. En aquest escenari, es planteja el disseny del control distribuït de tensió contínua, tenint en compte convertidors de diferents potències i considerant la distribució del flux de potència, així com els límits transitoris.

x

Contents

Contents

Nomenclature

2L	Two-level
ABB	ASEA Brown Boveri
AC	Alternating Current
AAM	Average Arm Model
CCSC	Circulating Current Suppressing Control
CIGRÉ	Conseil International des Grands Réseaux Électriques
CITCEA	Centre d'Innovació Tecnològica en Convertidors Estàtics i Accionaments
CM	Compensated Modulation
CSG	China Southern Power Grid
CTL	Cascaded Two-level
DC	Direct Current
DCC	Droop Controlled Converter
DFIG	Doubly-Fed Induction Generator
EIT	European Institute of Technology
EMTP	Electromagnetic Transient Program
FACTS	Flexible Alternating Current Transmission Systems
FOSG	Friends of Sustainable Grids
GFC	Grid-Forming Converter
HVDC	High Voltage Direct Current
HVAC	High Voltage Alternating Current
IGBT	Insulated-Gate Bipolar Transistor
INELFE	Interconexión Eléctrica Francia-España
IMC	Internal Model Control
LCC	Line-Commutated Converter
LPF	Low-Pass Filter
LQE	Linear Quadratic Estimator
LQG	Linear Quadratic Gaussian
LQR	Linear Quadratic Regulator
MIMO	Multiple-Input Multiple-Output
MMC	Modular Multilevel Converter

MT	Multi-terminal
NECP	National Energy and Climate Plans
NSWPH	North Sea Wind Power Hub
NSCOGI	North Seas Countries Offshore Grid Initiative
OWPP	Offshore Wind Power Plant
PCC	Point of Common Coupling
PI	Proportional-Integral
PID	Proportional-Integral-Derivative
PLL	Phase-Locked Loop
PR	Proportional-Resonant
PWM	Pulse-Width Modulation
REE	Red Eléctrica de España
RES	Renewable Energy Sources
RMS	Root Mean Square
SACOI	Sardinia and Corsica Islands
SCR	Short-Circuit Ratio
SISO	Single-Input Single-Output
SQP	Sequential Quadratic Programming
SRF	Synchronous Rotating Frame
SVD	Singular Value Decomposition
SSTI	Steady-State Time Invariant
TSO	Transmission System Operator
UCM	Uncompensated Modulation
UHVDC	Ultra High Voltage Direct Current
ULM	Universal Line Model
UPC	Universitat Politècnica de Catalunya
VSC	Voltage Source Converter
WFC	Wind Farm Converter
WPP	Wind Power Plant
XLPE	Cross-linked Polyethylene

Chapter 1

Introduction

1.1 Current context

Nowadays, the way electricity is produced and consumed has undergone important changes as compared to few years ago. It is undeniable that the power system is evolving at a high pace and that a new scenario is emerging. This difference is mainly found in the increase of renewable energy generation, particularly wind and solar power. It is obvious that these environmental-friendly resources of energy will gradually replace conventional thermal power plants. Also, it is remarkable that some environmental policies are pointing to the closure of nuclear facilities due to security and nuclear waste treatment concerns. Furthermore, storage, demand-side response and electric mobility will provide the power system with high flexibility, and the whole electric value chain is already influenced by digitalisation [1].

This near future scenario poses some new challenges. In most cases, these renewable sources will be located far away from the consumption areas, which means that there is a necessity of a new infrastructure that transports this energy, as well as optimising the already existing one. This is where power electronics, and more specifically high-voltage direct current (HVDC) technology, comes into play. It is well-known that high-voltage alternating current (HVAC) presents limitations related to reactive power. This is the case of long submarine and underground links, and also very long overhead connections. In such cases, beyond a certain distance it is more cost-effective to adopt direct current (DC) rather than alternating current (AC) technology [2].

Several HVDC connections already exist around the world. For instance, in the Spanish context, a 2×200 MW submarine connection between the Spanish peninsula and Mallorca island [3]), and the 2×1000 MW underground interconnection between Spain and France through the Pyrenees [4,5] (Fig. 1.1). A new project expected to be commissioned in 2025 is the Biscay Gulf project, another interconnection between Spain and France of 2×1000 MW. This 370 km link will be the first undersea connection between both

countries, with 280 km of submarine cable [6] (Fig. 1.2. Both are part of the Interconexión Eléctrica España-Francia (INELFE) project.

Fig. 1.1: Baixas (France) - Santa Llogaia (Spain) connection (INELFE) [7]
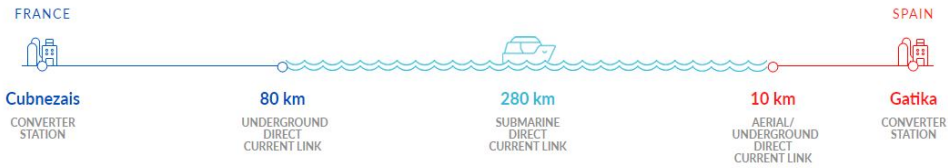
Fig. 1.2: Cubnezais (France) - Gatika (Spain) connection (INELFE) [7]

The 2030 National Energy and Climate Plans (NECPs) establish a 32% of renewable energy target in Europe. Therefore, the next 10 years will be crucial for each European country to develop and implement the necessary solutions to achieve that goal, and in such a context, wind energy will be a key player, both onshore and offshore [8]. The yearly onshore and offshore installations in Europe from 2013 to 2023, as well as the overall cumulative capacity, are shown in Fig. 1.3. The tendency is clearly upward, specially in the case of offshore wind (2023 estimate).

By 2023, Germany will remain as the first country with the largest wind fleet (a total amount of 72 GW in the Central Scenario, and the leader in onshore wind), followed by Spain (32 GW) and the UK (29 GW) [8]. Regarding offshore wind, the United Kingdom will remain on the top of the list (see Fig. 1.4). By 2050, Europe is expected to have a total amount of 450 GW of offshore wind power generation: 212 GW in the North Sea, 85 GW in the Atlantic Ocean, 83 GW in the Baltic Sea and 70 GW in Southern European waters [9].

Friends of Sustainable Grids (FOSG) is an institution that gathers several European organizations that are working on the idea of the Supergrid the future (Fig. 1.5), which is defined as a pan-European transmission network facilitating the integration of large-scale renewable energy and the balancing and transportation of electricity with the aim of improving the European market [10].
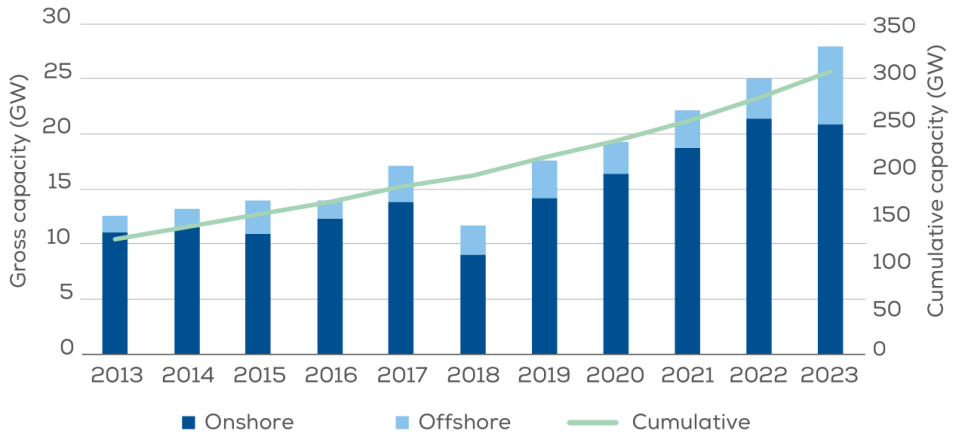
Fig. 1.3: Yearly and cumulative total wind generation capacity in Europe (2013-2023) [8]
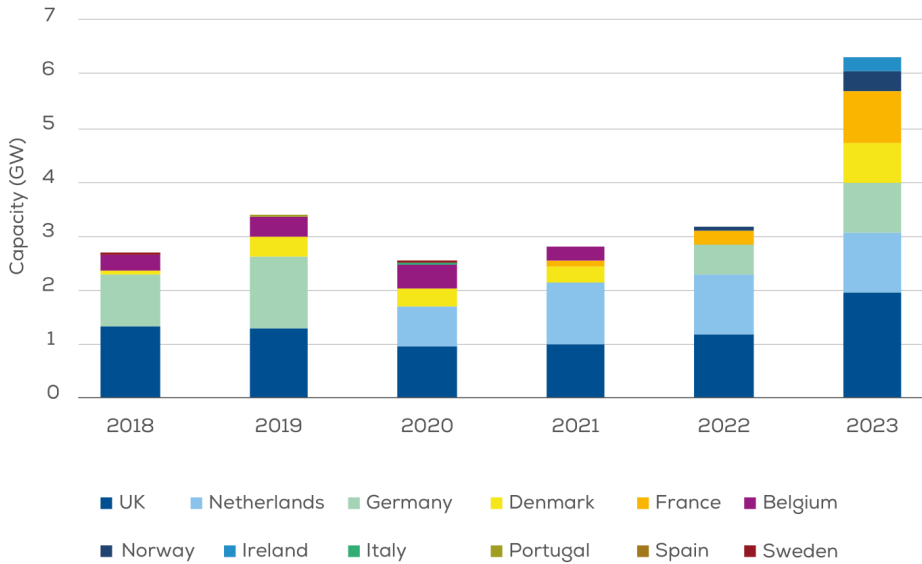
Fig. 1.4: Yearly offshore wind generation capacity in Europe (2018-2023) [8]

Fig. 1.5: The conceptualisation of the European Supergrid [10]

The Supergrid is a key enabler for a secure, cost-effective and sustainable power system. Such a grid, made of HVDC links, interconnectors and AC ultra-high power transmission, offers ways to extend the solidarity promoted by the EU energy policy in line with the evolution of the European power system. The bulk power highways provided by the Supergrid will complement the deployment of local renewable energy sources (RES) solutions and add flexibility to the new microgrids systems [10].

From a worldwide perspective, the number of offshore wind installations in the last years has been also relevant. China installed 1.8 GW of offshore in 2018, more than any other country in the world, and the emerging Asian market will surely take a leading role [11]. Besides, China is building its own hybrid AC/DC supergrid, the biggest in the world, with more than 30000 km of UHVDC (Ultra HVDC) lines (Fig. 1.6).

Although these supergrids contribute towards a more sustainable model, they present important technological challenges for the power system. This is due to the amount of power electronics devices that are (and will be) part of the whole transmission system. China is already seeing problems in the stability of the grid, which has led to operate the HVDC links at a low capacity to avoid potential cascaded blackouts in case of HVDC lines trips. One of the solutions they are studying is to keep increasing the number of HVAC lines to make the AC system more robust [12]. Most of the currently

installed HVDC links in China are thyristor-based, whereas with the latest advances in transistor-based HVDC technology most of these problems could be solved through meshed HVDC grids [13]. However, the transistor-based technology has not yet seen power levels as high as the thyristor-based one. Therefore, these different visions will likely co-exist and evolve during the upcoming years.
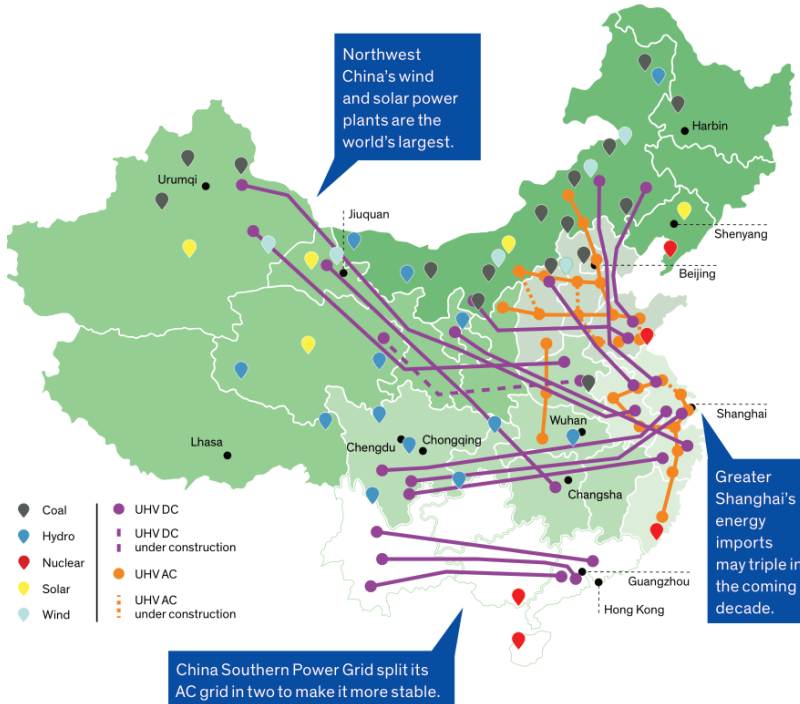
Fig. 1.6: China's hybrid AC/DC grids [12]

1.2 HVDC transmission

1.2.1 Converter technology

HVDC is becoming a relevant technology within the power system. Submarine connections for offshore wind integration, interconnection of asynchronous AC systems, and very long distances are its main applications [14]. There are two main converter technologies regarding HVDC transmission:

- **Line Commutated Converter**

  The Line-Commutated Converter (LCC) uses thyristors as switches, and it is already a well-established and mature technology for HVDC. However, it presents some disadvantages: polarity change is needed to enable power flow reversal, a stable AC grid has to be available for the feasible operation of the converter, and bulky filters are required. Thyristors are line-commutated devices, meaning that they can be triggered sending a pulse to its gate but they require an AC grid to switch off. Because of this fact, they cannot feed passive loads or create an isolated AC grid by themselves. They cannot control independently active and reactive power and require bulky filters. Nonetheless, this technology has achieved a high degree of reliability and maturity since many decades ago, and it is suitable for Ultra HVDC (UHVDC) (i.e. pole-to-pole DC voltages higher than 1000 kV), specially in China [12].

- **Voltage Source Converter (VSC)**

  Voltage Source Converters are based on Insulated Gate Bipolar Transistors (IGBTs). They are self-commutated devices, which means that they do not require the grid to commutate. For this reason, they are able to feed passive loads or create an isolated AC grid. Moreover, VSCs have black-start capability, and they can control active and reactive power independently [15]. Harmonics are reduced, which leads to a reduction of size of the filters and consequently the footprint of the converter, as compared to LCC. A drawback of VSCs is that their losses are higher than an LCC station of the same power. Besides, the power rating for VSCs is still smaller than for LCCs. Traditionally, VSC was based on two-level (2L) and three-level (3L) converters. However, new generations already use Modular Multilevel Converters (MMC), specifically for high voltage applications (Fig. 1.7). This converter uses sub-modules in series that are either inserted or bypassed, being able to synthesize an stepped sinusoidal voltage waveform with low harmonic content, which allows for further filters reduction [14]. Also, it presents lower losses, scalability and redundancy [16, 17].

  Although most of the offshore wind power plants (OWPPs) are connected through AC, VSC-HVDC based interconnections are key for remote OWPPs. The first VSC-HVDC based offshore wind farm was BorWin1 [18], built in the North Sea in 2009 by ABB. The converter technology used is the Cascaded two-level (CTL), which is a 2L-VSC with several IGBTs in series that switch together. Several VSC-HVDC
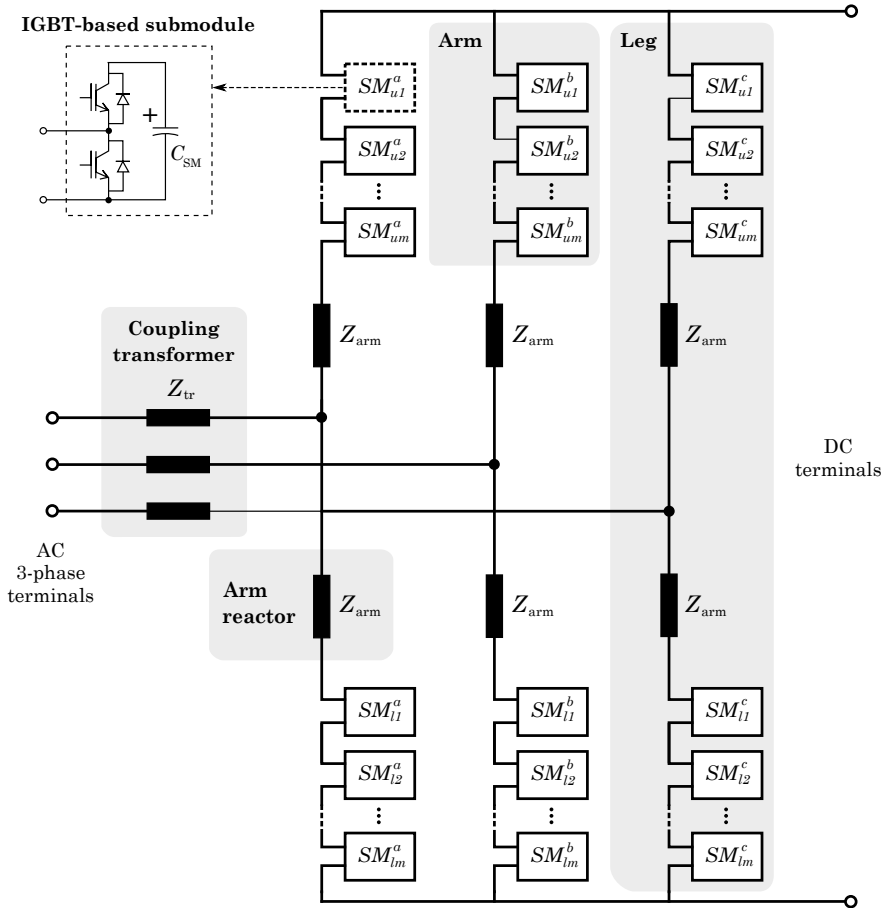
Fig. 1.7: MMC topology

links for integration of offshore wind have been commissioned success-fully in the North Sea since then, e.g. DolWin1 and DolWin2 [19] from ABB. In those cases, the technology was MMC, using a num-ber of series connected IGBTs in each submodule. Examples from Siemens are BorWin2, SylWin1, HelWin1, HelWin2 and BorWin3 [20], all of them belonging to TenneT [21], the German-Dutch transmis-sion system operator (TSO). In this case, the converter topology is MMC. Also, MMC-based VSC-HVDC has been used for several in-terconnectors, such as Trans Bay Cable [22] (USA, 2010), the afore-mentioned INELFE project [5] (Spain-France, 2015), Cobra Cable [23] (The Netherlands-Denmark, 2019) and the Maritime Link [24] (Canada, 2019), among others. Moreover, several are planned for 2020, such as NordLink [25] (Germany-Norway, ABB) and Eleclink [26] (Great Britain-France, Siemens).

A picture of one of the substations of the first INELFE project is shown in Fig. 1.8. This one corresponds to Santa Llogaia substation, in the Spanish side of the link. Different parts can be observed: the buildings with the MMCs inside, transformers, filters and the AC substation. A picture of the inside of the MMC building is shown in Fig. 1.9, which is composed by hundreds of submodules. A detailed picture of one submodule is shown in Fig. 1.10.

Fig. 1.8: INELFE project – Santa Llogaia substation in Spain (Courtesy of Siemens)

Fig. 1.9: INELFE project – MMC (Courtesy of Siemens)

Fig. 1.10: Power module of the MMC (Courtesy of Siemens)

1.2.2 Topologies and configurations

Depending on how the different converters of an HVDC system are distributed, they can be classified in the following topologies [2]:

- **Back-to-back**

  In this topology, both the rectifier and the inverter are located in the same place, connected either through a very short HVDC link or without any link. Back-to-back topology enables the interconnection of asynchronous AC systems, for instance in the case of two neighbouring areas working at different frequencies.

- **Point-to-point**

  This is the most extended topology, based on the connection of two converter stations, either separated by long distances, with the aim of bulk-power delivery, or subsea/underground connections usually longer than 60-80 km.

- **Multi-terminal**

  Multi-terminal (MT) systems contain, at least, three converter stations, separated and linked by DC transmission lines [27]. Within this topology, the power flows have only one path to go from one station to another. This scheme presents some advantages regarding flexibility, although its control and operation become challenging. Up to now, there are five MT-HVDC systems running worldwide. Three of them are LCC-based: Quebec-New England (Canada-USA), the SACOI system (Italy mainland-Sardinia and Corsica islands), and the UHVDC North-East Agra in India [16, 28]. The other two employ VSC-based HVDC, and have been installed in China: Nan'ao wind farm three-terminal project [29, 30] (2013), and Zhoushan five-terminal HVDC project [31, 32] (2014). Furthermore, the idea of combining the advantages of LCC and VSC through hybrid LCC-VSC systems has gained relevance in the last years [33]. The Wudongde project for hydro power transmission in the China Southern Power Grid (CSG) network is the first hybrid MT-HVDC installation in the world, which is planned to be in operation in the next years [34].

- **Meshed DC grid**

  Meshed DC grids are multi-terminal setups (with three or more stations) with DC interconnections conforming a mesh. This means that

power flows have different possible paths throughout the grid when flowing from one converter to the other. Meshed grids are more flexible than multi-terminal topologies. However, they may need additional devices to rule the power flows. There are different projects or initiatives calling for a DC grid interconnecting several countries of Europe. Some examples are the North Sea Wind Power Hub (NSWPH) [35] and the North Seas Countries' Offshore Grid Initiative (NSCOGI) [36]. Both could be building blocks of the so-called European Supergrid (Fig. 1.5). Another recent project is the four-terminal meshed DC grid in Zhangbei, aiming to integrate bulk wind, hydro and solar power resources into Beijing. Additional terminals are planned to be added and expand the original meshed DC grid in 2021 [37, 38].

Several configurations exist in terms of interconnecting the different converter stations within an HVDC system. The three main ones are listed in the following [39, 40]:

- **Asymmetrical monopole**

  One active conductor at the converter rated voltage and one neutral conductor (or metallic return) at near zero voltage are used in the asymmetrical monopole configuration (Fig. 1.11). The neutral conductor is rated at the nominal current, but the insulation is much lower as compared to the active conductor, thus implying a lower cost. In some cases, a ground return can be considered instead, if earth currents are allowed and both terminals are grounded. In order to prevent the neutral conductor to raise its voltage, it has to be low-impedance or solidly grounded. However, in case of faults, the current increases faster, and fault clearance schemes are needed. Therefore, it might be useful to consider other grounding schemes (resistive, inductive, etc.) to overcome steady-state and transient fault current and voltage issues [40].

- **Symmetrical monopole**

  Two active high-voltage conductors withstand half the converter rated voltage and operate at opposite DC voltages (positive and negative) in the symmetrical monopole configuration. A neutral point is usually available by means of symmetrical DC capacitors connected to each pole. This neutral point can be grounded with low or high impedances. After a fault, in the first case the voltage of the neutral point is close to zero, and the healthy pole raises its voltage until the converter rated
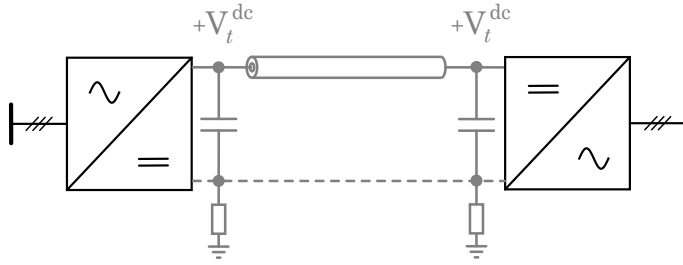
Fig. 1.11: Asymmetrical monopole configuration

voltage value. In the second case, the voltage of the neutral point is not zero, and the converter voltage is shared between the capacitors. The steady-state fault current is zero in all cases, unless the AC side transformer is star-grounded at the converter side, or omitted [40]. Thus, fault clearance strategies can be slower in the symmetrical monopole case, and usually they rely on the AC side protection. The present thesis focuses on this kind of configuration. However, as this work does not deal with faults, the impact of using this configuration or another one is not so significant.
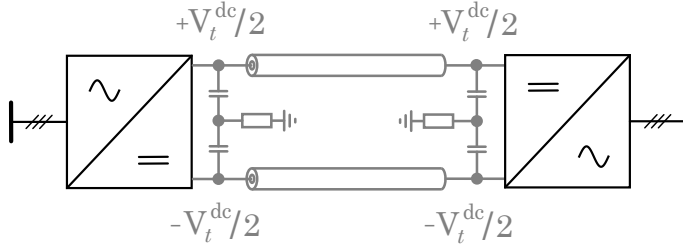
Fig. 1.12: Symmetrical monopole configuration

- **Bipole**

  In the bipolar configuration, two asymmetrical monopoles are connected through the ground connected pole, usually metallic return. In each of the AC sides, two converters operate in parallel, each of them with its own transformer. This configuration offers redundancy in the sense that it can remain in operation if one pole is lost. In that case, the remaining healthy pole operates as an asymmetrical monopole.
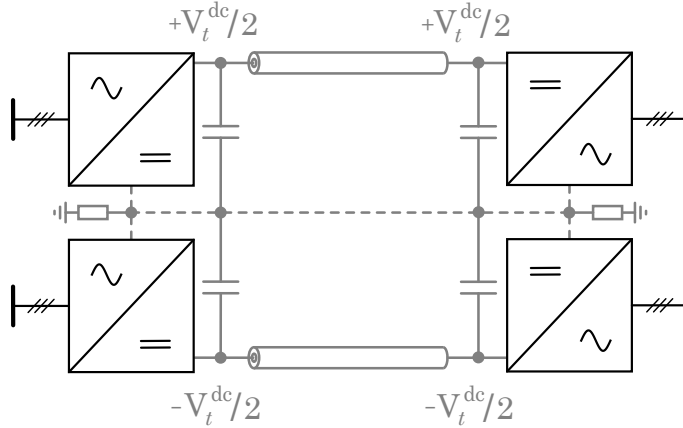
Fig. 1.13: Bipole configuration

1.3 Objectives and scope

Several past and more recent works in the literature deal with different kinds of VSC-based HVDC systems. The majority of these studies are based on 2L-VSC converters, as a way of simplifying the system and easing the analyses. In reality, at the power system transmission level, the converters used are in most cases MMCs. The main research question that this thesis aims to answer is the following:

- What is the impact and what are the capabilities of the MMC in HVDC applications?

Of course, this is a very broad topic, and some boundaries need to be established to address more specific questions. In general terms, the present work considers detailed MMC models, in order to thoroughly investigate the impact of the MMC in the different high-voltage systems under study, avoiding inaccuracies related to using equivalent 2L-VSC models. A conceptual scheme of the different control layers of the MMC is shown in Fig. 1.14. The main focus of this thesis is put on the **outer control** of the MMC, where the total energy plays a crucial role. Thus, an **energy-based control** approach is adopted, meaning that the energy of the MMC's arms is explicitly controlled, which will be discussed and justified later on. Whereas the internal current loops are considered in the models as they affect the system dynamics, the modulation and the submodule sorting algorithms are excluded, as these internal control layers are independent from the other ones. Instead, average models are used for the converters, as will be discussed in Chapter 2.
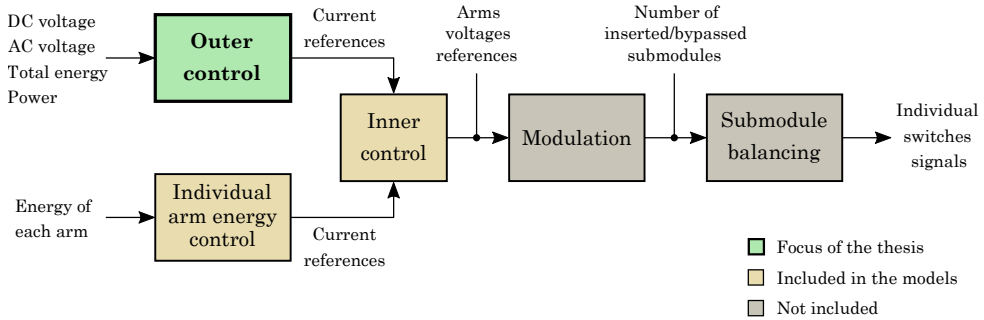
Fig. 1.14: Control layers of the MMC

Based on these premises, some more specific questions are formulated to better define the scope of this thesis, which correspond to the objectives of the thesis:

1. What control structures are reasonable to be implemented in MMCs controlling the DC voltage? How do they compare against each other, what is their impact and when are they more suitable?

2. What tuning techniques can be useful to optimally tune the MMC controllers under specific requirements, to achieve an adequate dynamic performance?

3. What role does the internal energy play in MMCs operating in grid-forming mode, under the classic frequency-droop control approach?

4. What is the impact of the MMC in multi-terminal HVDC systems where DC voltage droop control is adopted, and how can the control system be properly designed?

A conceptual overview of the different systems and applications analysed in this work is depicted in Fig. 1.15, which can be seen as a roadmap of the different objectives of the thesis. This system consists of a conceptualisation of the power system of the future, looking a few years ahead. Such a system includes a relevant number of power electronics devices (HVDC) integrated into the AC system, used to integrate renewable energy resources, connect islanded systems and interconnect the overall system to share clean energy resources. Different elements of such a complex power system are analysed in this thesis, aiming to answer the aforementioned questions.
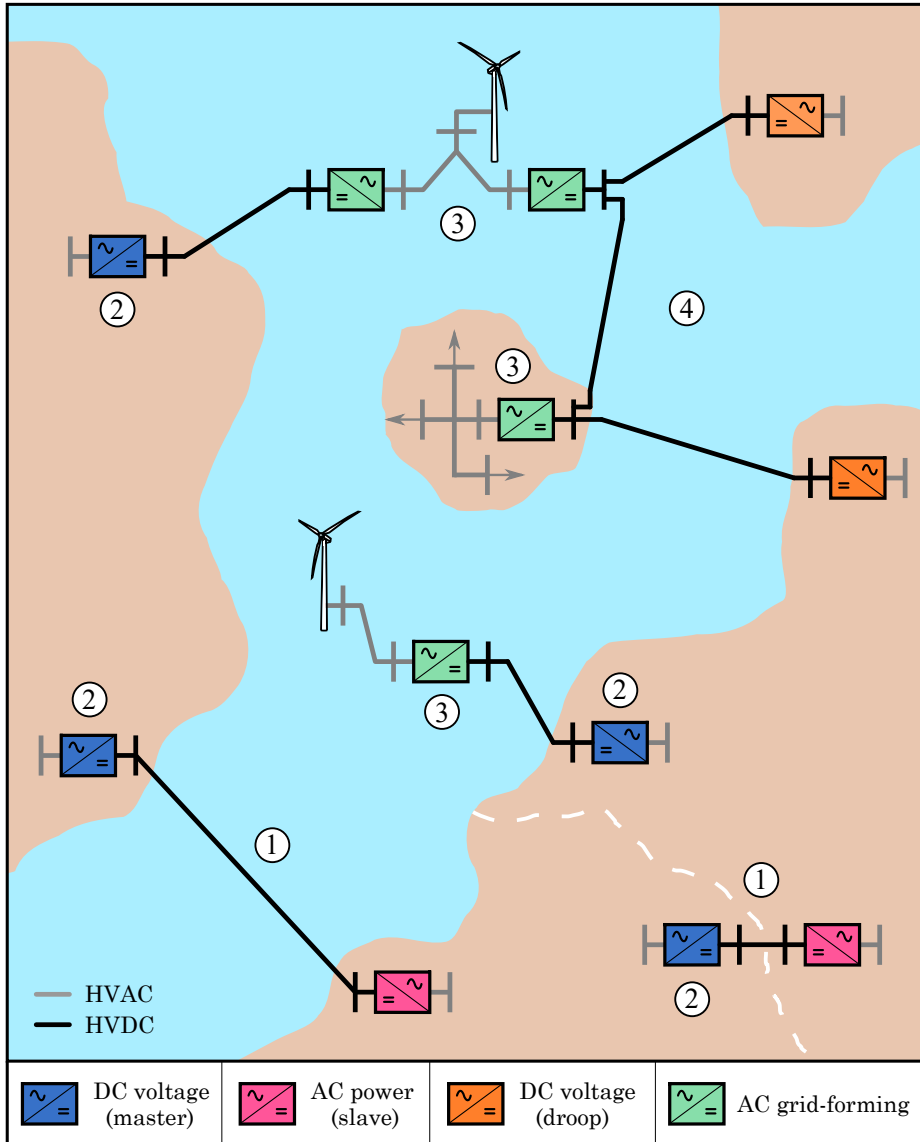
Fig. 1.15: Overview of the different systems under study in this thesis: point-to-point links, multi-terminal grids, offshore wind farms, and islanded systems

The numbers indicated in this figure correspond to the systems related to each of the objectives:

1. **Analysis of control structures of a master MMC in a point-to-point HVDC link**. Thanks to the degrees of freedom offered by the MMC topology, different alternatives for the control structure are discussed and analysed. Using a point-to-point HVDC link ① as a case study, small-signal analysis is performed, in order to identify potential instabilities and interactions in each case. Special emphasis is put on the effect of the link length. The reason to focus on the master converter is that the control of the DC voltage with MMCs is particularly challenging due to the lack of a big capacitance in the DC terminals, and the control structure is not clear. On the contrary, the control of a slave converter, which controls the AC power, can be implemented in the same way as in 2L-VSCs, and the energy control is implemented independently. That control scheme is already consistent and does not present relevant challenges as long as the DC voltage is stable, which is the responsibility of the master converter.

   - **Experimental laboratory validation of the MMC-based point-to-point HVDC link**. Complementarily to the previous objective, an experimental platform is set up and used to demonstrate the stable operation of the system. A scaled HVDC cable, as a crucial element of the system, is designed and built. A comparison between the simulated high-voltage real system and the laboratory-scaled low-voltage equivalent platform is performed to show the validity of the results.

2. **Design of an optimally tuned generic control structure for a master MMC and exploration of its dynamic performance capabilities**. Based on the control structures comparison carried out in the first stages of this research, a generic multivariable controller for a master MMC ②, which includes the controllers discussed in the previous point as particular cases, is presented. An optimal tuning of the control parameters based on different criteria and methods is investigated, while emphasising the effect of the external DC side energy and the internal MMC energy.

3. **Analysis of the role of the internal energy of the MMC in grid-forming operation**. Moving into the other main operation mode, i.e. when the converter generates the AC grid voltage and frequency ③, different control structures for the internal MMC energy are explored.

The mitigation and firewall capabilities of the MMC (i.e. the efficient use of the MMC internal energy to prevent the propagation of disturbances between the AC and DC sides) are investigated when frequency droop and AC voltage control are implemented in the MMC. These scenarios include remote offshore wind farm integration, islanded systems, and completely passive systems, in both single or multiple converter setups. The single grid-forming case is investigated through small-signal analysis and the different control structures are designed using optimal tuning, whereas a multiple grid-forming setup is simulated to extend the results.

4. **Design methodology of the MMC controllers in a multi-terminal setup**. A further and final step of the present work is to design the controllers of the MMCs that regulate the DC voltage within a MT-HVDC network (4), ensuring an adequate power sharing. As this scenario is an extended case study that includes some of the aforementioned applications, some of the previous outcomes are taken into account. Therefore, the study focuses on the DC voltage control through different droop structures in a generic scenario where the MMCs can be rated at different powers. Stability analysis, optimal tuning design and time-domain simulations are used to the present the results.

1.4 Thesis outline

The content of the thesis is organised in the following chapters and appendices:

- **Chapter 2** presents the overall MMC control used throughout the thesis, and the non-linear and linearised models of the elements that compose the different systems under study (previous work necessary to develop the objectives of the thesis).

- **Chapter 3** analyses different control structures of the MMC operating in DC voltage control mode, using a case study of a point-to-point HVDC link. It is emphasised how a short link can degrade the dynamic performance and the stability of the system (**objective 1**).

- **Chapter 4** presents a laboratory-scaled experimental setup of an MMC-based point-to-point HVDC link. A frequency dependant DC cable emulator is designed and built, and the performance of the HVDC link is validated experimentally (complementary to **objective 1**).

- **Chapter 5** investigates a generic multivariable controller for DC voltage control mode, focusing on its tuning via optimal control techniques under different requirements to achieve an adequate dynamic performance (**objective 2**).

- **Chapter 6** analyses the role of the MMC in grid-forming mode operation. Different structures are presented and their capabilities are investigated (**objective 3**).

- **Chapter 7** extends the aforementioned results to the MT-HVDC grid case, proposing a systematic control design for a generic system with DC voltage droop controlled MMCs (**objective 4**).

- **Appendix A** lists the publications from the author, both related and non-related to the thesis.

- **Appendix B** presents relevant mathematical transformations used throughout the thesis.

- **Appendix C** briefly covers the fundamentals of small-signal analysis, which has been widely used in the present work.

- **Appendix D** presents the characterisation of the MMC transformer from the experimental test bench, through open-circuit and short-circuit tests.

1.5 Work developed during the thesis

A summary of the work and the relevant activities that the author has been involved in during the development of the thesis is presented in this section. This is also summarised in Fig. 1.16.

In September 2015, a project with the Spanish TSO (REE) called "FACTS: state of the art" started. This work consisted of a review of the current trends in FACTS technology, relevant manufacturing companies, existing and ongoing installations and a thorough technical analysis, as well as design guidelines. Despite the confidentiality of such a reference guide, which REE will use for their own purposes, part of this work was published by Futured in the technical guide [O1]. This work is not included in the thesis.

In 2016, another project with REE started. It was related to the design and teaching of a course dealing with interactions of power electronics in power systems, with the objective of training engineers and technicians from

different departments of REE in this topic. There was a total amount of three editions of the course, that was taught during 2017. This work is not included in the thesis.

Also in 2016, the three-year project called "Breaking technical, economical and regulatory barriers for the development of DC Supergrids" (ENE2015-67048-C4-1-R), funded by Ministerio de Economía y Competitividad (Spanish Government), started. A relevant portion of the work carried out in this thesis is related to this project. The first article that was published was the conference paper [C1], based on an initial analysis of the impact of MMCs in droop controlled MT-HVDC grids. Following on this study, a more in-depth work on the MMC control was addressed, resulting in the journal paper [J1], comparing different control structures of an MMC controlling the DC voltage, e.g. the master converter of a point-to-point HVDC link, and highlighting the problem of short HVDC links. This was also done in collaboration with Imperial College London. Furthermore, based on this work, another conference paper [C2] was published, dealing with the impact of the DC and internal MMC capacitances in the performance of the converter.

The first international placement took place from November 2017 to March 2018, at the Automatic Control Laboratory, ETH Zürich, Switzerland. The topic was control of grid-forming converters and optimal tuning techniques, which resulted in the journal paper [J2]. After this first contact between CITCEA-UPC and ETH, an active collaboration has been established between both institutions.

The second international placement was carried out from September 2018 to December 2018, at the Control and Power research group, Imperial College London, United Kingdom. The topic was related to experimental validation of a scaled point-to-point MMC-based HVDC platform, and resulted in the conference paper [C3]. Future collaborations are also expected to be established in relation with this topic.

In 2019, another three-year project called "Control of a grid composed by multiple AC and DC grids interconnected through power electronics converters" (RTI2018-095429-B-I00), funded by Agencia Estatal de Investigación (Spanish Government), started. The project has also been closely related to the work developed in this thesis. So far, it has partially led to the aforementioned publication [J2], and to another journal paper [J3] dealing with the role of the internal energy through different control structures in MMCs operating in grid-forming mode.

Moreover, the author has collaborated with other researchers in the group, resulting in the respective outcomes: a conference paper [C5] and a journal paper [J4] related to fractional PR controllers in VSCs; a conference paper

[C6] and a journal paper [J5] dealing with DC voltage droop control design; and two conference papers on the topic of stability and interaction analysis of DFIG-based WPPs with MMC-based HVDC links [C7] and islanded power systems containing VSC and LCC HVDC links [C8].

The author is also a PhD Candidate of the EIT InnoEnergy PhD School programme. This European institution focuses on bolstering the connections between industry and academia in order to create collaborative opportunities between laboratories and the actual market. The InnoEnergy PhD School allows doctoral candidates to complement their research with essential entrepreneurial, business and innovation training, together with personal skills.
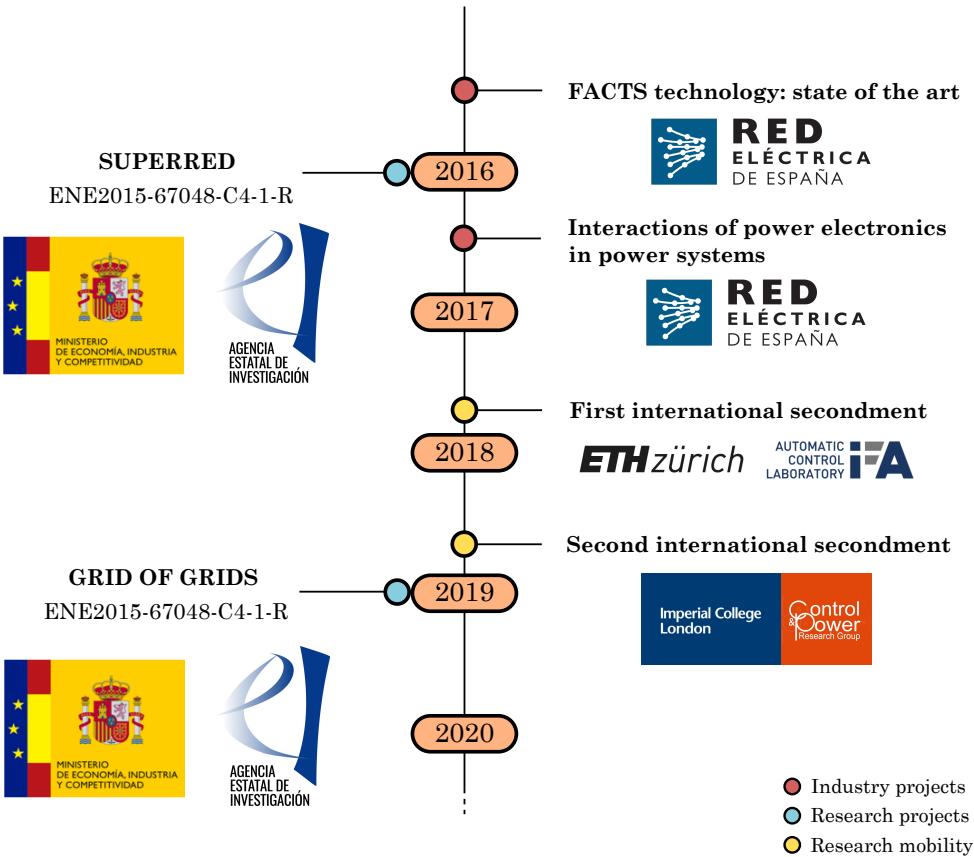

Fig. 1.16: Timeline of the projects and main activities carried out during the thesis

Chapter 2

System modelling and control

2.1 Introduction

As the work of this thesis is mainly based on the simulation of electrical systems and on the analysis of the dynamic properties of them, the modelling of the different elements and subsystems must be carefully addressed. This is a key aspect in the sense that these models aim to represent the real system elements. The modelling of power electronics converters can be addressed at different levels of detail. Seven different model types are presented in [41], from full physics models to RMS load-flow models. In a more general way, and from the point of view of the present work, three main types of models can be identified:

- Non-linear switched model: While different level of details can be expected in such a model [41], in general it includes an explicit representation of the submodules and switching events. It is mainly useful for the assessment of components stress, submodule control strategies, modulation and fault analysis. As it is not within the scope of this thesis to analyse the aforementioned issues, this model is not used in any of the studies that will be presented.

- Non-linear average model: This model avoids the modelling of the switches and the submodules, and hence does not consider neither the modulation nor the sorting algorithms. Instead, the internal arms are simplified and replaced by Average Arm Models (AAM), which considerably reduces the simulation time. This model and variations of the same concept are well established in recent literature [42,43], and has been also validated experimentally [44]. This model is widely accepted for analysis and controller design. In the present thesis, this model has been implemented in Matlab Simulink and it is used as a benchmark reference model.

- Linearised model: This model is based on the previous non-linear averaged model. Non-linear elements such as saturations are removed, and non-linear equations are linearised. As it will be seen next, the energy balance between arms and legs is also simplified, and a single overall energy equation is used. This model is suitable for small-signal analysis, allowing for the study of stability, modes of the system, participation factors, frequency response and also optimal control tuning based on different system metrics.

As mentioned in the introduction, the Modular Multilevel Converter (MMC) has emerged as the preferred VSC alternative because of low losses, low harmonic distortion, scalability and redundancy [16, 17]. However, the control of the MMC becomes more challenging than the classic two-level (2L) VSC, due to the extra degrees of freedom inherent to its topology. A description of the MMC control adopted in this work is presented in this chapter.

In order to obtain intrinsic information from the system that can not be retrieved from time-domain simulations (i.e. stability, inherent modes of the system, etc.), small-signal analysis (see Appendix C) has to be used. In that case, the analytical model of the system needs to be known, which can be a problem if some parts of the system are uncertain or unknown. Even if the analytical model is known, it has to be linear, which is not usually the case. If the model is non-linear, it must be linearised, meaning that the conclusions obtained from the subsequent analysis will be only valid at an area close to the operating point. The more non-linear the system, the smaller the region where the model is valid. In this chapter, the linearisation of such non-linear models is derived, which will be used throughout the thesis for the aforementioned purposes. It has to be noted that the small-signal analysis has to be complemented with non-linear simulations through an EMTP (Electromagnetic Transient Program), in order to validate the results and conclusions obtained with the linear analysis. In the present work, average models have been used, as fault studies have not been investigated in detail.

2.2 MMC electrical circuit and steady-state model

2.2.1 Electrical circuit

The MMC is composed by three upper arms and three lower arms. The upper arms are star-connected (top part of the electrical circuit in Fig. 2.1), and the same applies for the lower arms (bottom part of the electrical circuit in Fig. 2.1). Each of the nodes where the arms are connected correspond to

the positive and the negative poles of the DC side, respectively. Each pair of upper-lower arms corresponds to a leg, i.e. a phase, and the middle point of each leg is connected to the corresponding phase of a transformer or a phase reactor on the AC side.

Using voltage Kirchhoff's law, the MMC equations per phase ($j = a, b, c$) are

$$V_u^{\mathrm{dc}} - v_u^j - u^j - v_n = R_a i_u^j + L_a \frac{di_u^j}{dt} + R_s i_s^j + L_s \frac{di_s^j}{dt} \tag{2.1}$$

$$-V_l^{\mathrm{dc}} + v_l^j - u^j - v_n = -R_a i_l^j - L_a \frac{di_l^j}{dt} + R_s i_s^j + L_s \frac{di_s^j}{dt} \tag{2.2}$$

being

R_a, L_a: arm resistance and inductance.
R_s, L_s: AC grid filter (usually transformer) resistance and inductance.
V_u^{dc}, V_l^{dc}: upper and lower voltages of the HVDC link.
v_u^j, v_l^j: voltages applied by the upper and lower arms.
u^j: point of common coupling (PCC) voltage.
v_n: neutral point voltage.
i_u^j, i_l^j: current flowing through the upper and lower arms.
i_s^j: AC grid current.

For convenience, the following variable change is defined

$$
\begin{cases}
v_{\mathrm{diff}}^j \triangleq \dfrac{1}{2}(-v_u^j + v_l^j) \\
v_{\mathrm{sum}}^j \triangleq v_u^j + v_l^j \\
i_{\mathrm{sum}}^j \triangleq \dfrac{1}{2}(i_u^j + i_l^j) \\
R \triangleq R_s + \dfrac{R_a}{2} \\
L \triangleq L_s + \dfrac{L_a}{2}
\end{cases}
\quad , \quad
\begin{cases}
v_u^j = -v_{\mathrm{diff}}^j + \dfrac{1}{2}v_{\mathrm{sum}}^j \\
v_l^j = v_{\mathrm{diff}}^j + \dfrac{1}{2}v_{\mathrm{sum}}^j \\
i_u^j = \dfrac{1}{2}i_s^j + i_{\mathrm{sum}}^j \\
i_l^j = -\dfrac{1}{2}i_s^j + i_{\mathrm{sum}}^j
\end{cases}
\tag{2.3}
$$

being

v_{diff}^j: differential voltage, which is approximately equal to the AC voltage at the mid point of leg j.
i_{sum}^j: additive current, which circulates from the upper to the lower arm of leg j.
v_{sum}^j: additive voltage, which is approximately equal to the sum of the DC poles voltages.
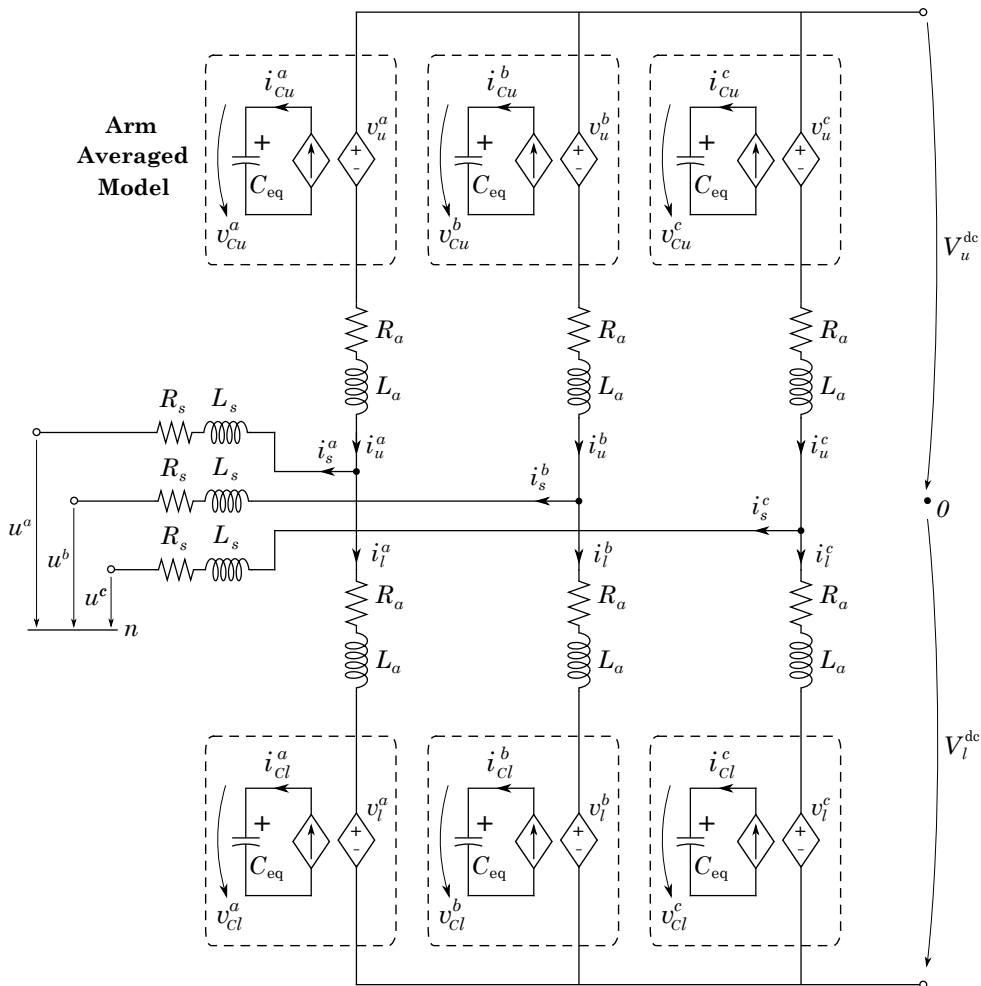
Fig. 2.1: Electrical circuit model of the MMC

Adding and subtracting (2.1) and (2.2), using the variable change from (2.3) leads to

$$\frac{1}{2}(V_u^{\text{dc}} - V_l^{\text{dc}}) + v_{\text{diff}}^j - u^j - v_n = Ri_s^j + L\frac{di_s^j}{dt} \tag{2.4}$$

$$v_{sum}^j - (V_u^{\text{dc}} + V_l^{\text{dc}}) = -2R_a i_{\text{sum}}^j - 2L_a\frac{di_{\text{sum}}^j}{dt} \tag{2.5}$$

Equations (2.4) and (2.5) ($j = a, b, c$) only contain a single derivative term (i_s^j and i_{sum}^j, respectively). This is suitable for state-space representation, as well as for designing a control scheme where each component has a clear role, as will be seen next.

Regarding the internal capacitors of the converter arms, an Average Arm Model (AAM) [45] has been considered for each of the six arms of the MMC (see Fig. 2.1), i.e. an overall capacitance C_{eq} aggregating all the submodules capacitors is considered for each arm. Each equivalent capacitance voltage[1] $v_{Cul}^{abc} \in \mathbb{R}^6$ depends on the power exchanged by each arm, which is reflected as a charging current $i_{Cul}^{abc} \in \mathbb{R}^6$ in each capacitor circuit (2.6). Note that $\mathcal{I}_6 \in \mathbb{R}^{6 \times 6}$ is the identity matrix. Furthermore, the modulated currents and voltages of each arm are calculated as (2.7) and (2.8), respectively. Note that $\circ$ denotes the element-wise product of vectors.

$$i_{Cul}^{abc} = C_{\text{eq}}\mathcal{I}_6\frac{dv_{Cul}^{abc}}{dt} \tag{2.6}$$

$$i_{Cul}^{abc} = m_{ul}^{abc} \circ i_{ul}^{abc} \tag{2.7}$$

$$v_{ul}^{abc} = m_{ul}^{abc} \circ v_{Cul}^{abc} \tag{2.8}$$

This recalls the well-known 2L-VSC average model, where a single average model composed by a DC current source and three AC voltage sources is used to couple the AC and DC side powers. In the MMC case, six average models composed by one DC current source and one AC voltage source are used to independently establish the power balance of each of the six internal arms.

---

[1]Notation x_{ul}^{abc} will be used from now on, which is defined as $x_{ul}^{abc} = (x_u^a \ x_u^b \ x_u^c \ x_l^a \ x_l^b \ x_l^c)^T$

2.2.2 Steady-state analysis

In order to understand the degrees of freedom offered by the MMC, a steady-state analysis is carried out. Using the following definitions

$$V_{\text{off}}^{\text{dc}} \triangleq \frac{1}{2}(V_u^{\text{dc}} - V_l^{\text{dc}}) \ , \qquad V_t^{\text{dc}} \triangleq V_u^{\text{dc}} + V_l^{\text{dc}} \tag{2.9}$$

equations (2.4) and (2.5) can be expressed as

$$v_{\text{diff}}^{abc} - u^{abc} + (V_{\text{off}}^{\text{dc}} - v_n)[1\ 1\ 1]^T = R\boldsymbol{\mathcal{I}_3}i_s^{abc} + L\boldsymbol{\mathcal{I}_3}\frac{di_s^{abc}}{dt} \tag{2.10}$$

$$v_{\text{sum}}^{abc} - V_t^{\text{dc}}[1\ 1\ 1]^T = -2R_a\boldsymbol{\mathcal{I}_3}i_{\text{sum}}^{abc} - 2L_a\boldsymbol{\mathcal{I}_3}\frac{di_{\text{sum}}^{abc}}{dt} \tag{2.11}$$

where $v_{\text{diff}}^{abc}, u^{abc}, v_{\text{sum}}^{abc}, i_s^{abc}, i_{\text{sum}}^{abc} \in \mathbb{R}^3$, and $\boldsymbol{\mathcal{I}_3} \in \mathbb{R}^{3\times3}$ is the identity matrix. Assuming $V_{\text{off}}^{\text{dc}}$ is zero and v_n is the zero reference voltage, the MMC can be fundamentally seen as two separate models: the AC side model and the internal model (Fig. 2.2).

(a) AC side model   (b) Internal model
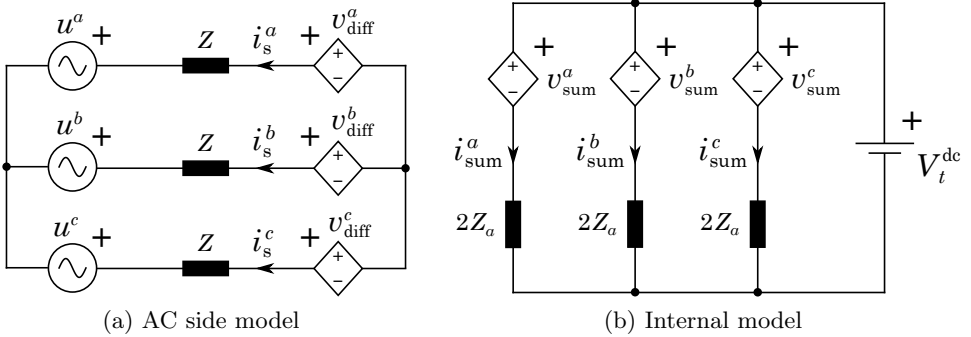
Fig. 2.2: MMC diff and sum models

The voltage applied by the arms and the current flowing through them can contain AC and DC terms. Note that this is indicated by the generic controllable voltage sources in Fig. 2.2. Each of these components have different roles in the power exchange between the converter and the AC or DC grids, and within the converter's legs and arms, as extensively discussed in [46]. A comprehensive summary is presented next.

DC analysis

First, the DC analysis is addressed. The derivative terms in (2.10) and (2.11) are removed, and the Clarke transformation (see Appendix B, (B.1)) is applied to each vector for convenience. On one hand, (2.12) is obtained. Note that the term U has been removed from the equation, assuming that the AC grid does not have any DC component (u^{abc} in Fig. 2.2a). It can be seen that $I_s^{\alpha\beta\mathrm{dc}}$ could flow to the AC side. Therefore, these components should be controlled to zero through $V_{\mathrm{diff}}^{\alpha\beta\mathrm{dc}}$, in order to avoid transformer saturation. Second, $I_s^{0\mathrm{dc}}$ is not present in the system due to the three-wire connection.

$$V_{\mathrm{diff}}^{\alpha\beta\mathrm{dc}} = R I_s^{\alpha\beta\mathrm{dc}} \tag{2.12}$$

On the other hand, (2.13) is obtained. In order to see what is the role of these components, the following must be noted:

- The additive component (v_{sum}^{j}) of both upper and lower arms voltages (v_u^{j}, v_l^{j}) is the same (see (2.3)).

- It is required that there is no DC current flowing towards the AC side.

$$I_{\mathrm{sum}}^{\alpha\beta 0\mathrm{dc}} = -\frac{1}{2R_a}\left(V_{\mathrm{sum}}^{\alpha\beta 0\mathrm{dc}} - V_t^{\mathrm{dc}}[0\ 0\ 1]^T\right) \tag{2.13}$$

Based on these two points, it is not possible to exchange power between the upper and lower arms within the same leg using these DC current components. This can be clearly seen by the fact that, within the same leg, the DC power flowing through the upper and the lower arms is the same (DC current and DC voltage are identical in each of the two arms). However, the DC power that flows through each leg can be different. Indeed, $I_{\mathrm{sum}}^{\alpha\beta\mathrm{dc}}$ can be used to exchange power between legs through the control of $V_{\mathrm{sum}}^{\alpha\beta\mathrm{dc}}$, whereas $I_{\mathrm{sum}}^{0\mathrm{dc}}$ exchanges DC power with the DC grid through $V_{\mathrm{sum}}^{0\mathrm{dc}}$.

AC analysis

To address the AC analysis, (2.10) and (2.11) are expressed in phasor domain. Also, Fortescue transformation (see Appendix B, (B.5)) is applied to each phasor vector for convenience. Note that $\underline{Z} = R + j\omega L$. On one hand, (2.14) is obtained. The AC current components $\underline{I}_s^{+-}$ (positive and negative sequence) exchange power with the AC grid through the control of $\underline{V}_{\mathrm{diff}}^{+-}$, as can be clearly seen in the circuit from Fig. 2.2a. The zero-sequence component

$\underline{I}_s^0$ does not exist due to the three-wire connection.

$$\underline{I}_s^{+-} = \frac{1}{\underline{Z}} \left(\underline{V}_{\text{diff}}^{+-} - \underline{U}^{+-} \right) \tag{2.14}$$

On the other hand, (2.15) is obtained. The positive and negative sequence components $\underline{I}_{\text{sum}}^{+-}$ are responsible for the exchange of power between the upper and lower arms through the control of the $\underline{V}_{\text{sum}}^{+-}$ voltages.

$$\underline{I}_{\text{sum}}^{+-0} = -\frac{1}{2\underline{Z}_a} \underline{V}_{\text{sum}}^{+-0} \tag{2.15}$$

However, this phenomena is not as obvious as in the DC analysis, and some further reasoning is needed. As the impedances of both the AC side and the arms are relatively small, the voltages applied by the arms can be considered to be equal to the AC grid voltage. Under normal AC grid voltage conditions, the negative voltage component is zero. Thus, the AC grid voltage can be approximated as

$$v_l^{abc} \approx -v_u^{abc} \approx \sqrt{2} \begin{bmatrix} U^+ \cos(\omega t) \\ U^+ \cos(\omega t - \frac{2\pi}{3}) \\ U^+ \cos(\omega t + \frac{2\pi}{3}) \end{bmatrix} \tag{2.16}$$

Independently from assuming that the AC network does not have a negative sequence voltage component, the MMC's additive AC currents may have both positive and negative sequence components. This current is expressed as

$$i_{\text{sum}}^{abc} = \sqrt{2} \begin{bmatrix} I_{\text{sum}}^+ \cos(\omega t + \phi) + I_{\text{sum}}^- \cos(\omega t + \alpha) \\ I_{\text{sum}}^+ \cos(\omega t + \phi - \frac{2\pi}{3}) + I_{\text{sum}}^- \cos(\omega t + \alpha + \frac{2\pi}{3}) \\ I_{\text{sum}}^+ \cos(\omega t + \phi + \frac{2\pi}{3}) + I_{\text{sum}}^- \cos(\omega t + \alpha - \frac{2\pi}{3}) \end{bmatrix} \tag{2.17}$$

Multiplying the voltage and the current, while eliminating the double frequency oscillatory terms, leads to the lower-to-upper arm power of each phase

$$P_{u \to l}^{abc} = \begin{bmatrix} U^+ I_{\text{sum}}^+ \cos\phi + U^+ I_{\text{sum}}^- \cos\alpha \\ U^+ I_{\text{sum}}^+ \cos\phi + U^+ I_{\text{sum}}^- \cos(\alpha + \frac{4\pi}{3}) \\ U^+ I_{\text{sum}}^+ \cos\phi + U^+ I_{\text{sum}}^- \cos(\alpha - \frac{4\pi}{3}) \end{bmatrix} \tag{2.18}$$

With (2.18), it is shown that $\underline{I}_{\text{sum}}^{+-}$ components can be used to exchange power between upper and lower arms. Finally, in order to avoid AC components flowing into the DC grid, $\underline{I}_{\text{sum}}^0$ must be controlled to zero.

Based on the DC and AC analysis, the role of each current component described before is summarised in Table 2.1.

Table 2.1: Converter current components and their uses

Comp.	Freq.	Comp.	Use
i_s	AC	+,-	Current from the AC grid (Fortescue components).
		0	Equal to 0 due to three-wire connection.
	DC	α,β	Controlled to zero to prevent DC current flowing through the AC grid (Clarke coordinates).
		0	Equal to 0 due to three-wire connection.
i_{sum}	AC	+,-	Internal power exchange between upper and lower arms (Fortescue components).
		0	Controlled to zero to avoid AC distortion in the DC grid.
	DC	α,β	Internal power exchange between the legs of the converter (Clarke coordinates).
		0	Power flowing onto the DC grid.

2.3 MMC control

Different control approaches for MMCs have been proposed in the literature over the last years [47]. Although several implementations can be found, they can be essentially classified in two main groups depending on how the modulation indexes are calculated.

On one hand, in the Uncompensated Modulation (UCM) [48], the modulation indexes are calculated using the DC voltage (2.19) instead of the arms' voltages. In other words, UCM does not include any compensation for the impact of the oscillations in the equivalent arm capacitance voltages on the modulated output voltages. This implies that the internal energy is self-balanced, and it is not necessary to explicitly control it.

$$m_u^j = \frac{v_u^j}{V_t^{\mathrm{dc}}}, \quad m_l^j = \frac{v_l^j}{V_t^{\mathrm{dc}}}, \quad j = a, b, c \qquad (2.19)$$

The so-called direct modulation [49] and open-loop modulation [50] can be included in this group. The UCM approach inherently yields an asymp-

totically stable system [42]. However, the internal dynamics depend on the converter impedances rather than being imposed by a controller. This may lead to slow time constants and undesirable overshoots, specially in faulty scenarios [46]. Furthermore, they also inherently produce circulating currents, although they are typically eliminated including a Circulating Current Suppressing Control (CCSC) [51]. In [52], a UCM approach is used, taking the DC voltage measurement for the modulation indexes calculation, whereas in [53, 54] the DC voltage reference is used instead. Although it is not necessary to explicitly control the internal energy, an additional total energy controller was included in [55], thus improving the performance and the stability of the system. Therefore, although UCM is typically used under a non-energy-based control approach (i.e. without energy regulators) it could also include energy controllers.

On the other hand, in the Compensated Modulation (CM) [56] the modulation indexes are calculated using the actual arm voltage measurement (2.20). In other words, CM includes an online compensation for the impact of the arm oscillations. In this case, the internal energy of the MMC has to be explicitly controlled in order to ensure an asymptotically stable system [47]. With an adequate control tuning, this approach exhibits a superior performance [46] as compared to UCM-based schemes. In the present thesis, the energy-based control is always applied under a CM approach.

$$m_u^j = \frac{v_u^j}{v_{Cu}^j}, \quad m_l^j = \frac{v_l^j}{v_{Cl}^j}, \quad j = a, b, c \tag{2.20}$$

In the present work, the control architecture from [46] is adopted. An overall picture can be seen in Fig. 2.3, and the different parts of the block diagram are further detailed below for completeness.

AC grid current control

The AC side current control is equivalent to the one used for 2L-VSCs. Although several implementations exist, in the present work a classic current vector control in $qd0$ coordinates is used [57] (Fig. 2.4). A feed-forward of the PCC voltage is included, as well as well as the classic decoupling loops. Note that a dynamic saturation of the current references is also included, which keeps the angle between the qd components constant and reduces proportionally each component until the maximum allowed value, which is typically 1 p.u. of current or slightly higher.
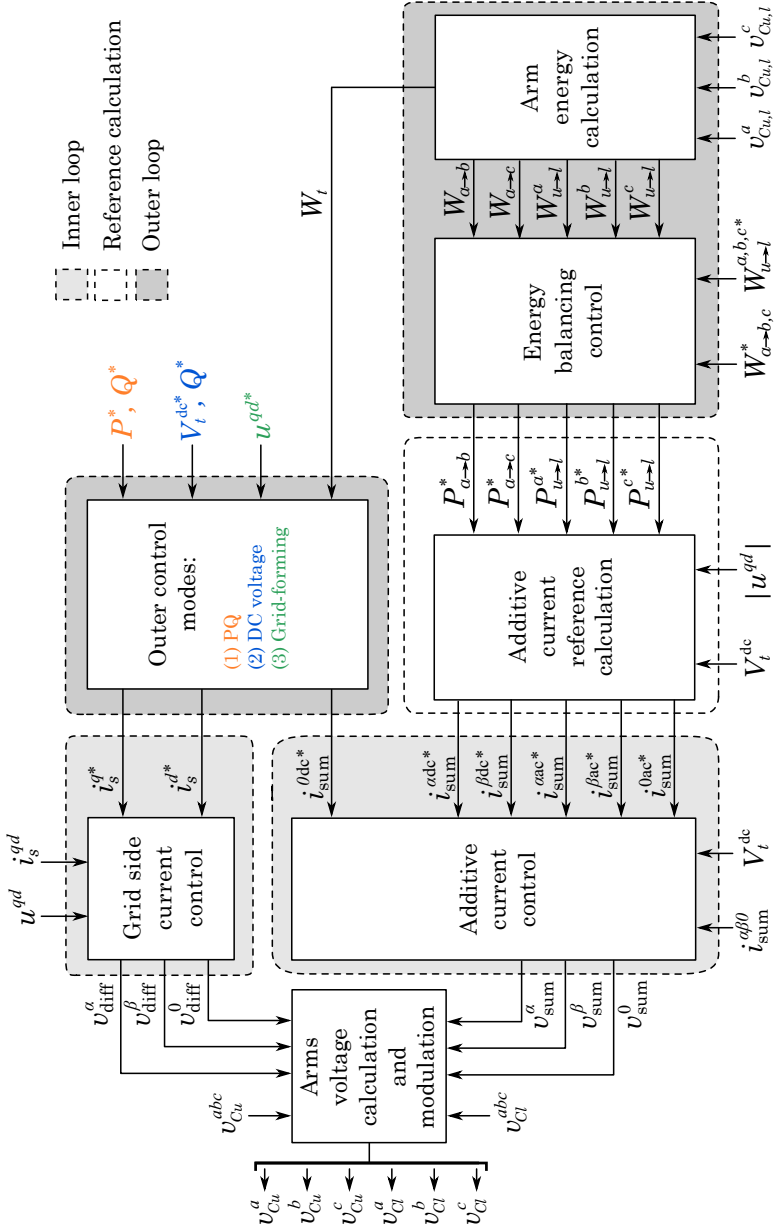
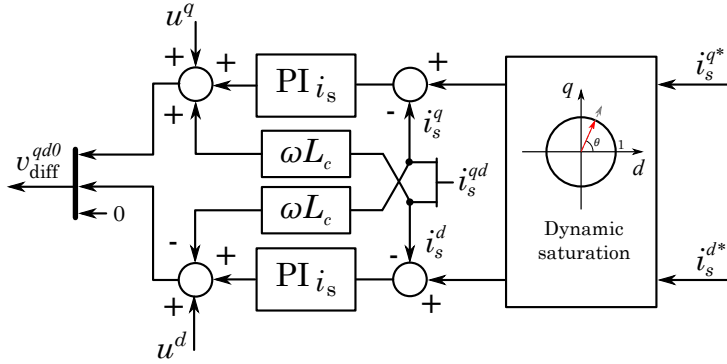Fig. 2.3: Overall control of the MMC

Fig. 2.4: AC grid current control

Regarding the AC side, it is important to distinguish between grid-following and grid-forming controls. On one hand, in grid-following mode the converter synchronises to an existing AC grid. To this end, a Phase-Locked Loop (PLL) [58] (Fig. 2.5a) is typically used, which yields the AC grid angle to be used by the AC side controllers, in order to apply the corresponding voltages according to the desired control objective. On the other hand, in grid-forming mode the converter *generates* the AC grid. Thus, the angle reference is internally generated by the converter, and it is no longer measured from any existing AC grid. In such a case, many control alternatives exist, as will be further explained in Chapter 6. One of the most typical ones is the frequency-droop scheme (Fig. 2.5b), where the frequency is calculated based on the active power exchange. Usually, a low-pass filter (LPF) is included in the power measurement. This strategy is useful when multiple units are operating in grid-forming, as it allows for active power sharing.
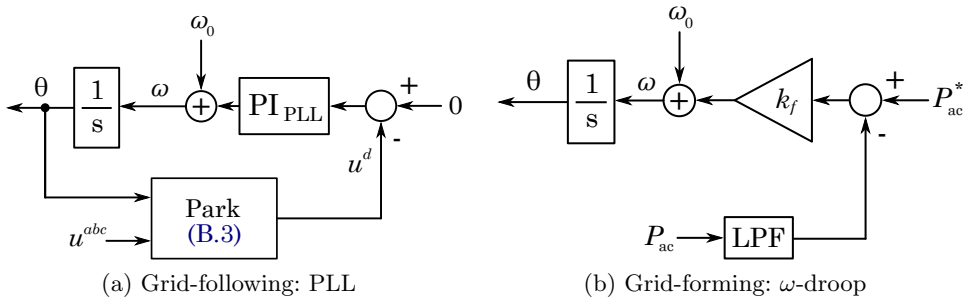

(a) Grid-following: PLL

(b) Grid-forming: ω-droop

Fig. 2.5: Reference angle calculation in grid-following and grid-forming cases

Additive current control

The additive current control deals with both AC and DC components at the same time. In the present thesis, based on the approach from [46], both components are separated, and a lead-lag compensator is applied to the AC current references so that it has a unity gain and no phase delay at the nominal frequency (Fig. 2.6). Then, thanks to the compensator, these AC current references are transformed into constant magnitudes that can be added up with the DC current references. After, three PI controllers can be used to control the three components of the additive current.
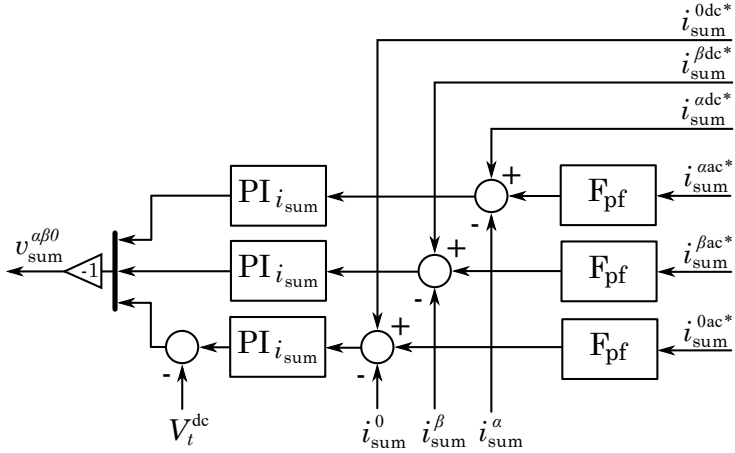

Fig. 2.6: Additive current control

Additive current reference calculation

The most complex part of this MMC control architecture comes with the reference calculation of the additive current components. Regarding the DC components, which are used to either exchange power between legs ($\alpha\beta$ components) or with the DC grid (0 component), the following definitions and approximation (that assumes a negligible voltage drop in each arm impedance) are used:

$$P_{a \to b} \triangleq P_a - P_b, \qquad P_{a \to c} \triangleq P_a - P_c, \qquad P_t \triangleq \sum_{j=a,b,c} P_j, \qquad P_j \simeq V_t^{\mathrm{dc}} i_{\mathrm{sum}}^{j\mathrm{dc}}$$

$$(2.21)$$

Therefore, the DC additive current references in Clarke's coordinates are derived as

$$\begin{bmatrix} i_{\text{sum}}^{\alpha \text{dc}^*} \\ i_{\text{sum}}^{\beta \text{dc}^*} \end{bmatrix} = \frac{1}{3\,V_t^{\text{dc}}} \begin{bmatrix} 1 & 1 \\ \sqrt{3} & -\sqrt{3} \end{bmatrix} \begin{bmatrix} P_{a \to b}^* \\ P_{a \to c}^* \end{bmatrix} \tag{2.22}$$

$$i_{\text{sum}}^{0\text{dc}^*} = \frac{1}{3V_t^{\text{dc}}} P_t^* \tag{2.23}$$

The $\alpha\beta$ components exchange power between legs, whereas the zero-sequence component corresponds to the DC current flowing to the DC side. With respect to the derivation of the AC components, it is a more complex procedure. A block diagram of the overall additive current references (DC and AC) is presented in Fig. 2.7, and further details can be found in [46]. Note that this controller is valid for the basic case of a balanced AC grid. A more recent version considering AC grid imbalances can be found in [59], with extra capabilities. Also note that Clarke transformation is used for convenience (B.1), and the counter-clockwise rotation (2.24) and the clockwise rotation (2.25) matrices are introduced:

$$\mathbf{R}_{\circlearrowleft} = \begin{bmatrix} \cos\Theta & -\sin\Theta & 0 \\ \sin\Theta & \cos\Theta & 0 \\ 0 & 0 & 1 \end{bmatrix} \tag{2.24}$$

$$\mathbf{R}_{\circlearrowright} = \begin{bmatrix} \cos\Theta & \sin\Theta & 0 \\ -\sin\Theta & \cos\Theta & 0 \\ 0 & 0 & 1 \end{bmatrix} \tag{2.25}$$

Energy balancing control and arm energy calculation

The balancing power references are given by the five energy balancing PI controllers, as depicted in Fig. 2.8. Note that in normal operation the five energy balancing references are set to zero. Note that a notch filter tuned at twice the nominal frequency is used to filter out the oscillating component that appears in the energy difference between legs. Equivalently, a notch filter tuned at the nominal frequency filters out the oscillating component that appears in the energy difference between arms [46]. The energy difference signals can be obtained as shown in Fig. 2.9, calculating the total stored energy of each arm, and adding or subtracting the energy values as necessary.
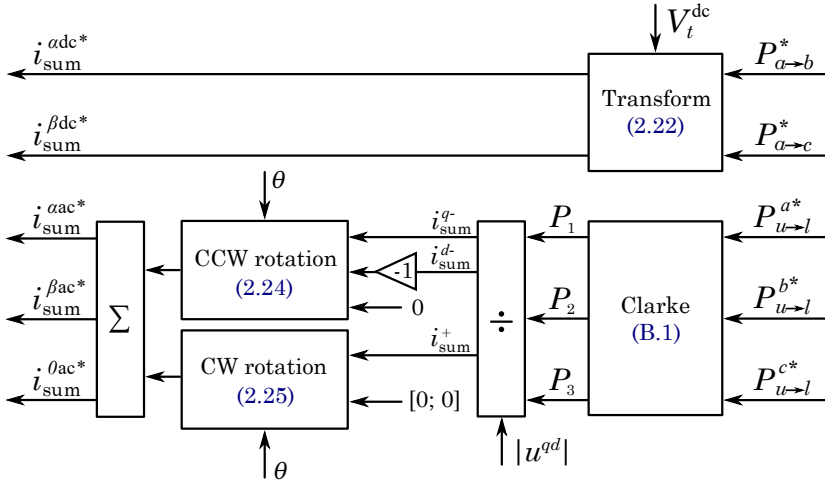
Fig. 2.7: Additive current reference calculation

Arms voltage calculation and modulation indexes

Once the differential and additive voltages are calculated by the respective inner controllers (Figs. 2.4 and 2.6, respectively) they need to be converted back to the *abc* and upper-lower reference frame in order to be modulated by the six MMC arms. The variable change from (2.3) is recalled, and the detailed calculations are presented in Fig. 2.10. Note that the modulation indexes are saturated, as the converter arms are not capable of modulating a voltage that exceeds the available voltage in the submodules altogether. In the present thesis, half-bridge submodules are considered, meaning that the saturation of the modulation indexes is from 0 to 1, as polarity change (-1) is not possible within the arm. However, the overall control scheme presented in this chapter is not only limited to MMCs with half-bridge submodules, but it is also applicable to MMCs with full-bridge submodules with a convenient saturation of the modulation indexes.
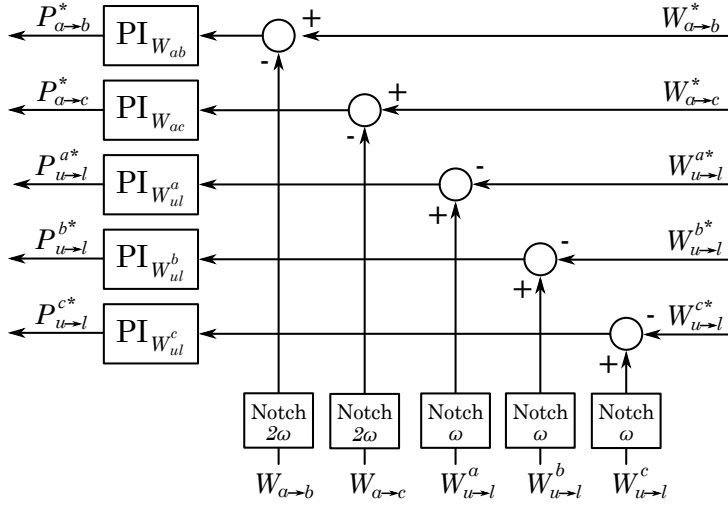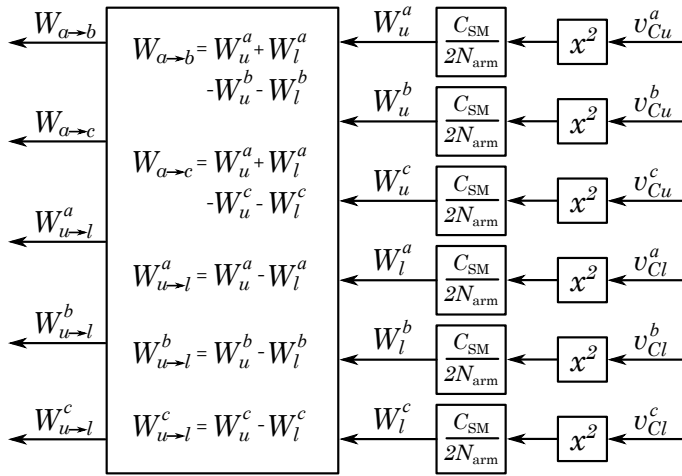
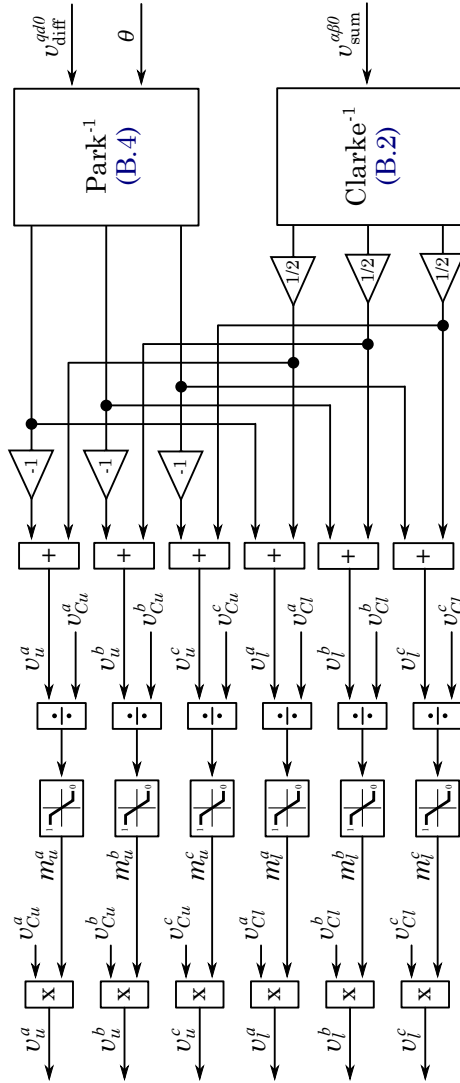Fig. 2.8: Energy balancing control

Fig. 2.9: Arm energy calculation

Fig. 2.10: Arms voltages calculation and modulation

2.4 MMC linear model

In order to be able to conduct linear analysis, the non-linear equations of the system must be linearised. This section presents the linearised equations of different parts of the system that will be used in the different case studies throughout the thesis.

2.4.1 MMC internal dynamics

In order to obtain a linear model that enables small-signal analysis, a steady-state time-invariant (SSTI) model of the system is necessary, i.e. a model where all the variables settle to a constant value (i.e. non-oscillatory) in steady-state. Capturing the overall MMC dynamics without simplifications in an SSTI model is a challenging problem by itself [60]. The main obstacle is that the circulating currents contain DC and several AC components at the same time. An extensive mathematical manipulation using a set of Synchronous Rotating Frames (SRF) at different frequencies can be performed [61]. However, this comes at the expense of having a large and complex model.

Nevertheless, the system can be re-formulated to enable the derivation of an SSTI model that uses energies as state variables instead of voltages (2.6). This approach is suitable if an energy-based control approach is used [62], i.e. if the energy stored in the arms is explicitly controlled. This formulation typically only considers the total energy and the circulating current zero-sequence component [56] and was recently generalised to include the arm balancing dynamics [62]. It is shown that the simplified model from [56] is suitable from a macroscopic point of view, and effectively captures the AC and DC dynamics, assuming that the internal vertical and horizontal energy balancing controls are properly tuned. The tuning of the MMC's internal energy balancing controllers is typically only relevant in scenarios with unbalanced AC voltage sags or DC pole imbalances [63]. As this thesis does not deal with such scenarios, the simplified linear model from [56] can be used. To this end, (2.6) is reformulated into

$$\frac{dW_t}{dt} = -\frac{3}{2} v_{\mathrm{diff}}^{qd} i_s^{qd} + 3 i_{\mathrm{sum}}^{0\mathrm{dc}} v_{\mathrm{sum}}^{0\mathrm{dc}} \qquad (2.26)$$

Then, assuming $V_{\text{off}}^{\text{dc}}$ and v_n to be 0, which is true in normal conditions, expressing (2.10) in Park's (qd^2) coordinates (2.27)-(2.28), and considering only the zero-sequence component of (2.11), as shown in (2.29), leads to an SSTI system.

$$v_{\text{diff}}^q - u^q - L\omega_0 i_s^d = Ri_s^q + L\frac{di_s^q}{dt} \tag{2.27}$$

$$v_{\text{diff}}^d - u^d + L\omega_0 i_s^q = Ri_s^d + L\frac{di_s^d}{dt} \tag{2.28}$$

$$v_{\text{sum}}^{0\text{dc}} - V_t^{\text{dc}} = -2R_a i_{\text{sum}}^{0\text{dc}} - 2L_a \frac{di_{\text{sum}}^{0\text{dc}}}{dt} \tag{2.29}$$

By linearising (2.26)-(2.29), equations (2.30)-(2.33) are obtained. Hereinafter, subindex 0 refers to the operating point for the linearisation. Note that in case the frequency is constant, the state $\Delta\omega$ is removed from the equations.

$$\Delta\dot{W}_t = -\frac{3}{2}(\Delta v_{\text{diff}}^q i_{s0}^q + \Delta v_{\text{diff}}^d i_{s0}^d + \Delta i_s^q v_{\text{diff}0}^q + \Delta i_s^d v_{\text{diff}0}^d)$$
$$+ 3(\Delta i_{\text{sum}}^{0\text{dc}} v_{\text{sum}0}^{0\text{dc}} + \Delta v_{\text{sum}}^{0\text{dc}} i_{\text{sum}0}^{0\text{dc}}) \tag{2.30}$$

$$\Delta\dot{i}_s^q = -\frac{R}{L}\Delta i_s^q - i_{s0}^d \Delta\omega - \omega_0 \Delta i_s^d + \frac{1}{L}\Delta v_{\text{diff}}^q - \frac{1}{L}\Delta u^q \tag{2.31}$$

$$\Delta\dot{i}_s^d = -\frac{R}{L}\Delta i_s^d + i_{s0}^q \Delta\omega - \omega_0 \Delta i_s^q + \frac{1}{L}\Delta v_{\text{diff}}^d - \frac{1}{L}\Delta u^d \tag{2.32}$$

$$\Delta\dot{i}_{\text{sum}}^{0\text{dc}} = -\frac{R_a}{L_a}\Delta i_{\text{sum}}^{0\text{dc}} - \frac{1}{2L_a}\Delta v_{\text{sum}}^{0\text{dc}} + \frac{1}{2L_a}V_t^{\text{dc}} \tag{2.33}$$

2.4.2 Multiple qd reference frames

In a linear system, when multiple qd frames are present in the same AC subsystem, a common (global) qd reference frame has to be established. The other qd frames present in the system (auxiliary) will be referred to the global one through the corresponding transformations, as detailed next. This has been a well-known issue in classic multi-machine power systems small-signal studies [65]. This work does not cover multi-machine systems, but the same idea applies to the following cases:

- Case 1: A grid-following converter synchronised to the AC grid through a PLL.

---

[2]Note that qd electrical machinery notation from [64] will be used in this thesis, being the q component related to active current and the d component related to reactive current.

- Case 2: A grid-following converter synchronised to a grid-forming converter through a PLL.

- Case 3: Multiple grid-forming converters sharing the generation of the AC grid.

The linearised transformations that are used to transform variables from one frame to another [66] are established as follows.

$$\Delta x^{qdc} = \mathbf{T_c^{qd}}(\Delta x^{qd}, \Delta e_\theta)^T \tag{2.34}$$

is used to obtain the feedback variables i_s^{qdc} and u^{qdc}, whereas the inverse transformation

$$\Delta x^{qd} = \mathbf{T_c^{qd}}^{-1}(\Delta x^{qdc}, \Delta e_\theta)^T \tag{2.35}$$

is used to obtain the modulated voltage v_{diff}^{qd}. Matrices $\mathbf{T_c^{qd}}$ and $\mathbf{T_c^{qd}}^{-1}$ are defined as

$$\mathbf{T_c^{qd}} = \begin{bmatrix} \cos\left(e_{\theta 0}\right) & -\sin\left(e_{\theta 0}\right) & -\sin\left(e_{\theta 0}\right)x_0^q - \cos\left(e_{\theta 0}\right)x_0^d \\ \sin\left(e_{\theta 0}\right) & \cos\left(e_{\theta 0}\right) & \cos\left(e_{\theta 0}\right)x_0^q - \sin\left(e_{\theta 0}\right)x_0^d \end{bmatrix} \tag{2.36}$$

$$\mathbf{T_c^{qd}}^{-1} = \begin{bmatrix} \cos\left(e_{\theta 0}\right) & \sin\left(e_{\theta 0}\right) & -\sin\left(e_{\theta 0}\right)x_0^q + \cos\left(e_{\theta 0}\right)x_0^d \\ -\sin\left(e_{\theta 0}\right) & \cos\left(e_{\theta 0}\right) & -\cos\left(e_{\theta 0}\right)x_0^q - \sin\left(e_{\theta 0}\right)x_0^d \end{bmatrix} \tag{2.37}$$

As be seen in (2.36)-(2.37), these matrices correspond to a linearised counter-clockwise and clockwise rotations, respectively, that take into account the initial angle between both reference frames. It is important to remark that:

- The angle error Δe_θ is calculated as the integral of the frequency given by one subsystem (e.g. the PLL in cases 1 and 2, and a grid-forming converter in case 3) minus the frequency of the reference subsystem (e.g. the AC grid angle in cases 1 and 2, and the reference grid-forming converter in case 3) (2.38).

- The magnitudes at the operating point (x_0^{qd}, x_0^{qdc}) are expressed in the reference frame before applying the transformation, i.e. the global one in case of (2.36) and the corresponding auxiliary one in case of (2.37).

$$\Delta e_{\theta_0} = \frac{\omega_i - \omega_0}{s} \tag{2.38}$$

2.4.3 Active and reactive powers

Active and reactive power signals, which are necessary for some of the control loops, are linearised as

$$\Delta P_{\text{ac}} = \frac{3}{2}(\Delta u^q i_{s0}^q + \Delta u^d i_{s0}^d + \Delta i_s^q u_0^q + \Delta i_s^d u_0^d) \qquad (2.39)$$

$$\Delta Q_{\text{ac}} = \frac{3}{2}(-\Delta u^q i_{s0}^q + \Delta u^d i_{s0}^d + \Delta i_s^q u_0^q - \Delta i_s^d u_0^d) \qquad (2.40)$$

2.5 HVDC cable linear model

In the simulation of HVDC systems, the so-called Wideband Model or Universal Line Model (ULM) [67] is the most commonly accepted model for EMT simulations, which accounts for the cable parameters frequency dependence. This behaviour depends on the physical and geometric characteristics of the cable. In the present work, the 320 kV XLPE insulated cable from [68] is used as the reference. Furthermore, as the simulations are carried out using Matlab Simulink, the ULM model from the Simulink toolbox developed in the BestPaths project [69] has been used.

The formulation of the ULM cable model equations does not allow for the derivation of an equivalent state-space linear model. This is an issue from the point of view of analysing power systems that involve HVDC, as it might lead to mistaken conclusions in terms of stability and interactions when small-signal analysis is performed.

In many studies over the last decades, the well-known π-section model has been used to represent HVDC cables, usually with several cascaded sections. However, this model is inefficient to represent the real behaviour of the cable, leading to unrealistic resonances [70]. An improvement of the π-section was proposed in [71], taking into account the coupling between the core and the screen of the cable, but still failing to represent its frequency-dependent characteristic. Consequently, a frequency-dependent model was presented in [70], motivated by the necessity of accurately represent HVDC systems through a linear model in order to conduct reliable small-signal analysis. This model consists of an extension of the π-section using several parallel branches with different constant parameters. The number of branches, and also the number of sections, determines the accuracy of the model.

This model is shown in Fig. 2.11 (v^+ refers to the positive monopole, corresponding to $\frac{1}{2}V_t^{\text{dc}}$ in normal conditions). Taking n as the number of

sections, $1 + 4n$ differential equations are obtained (2.41). Note that (2.41d) is only necessary when $n \geq 2$. A detailed analysis of this cable model using different branches and sections is presented in Chapter 4. In the rest of the chapters, the HVDC cable that has been used in the case studies consists of 1 section and 3 branches, similar to [71, 72]. For the studies carried out in this thesis, no major differences were observed between this model and a model with several sections in series. Therefore, 1 single section was used, as it reduces the size of the linear model.
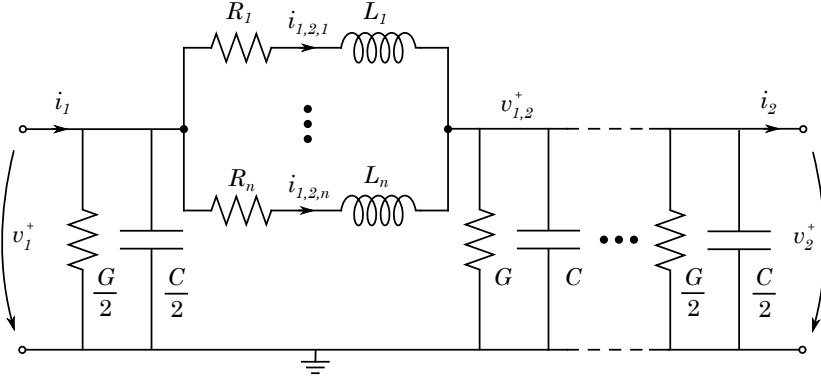
Fig. 2.11: Cable model with parallel series branches

$$\frac{dv_1}{dt} = \frac{4}{C}\left(i_1 - \sum_{k=1}^{3} i_{1,2,k} - \frac{G}{4}v_1\right) \tag{2.41a}$$

$$\frac{di_{i,i+1,k}}{dt} = \frac{1}{2L_k}v_1 - \frac{1}{2L_k}v_{i,i+1} - \frac{R_k}{L_k}i_{i,i+1,k},$$
$$i = 1, ..., n, \ \ k = 1, 2, 3 \tag{2.41b}$$

$$\frac{dv_2}{dt} = \frac{4}{C}\left(\sum_{k=1}^{3} i_{n,n+1,k} - i_2 - \frac{G}{4}v_2\right) \tag{2.41c}$$

$$\frac{dv_{i,i+1}}{dt} = \frac{2}{C}\left(\sum_{k=1}^{3} i_{i,i+1,k} - \sum_{k=1}^{3} i_{i+1,i+2,k} - \frac{G}{2}v_{i,i+1}\right),$$
$$i = 1, ..., n, \ \ n \geq 2 \tag{2.41d}$$

being

i_1, i_2: input and output currents of the cable.

v_1, v_2: total voltages at each cable terminal.

$v_{i,i+1}$: total voltage after section $i, i + 1$.

$i_{i,i+1,k}$: current flowing through section $i, i + 1$, branch k.

R_k, L_k: equivalent pole resistance/inductance of branch k.

C, G: equivalent pole capacitance/admittance.

2.6 AC grid dynamics

Regarding the AC grid, three main different elements have been used in the case studies, as described next. Note that despite these models are linear, the equations are written in small-signal form (Δ) due to the linearisation with respect to the frequency in the qd frame.

- A voltage-sourced AC grid is represented using a Thévenin equivalent (Fig. 2.12a) (2.42)-(2.43). A grid-following MMC would be typically synchronised to such a grid (see, for instance, Chapters 3 and 5). This model represents, for instance, a large AC network containing classic generation. In all the cases presented in this work, the AC grid is stable and relatively strong. Therefore, it is not within the scope of this thesis to deal neither with weak or disturbed AC grids, nor complex AC grid models.

$$\Delta \dot{i}_s^q = -\frac{R_g}{L_g}\Delta i_s^q - i_{s0}^d \Delta\omega - \omega_0 \Delta i_s^d + \frac{1}{L_g}\Delta u^q - \frac{1}{L_g}\Delta v_g^q \qquad (2.42)$$

$$\Delta \dot{i}_s^d = -\frac{R_g}{L_g}\Delta i_s^d + i_{s0}^q \Delta\omega - \omega_0 \Delta i_s^q + \frac{1}{L_g}\Delta u^d - \frac{1}{L_g}\Delta v_g^d \qquad (2.43)$$

- AC lines are represented using π-section equivalents (Fig. 2.12b). In all the scenarios covered in this work, a single section is used (2.44)-(2.49). AC lines are used, for instance, in Chapters 6 and 7.

$$\Delta \dot{u}^q = -\frac{2}{C_c}\Delta i_s^q - u_0^d \Delta\omega - \omega_0 \Delta u^d - \frac{2}{C_c}\Delta i_c^q \qquad (2.44)$$

$$\Delta \dot{u}^d = -\frac{2}{C_c}\Delta i_s^d + u_0^q \Delta\omega - \omega_0 \Delta u^q - \frac{2}{C_c}\Delta i_c^d \qquad (2.45)$$

$$\Delta \dot{i}_c^q = -\frac{R_c}{L_c}\Delta i_c^q - i_{c0}^q \Delta\omega - \omega_0 \Delta i_c^d + \frac{1}{L_c}\Delta u^q - \frac{1}{L_c}\Delta u_g^q \qquad (2.46)$$

$$\Delta \dot{i}_c^d = -\frac{R_c}{L_c}\Delta i_c^d + i_{c0}^d \Delta\omega - \omega_0 \Delta i_c^q + \frac{1}{L_c}\Delta u^d - \frac{1}{L_c}\Delta u_g^d \qquad (2.47)$$

$$\Delta \dot{u}_g^q = -\frac{2}{C_c}\Delta i_c^q - u_{g0}^d \Delta \omega - \omega_0 \Delta u_g^d - \frac{2}{C_c}\Delta i_g^q \qquad (2.48)$$

$$\Delta \dot{u}_g^d = -\frac{2}{C_c}\Delta i_c^d + u_{g0}^q \Delta \omega - \omega_0 \Delta u_g^q - \frac{2}{C_c}\Delta i_g^d \qquad (2.49)$$

- A current-sourced AC grid is represented using current sources in parallel with capacitors (Fig. 2.12c) (2.50)-(2.51). This could be the case, for instance, of a power electronics interfaced system that injects or absorbs power (e.g. a wind farm or an islanded system). Note that the capacitors correspond either to the equivalent capacitance of an AC line, or to a physical filter. This AC node is used as a constant power node, as will be shown in Chapters 6 and 7. In the present work, the capacitance is always half the one corresponding to the AC line (i.e. $C_{\text{ac}} = C_c/2$). Therefore, in such a case equations (2.50)-(2.51) are the same as (2.48)-(2.49).

$$\Delta \dot{u}_g^q = -\frac{1}{C_{\text{ac}}}\Delta i_c^q - u_{g0}^d \Delta \omega - \omega_0 \Delta u_g^d - \frac{1}{C_{\text{ac}}}\Delta i_g^q \qquad (2.50)$$

$$\Delta \dot{u}_g^d = -\frac{1}{C_{\text{ac}}}\Delta i_c^d + u_{g0}^q \Delta \omega - \omega_0 \Delta u_g^q - \frac{1}{C_{\text{ac}}}\Delta i_g^d \qquad (2.51)$$
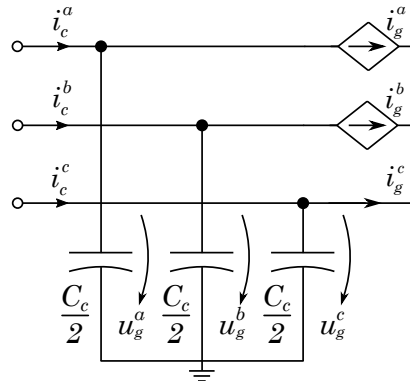
2.7 Linear model validation

After introducing the different parts of the MMC that require linearisation, a simple case is considered to evaluate the mismatch between the detailed and the linearised models. An MMC in DC voltage control mode, connected to an HVDC cable on the DC side and to a Thévenin equivalent in the AC side, is considered (Fig. 2.13). The system is linearised at 0.5 p.u. of DC current (flowing from the DC side to the MMC), and steps of 0.01, 0.05, 0.10 and 0.20 p.u. of current are performed. In Fig. 2.14, the errors between the detailed and the linearised models for different magnitudes are plotted. This is indicated with $e()$. The superscript c in i_s^{qd} and u^{qd} refers to the converter (auxiliary reference). None of the MMC variables reach saturation in any of the cases, in order to avoid mismatches related to these non-linearities that are not represented in the linear model. Whereas for 0.01 p.u. of DC current increase the error is not noticeable, the mismatch becomes much more relevant when the increase is higher than 0.05 p.u. of current. As it was expected, the linear model is an accurate approximation of
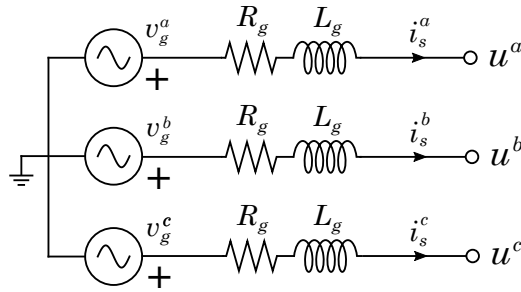
(a) Voltage-sourced AC grid (Thévenin equivalent)
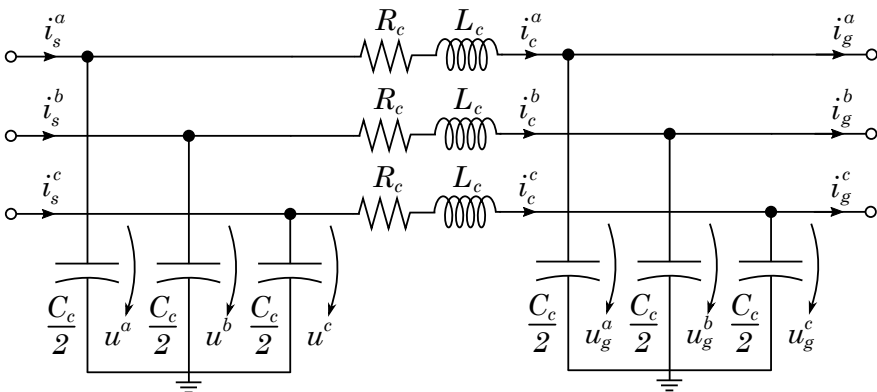
(b) AC line

(c) Current-sourced AC grid

Fig. 2.12: Electrical circuits of AC side elements

the benchmark reference model only when the deviation from the operating point is sufficiently small.
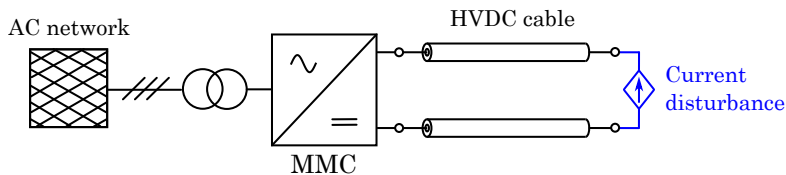

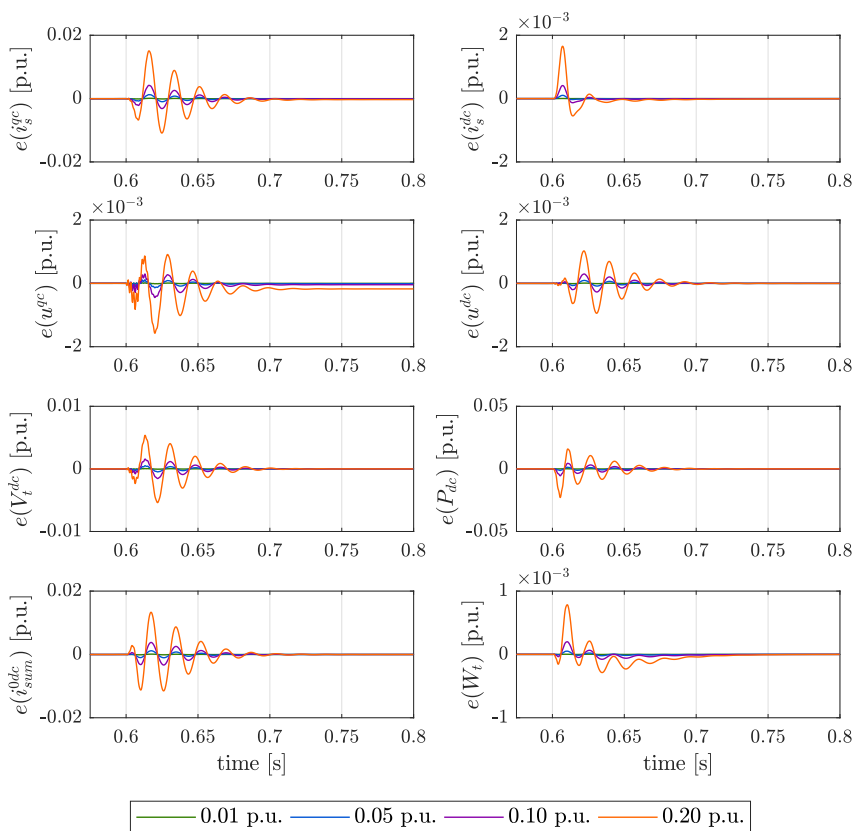Fig. 2.13: Test scenario used for the linear model validation

Fig. 2.14: Linear model validation of an MMC in DC voltage control mode –
Magnitude errors between the non-linear and the linear models

2.8 Conclusion

In this chapter, the fundamentals about the control and the modelling of the MMC and other parts of the system have been described in detail. These models are crucial for the development of the different studies carried out in this thesis. On one hand, they allow for running time-domain simulations using the complete detailed (average) model with the overall control scheme. On the other hand, small-signal analysis and control design can be addressed using the linearised models. Also, the model of the HVDC cable has been described, as it will be a key element in several case studies throughout the thesis. Furthermore, the different models related to the AC side network have been introduced. Along the next chapters, these different blocks are conveniently put together to build the specific scenarios of the different case studies.

Chapter 3

Control structures of the MMC in DC voltage control mode

3.1 Introduction

As mentioned in Chapter 2, the different control schemes of the MMC available in the literature can be classified as follows. On one hand, the ones based on Uncompensated Modulation (UCM) [48], such as direct voltage modulation [42] or open-loop modulation [50]. These are known to be asymptotically stable but their transients depend on the converter impedances rather than being imposed by a controller, which can lead to slow time constants or undesirable overshoots. Furthermore, they cause disturbances that lead to circulating currents. However, they are typically eliminated including the so-called Circulating Current Suppressing Control (CCSC) [51]. On the other hand, the control schemes based on Compensated Modulation (CM) [56] do not exhibit parasitic voltage components, but arm-energy controllers are needed to ensure an asymptotically stable system [47].

Linear models are useful for small-signal analysis (stability, eigenvalues, participation factors) [48, 72, 73] and for control design assessment by means of linear tools [71]. Several efforts have been made regarding the linear modelling of the MMC, for both energy-controlled and non-energy-controlled approaches. A steady-state time-invariant (SSTI) model is required to enable linearisation, as presented in Chapter 2. In the present work, an energy-controlled scheme is considered, as it presents the advantage of controlling the internal energy of the MMC, which improves the performance and the stability, avoiding poorly damped oscillation modes introduced by the CCSC in

the non-energy-controlled approach [55]. However, there are some challenges in this field that the existing literature has not tackled in detail. Usually, only small step changes are performed in the simulated case studies, ignoring the transient performance in more extreme scenarios. Moreover, the size of the capacitor included in the DC terminals is usually representative of relatively long cables, avoiding the case of short HVDC links. Some examples are summarised next.

In [56], a small-signal model of an MMC with droop DC voltage control and total energy control is derived. A relatively big capacitor is included in the DC terminals, which may improve the DC dynamics and is not a proper approach for the case of a short HVDC link. Also, no strict constraints are considered for the transient performance. In [70], a comparison between two-level and MMC approaches for an HVDC link is presented, showing a significant difference regarding the DC capacitance. However, the length of the cable is unknown and the performance is not the matter of study of the mentioned paper. In [74], the output of the DC voltage controller is used as a reference for the zero-sequence circulating current, whereas the output of the total energy controller is used as a reference for the grid active current, thus inverting the classic control structure and yielding a more consistent transient performance. However, no insight is given for the case of smaller capacitances and for higher transient requirements.

The objective of this chapter is to evaluate different control structures for the outer loops of the master converter in an MMC-based HVDC link. Small-signal analysis and frequency-domain tools are used in order to evaluate the performance in the whole frequency range, complemented by the time-domain simulations. The effect of the capacitance on the DC side is emphasised, yielding worse results as its value decreases, which corresponds to shorter links.

3.2 System description

The system under study consists of a point-to-point MMC-based HVDC link. One of the converters acts as the master, which controls the DC voltage, whereas the other converter acts a the slave, controlling the active power (Fig. 3.1). Each converters is able to independently control the reactive power exchanged with its respective AC network.
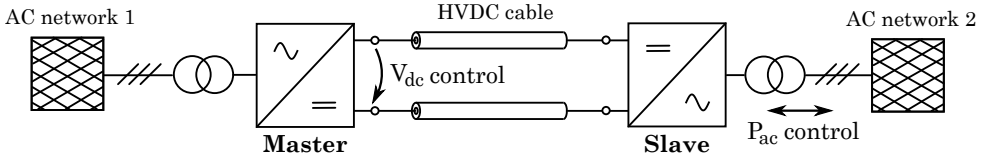
Fig. 3.1: HVDC point-to-point link with master-slave control

3.3 Control structures

3.3.1 Slave control

Before starting with the master MMC control structures, the control of a slave MMC is presented (Fig. 3.2). This control structure is equivalent to the one used in 2L-VSCs, including a total energy controller cascaded with a zero-sequence circulating current controller. As mentioned in Chapter 1, this control scheme does not present a significant control challenge as long as the DC voltage is stable, which depends on the master converter. On one hand, the active power loop is cascaded with the AC active current control. Typically, the active power loop dynamic response requirements are not stiff [75]. Therefore, there is enough time-scale separation between the active power and the inner current loop, which is several times faster, making the control design straightforward. On the other hand, the total energy control can be tuned independently, and as the active power dynamics are relatively slow, the energy control does not need to be very fast either. Note that L is defined in (2.3).

3.3.2 Master classic control

A common control scheme for MMCs which is widely reported in the literature is inspired on the control structure used in 2L-VSCs: the outer DC voltage loop yields the active current reference for the AC side inner current loop, and because of that the immediately obvious solution to complete the control scheme is to connect the outer total energy loop output to the inner circulating current loop reference. This will be called *classic* control from now on (Fig. 3.3). It has to be noted that a feed-forward of the measured AC power is added at the energy controller output. Otherwise, the gain of the energy controller has to be notably high to stabilise the system. Although other alternatives exist, e.g. not including any feed-forward signal [56,76], or using the power reference instead [55], the measured power will be considered in the present case.
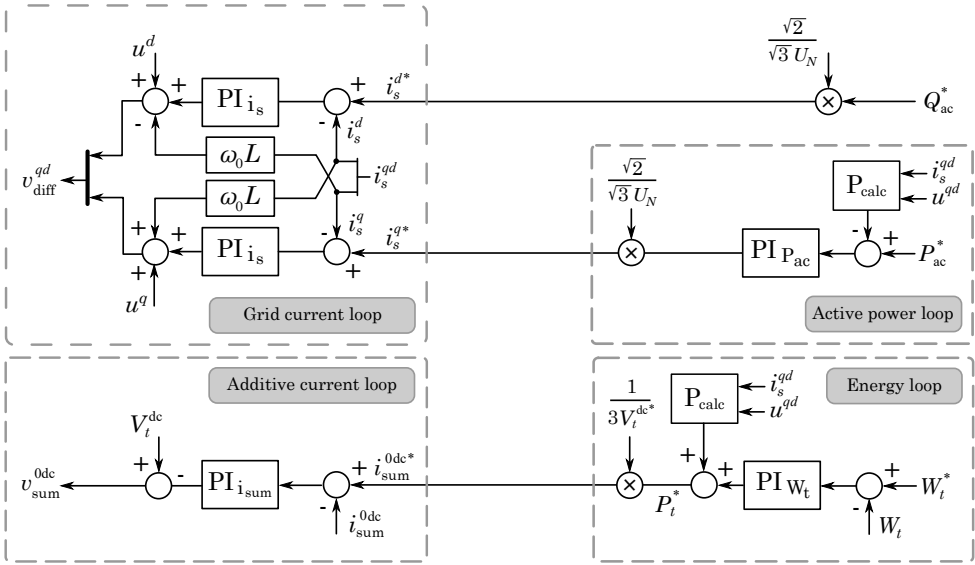
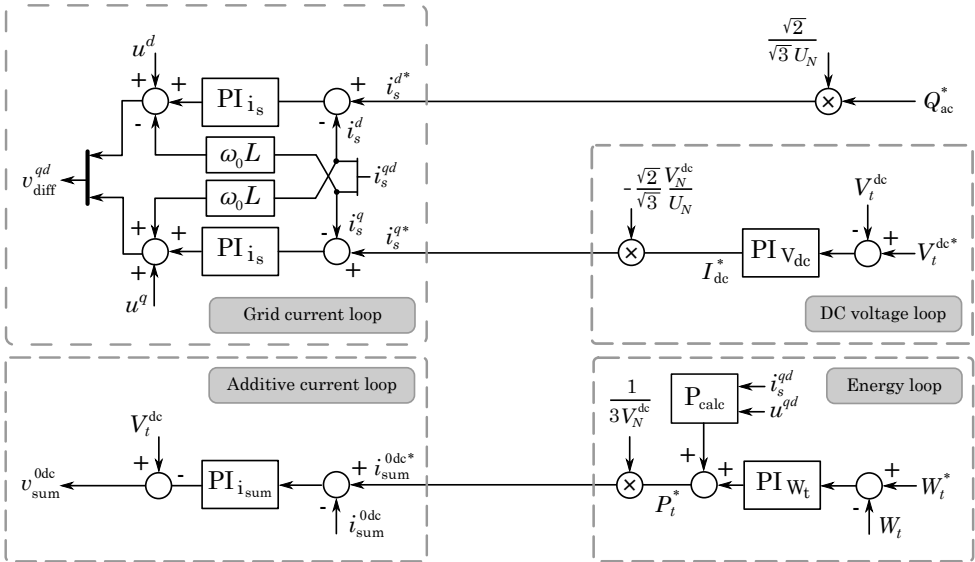Fig. 3.2: Detailed MMC slave control structure

Fig. 3.3: Detailed MMC master classic control structure

This structure relies on the assumption that there is a relatively big capacitance on the DC side of the converter. Otherwise, undesired transient deviations of the DC voltage are obtained when there is a change in the DC power flowing through the link. Whereas in a non-energy-based control strategy a capacitance equal to $6 \cdot C_{SM}/N_{arm}$ is seen by the DC side according to [42], in the case of an energy-based approach the DC side does not see such an equivalent capacitance. Then, if the classic control scheme is used, some dynamics will depend strongly on the equivalent capacitance on the DC terminals, e.g. the length of the line in the case of the HVDC link, or the overall capacitance in the case of more complex systems such as multi-terminal HVDC grids.

3.3.3 Master cross control

In the MMC, the power balance between the AC and the DC sides is not instantaneous as in the 2L-VSC case, as the MMC's arms act as an energy buffer. Therefore, it is intuitive to cascade the DC voltage loop with the DC current loop (which corresponds to three times i_{sum}^{0dc}) instead of the AC side current loop (i_s^q). This leads to a different control structure, shown in Fig. 3.4, and referred to as *cross* control from now on. Note that the control of the energy balance between phases and between arms is independent from the outer control structure used.
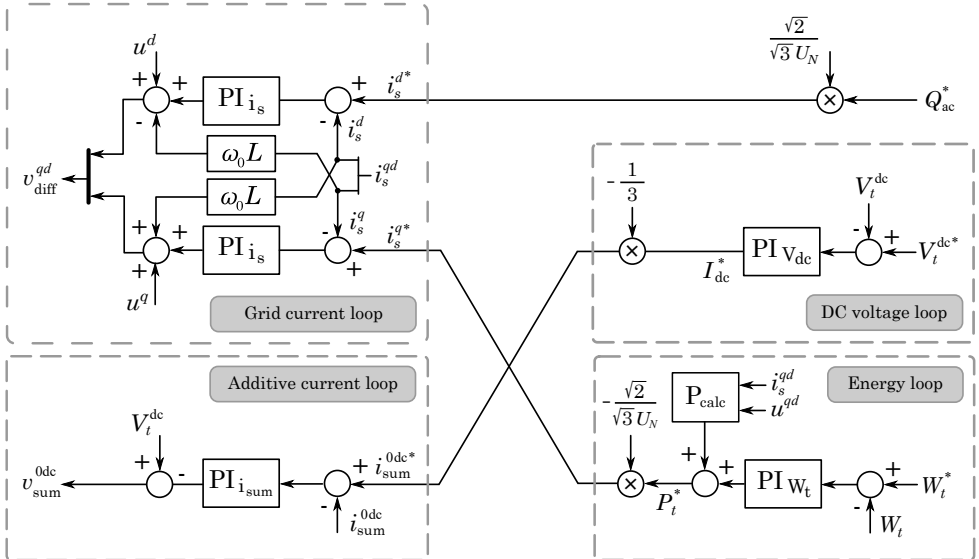

Fig. 3.4: Detailed MMC master cross control structure

3.3.4 Master weighted control

With all above, a new control structure can be considered, consisting of the summation of both outer controllers outputs multiplied by weight factors k_1, k_2, k_3 and k_4 (Fig. 3.5). This option arises as a combined structure, containing both the classic and the cross approaches as particular cases and a whole range of intermediate options. This structure will be referred to as *weighted* control. Parameters K_i $(i = 1, \dots, 4)$ from Fig. 3.5 are defined as in (3.1), taking into account the corresponding unit conversion ratio, thus preserving the same tuning for the DC voltage and energy controllers.

$$K_1 = -\frac{\sqrt{2}}{\sqrt{3}}\frac{V_N^{\text{dc}}}{U_N}k_1 \ , \ \ K_2 = -\frac{\sqrt{2}}{\sqrt{3}}\frac{1}{U_N}k_2$$

$$K_3 = -\frac{1}{3}k_3 \ , \ \ K_4 = \frac{1}{3}\frac{1}{V_N^{\text{dc}}}k_4 \tag{3.1}$$
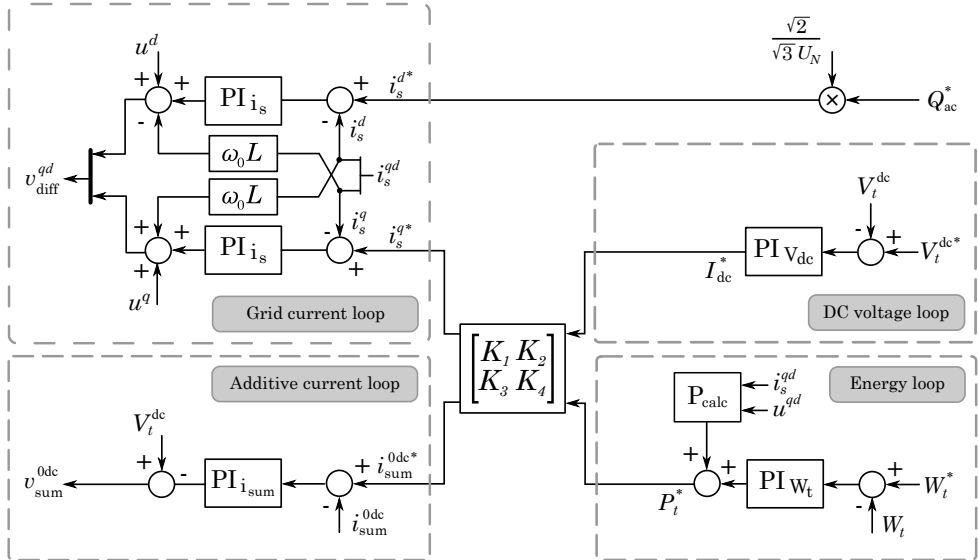
Fig. 3.5: Detailed MMC master weighted control structure

3.3.5 Master constant DC voltage control

In case of short and very short lines, the problem of the aforementioned approaches is that the capacitance at the DC terminals is very small, which may cause large voltage deviations during transients. This will be thoroughly

analysed in the next section. For this reason, a new control structure should be explored. Such alternative consists of eliminating the DC voltage closed-loop in the cross control option, making it open-loop with a constant reference for $v_{\text{sum}}^{0\text{dc}}$, which is the DC voltage set-point $V_t^{\text{dc}*}$. The control scheme is shown in Fig. 3.6, and it will be referred to as *constant DC voltage* control. This scheme would be also suitable for the back-to-back case, which is the most extreme case of a very short line.
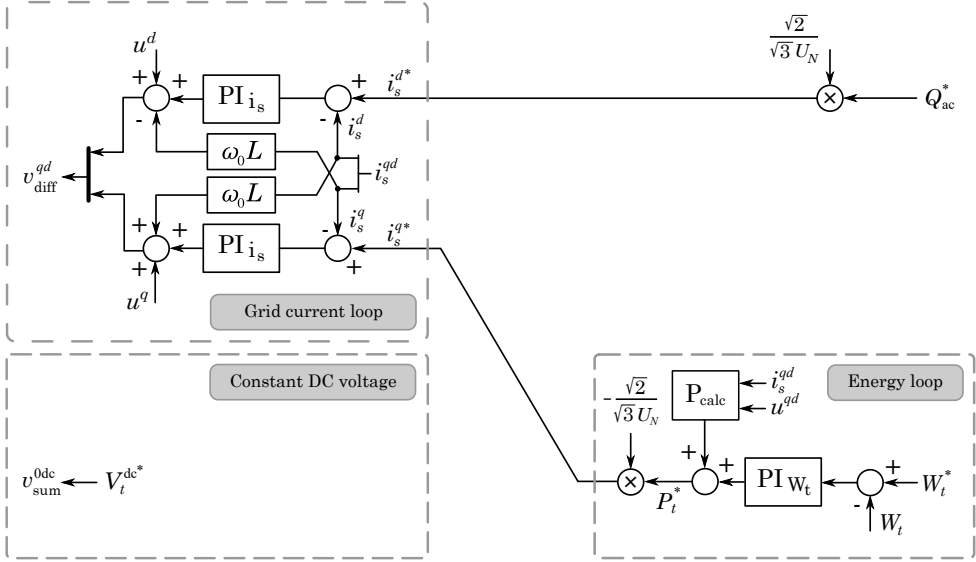
Fig. 3.6: Detailed MMC master constant DC voltage control structure

3.4 Evaluation and analysis of the control structures

This section aims to present a comparison among the different control structures described before, in order to shed some light on how to improve the dynamics of the MMC. As mentioned before, a point-to-point HVDC link with a master-slave control approach is considered. On one hand, small-signal analysis is performed, using a linearised model. Insights with respect to stability, modes of the system and participation factors of critical modes is presented, as well as frequency-domain analysis of the relevant transfer functions of the system via Bode gain plots. On the other hand, the transient performance will be analysed through time-domain simulations using the complete non-linear model of the system.

3.4.1 Linear model

A block diagram of the whole linear system is depicted in Fig. 3.7. This generic scheme is valid for all the control structures, except for the constant DC voltage control, where some states are eliminated. The HVDC cable consists of one section for simplicity, as the length of the cables under study is relatively short, and the number of parallel branches is 3. The overall system has 27 states (11 related to each MMC, and 5 related to the cable).
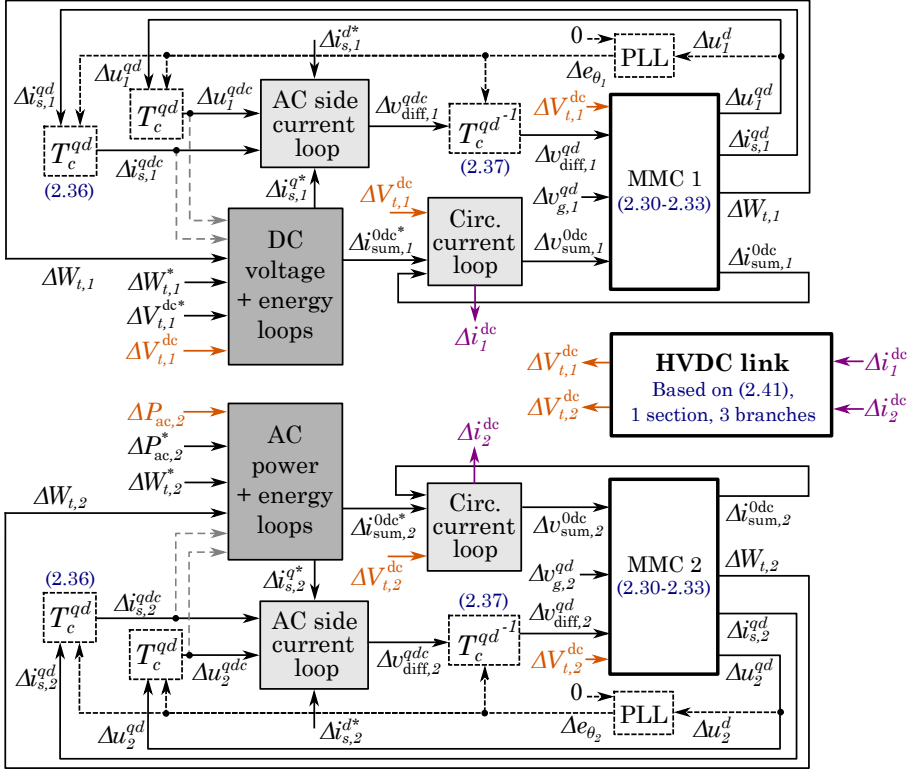

Fig. 3.7: Linear model of the HVDC point-to-point link with a master-slave control

3.4.2 Tuning criteria

In order to perform a fair comparison of the different control structures, a tuning criteria for the DC voltage controller has to be established. On one hand, the current loops (i_s^{qd} and i_{sum}) are tuned to achieve a fast response, according to the real modulation limits of the converter [77]. Such inner

controllers are the physical limit of the converter control action or, in other words, the maximum speed response of the converter. Here, the current controllers have been designed to produce a first-order closed-loop response with a time constant $\tau_{cc} = 1$ ms using Internal Model Control [57] (3.2)-(3.3).

$$k_{p-is} = \frac{L_{\text{eq}}}{\tau_{cc}} \ , \ k_{i-is} = \frac{R_{\text{eq}}}{\tau_{cc}} \tag{3.2}$$

$$k_{p-isum} = \frac{2L_{\text{arm}}}{\tau_{\text{sum}}} \ , \ k_{i-isum} = \frac{2R_{\text{arm}}}{\tau_{\text{sum}}} \tag{3.3}$$

The PLL is tuned to track the grid angle within approximately 25 ms. The controller parameters are calculated based on a desired second order response with damping ratio $\xi = 0.707$ and settling time $t_{st} = 25$ ms as

$$k_{p-pll} = \frac{\sqrt{6}\xi\omega_n}{U_N} \ , \ k_{i-pll} = \frac{\sqrt{3}\omega_n^2}{\sqrt{2}U_N} \tag{3.4}$$

where $\omega_n = 4/(t_{st}\xi)$. On the other hand, the energy controller has been designed considering a disturbance rejection problem and using a loop shaping strategy, specifying a maximum energy deviation of 15% and a settling time of 150 ms, in a similar way than in [46].

The DC voltage controller (master converter) is designed considering the cable equivalent capacitance seen by the converter as the plant (C_{dc}). More specifically, half of the overall capacitance of the cable is considered to be lumped at the terminal where the master converter is connected. Then, a simplified closed-loop of the system is calculated (Fig. 3.8), considering a PI controller. The PI constants are defined comparing the coefficients of the denominator of (3.5) with a second-order characteristic polynomial (3.6), specifying the settling time and the natural frequency as in (3.7). Note that this is an approximation, as (3.5) has an additional zero as compared to the standard second order system (3.6). Parameters $\xi = 0.707$ and $\omega_n = 2\pi(1/15\tau_{cc})$ are chosen to have enough time-scale separation between the current and the DC voltage controllers [57]. The AC power controller (slave converter) is designed using robust control techniques, specifying a first order response of approximately 100 ms [75].

$$G_{\text{cl}}(s) = \frac{G(s)}{1+G(s)} = \frac{(k_p + \frac{k_i}{s})(\frac{1}{C_{\text{dc}}s})}{1 + (k_p + \frac{k_i}{s})(\frac{1}{C_{\text{dc}}s})} = \frac{\frac{k_p}{C_{\text{dc}}s} + \frac{k_i}{C_{\text{dc}}}s}{s^2 + \frac{k_p}{C_{\text{dc}}}s + \frac{k_i}{C_{\text{dc}}}} \tag{3.5}$$
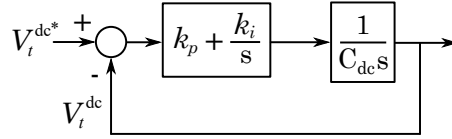
Fig. 3.8: Simplified closed-loop of the DC voltage controlled system

$$G_{\text{2nd}}(s) = \frac{\omega_n^2}{s^2 + 2\xi\omega_n s + \omega_n^2} \tag{3.6}$$

$$k_p = 2\xi\omega_n C_{\text{dc}} \ , \ k_i = \omega_n^2 C_{\text{dc}} \tag{3.7}$$

3.4.3 Scenario configuration

Regarding the transient performance, the following scenarios are considered:

- Case 1: a fast AC power reference change from 0 % to 100 % in the slave converter.

- Case 2: a fast AC power reference change from 100 % to 0 % in the slave converter.

More severe scenarios could be considered, e.g. sudden disconnection of the slave converter while transmitting full power. However, for the purpose of this chapter, which consists of comparing the different control structures presented, those kind of scenarios are not practical, as they might cause relevant saturations in the converter, making the comparison cumbersome. In case of unbalanced faults, other kind of control strategies should be employed together with the ones in normal operation [59].

First of all, the effect of the operating point is analysed in order to identify the worst possible case (whole range of power) in terms of small-signal stability. The operating point (AC power reference of the slave converter) is changed from -1 p.u. to 1 p.u. of power. It can be seen in Fig. 3.9a that a pair of complex poles move towards the imaginary axis when the power flow increases, being 1 p.u. the operating point closest to instability (full power flowing from the master to the slave converter, i.e. master converter operating in rectifier mode). This is due to the fact that the system is non-minimum-phase in rectifying mode, which has a negative impact in the stability and performance of the system [78]. Therefore, that operating point will be the one considered for the small-signal analysis.

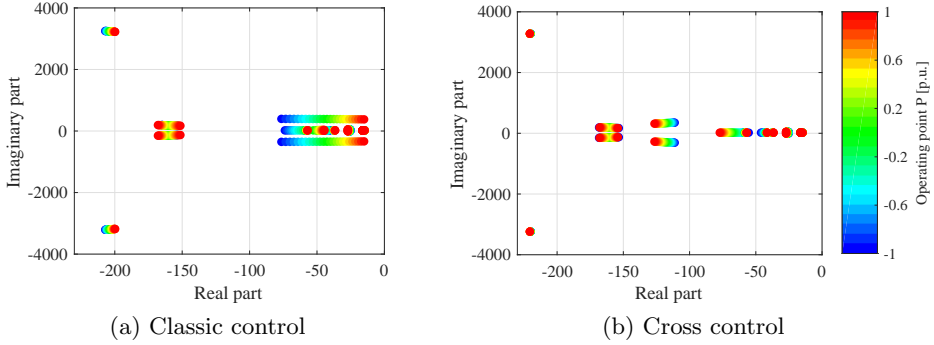(a) Classic control   (b) Cross control

Fig. 3.9: Eigenvalues of the point-to-point link system – Effect of the operating point

The small-signal analysis is performed using the linearised model. Such a model has the limitation of being reliable only at the vicinity of the operating point, where the non-linear model is linearised. For that reason, the performance will be verified through time-domain simulations using the complete non-linear model. For the frequency-domain analysis, the following transfer functions are of interest:

$$
\begin{aligned}
G_1(s) &= \frac{\Delta V_t^{\mathrm{dc}}(s)}{\Delta P_2(s)} & G_2(s) &= \frac{\Delta W_t(s)}{\Delta P_2(s)} \\
G_3(s) &= \frac{\Delta i_s^q(s)}{\Delta P_2(s)} & G_4(s) &= \frac{\Delta i_{\mathrm{sum}}^{0\mathrm{dc}}(s)}{\Delta P_2(s)}
\end{aligned}
\tag{3.8}
$$

The specifications are defined fixing a limit in the maximum gain of such transfer functions as

$$
|G_i(0)| \leq \frac{\|y_i(0)\|_2}{\|u_i(0)\|_2}
\tag{3.9}
$$

being $u_i(0)$ the input and $y_i(0)$ the corresponding output:

- $u_i(0) = P_N$, $i = 1, \ldots, 4$

- $y_1(0) = 0.10\ V_N^{\mathrm{dc}}$ (10% overvoltage)

- $y_2(0) = 0.10\ W_t^*$ (10% energy overshoot)

- $y_3(0) = 1.20\ (\sqrt{2}V_N^{\mathrm{dc}}/(\sqrt{3}U_N))$ (20% i_s^q overcurrent)

- $y_4(0) = 1.20 \ (P_N/(3V_N^{\mathrm{dc}})) \ (20\% \ i_{\mathrm{sum}}^{0\mathrm{dc}} \ \text{overcurrent})$

The different parameters are defined in Tables 3.1-3.2. With all above, time-domain and frequency-domain analyses are performed. The transient performance of the MMC with the classic, cross, weighted and constant DC voltage control structures is compared for different cable lengths. All the controllers constants remain unchanged except for the DC voltage, which is tuned according to the cable length equivalent capacitance (3.7). In Chapter 5, two tuning methods to calculate the outer controllers parameters according to these specifications will be presented. The power reference changes are summarised in Table 3.3. The energy-to-power ratio of the MMC is defined as

$$H_c = 6\frac{1}{2}\frac{C_{\mathrm{SM}}}{N_{\mathrm{arm}}}\frac{V_N^{\mathrm{dc}2}}{P_N} \tag{3.10}$$

Table 3.1: MMC and AC grid parameters [46]

Parameter	Symbol	Value	Units
Rated apparent power	S_N	526	MVA
Rated power factor	$\cos\varphi$	0.95 (c)	-
Rated active power	P_N	500	MW
AC side voltage	U_N	320	kV (rms ph-ph)
HVDC link voltage	V_N^{dc}	640 ($\pm$320)	kV
AC short-circuit ratio	SCR	10	-
Coupling impedance	$R_s + jL_s$	0.01+j 0.2	p.u.
Arm reactor impedance	$R_a + jL_a$	0.01+j 0.2	p.u.
Converter modules per arm	N_{arm}	400	1
Average module voltage	V_{SM}	1.6	kV
Sub-module capacitance	C_{SM}	8	mF
MMC energy-to-power ratio	H_c	49.2	ms

Table 3.2: Cable parameters (single monopole) [60]

Symbol	Value	Units	Symbol	Value	Units
r_1	0.1265	Ω/km	l_1	0.2644	mH/km
r_2	0.1504	Ω/km	l_2	7.2865	mH/km
r_3	0.0178	Ω/km	l_3	3.6198	mH/km
c	0.1616	μF/km	g	0.1015	μS/km

Table 3.3: Power reference set-points for the slave converter

Time	0 s	1 s	1.4 s	1.8 s	2.2 s
Power reference	0 p.u.	1 p.u.	0 p.u.	−1 p.u.	0 p.u.

3.4.4 Dynamic performance and small-signal analysis

Classic and cross control

Time-domain simulations of the classic and cross structure cases are shown in Figs. 3.10 and 3.12. Note that only stable cases are shown. In the first place, a relevant difference between the smoothness of the dynamics is noticeable. It is worth noting that in the classic control structure dynamics are more coupled than in the cross control structure: a change on the DC side will directly affect i_s^{q*}, changing the AC side power, in turn affecting i_{sum}^{0dc*}. This effect is more remarkable as the length of the line decreases.

In the case of the cross control structure, the dynamics of the DC side are clearly decoupled from the AC side. In other words, the energy loop will impose its slow dynamics on the AC side, regardless of the power behaviour on the DC side. Furthermore, the DC magnitudes are smoother in the cross control case. In conclusion, better performance is obtained in general, specially for shorter links. Nevertheless, the energy deviation appears to be larger than in the classic structure. The fact that the AC current steady-state is above 1 p.u. is due to the losses of the system between the AC side terminals 1 and 2, as the slave is injecting 1 p.u. of power to AC grid 2.

Eigenvalue comparison from 100 km to 2 km is shown in Figs. 3.11 and 3.13. The oscillation modes and their damping ratios are different for each alternative. This can be seen qualitatively with the imaginary part of the poles (which corresponds directly to the oscillation frequency of that particular mode, in rad/s) and with the angle formed by the vertical axis and a segment between a pole and the origin (the smaller the angle, the smaller the damping). A non-linear scale for the line length values has been used in order to properly show the trajectory of the poles of the short line cases.

Note that a complex unstable mode appears when the length of the line is decreased below a certain value. In particular, with the control parameters used, for the classic structure (Fig. 3.11) this value is approximately 25 km, whereas for the cross structure (Fig. 3.13) it is approximately 10 km.

Participation factors of such mode (namely $\lambda_{1,2}$) are shown in Figs. 3.14 and 3.15. The following notation is used: γ indicates the integral state of i_s^q, ξ is the integral state of i_{sum}^{0dc}, σ_v corresponds to the integral state of the error
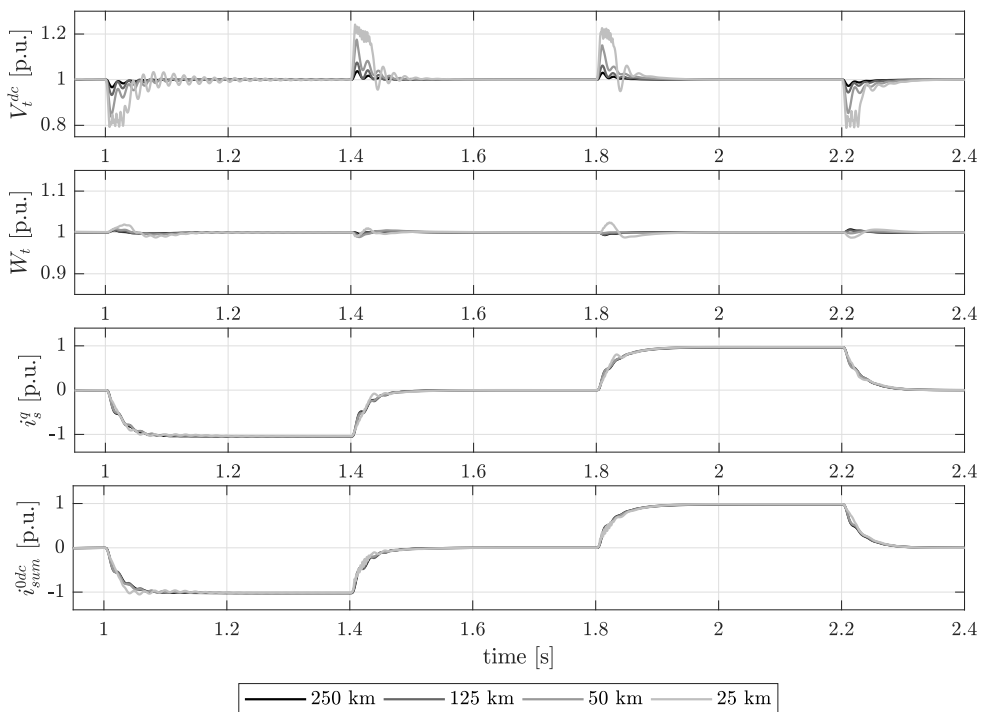
61

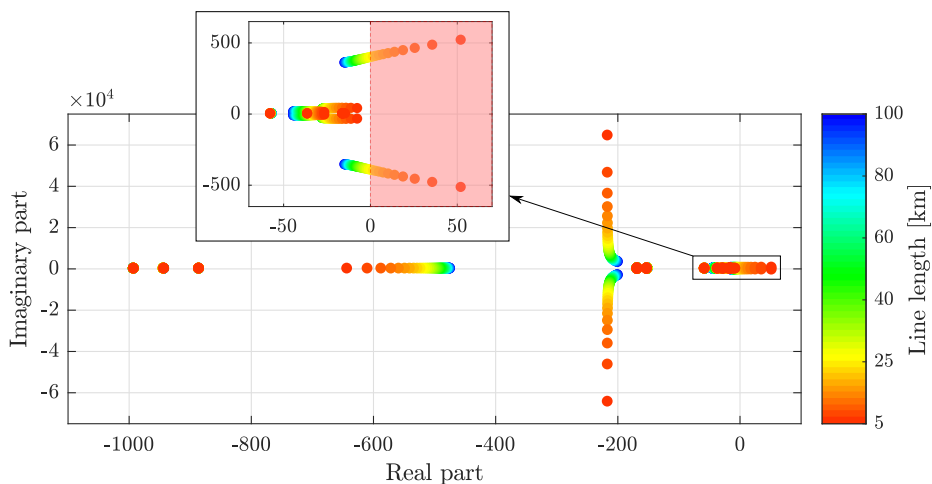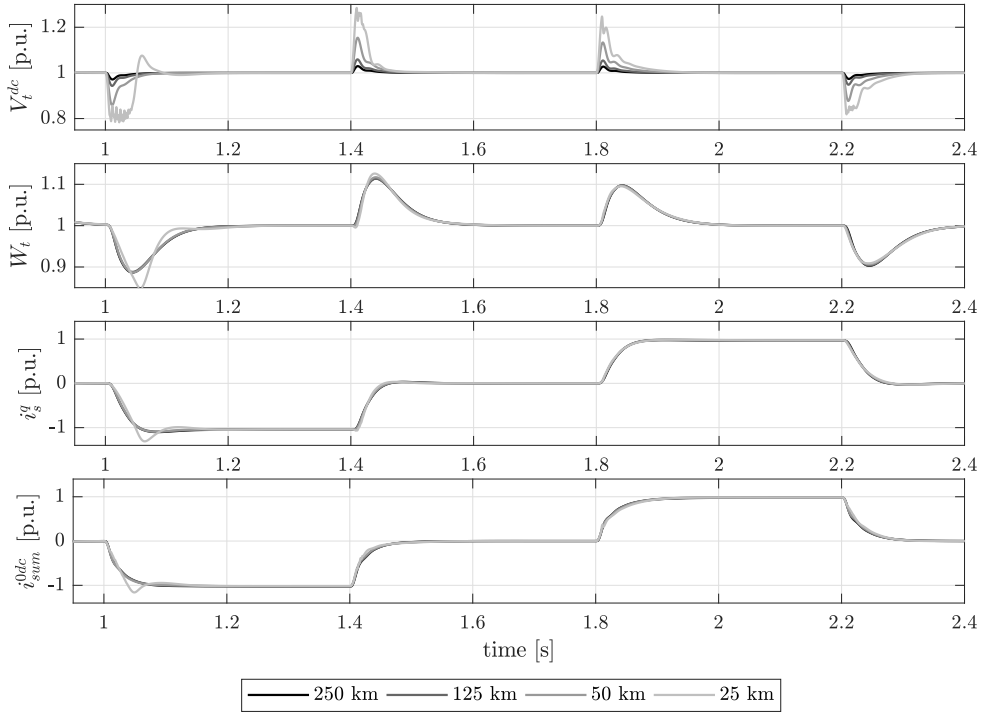Fig. 3.10: Time-domain simulation of the point-to-point link – MMC 1 (classic control)

Fig. 3.11: Eigenvalues of the point-to-point link system – Effect of the length of the link (classic control)

Fig. 3.12: Time-domain simulation of the point-to-point link – MMC 1 (cross control)
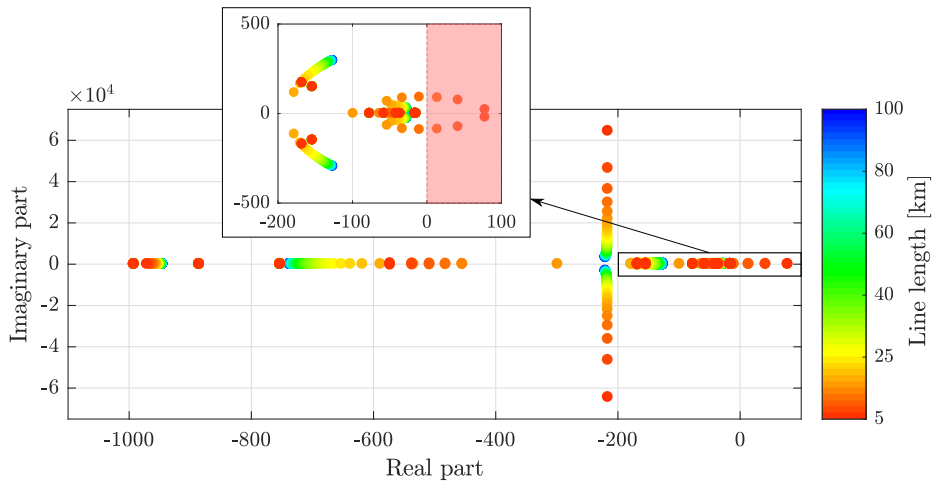

Fig. 3.13: Eigenvalues of the point-to-point link system – Effect of the length of the link (cross control)

of V_t^{dc} and κ_w refers to the integral state of the error of W_t. Subindexes 1 and 2 refer to the master converter (MMC 1) or the slave converter (MMC 2), respectively.

Regarding the classic control case, the strongest contributions come from the master converter MMC 1 (i_{s1}^q, $i_{\mathrm{sum1}}^{\mathrm{0dc}}$, W_{t1} and σ_{v1}). Secondly, the cable ($V_{t1,2}^{\mathrm{dc}}$) also has a remarkable participation. Finally, the slave converter MMC 2 also has some impact, to a lesser extent (W_{t2}). This means that the tuning of the DC voltage controller and the tuning of both energy controllers (MMC 1 more than MMC 2) would have a remarkable effect on $\lambda_{1,2}$.
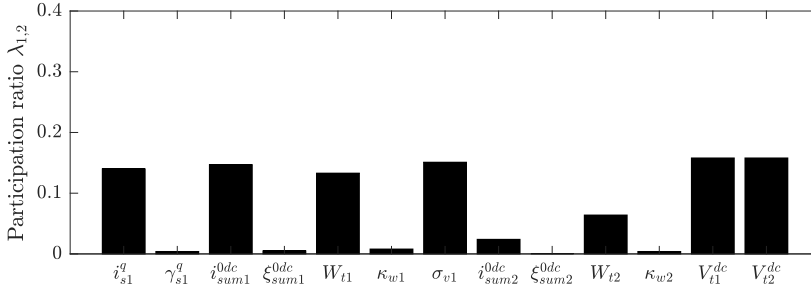
Fig. 3.14: Participation factors of the unstable mode $\lambda_{1,2}$ – MMC 1 with classic control, line length of 25 km

With respect to the cross control, the highest participation is observed in the DC voltage control of the master (σ_{v1}) and the energy of the slave (W_{t2}, κ_{w2}), whereas the DC currents ($i_{\mathrm{sum1,2}}^{\mathrm{0dc}}$) and the cable voltages ($V_{t1,2}^{\mathrm{dc}}$) participate to a much lesser extent. Due to the decoupling between the AC and the DC sides of MMC 1, the AC side is not participating at all in the unstable mode $\lambda_{1,2}$. Overall, as compared to the classic control case, MMC 1 participates slightly less, whereas MMC 2 importance is increased by around 5 times. This can be explained by the fact that in the slave converter control structure, W_{t2} is directly related to the DC side.

Weighted control

The weighted control alternative offers a new range of possibilities, as it results in a combination of the classic and cross approaches. First of all, the transient response is evaluated for a parametric sweep between the classic ($k_1 = 1$, $k_2 = 0$, $k_3 = 0$ and $k_4 = 1$) and the cross ($k_1 = 0$, $k_2 = 1$, $k_3 = 1$ and $k_4 = 0$) options, for a 50 km line (Fig. 3.16).

For this generic structure, intermediate results between both options are
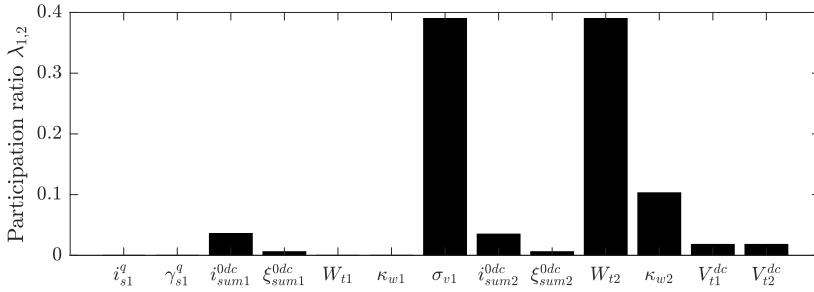
Fig. 3.15: Participation factors of the unstable mode $\lambda_{1,2}$ – MMC 1 with cross control, line length of 10 km
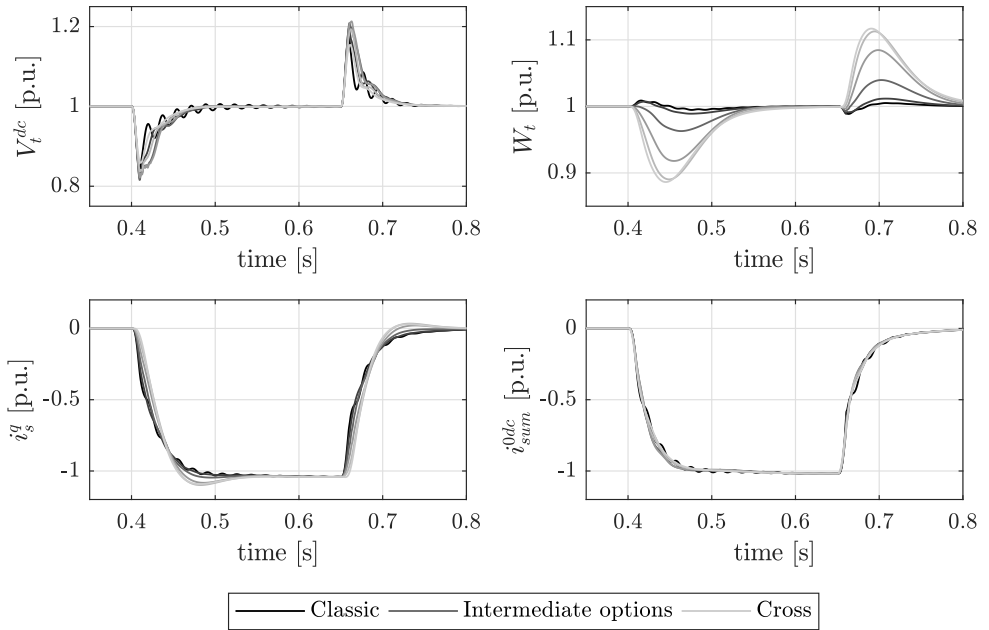

Fig. 3.16: Time-domain simulation of the point-to-point link – Effect of the weighted control parameters, line length of 50 km

obtained. Weight factors have been changed proportionally between 0 and 1, or vice versa (Tab. 3.4). It is shown that the cross structure has a smoother response in all magnitudes during the transient, except for the energy deviation, which is the highest. Also, a higher overshoot is observed in i_s^q for the combinations close to the cross control option. Then, an intermediate solution can be adopted in order to achieve acceptable performance in all magnitudes and thus a better overall performance.

Table 3.4: Weights evaluation for the weighted control structure

Parameter	Classic	Int. 1	Int. 2	Int. 3	Int. 4	Cross
k_1	1	0.8	0.6	0.4	0.2	0
k_2	0	0.2	0.4	0.6	0.8	1
k_3	0	0.2	0.4	0.6	0.8	1
k_4	1	0.8	0.6	0.4	0.2	0

This alternative enables a whole range of combinations and would require a thorough tuning in order to clearly see its specific advantages in a particular case, as it has more degrees of freedom than the classic and cross structure cases. Also, all weight factors can be either positive or negative. The purpose of this initial result is to show that a compromise solution could be taken, in order to affect the MMC magnitudes to a greater or a lesser extent. In Chapter 5, this thorough tuning will be addressed.

The time-domain response and the eigenvalue representation are shown in Figs. 3.17 and 3.18, respectively. Regarding the time-domain response, a better performance is obtained as compared to classic and cross control alternatives. This can be observed in the smaller overshoot of V_t^{dc} and W_t, and also in the smoother response in the currents. Actually, in the critical case of 25 km cable length, this structure performs reasonably well, avoiding saturation as in previous cases. In this case, the weight factors used are $k_1 = k_2 = k_3 = k_4 = 1$, which means that classic and cross structures have been directly combined, without any further scaling. The critical eigenvalue $\lambda_{1,2}$ becomes unstable at approximately 5 km, so the system is stable for a smaller length as compared to previous control structures.
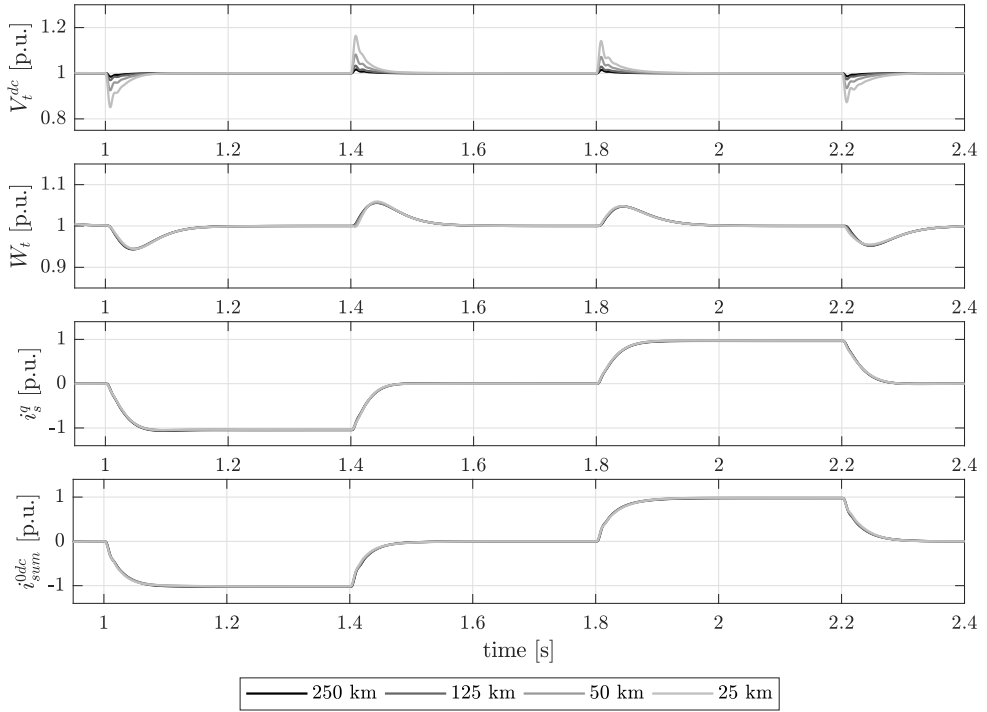
Fig. 3.17: Time-domain simulation of the point-to-point link – MMC 1 (weighted control, $k_1 = k_2 = k_3 = k_4 = 1$)
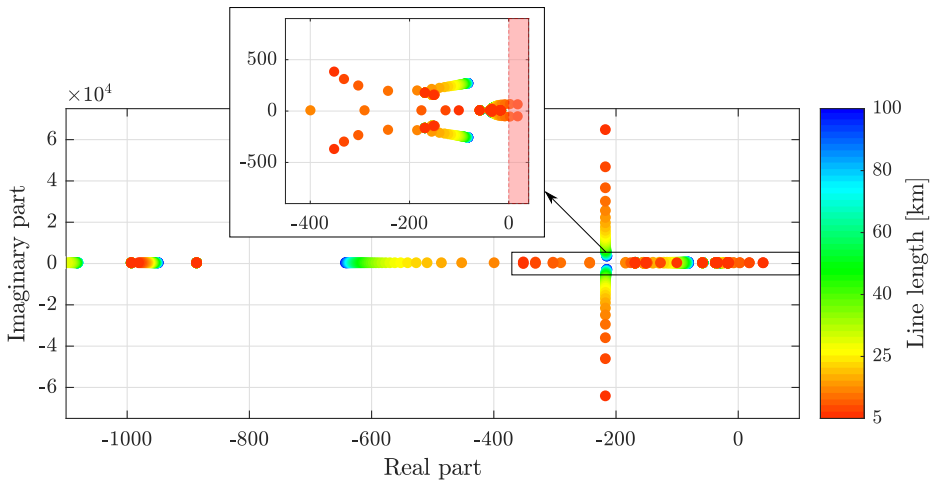

Fig. 3.18: Eigenvalues of the point-to-point link system – Effect of the length of the link (weighted control, $k_1 = k_2 = k_3 = k_4 = 1$)

Participation factors are shown in Fig. 3.19. It is shown that they are similar to cross structure ones, rather than the ones of the classic structure. However, MMC 1 slightly gains importance, which is related to the classic structure contribution.
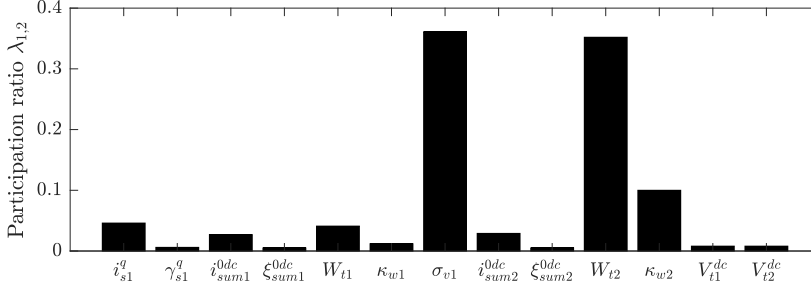

Fig. 3.19: Participation factors of the unstable mode $\lambda_{1,2}$ – MMC 1 with weighted control, line length of 5 km

Constant DC voltage control

If the HVDC link length is further decreased, the aforementioned structures start presenting more overshoot and saturation issues. Despite the fact that increasing the gain of the DC voltage controller might result in an overshoot reduction, it is not a feasible solution for very short cables, as this would lead to an unstable system due to inherent issues of cascaded closed-loop control. Therefore, a different solution is needed for such cases and for the back-to-back connection case (i.e. link length equal to 0). As presented in the previous section, the constant DC voltage control is proposed as a solution. In Fig. 3.20, the time-domain response under this control structure is shown. The most remarkable aspect is that the DC voltage error is remarkably small for the whole range of line lengths, compared to the previous cases. The reason is that the converter is generating a constant DC voltage without any closed-loop control behind it. The main concern, however, is that the DC current is not controlled, and therefore cannot be limited (saturations) as in the previous cases. Also, some oscillations appear, not only for the short line cases but also for the long line ones, between approximately 100 Hz and 400 Hz, which can be observed in the DC voltage (see zoomed-in-view in Fig. 3.20). Also, note that the energy response is very similar to the cross option (Fig. 3.12), as the two alternatives effectively decouple the AC and DC sides, and this part of the control structure is the same in both alternatives.
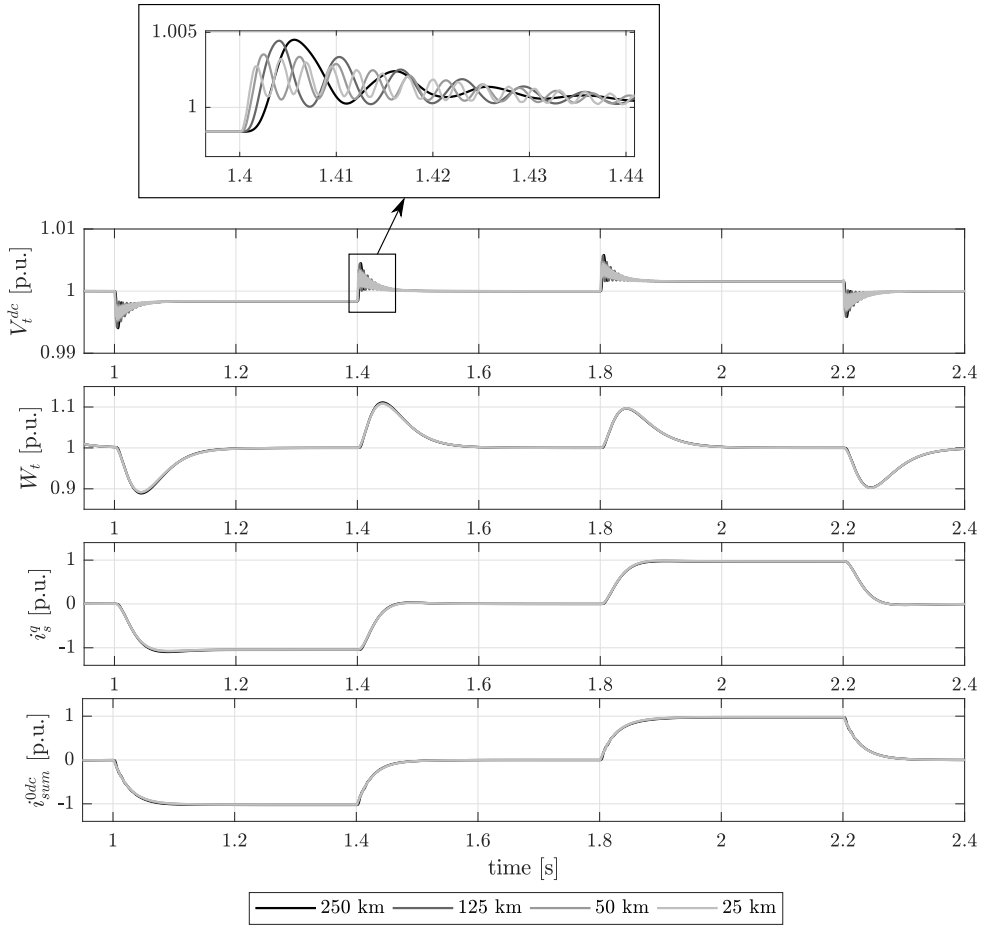
Fig. 3.20: Time-domain simulation of the point-to-point link – MMC 1 (constant DC voltage control

Regarding the eigenvalues (Fig. 3.21), it is worth noting that the system is still stable for very short lines, as the critical eigenvalue asymptotically approaches $x = -10$ (zoomed-in-view in Fig. 3.21). However, the shorter the line the higher the frequency and the lower the damping of that mode.
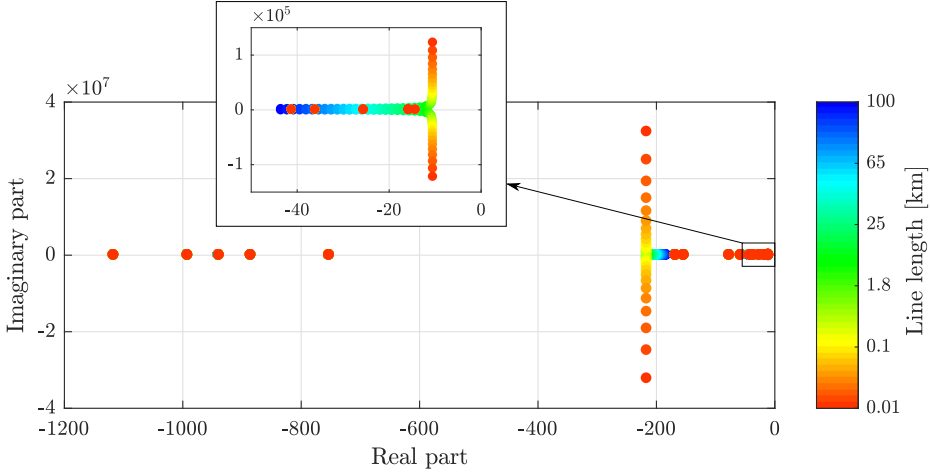

Fig. 3.21: Eigenvalues of the point-to-point link system – Effect of the length of the link (constant DC voltage control)

Taking a look at the participation factors (Fig. 3.22), the only contribution to the critical mode $\lambda_{1,2}$ comes from the DC current of MMC 1 (i_{sum1}^{0dc}) and the cable ($V_{t1,2}^{dc}$). However, as the DC current cannot be controlled under this control structure, MMC 1 cannot influence this mode. Under these circumstances, the characteristics of this mode (frequency, damping) only change if the HVDC link length is changed (see Fig. 3.21).
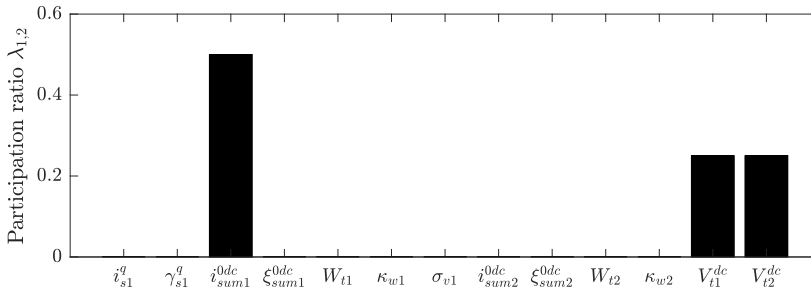
Fig. 3.22: Participation factors of the unstable mode $\lambda_{1,2}$ – MMC 1 with constant DC voltage control, line length of 1 km

Frequency domain analysis: wrap-up of all control structures

In order to complementarily analyse the system in the frequency-domain, Bode plots of all cases are shown in Figs. 3.23-3.24. In these Bode plots, it can be seen whether one particular length case of a specific control structure exceeds or not the four transient requirements presented before (3.9), as a way to qualitatively compare different alternatives, maintaining the same tuning rules. Some peaks are noticed in the high frequency range (close to 10^4 Hz) due to the cable. However, these peaks are not important as the attenuation is very high at those frequencies.

Results are consistent with the corresponding time-domain simulations in terms of transient requirements and resonance frequencies. It is remarkable that in the classic alternative (Fig. 3.23a) there are peaks at different frequencies, whereas in the cross alternative (Fig. 3.23b) the peaks are reduced. This is shown also in the time-domain response (Figs. 3.10 and 3.12), which is smoother when using the second structure. Regarding the weighted case, it again proves that it is an intermediate option between the classic and the cross alternatives. As mentioned before, the case shown corresponds to $k_1 = k_2 = k_3 = k_4 = 1$. Again, a more thorough study should be conducted here analysing different possibilities of the control system overall, which will be done in Chapter 5. Finally, the constant DC voltage structure presents the lowest error in the DC voltage. However, a steady-state error (left part of Fig. 3.24b, $G_1(s)$) is observed, even though it is very small. Also, resonant peaks are more noticeable than in other alternatives.
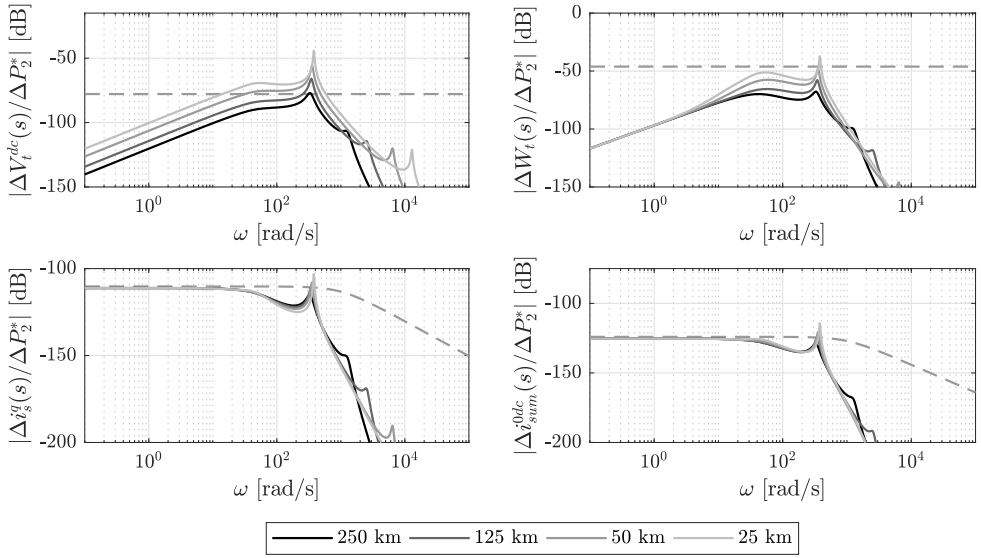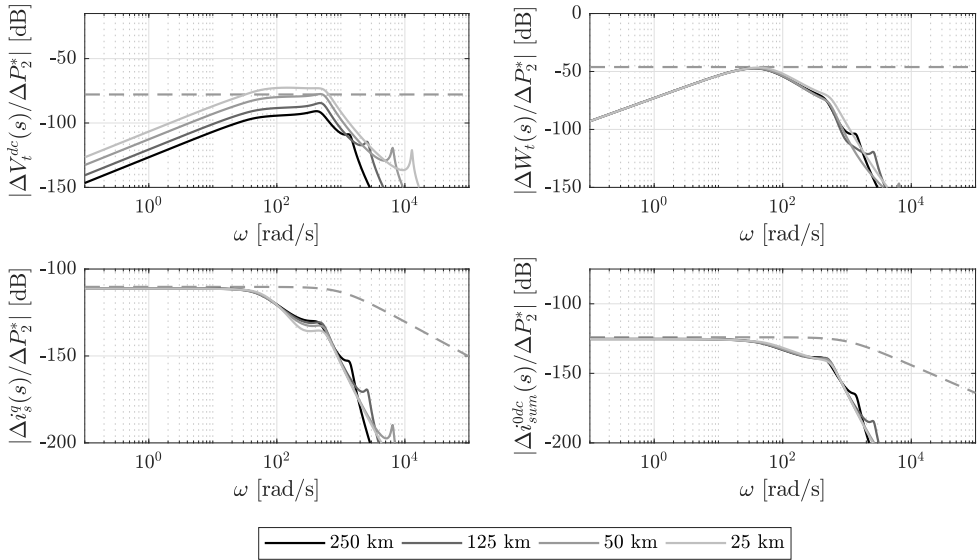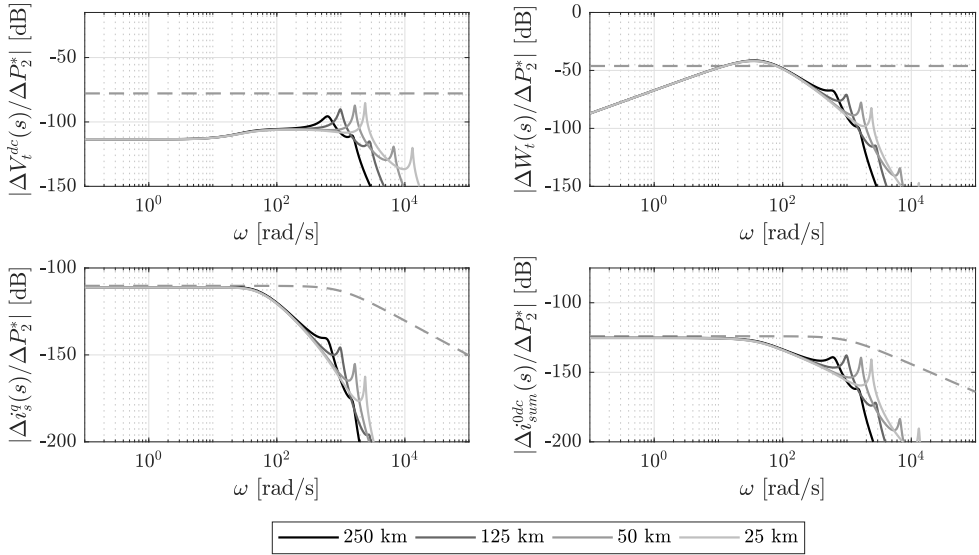
(a) Classic control structure
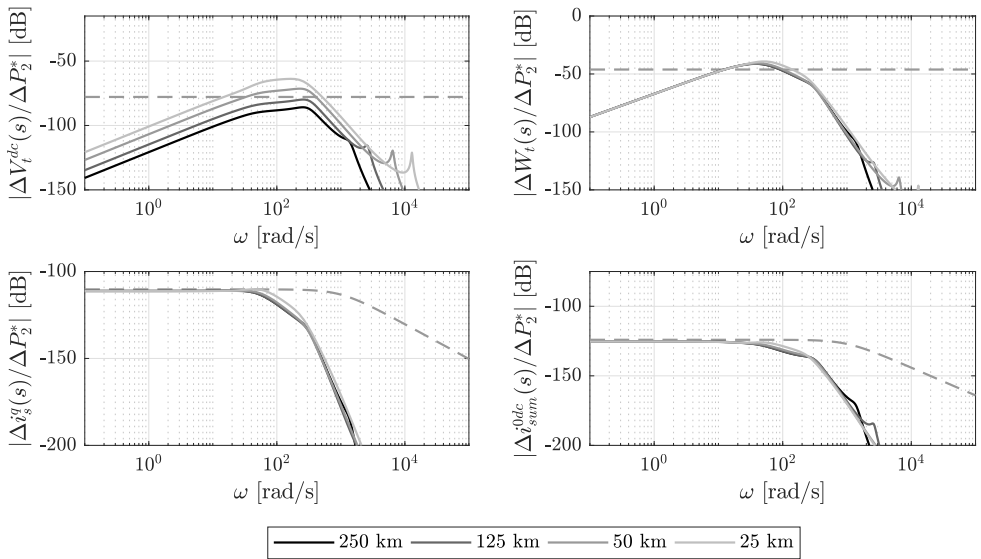
(b) Cross control structure

Fig. 3.23: Bode gain plots of the point-to-point link system $G_i(s)$ ($i = 1, \ldots, 4$) and gain limits – Classic control and cross control

(a) Weighted control structure

(b) Constant DC voltage control structure

Fig. 3.24: Bode gain plots of the point-to-point link system $G_i(s)$ ($i = 1, \ldots, 4$) and gain limits – Weighted control and constant DC voltage control

3.5 Conclusion

Different alternatives for the control of a point-to-point MMC-based HVDC link using a master-slave approach have been evaluated. A complete linear model of the system that enables linear analysis has been derived, complementing time-domain simulations with eigenvalue and frequency-domain analysis. Results show that the classic 2L-VSC control structure extrapolated to the MMC (i.e. using the DC voltage control output as a reference for the AC active current, and therefore the total energy control output as a reference for the DC current) does not perform well for medium and short links, due to the high reduction of the capacitance in the DC bus, which depends exclusively on the cable length. A cross structure (i.e. using the DC voltage control output as a reference for the DC current, and the total energy control output as a reference for the AC active current) has demonstrated to improve the results, as the AC and the DC sides are highly decoupled. Also, a generic weighted structure combining both options has been presented, which enhances a control system with more degrees of freedom that could be helpful to adjust the final transient response through a thorough tuning. This will be investigated in Chapter 5. However, for links of a few kilometres and back-to-back applications, these alternatives may still lead to an unacceptable transient performance, and even instability. A constant DC voltage open-loop control has been evaluated as a possible solution, improving the DC voltage transient response and simplifying the control system. However, its limitations are that the DC current is not controlled or cannot be saturated, and that some undesired oscillations and a small steady-state DC voltage error appear.

Chapter 4

Experimental validation of a laboratory-scaled MMC-HVDC link

This chapter is based on the work done in collaboration with Imperial College London during a secondment of three months, and it is related to the following publication:

[C3] E. Sánchez-Sánchez, A. Junyent-Ferré, E. Prieto-Araujo, O. Gomis-Bellmunt and T. Green, "Modelling and experimental validation of a laboratory-scaled HVDC cable emulator tested in an MMC-based platform", in *22nd European Conference on Power Electronics and Applications (EPE'20 ECCE Europe)*, Lyon, France, Sept. 2020.

4.1 Introduction

It was seen in Chapter 3 that using the classic control scheme of 2-level VSCs can lead to severe problems in the MMC case, due to the lack of capacitors connected to the DC bus. This issue reveals that HVDC cables play a relevant role in the performance and stability of the system, as they provide an equivalent capacitance at the MMC DC terminals. The so-called Wideband Model or Universal Line Model (ULM) [67] is the most commonly accepted model for EMT simulations, which accounts for the cable parameters frequency dependence. However, it is not clear what is the best way to experimentally realise an HVDC cable in a low-voltage laboratory-scaled platform. Typically, π-sections are used [79]. As the π-section model does not represent the real cable accurately [70], other studies have proposed the use of a scaled real cable with the same voltage drop and wave propagation characteristics as the real high-voltage cable [80].

As discussed in [70], an approximate linear mathematical model with multiple parallel branches can be obtained using the cable data and vector fitting techniques. This model uses time-invariant concentrated parameters and it can be used for small-signal studies. An experimental realisation of a scaled HVDC cable inspired on this idea is proposed in this chapter. Different possibilities are discussed considering the feasibility in terms of volume and cost of such a cable emulator. Furthermore, a decoupled DC voltage control using

the cross control structure is implemented in an MMC-based point-to-point HVDC test bench of 15 kVA controlled by OPAL-RT units, which allows for fast prototyping of the control system, as the OPAL-RT code is compiled directly from the Simulink control blocks. The cable emulator is included between both terminals, with the objective of testing and validating the stability of the system and its dynamic performance.

4.2 System description

As in Chapter 3, the system under study consists of a point-to-point MMC-based HVDC link, with the focus on the master MMC (i.e. an MMC that controls the DC voltage). Using an energy-based control approach, which is a reliable control approach in terms of dynamic performance [46], the internal energy of the converter and the energy of the DC side can be regulated independently. The first one depends on the capacitance installed in the submodules of the converter, which is linked to the rating of the converter. The second one depends on the equivalent capacitance of the DC network, which is proportional to the length of the HVDC lines (see Fig. 4.1). While the internal MMC capacitance is relatively big, the DC side capacitance can be very small in short and medium length point-to-point links. This can compromise the controllability of the DC voltage in the HVDC system when a DC voltage closed-loop control is used, as seen in Chapter 3.
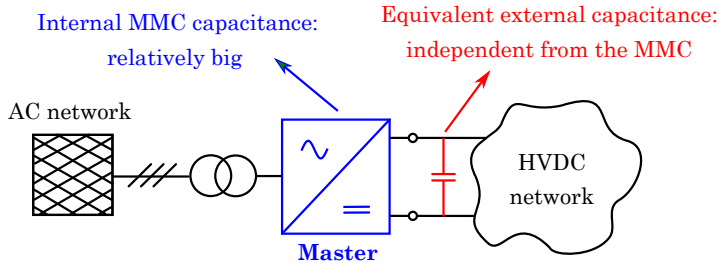

Fig. 4.1: Internal and external equivalent capacitances

Different control structures for a master MMC exist in the literature. In this case, cross control has been used: DC voltage (V_t^{dc}) controls DC current (i^{dc}), and total energy (W_t) controls AC current (i_s). This approach provides decoupling between AC and DC sides, as the control sequence affect the different variables in a cascaded way (see Fig. 4.2) and yields an appropriate dynamic performance.
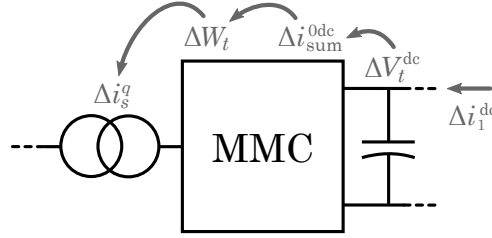
Fig. 4.2: Conceptual control sequence of an MMC under cross control structure

4.3 Cable model

As mentioned in the Introduction, HVDC cables present frequency-dependent behaviour in their equivalent cable parameters. In EMTP simulations, the well-known ULM is typically used, as it takes into account this effect based on the physical and geometric characteristics of the cable. The complexity of this model makes analytical derivations for system-level studies impractical in many cases. A concentrated-parameter linear model to enable small-signal studies would be preferable in many situations. However, wrong fitting of the approximate linear model could lead to wrong conclusions.

As mentioned in Chapter 2, the frequency-dependent model from [70] is used, consisting of a different number of RL parallel branches, and several cascaded sections (Fig. 2.11). The number of branches and sections defines the accuracy of the model, and the method to calculate those parameters is briefly described next.

4.3.1 Vector fitting fundamentals

The methodology used to obtain the parameters of the different branches (Fig. 2.11) is based on the vector fitting algorithm presented in [81]. Basically, the method consists of iteratively relocate the poles of the system until convergence is achieved, which is usually fast. This formulation uses simple fractions, therefore avoiding ill-conditioning problems inherent to other approaches based on polynomials. Unstable poles are forced to be stable by moving them to the left hand side of the Laplace plane. Vector fitting is applicable to high order systems and wide frequency bands [81].

The general problem formulation is given as (4.1), where $f(s)$ is the adjusted function, N is the order of the system, r_i are the residues, a_i are the

poles, and d and h are real values.

$$f(s) = \sum_{i=1}^{N} \frac{r_i}{s - a_i} + d + sh \tag{4.1}$$

The vector fitting technique aims to match the frequency response of a real system with the frequency response of $f(s)$ (4.1), by adjusting the parameters r_i, a_i, d and h iteratively as briefly described before. Then, the first step is to obtain the transfer function of the cable model from Fig. 2.11. Assuming that the shunt conductance and capacitance do not change substantially in the frequency-domain [70], the system in Fig. 4.3 is considered. The equivalent estimated admittance is derived as (4.2). Note that $\hat{Y}(s)$ is equivalent to (4.1) dropping d and h.

$$\hat{Y}(s) = \frac{I(s)}{V(s)} = \sum_{i=1}^{N} \frac{1}{l_{z,i}s - (-r_{z,i})} \tag{4.2}$$
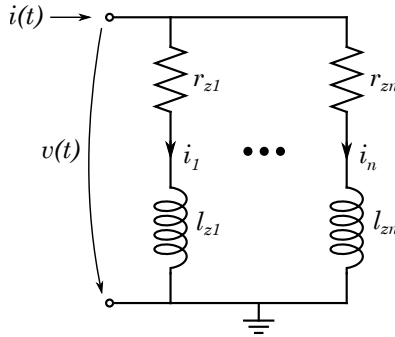
Fig. 4.3: Series parallel branches corresponding to one section of the cable model from Fig. 2.11

The 320 kV XLPE insulated cable from [68], consisting of a core conductor, a lead sheath and steel armor, is used as the reference. The vector fitting algorithm iteratively adjusts the parameters from (4.2) in order to fit the frequency response of the ULM cable. It has to be noted that the vector fitting algorithm offers different configuration options, such as number of iterations, initial poles, and frequency weights. In this case, initial real poles logarithmically distributed [81], 10 iterations, and the same initial value for the weights have been set. The function `vectfit3` returns the poles of $\hat{Y}(s)$ and the associated state-space representation, and then function `ss2pr` transforms it

into a pole-residue model (both functions are available at [82]). Finally, the branch resistances and inductances are derived as

$$l_{z,i} = \frac{1}{\text{Res}_{z,i}}; \qquad r_{z,i} = -\lambda_{z,i} l_{z,i},$$
(4.3)

where Res is the residue and λ the pole associated to branch i.

4.3.2 Cable emulator based on the parallel branches model

While prior work in the literature has discussed the trade-offs of replicating the relevant dynamics of 2L-VSCs and MMCs in small-scale platforms, very little has been published about replicating the complex dynamics of HVDC cables in small-scale platforms for converter interaction studies. The approach presented here is inspired by the work on simplified cable simulation described in the previous sections. The implementation is based on the physical realisation of the equivalent circuit models obtained by these methods. The parameters of the branches are calculated using vector fitting using the cable data from [68].

In order to validate the dynamics of the cable model, an open-circuit test (Fig. 4.4) of the different models is performed. The effect of changing the number of sections and the number of branches on the cable model accuracy is shown in Figs. 4.5 and 4.6, as compared to the ULM model (from the BestPaths project Simulink toolbox [69]) and the π-section model. Note that the π-section model has been calculated based on the equivalent RL series impedance of the cable. A step of 1 p.u. of voltage is applied at t = 0 s, and the cable length is 250 km. The parameters of the π-section and parallel branches models are shown in Table 4.1. Note that, in the 9-branches case, very large parameters of L are obtained. The shunt parameters are $c = 0.1616\ \mu\text{F/km}$ and $g = 0.1015\ \mu\text{S/km}$ in all cases, as the vector fitting only deals with the RL parameters.
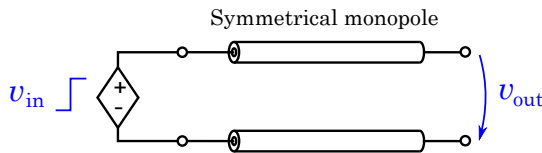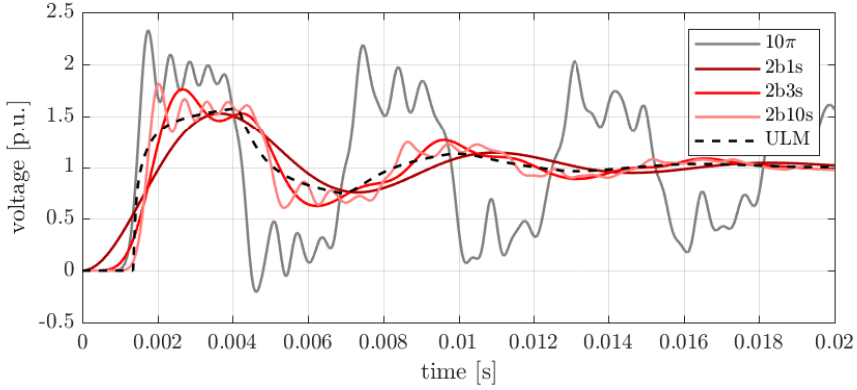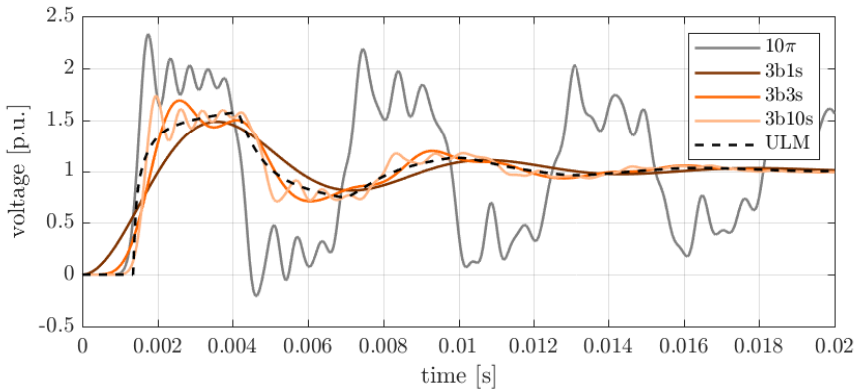

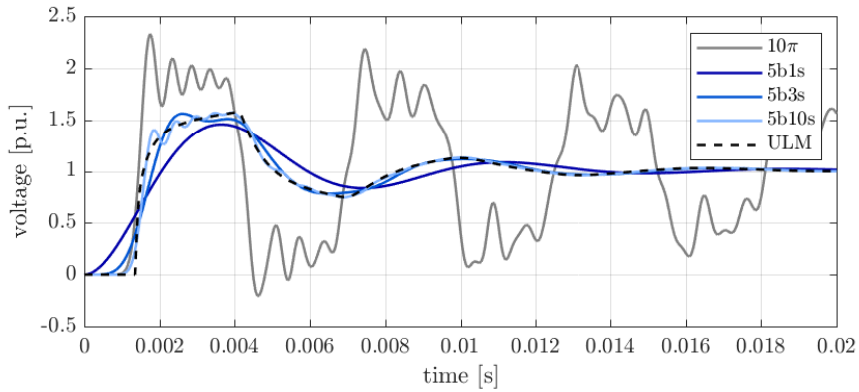Fig. 4.4: Open-circuit test of the symmetrical monopole
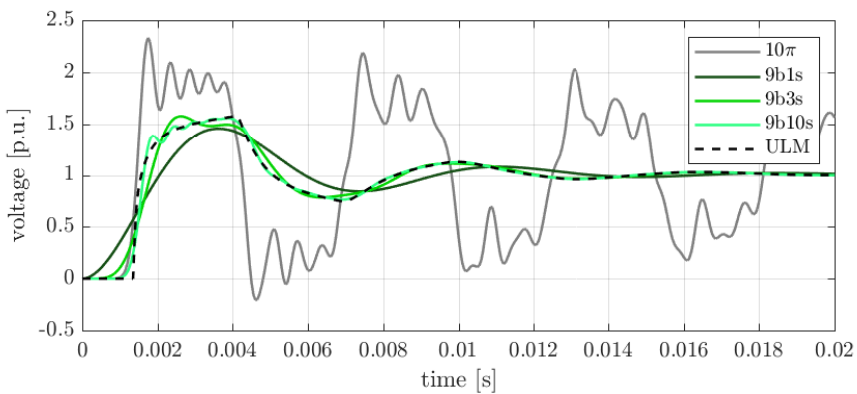
(a) 2 parallel branches

(b) 3 parallel branches

Fig. 4.5: Symmetrical monopole 2 and 3 branches models transient responses (250 km) – Open-circuit test: voltage step of 1 p.u. in one side, open circuit in the other side

(a) 5 parallel branches

(b) 9 parallel branches

Fig. 4.6: Symmetrical monopole 5 and 11 branches models transient responses (250 km) – Open-circuit test: voltage step of 1 p.u. in one side, open circuit in the other side

Table 4.1: Cable models RL parameters from vector fitting

Parameters	π-sect.	3-bran.	5-bran.	9-bran.	Units
R_1	0.014	0.132	1.889	70.76	[Ω/km]
R_2	-	0.242	0.135	4.348	
R_3	-	0.017	0.511	0.331	
R_4	-	-	0.020	0.200	
R_5	-	-	0.081	0.876	
R_6	-	-	-	0.097	
R_7	-	-	-	0.021	
R_8	-	-	-	0.332	
R_9	-	-	-	3.119	
L_1	0.188	0.263	0.689	3.014	[mH/km]
L_2	-	6.509	0.321	1.026	
L_3	-	3.282	10.19	0.494	
L_4	-	-	3.276	0.635	
L_5	-	-	30.87	19.03	
L_6	-	-	-	9.646	
L_7	-	-	-	4.133	
L_8	-	-	-	199.8	
L_9	-	-	-	14050	

A short-circuit test (Fig. 4.7) is performed to compute the frequency responses, as the symmetrical monopole is seen as an impedance. The frequency response of the models with different number of branches and 10 sections per pole is presented in Figs. 4.8-4.9, considering lengths of 250 km and 50 km.
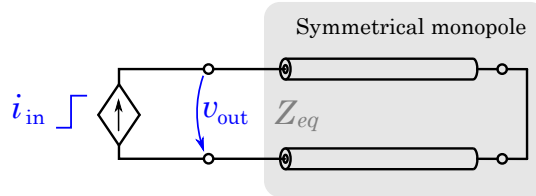
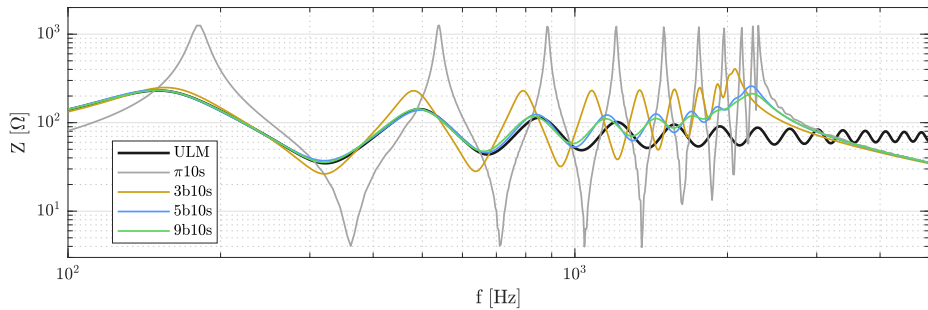Fig. 4.7: Short-circuit test of the symmetrical monopole

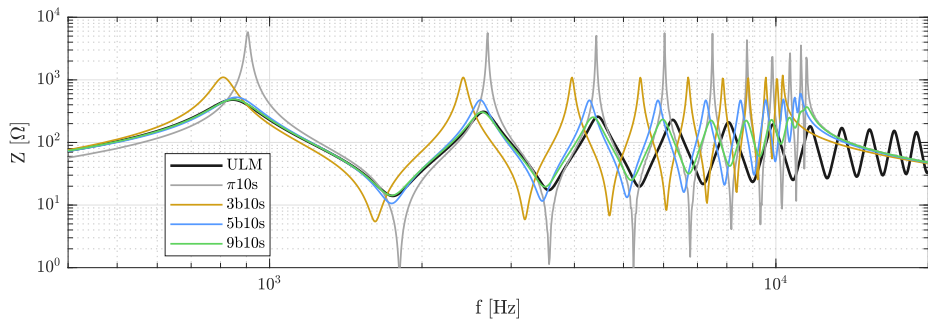Fig. 4.8: Symmetrical monopole impedance vs frequency (250 km) – Short-circuit test on different models

Fig. 4.9: Symmetrical monopole impedance vs frequency (50 km) – Short-circuit test on different models

From Figs. 4.5-4.6 and Figs. 4.8-4.9 it can be noted that:

- A high number of sections makes the model replicate the travelling wave effect and the main frequency components, but causes a high frequency oscillation to appear.

- A high number of branches mitigates the high frequency oscillatory terms inherent to the parallel branches model.

- The π-section exhibits a very undamped time-domain response, as well as relatively high resonance impedance peaks, as compared to the other models and to the ULM.

Therefore, ideally it is desirable to include as many sections and branches as possible. However, this is obviously not feasible from an experimental platform point of view, due to hardware volume and cost constraints. Then, a compromise solution has to be established, as discussed in the next section.

4.4 Experimental platform

This section presents the details of a low-voltage experimental platform, specially emphasising on the cable emulator design which aims to emulate the real high-voltage cable dynamics for small-signal stability studies. Testing and validating HVDC systems in laboratory-scaled platforms as opposed to using computer simulations has been a controversial topic of discussion among the academic and the power industry communities over the last years. Scaled platforms inevitably miss some details (e.g. lower efficiency than the real system) [83]. Special attention has to be paid in identifying the limitations of the model, in order for the conclusions drawn to be extrapolated back to the real full-scale system.

The different systems used in the present study are summarised in Fig. 4.10. Firstly, the original detailed simulation model of an HVDC system is scaled-down. Secondly, a highly detailed simulation model of the experimental platform is used as a previous validation step before carrying out the actual experiments as the third and last step of the process. Simulations are carried out with Matlab Simulink, and the ULM cable model from [69] is used in the simulated real system, as mentioned before.

Bearing that in mind, the present study aims to maximise the validity of the results using an accurate MMC low-voltage platform and an improved cable emulator. The test bench (Fig. 4.11) consists of a master MMC that controls the DC voltage, a DC source that emulates the slave MMC, and a
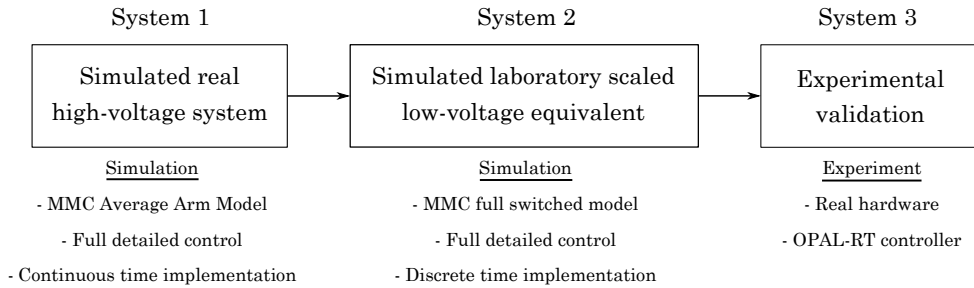
Fig. 4.10: Overview of the different systems involved in the results validation

cable emulator between them. In order to have a balanced and harmonic-free AC grid voltage, a programmable AC voltage source is used to emulate a stiff AC system to which the MMC converter is connected. The OPAL-RT unit controls the MMC prototype and takes all the necessary measurements, whereas the CompactRIO controller is used for supervision purposes, as well as for managing the switchgear that sets the configuration (i.e. length) of the cable.
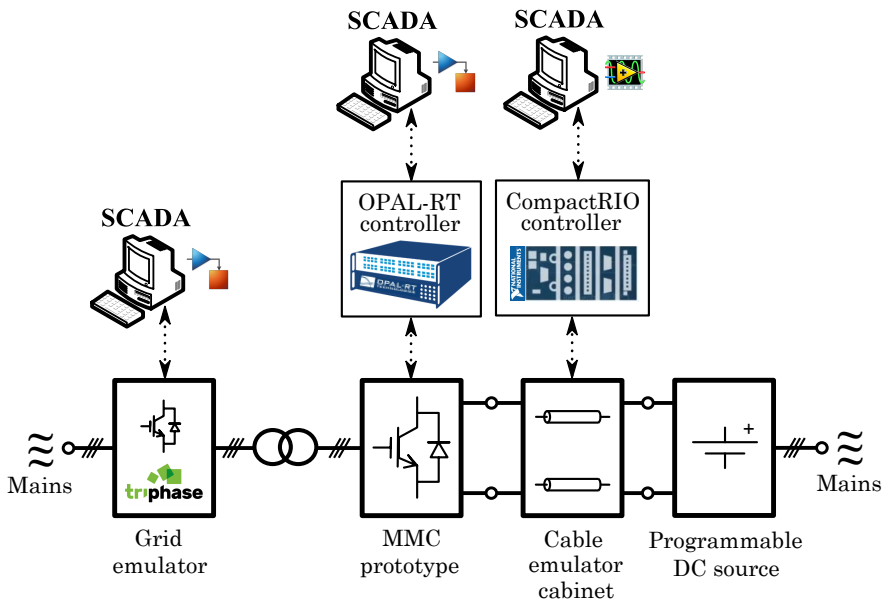
Fig. 4.11: Laboratory-scaled experimental platform MMC-based HVDC link

4.4.1 MMC prototype

The parameters of the real high-voltage MMC and the scaled low-voltage MMC prototype are summarised in Table 4.2. The base impedances (DC and AC) of both systems can be calculated as (4.4). Note that the energy-to-power ratio of the MMC (H_c) is practically the same for both systems, and that the arm reactor impedance in per-unit is also very similar. This shows a good match between the two systems in relative terms. On the other hand, the transformer leakage inductance of the laboratory setup is significantly lower than it would be expected in the large scale system (0.01 p.u. against 0.2 p.u., see the transformer tests in Appendix D) due to the transformer physical characteristics. However, the fast control and the voltage feed-forward terms used in the inner current control (see Section 4.4.3) do not make this difference relevant in terms of dynamics.

$$Z_{\text{dc}} = \frac{V_t^{\text{dc}2}}{S_N}, \quad Z_{\text{ac}} = \frac{U_{N,s}^2}{S_N} \tag{4.4}$$

Table 4.2: Parameters of the real system and the scaled prototype

Parameter	Symbol	Real syst.	Scaled prot.
Rated power	S_N	500 MVA	15 kVA
HVDC link voltage	V_N^{dc}	640 kV	1500 V
Line AC voltage (primary)	$U_{N,p}$	400 kV	340 V
Line AC voltage (secondary)	$U_{N,s}$	320 kV	816 V
Submodules per arm	N_{SM}	400	10
Submodules capacitance	C_{SM}	8 mF	1,1 mF
MMC energy-to-power ratio	H_c	49.2 ms	49.5 ms
Base DC impedance	Z_{dc}	819.2 Ω	150 Ω
Base AC impedance	Z_{ac}	204.8 Ω	40.56 Ω
Arm resistance	R_{arm}	0.0100 p.u.	0.0099 p.u.
Arm inductance	L_{arm}	0.2000 p.u.	0.1743 p.u.
Transf. leakage resistance	R_{tr}	0.0100 p.u.	0.0364 p.u.
Transf. leakage inductance	L_{tr}	0.2000 p.u.	0.0113 p.u.

The cabinets of the AC grid emulator (90 kVA converter from Triphase), the slave MMC emulator (15 kVA DC source from Magna Electronics), and the master MMC prototype (an in-house design from Imperial College London [84]) used in the laboratory experiments are shown in Fig. 4.12.

(a) AC grid emulator

(b) Slave MMC emulator (DC source)

(c) Master MMC prototype (closed)

(d) Master MMC prototype (open)

Fig. 4.12: Pictures of different cabinets of the platform

4.4.2 HVDC cable emulator

The DC impedance ratio between the real and the scaled systems is used to properly scale the series and shunt parameters of the cable, as indicated in (4.5). Thus, the per-unit values are equivalent in both the real system and the laboratory prototype, using the respective base impedances.

$$R_{dc}^{lab} = R_{dc}^{real} \frac{Z_{dc}^{lab}}{Z_{dc}^{real}} \tag{4.5a}$$

$$L_{dc}^{lab} = L_{dc}^{real} \frac{Z_{dc}^{lab}}{Z_{dc}^{real}} \tag{4.5b}$$

$$G_{dc}^{lab} = G_{dc}^{real} \frac{Z_{dc}^{real}}{Z_{dc}^{lab}} \tag{4.5c}$$

$$C_{dc}^{lab} = C_{dc}^{real} \frac{Z_{dc}^{real}}{Z_{dc}^{lab}} \tag{4.5d}$$

The design of the parallel branches of the new sections is based on adapting an existing design based on π-sections built for a different purpose. The main difference compared to a design done from scratch is that some of the initial specifications (e.g. the length of emulated cable per model section) were adapted in order to reuse some of the existing material aiming at a reasonable cost and similar physical footprint. The present procedure is focused on this specific experimental platform. A more extensive analysis could be done in terms of selecting the most appropriate number of branches and sections. In fact, algorithms for selecting the optimal number of branches and sections for HVDC cables based on different metrics are presented in [85]. That is presented in terms of models for small-signal analysis, where a trade-off between accuracy and model order is key. From the experimental point of view, though, cost and footprint are the major constraints, as will be described next.

The procedure to determine the number of branches of the cable section is presented in Fig. 4.13. The first step is to obtain the state-space model using the function `vectfit3`. This function, as mentioned in Section 4.3.1, fits the frequency response of a generic model to a specific given frequency response, in this case from the ULM cable data. The algorithm iterates and tries to obtain the best solution based on the root-mean-square error. After fitting the state-space model, the pole-residue model is obtained using the function `ss2pr`, which gives the branch parameters $(r_{z,i}, l_{z,i}, \forall i)$. As these parameters correspond to the high-voltage real system, they are scaled in order to be

used in the prototype system accordingly. The process ends at this stage if the obtained $l_{z,i}$ are feasible in terms of volume and cost. Otherwise, the number of branches is reduced by 1, and the process is started again. The reference value for $l_{z,i}$ is the original series inductance of the existing π-section (5.125 mH), and the following high-level objectives are pursued:

- Length range: the upgraded section should correspond to a few kilometres of emulated cable, in order to reach a relatively long distance when combining all sections in the cabinet.

- Section size: the upgraded section volume and weight must be similar to the original one, in order to avoid making major changes to the cable emulator cabinet.

The largest inductor of the upgraded section is the largest of the original π-section. It is desirable to use it to model a few kilometres and to keep all other inductors smaller in order to keep the physical footprint small. The parameters obtained for different number of branches (N_b) are shown in Table 4.3. As mentioned before, the shunt parameters (independent from the number of branches) are $c = 0.1616$ μF/km and $g = 0.1015$ μS/km (real system), and $c = 0.8824$ μF/km and $g = 0.5543$ μS/km (scaled prototype).

The largest inductance in the 5-branches model is 5.653 mH. This is approximately the same as the original value and it corresponds to approximately 1 km of cable. This is a sufficient condition to not use this model, as it constraints the maximum distance the emulator can reach with the existing number of sections. Regarding the 3-branches model, the largest inductance is 1.1918 mH, and the second largest is 0.6009 mH. This model is more feasible than the previous one, but still requires relatively large additional components, with the corresponding increase in cost and volume. As the difference in accuracy between a 3-branches and a 2-branches model is relatively small (see Fig. 4.5), the 2-branches option is explored. In this case, the largest inductance is 0.5303 mH. This means that an inductance of 5.125 mH corresponds to 9.63 km, which is reasonable for scalability purposes. Consequently, the 2-branches model is chosen for the implementation. The rest of the parameters are summarised in Table 4.4. Note that, in the π-section case, an original resistance of 50 mΩ is included. However, the actual value of the series resistance is 130 mΩ, as the parasitic resistance of the inductor is 80 mΩ. Also note that the final upgraded section R_2 component is around 2.75 times higher than the desired ideal one, meaning that the steady-state voltage drop at the cable will be higher than expected.

Table 4.3: Parallel branches models parameters of the real system and the scaled prototype

	N_b	$l_{z,1}$	$l_{z,2}$	$l_{z,3}$	$l_{z,4}$	$l_{z,5}$	$r_{z,1}$	$r_{z,2}$	$r_{z,3}$	$r_{z,4}$	$r_{z,5}$	c	g
				Parallel branches								Shunt parameters	
Real system	5	0.689	0.321	10.2	3.28	30.9	1889	135	511	21	81	0.1616	0.1015
	3	0.263	6.51	3.28	-	-	132	242	17	-	-		
	2	0.272	2.9	-	-	-	114	16	-	-	-		
Scaled prototype	5	0.1262	0.0588	1.8660	0.5999	5.65530	346	25	94	4	15	0.8824	0.5543
	3	0.0482	1.1918	0.6009	-	-	24	44	3	-	-		
	2	**0.0498**	**0.5303**	-	-	-	**21**	**3**	-	-	-		
		mH/km					mΩ/km					μF/km	μS/km

Table 4.4: HVDC cable prototype section parameters

Parameter	Original π-section	Upgraded section (ideal)	Upgraded section (available)	Units
L_1	-	0.481	0.470	[mH/section]
L_2	5.125	5.125	5.125	[mH/section]
R_1	-	203	237	[mΩ/section]
R_2	130	29	80	[mΩ/section]
C	3.600	8.524	8.660	[μF/section]
G	-	5.355	-	[μS/section]

A few further adjustments are made in order to enable the physical implementation of the circuit. Firstly, parameters are adapted to correspond to the those of the closest commercial components available. In the case of R_2 this leads to a greater error because its ideal value is lower than the effective series resistance of L_2. Consequently, no discrete resistor is added in series with L_2 in the second branch. Also, G is not included in the circuit given that it has little effect on the dynamics.

Regarding the current rating of the components, it is worth noting that the cable emulator is designed to carry out small-signal experiments. Therefore, all components are sized to withstand the rated current of the cable with an additional safety margin but they are not suitable to carry out realistic short-circuit studies as the transient current would exceed the saturation point of the inductors.

The original cable emulator cabinet (Fig. 4.14) included two full symmetrical monopoles built for a four-terminal DC system. Each of the four cables had 11 π-sections (Fig. 4.15). At this stage, only two of the four cables were upgraded to the new design because this was the minimum required in order to build a point-to-point DC link. Therefore, the cabinet contains a total of 22 upgraded parallel branches sections, allowing for a maximum length of around 106 km of equivalent cable. The other 22 sections remain as π-sections and are not used in the present study.
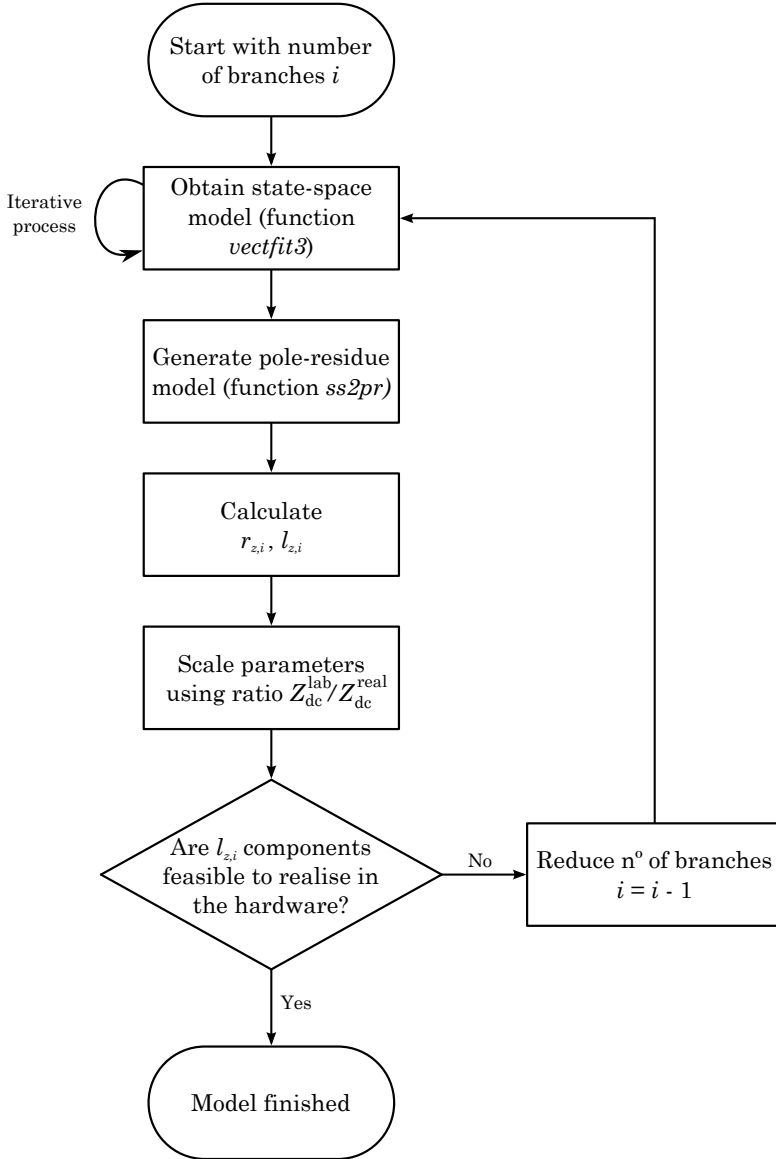
Fig. 4.13: Flow chart of the cable section design procedure
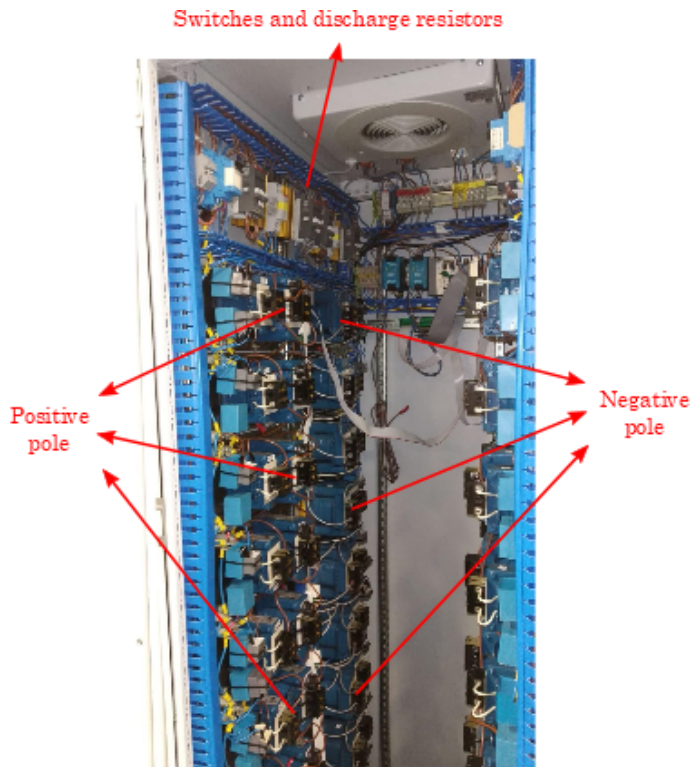
Fig. 4.14: HVDC cable emulator cabinet
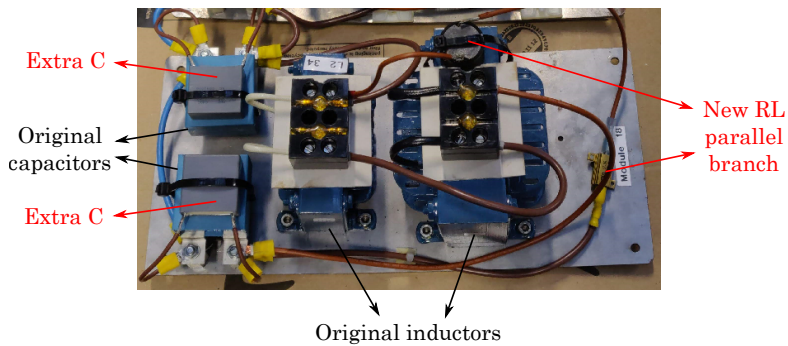
Fig. 4.15: Detailed cable section, corresponding to 9.63 km of cable

4.4.3 MMC control

The control approach implemented in the experimental platform presents some differences as compared to the control approach used throughout this thesis, which has been previously described in Chapter 2. The reason to use a different approach is that both the hardware and the control design of the MMC platform used in the present experimental tests were thoroughly developed and tested during previous research projects [86, 87]. Therefore, due to a limited amount of time to carry out the experiments, and to take advantage of previous research works, the already well-tested and reliable control approach of the MMC platform has been used in the experiments. Rather than implementing the control approach used throughout the thesis (Control I), a validation and a dynamic analysis comparison between Control I and the one used in the experimental setup (Control II) has been performed. Thus, as will be shown next, it can be stated that both approaches are fundamentally equivalent.

On one hand, in Control I (Fig. 4.16a), a variable change (diff-sum) is used to identify the roles of each AC and DC current component, thus obtaining decoupled equations. Then, specific feedback controllers are designed for each component, making their tuning relatively straightforward, in a Single-Input Single-Output (SISO) fashion. In this case, Park transform is used in the case of the AC grid current, enabling the use of PI controllers, and also PI controllers together with lead-lag filters (see Chapter 2) are used for the additive current components inside the MMC. This control approach is implemented in a continuous-time average model, as discussed in previous chapters.

On the other hand, Control II (Fig. 4.16b) is addressed directly in the upper-lower $(u - l)$ frame, and without addressing separately the AC and DC components of the currents, obtaining an overall state-space model with mixed AC and DC components. In this case, a feed-forward controller is firstly designed to compensate for external AC and DC voltages (uncontrollable inputs) as well as the inductive and resistive voltage drops of the system. Additionally, a feedback controller is added to bring states back to their references, although most of the control effort is supplied by the feed-forward controller. Regarding the feedback control, it is usually complex to manually tune such a Multiple-Input Multiple-Output (MIMO) controller. To overcome this challenge, a Linear-Quadratic Regulator (LQR) is used. LQR allows for tuning a complex multivariable system more intuitively by treating it as an optimisation problem, assigning costs to the different errors and inputs of the system. The LQR controller is a proportional controller, and

the costs are tuned iteratively to achieve the desired performance. A similar approach was followed in [88]. This control approach is implemented in a discrete-time switched model. That model was built in the past for various research purposes [86, 87] as a detailed and reliable representation of the laboratory-scaled experimental platform. Thus, simulations are run in this model for verification purposes before downloading the designed controls into the OPAL-RT unit that controls the experimental platform.
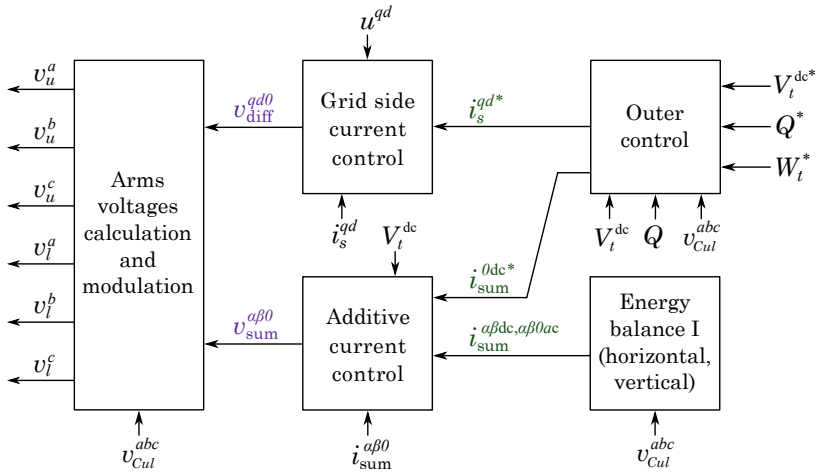
(a) Control I: approach used throughout the thesis
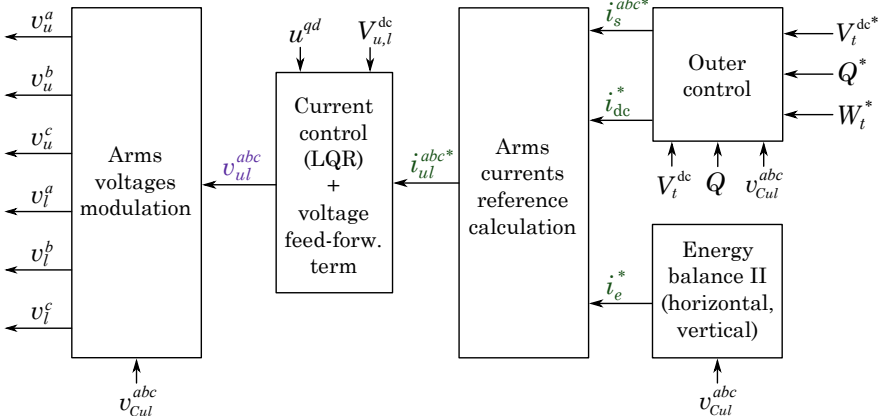
(b) Control II: approach used in the experimental platform

Fig. 4.16: Different inner control approaches for the MMC (energy-based)

In Figs. 4.17-4.19, the dynamics of both control approaches are compared through simulations. As mentioned before, Control I is implemented in

a continuous-time average model, whereas Control II is implemented in a discrete-time switched model, for the aforementioned practical reasons. Starting with an operating point of 0.75 p.u. of DC power flowing from the slave MMC to the master MMC, a step to 1 p.u. of DC power is performed at t=2 s. Some additional ripples on top of the main components are observed in the magnitudes of the experimental platform model. This is due to the switches rather than to the control approach itself, and those are not observed in average models. Also, small differences are observed on the AC side current and power, which are due to the extra losses of the experimental platform model (i.e. switching losses). Furthermore, the energy differences (Fig. 4.19) present phase shift and a small difference in the amplitude of the ripples. In this case, this is due to the energy balancing control approach, which is different in Control I and Control II. However, these differences are not relevant and do not affect the normal operation of the converter. Overall, it can be concluded that both models exhibit essentially the same dynamic characteristics. Therefore, it is reasonable to use one approach or the other indistinctly, and it can be also stated that the average model essentially matches the more detailed switched model. In the next section, the high-voltage system simulation (using Control I) is compared to the experimental results of the laboratory platform (using Control II).

(a) DC side current

(b) DC side voltage (secondary side of the transformer)
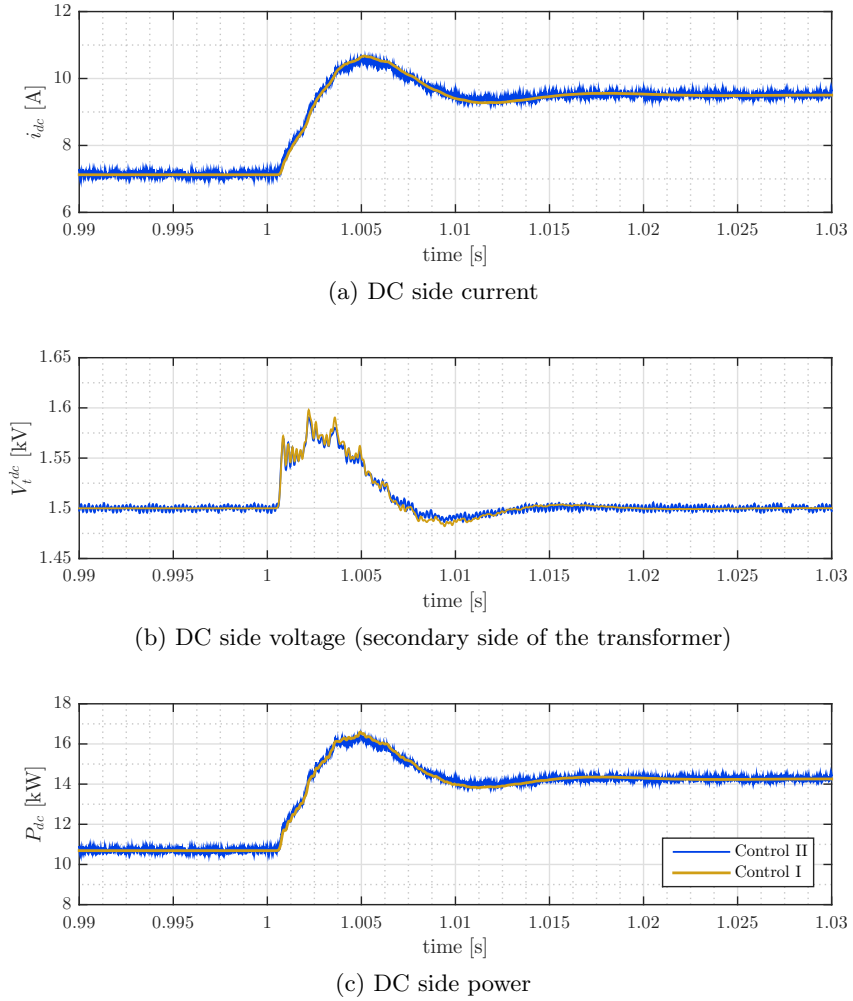
(c) DC side power

Fig. 4.17: Dynamic response simulation models comparison: Control I and Control II – DC magnitudes
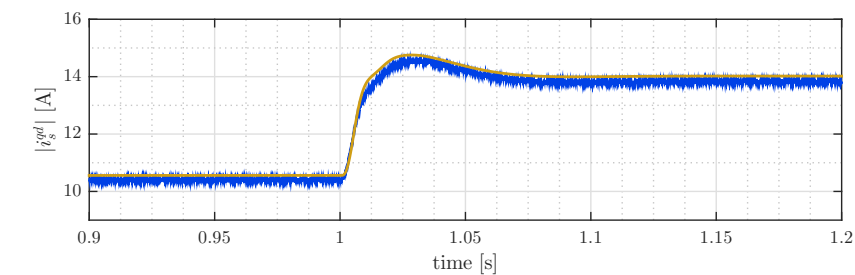
(a) AC side current
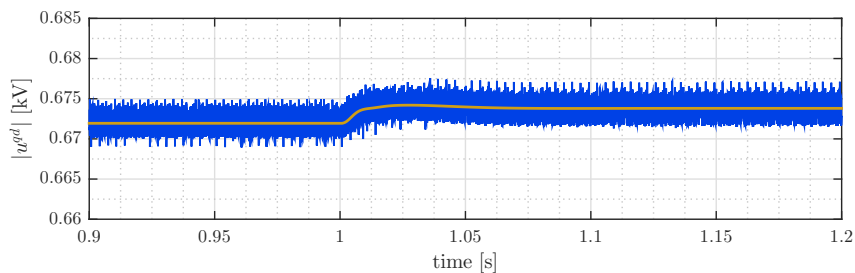
(b) AC side voltage (secondary side of the transformer)
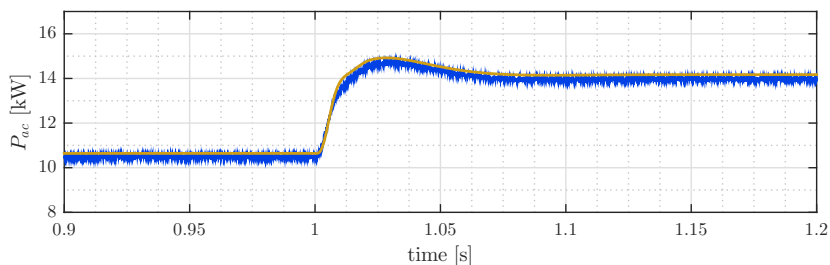
(c) AC side power
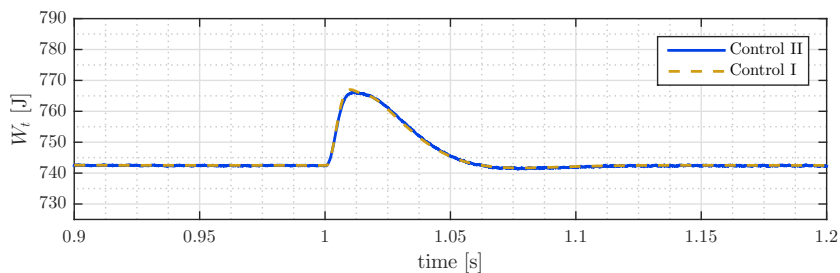
(d) MMC total energy

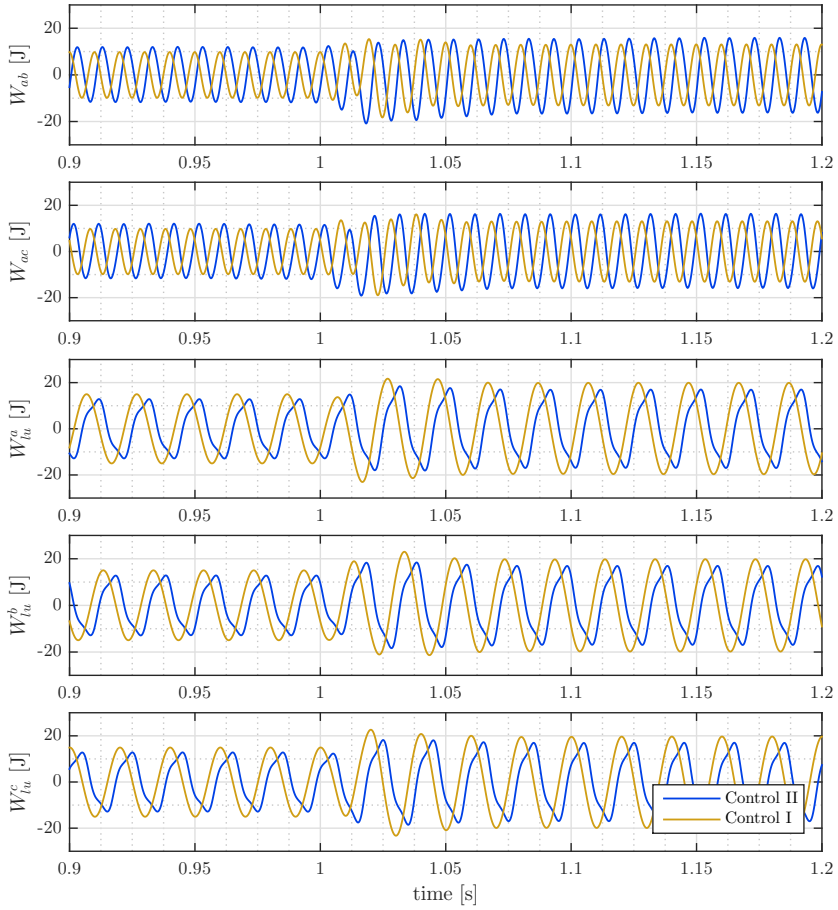Fig. 4.18: Dynamic response simulation models comparison: Control I and Control II – AC magnitudes

Fig. 4.19: Dynamic response simulation models comparison: Control I and Control II – Internal MMC energy differences

4.5 Dynamic performance of the system

The point-to-point system is tested under a DC current disturbance injection, from 0 to rated current in approximately 500 ms. The length of the link is set to 48.14 km, which corresponds to 5 sections for each pole. The simulation of the real system, using the ULM cable and the Average Arm Model (AAM) of the MMC, the simulation of the low-voltage detailed system that represents the experimental platform, and the experimental results are presented in Figs. 4.20-4.21. The slave converter is modelled as a DC source with a first order response of 500 ms. The disturbance is applied from the DC source operating in current control mode.

It can be seen that the simulated real high-voltage system (system 1), the simulated laboratory-scaled low-voltage equivalent (system 2) and the experimental setup (system 3) exhibit similar dynamic behaviour. The main difference is found in the DC voltage ripple in systems 2 (Fig. 4.20e) and 3 (Fig. 4.20f), and to a lesser extent in the AC voltages in system 3 (Fig. 4.21i). As the AC grid is ideally balanced and harmonic-free, and because the MMC model is an average model without switching states, these ripples do not appear in the real system simulation (system 1). Also, the AC voltages are slightly higher in system 3 (Fig. 4.21i). This could be related to a higher impedance in the AC side, which causes a higher voltage drop.

The frequency response of the cable emulator (using the setup from Fig. 4.7) is presented in Figs. 4.22-4.23. As the number of sections used determines the cable length, different cases are plotted. In order to compare the frequency response of the cable emulator with the one from the ULM cable, the values of the components used in the laboratory platform are scaled back to the high-voltage system, using the relations from (4.5). Also, the π-section model has been included for reference, with its RL parameters corresponding to the equivalent RL of the cable, as mentioned before. Therefore, the parameters of the π-section model shown in these plots correspond to the ideal case where it is possible to use the desired series resistance. Note that the whole symmetrical monopole is considered in all cases.

It can be seen that the peaks in the case of the π-section are the largest in all cases. The 2-branches model reduces these peaks, and also results in a better representation of the cable at the lower frequency range. The initial resonance peak is not as close to the ULM model as the π-section in the case of one or few sections in series. In case of several sections in series (Fig. 4.23), the 2-branches model exhibits a better match both with the location of the initial peak and its impedance value (as well as a good match at the lower frequency range). It has to be noted that the equivalent series resistance (i.e.
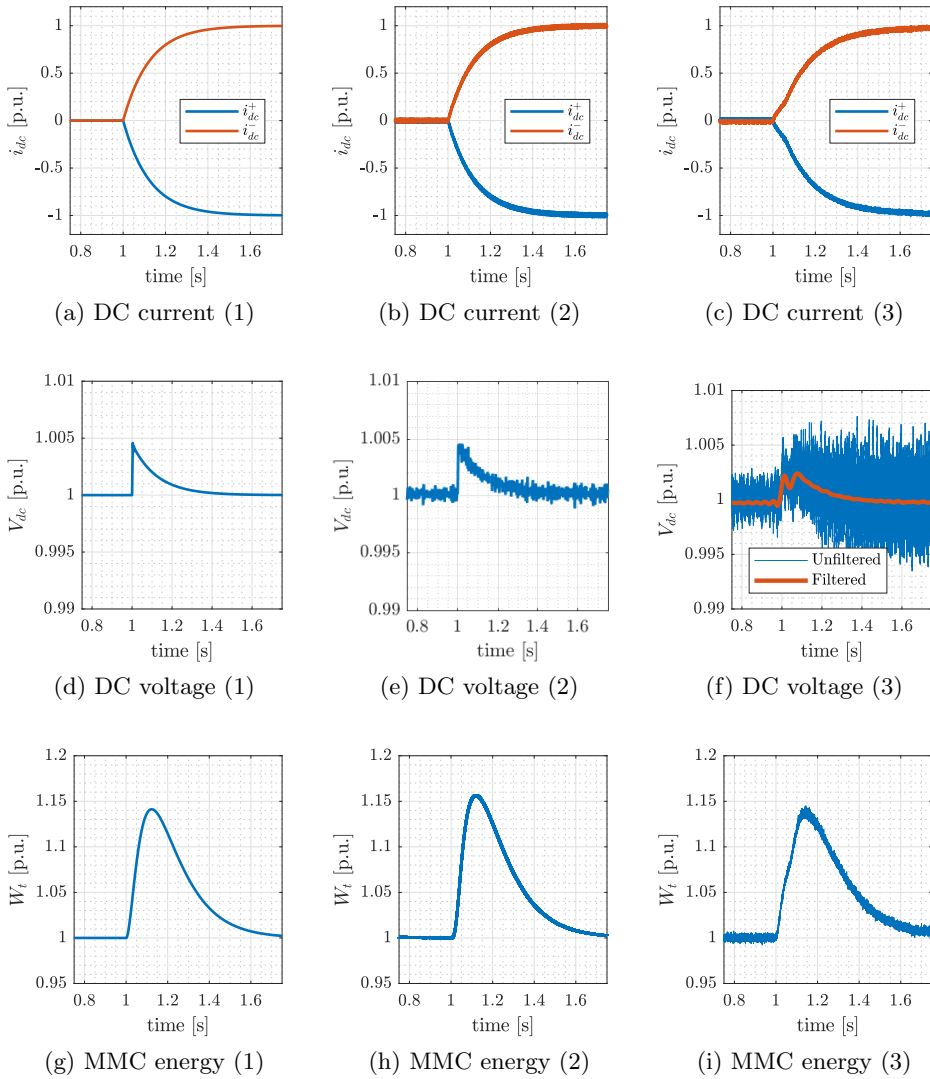
Fig. 4.20: Dynamic response of the DC current, DC voltage and internal MMC energy – Simulated real high-voltage system (system 1), simulated laboratory-scaled low-voltage equivalent (system 2), and experimental setup (system 3)
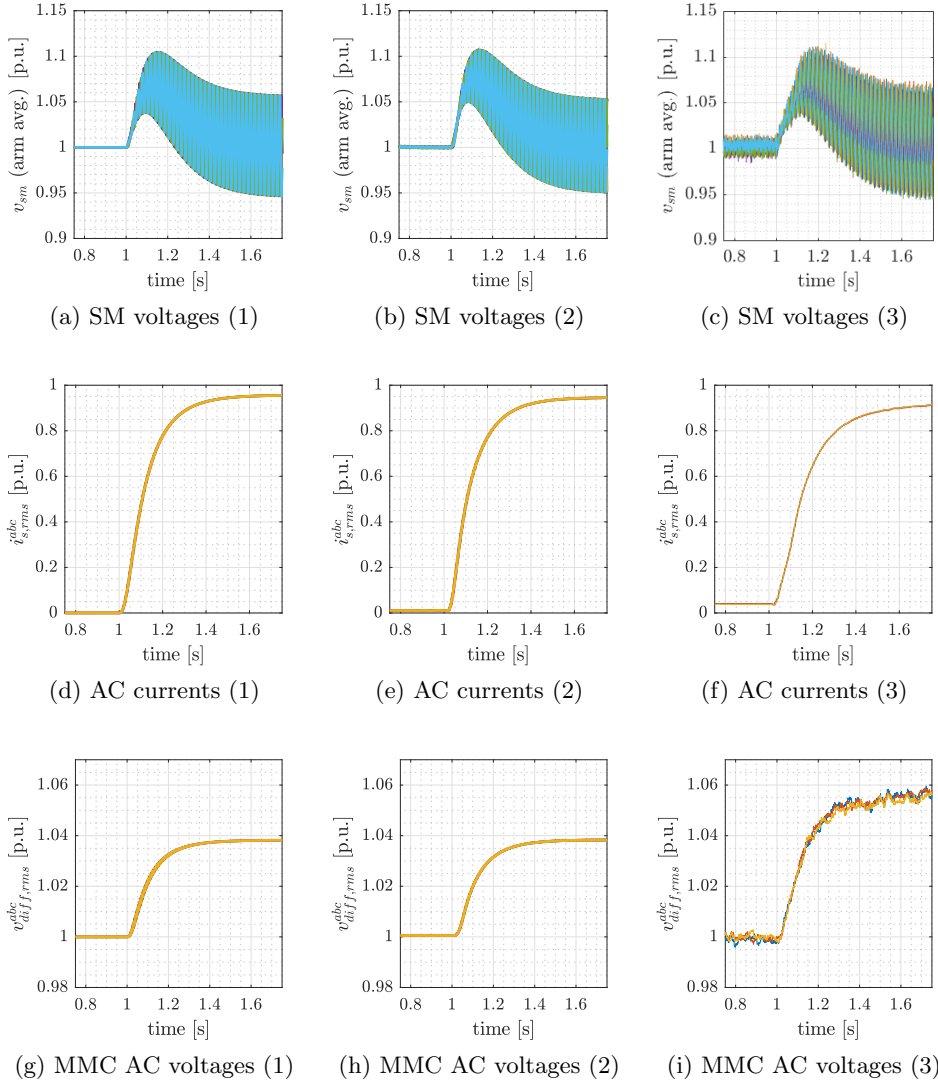
(a) SM voltages (1)

(b) SM voltages (2)

(c) SM voltages (3)

(d) AC currents (1)

(e) AC currents (2)

(f) AC currents (3)

(g) MMC AC voltages (1)

(h) MMC AC voltages (2)

(i) MMC AC voltages (3)

Fig. 4.21: Dynamic response of the arms voltages, AC currents and AC voltages – Simulated real high-voltage system (system 1), simulated laboratory-scaled low-voltage equivalent (system 2), and experimental setup (system 3)

the impedance corresponding to 0 Hz) is not the expected one in the case of the 2-branches model. This is because the minimum possible resistance for the hardware setup is constrained by the parasitic resistance of the inductor, which is around 2.75 times higher than the desired one (see R_2 in Table 4.4). Finally, note that the number of resonant peaks is related to the number of cable sections in series as expected.
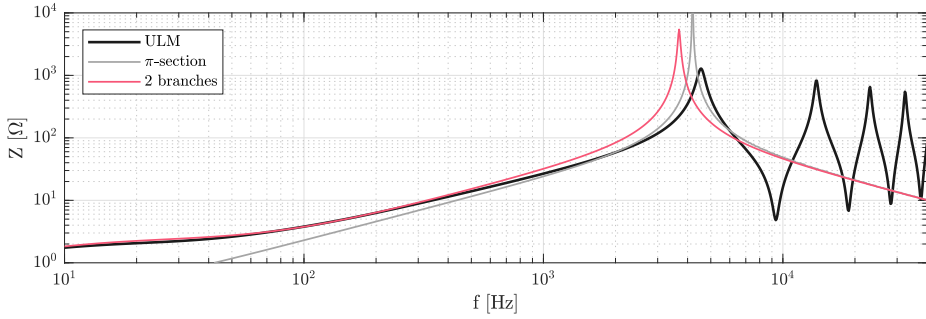
(a) 1 section (9.63 km)
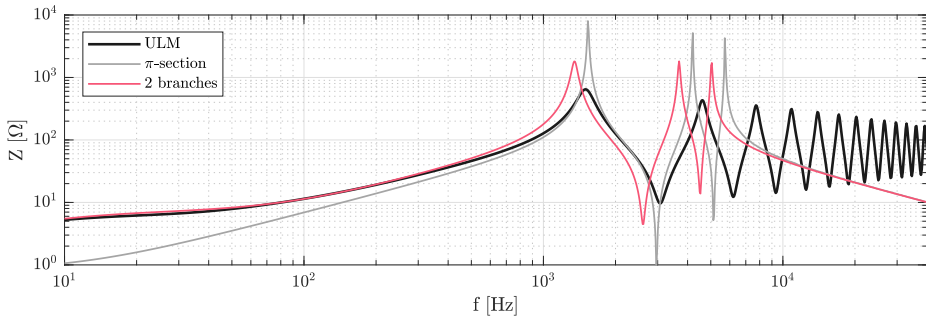
(b) 3 sections (28.88 km)

Fig. 4.22: Cable emulator model frequency response – 1 and 3 sections, comparison with ULM and π-section

Peaks appear in the range between 0.7 kHz and 5 kHz regardless of the number of sections under test (i.e. 1, 3, 5 and 11). This frequency range is close to the effective switching frequency of the converter and the update frequency of its controller (both 10 kHz). Therefore, these peaks may be excited by the action of the MMC. Even though 5 kHz is apparently above the bandwidth of the DC voltage controller, the DC voltage measurement is found to cause unstable behaviour in both simulations and experiments.

Therefore, a low-pass filter (LPF) is added to the DC voltage measurement to further reduce the gain at the resonant frequencies. This is found to cause
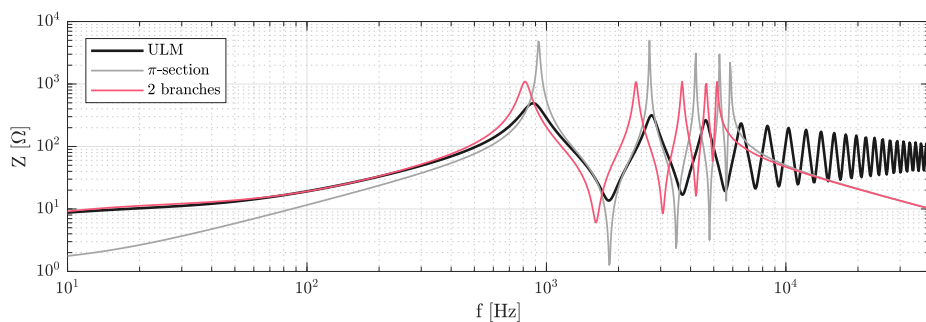
(a) 5 sections (48.14 km)
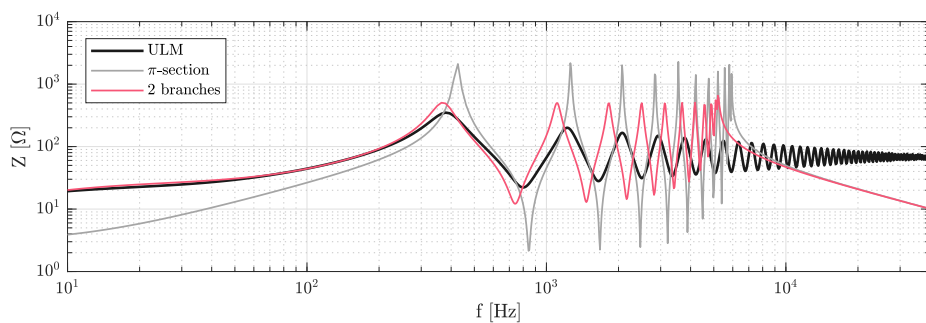
(b) 11 sections (105.91 km)

Fig. 4.23: Cable emulator model frequency response – 5 and 11 sections, comparison with ULM and π-section

negligible effect on the reference tracking capability of the controller. The equation of the LPF is given by (4.6), where T_s is the sampling frequency (100 μs in this case) and T_{LPF} is the time constant of the filter, which was set to be of 1 ms. This effectively mitigates the problem described above. The transient response upon by-passing the LPF at time $t = 1.2$ s is shown in Fig. 4.24 for illustrative purposes. Please note that the operation before the disconnection of the filter is perfectly stable.

$$G_{\mathrm{LPF}}(s) = \frac{\frac{T_s}{T_{\mathrm{LPF}}}}{z + \left(\frac{T_s}{T_{\mathrm{LPF}}} - 1\right)} \tag{4.6}$$

(a) DC side voltage

(b) Internal MMC energy

(c) AC side voltage

(d) AC side power
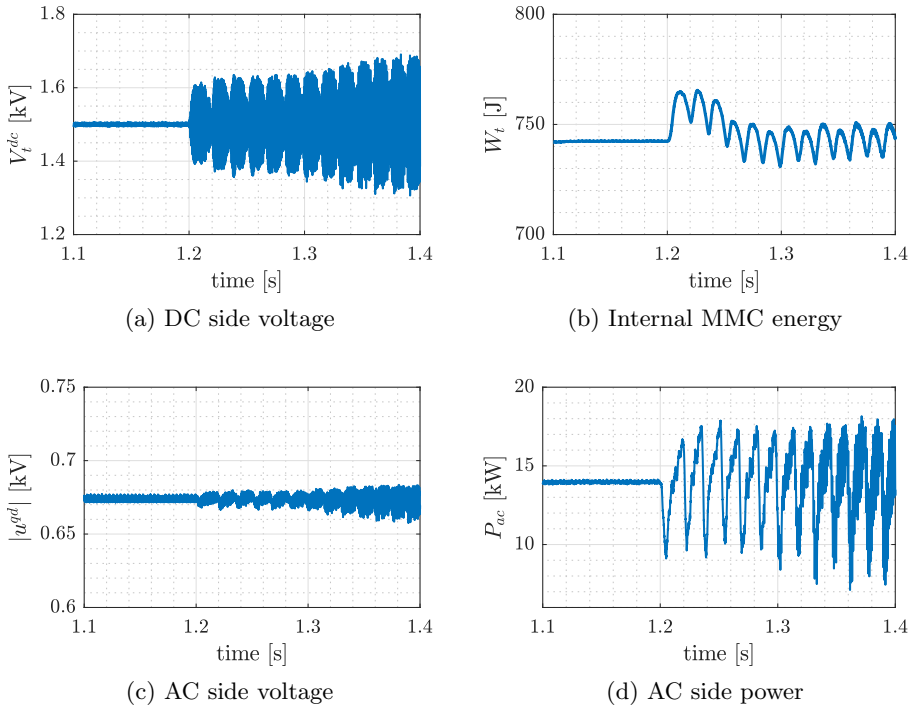
Fig. 4.24: Experimental platform simulation model – Without LPF

105

4.6 Conclusion

An MMC-based HVDC link with a relatively short cable has been tested in a low-voltage test bench. The frequency dependent behaviour of the cable is improved using the parallel branches approach, as compared to the classic π-section. However, a high number of components (and large) are required if one seeks for a very detailed match of this cable model with the benchmark ULM cable model, which is highly impractical from a laboratory-scaled platform point of view. It has been found that using only two parallel branches leads to a significant improvement over the classic π-section. However, a high-frequency oscillation is introduced on top of the main frequency component. Also, a series of low-damping peaks appear in the frequency response of the cable model. These may be excited by the action of the MMC, as they are relatively close to the effective switching frequency of the converter. This can cause instability, which may be prevented by adequate filtering of the DC voltage measurement in the feedback path. The bandwidth of this filter is greater than that of the DC voltage regulator. Therefore, it may not interfere with the relevant dynamics of the system.

Chapter 5

Optimal control tuning of the MMC in DC voltage control mode

This chapter is based on the following publications:

[J2] E. Sánchez-Sánchez, D. Groß, E. Prieto-Araujo, Florian Dörfler and O. Gomis-Bellmunt, "Optimal multivariable MMC energy-based control for DC voltage regulation in HVDC applications", *IEEE Transactions on Power Delivery*, vol. 35, no. 2, pp. 999-1009, 2020.

[C2] E. Sánchez-Sánchez, E. Prieto-Araujo and O. Gomis-Bellmunt, "On the performance of the energy-controlled MMC: Impact of the internal and the DC capacitances in HVDC applications", in *15th IET Int. Conf. on AC and DC Power Transmission*, Coventry, United Kingdom, Feb. 2019.

5.1 Introduction

In Chapter 3, four different control structures for an energy-based MMC controlling the DC voltage were presented, namely classic, cross, weighted and constant DC voltage control. Transient issues were observed when the equivalent DC side capacitance is relatively small, e.g. in a medium or short HVDC link. The weighted control, which is a combination of the classic and the cross structures, provides the control system with extra degrees of freedom, due to the tunable weights included in the control scheme. This chapter aims to address the tuning of these weights based on different objectives via optimisation. The first method that will be presented is based on the $\mathcal{H}_\infty$-norm, which was presented in the conference paper [C2]. After, and based on the work done in [J2], a more general version of the weighted control, namely multivariable control, is presented, and a second method, in this case based on the $\mathcal{H}_2$-norm, is used.

5.2 Brief overview on optimal, robust control and system norms

Optimal control aims to obtain a controller that, for a given system, satisfies a certain optimality criterion, usually by minimising a specific performance index, and ensuring stability. Optimal control was introduced in the decade of 1940, and it reached maturity in the decade of 1960 with the Linear Quadratic Gaussian (LQG) control, which name arises from using a linear model, an integral quadratic cost function, and Gaussian stochastic processes that model disturbances and noise [89].

Two well-known performance metrics in optimal control theory are the $\mathcal{H}_2$ and $\mathcal{H}_\infty$ norms. They are defined in the frequency-domain as

$$\|G(s)\|_2 = \sqrt{\frac{1}{2\pi} \int\limits_{-\infty}^{+\infty} \text{trace}[G(j\omega)G(j\omega)^H]d\omega}, \tag{5.1}$$

$$\|G(s)\|_\infty = \sup_\omega \sigma_{\max}[G(j\omega)], \tag{5.2}$$

where $G(s)$ is a stable transfer function, superscript H denotes the complex conjugate transpose, and $\sigma_{\max}$ denotes the maximum singular value.

LQG is the combination of a Linear Quadratic Regulator (LQR), which is a special case of $\mathcal{H}_2$ norm minimisation for full-state feedback, and a Linear Quadratic Estimator (LQE), which is a special case of $\mathcal{H}_2$ applied to a linear observer. $\mathcal{H}_\infty$ came out later on, in the 1980's, mainly motivated by the robustness concerns of LQG control [90]. However, in terms of their solution process, these two approaches appeared to be more closely related than it was originally thought. These similarities are more evident in terms of the algorithms used to solve those problems, such as the widely known state-space solutions from [91]. For instance, they both require to solve two Riccati equations, they yield a controller of the same dimension as the plant, and they exhibit separation in the controller structure, i.e. they result in a combined optimal state feedback and estimation, as in the case of LQG [89].

On one hand, traditional $\mathcal{H}_\infty$ (or $\mathcal{H}_2$) synthesis methods deal with the design of controllers without structure, usually resulting in high-order controllers. Therefore, the results might be hard to map into a real-world control architecture. Additionally, it requires expressing the design requirements in terms of a single weighted multivariable transfer function. In contrast, structured $\mathcal{H}_\infty$ (or $\mathcal{H}_2$) synthesis methods allow for describing and tuning a specific

control system that, for instance, needs to be improved. The control architecture, complexity, structure, and parametrisation of each tunable component in the control system, such as PID controllers, gains, and fixed-order transfer functions, can be specified [92].

It is not within the scope of this work to deeply analyse or improve upon the algorithms and methods related to one or another optimal control technique, but rather to apply them to some of the present thesis case studies to achieve enhanced (optimal) performance using a fixed-structure controller (i.e. keeping the same control structure and tuning the corresponding gains). Furthermore, the present work does not aim to provide a rigorous mathematical comparison between the $\mathcal{H}_\infty$ and $\mathcal{H}_2$ norms based methods that concludes which one is better. This would imply moving to a more control theory related topic, and therefore falls outside the scope of the present work. Moreover, the results obtained in such a comparison might not be relevant enough to claim such statement, and also might be case dependent. Instead, this chapter aims to present both methods as effective solutions to obtain optimally and robustly tuned controllers, and to emphasise on the practical aspects in their application.

The minimisation of the aforementioned norms can be interpreted as follows:

- The $\mathcal{H}_\infty$-norm [92, 93] minimises the peak of the Bode plot (the maximum singular value in the MIMO case) in the frequency domain, and the worst-case $\mathcal{L}_2$ gain in the time domain (i.e. worst-case disturbance amplification).

- The $\mathcal{H}_2$-norm [94, 95] minimises the area under the Bode plot (the integral of the trace in the MIMO case) in the frequency domain. This can be interpreted as minimising the output energy after an impulse ($\mathcal{H}_2$), minimising the output variance for a white noise input ($\mathcal{H}_2$), or minimising the output energy when starting from a non-zero initial condition (LQR).

Essentially, $\mathcal{H}_\infty$ minimises worst-case performance whereas $\mathcal{H}_2$ minimises average performance. Even though none of these two methods explicitly optimise time-domain criteria, they can be tuned so that an acceptable time-domain performance is obtained.

Both norms have been shown useful for the present work purposes in tuning gains of fixed-structure controllers. In order to avoid misleading generic statements, some particular aspects on both system norms should be highlighted to remark their differences:

- The $\mathcal{H}_2$-norm is a smooth function (i.e. several continuous derivatives) of the system and control parameters, whereas $\mathcal{H}_\infty$ is non-smooth.

- The full-state feedback (LQR) and observer feedback (LQG) can be formulated as convex optimisation problems.

- The structured $\mathcal{H}_2$ state feedback problem is non-convex and NP-hard [96].

- Convex reformulations exist for special $\mathcal{H}_\infty$ problems. However, optimising the $\mathcal{H}_\infty$-norm of structure feedback problems results in a non-convex (i.e. many local minima and maxima) optimisation problem.

These two points make $\mathcal{H}_2$ in general more numerically and computationally tractable as compared to $\mathcal{H}_\infty$-based techniques. $\mathcal{H}_\infty$ will likely result in different solutions, depending on the initial conditions, step size, number of sampling random steps, and so on. In the case of $\mathcal{H}_2$, a gradient descent will reliable bring the solution to a local minimiser, which often will turn out to be the global minimiser.

5.3 Initial evaluation of the dynamic performance

As in previous Chapters 3 and 4, the system under study is a master MMC, for instance operating in a point-to-point link. In this chapter, the slave converter is simplified to ease the analysis carried out in this chapter. Furthermore, this simplification can be also seen as a generalisation, as the slave converter slow dynamics could constrain the capabilities of the master converter in other scenarios. Instead, a current source in the slave DC terminals of the HVDC link is considered.

5.3.1 Linear model

The linear model is the same as the one presented in Chapter 3 (Fig. 3.7), simplifying the slave converter dynamics to a first-order response. The state and input vectors of the MMC $\Delta x_{\mathrm{MMC}} \in \mathbb{R}^{11}$ and $\Delta u_{\mathrm{MMC}} \in \mathbb{R}^6$ are given by

$$\Delta x_{\mathrm{MMC}} = (\Delta\zeta_{\mathrm{pll}}^{12}, \Delta i_s^{qd}, \Delta i_{\mathrm{sum}}^{0dc}, \Delta W_t, \Delta\gamma_s^{qd}, \Delta\xi_{\mathrm{sum}}^{0dc}, \Delta\sigma_v, \Delta\kappa_w)$$

$$\Delta u_{\mathrm{MMC}} = (\Delta V_t^{dc*}, \Delta W_t^*, \Delta V_t^{dc}, \Delta Q_{\mathrm{ac}}^*, \Delta v_g^{qd}), \tag{5.3}$$

where $\Delta\zeta_{\mathrm{pll}}^{12}$ are the two integral states related to the PLL dynamics; $\Delta\gamma_s^{qd}$ are the two integral states related to the i_s^{qd} controllers; $\Delta\xi_{\mathrm{sum}}^{0dc}$ is the integral

state related to the $i_{\text{sum}}^{0\text{dc}}$ controller; and $\Delta\sigma_v$ and $\Delta\kappa_w$ are the integral states of the V_t^{dc} and W_t outer controllers.

Regarding the cable, the corresponding states $\Delta x_{\text{cable}} \in \mathbb{R}^5$ and inputs $\Delta u_{\text{cable}} \in \mathbb{R}^2$ are given by

$$
\begin{aligned}
\Delta x_{\text{cable}} &= (\Delta V_{t1}^{\text{dc}}, \Delta i_{1-2,1}, \Delta i_{1-2,2}, \Delta i_{1-2,3}, \Delta V_{t2}^{\text{dc}}), \\
\Delta u_{\text{cable}} &= (\Delta i_1, \Delta i_2).
\end{aligned}
\tag{5.4}
$$

Finally, the linear model of the overall system is obtained by interconnecting the models of the MMC and the cable through the DC voltage V_t^{dc}. As mentioned before, in order to reduce the model order, the slave converter is modelled as a controlled DC current source with a first-order low-pass filter (extra state $\Delta x_{\text{slave}} \in \mathbb{R}$). The time constant of the low-pass filter can be seen as an equivalent to the time constant of the slave converter AC power loop (τ_p). Then, the state space of the overall linear system is defined by $\Delta x \in \mathbb{R}^{17}$ and $\Delta u \in \mathbb{R}^6$ given by

$$
\begin{aligned}
\Delta x_{\text{overall}} &= (\Delta x_{\text{MMC}}, \Delta x_{\text{cable}}, \Delta x_{\text{slave}}), \\
\Delta u_{\text{overall}} &= (\Delta V_t^{\text{dc}*}, \Delta W_t^*, \Delta Q_{\text{ac}}^*, \Delta v_g^{qd}, \Delta P_2^*).
\end{aligned}
\tag{5.5}
$$

5.3.2 Impact of the DC capacitance

As presented in Chapter 3, the tuning of the DC voltage controller in an energy-based approach is not straightforward in the case of short links, as the capacitance seen at the DC terminals is small. A common tuning rule (adopted from the 2L-VSC topology) consists of taking the equivalent DC capacitance as the plant (in this case, the capacitance of the whole symmetrical monopole link), and compute the closed loop with the PI controller, defining the desired time-domain response (3.5)-(3.7). Even though this is a reference tracking criteria, if the DC capacitance (C_{dc}) is big enough, the disturbance rejection capability is acceptable.

A first-order rated power disturbance from the other end of the HVDC cable with a settling time of 40 ms is performed at $t = 0.23$ s. A comparison among the three different control structures for 125 km (dashed lines) and 25 km (solid lines) cable lengths is shown in Fig. 5.1. The submodule's capacitor is 8 mF (120 μF overall internal capacitance, see Table 3.1). In the 125 km case (10.1 μF DC capacitance, see Table 3.2), all structures perform well and the transient responses are similar. On the other hand, when the 25 km cable (2 μF, see Table 3.2) is considered, the performance worsens notably, specially in the classic structure case, where the system is close to instability

(if the AC power feed-forward is removed, the system is unstable for both cable lengths).
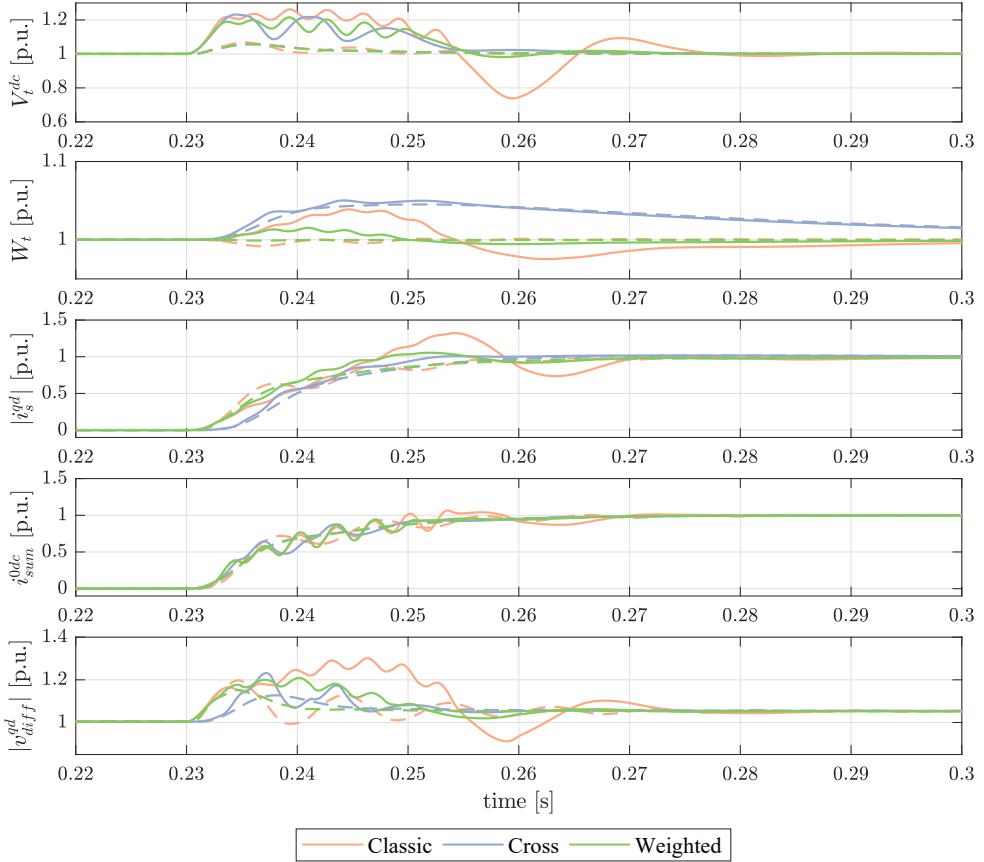

Fig. 5.1: Time-domain simulation of the master MMC system – DC capacitance impact (dashed: 125 km, solid: 25 km)

5.3.3 Impact of the internal capacitance

The aforementioned tuning problem is much less problematic in the case of the energy control, as the internal MMC capacitance is determined by adding up all the submodules' capacitors, resulting in a relatively big capacitance. The sizing of these capacitors depends on the admissible voltage ripple, which should be small in order to avoid modulation issues. Also, it is an interesting feature of the MMC to have a certain amount of internal energy (e.g. for damping purposes between the AC and the DC sides). Therefore, it is not

realistic to reduce the sizing of these capacitors drastically. In this case, an empirical tuning of the total energy controller with $k_p = 300$ W/J and $k_i = 7500$ W/(Js) has been used ($k_p = 100$ W/J and $k_i = 500$ W/(Js) for the vertical and horizontal energy balancing).

A similar comparison to the one in Fig. 5.1 is shown in Fig. 5.2, considering the original submodule capacitor of 8 mF (dashed lines) and a second case with 2 mF (30 μF) (solid lines), both with a 125 km cable and the same disturbance. In the first case, the three structures provide the system with good performance. When a smaller internal capacitance is considered, the classic structure (and consequently the weighted one) exhibits an oscillatory behaviour, whereas the cross structure shows a more consistent transient performance. However, in this last case a fine tuning would be necessary to avoid the overshoot in the total energy.

5.4 Optimal tuning based on $\mathcal{H}_\infty$-norm

5.4.1 Methodology

As seen so far, the tuning of the DC voltage and the total energy controllers is not obvious, and it is specially critical in the case of a small DC capacitance. Therefore, an optimal tuning procedure using the complete linear model of the system is proposed in this section. The classic, the cross and the weighted structures will be considered for the optimisation.

This procedure consists of defining a maximum gain curve in the frequency domain for a specific set of transfer functions of the system. In this case, the following ones have been considered:

$$
G_1(s) = \frac{\Delta V_t^{\mathrm{dc}}(s)}{\Delta i_2(s)} \qquad\qquad G_2(s) = \frac{\Delta W_t(s)}{\Delta i_2(s)}
$$
$$
G_3(s) = \frac{\Delta i_s^{q*}(s)}{\Delta i_2(s)} \qquad\qquad G_4(s) = \frac{\Delta i_{\mathrm{sum}}^{0\mathrm{dc}*}(s)}{\Delta i_2(s)} \tag{5.6}
$$

The input disturbance is the power reference P_2^*, corresponding to the slave terminal, and the magnitudes to be constrained are the DC voltage, the total energy, and the current references. Note that, as compared to the case study in Chapter 3, in the present case the slave MMC dynamics are represented by a first-order function for simplicity. The current references are considered for the constraints, instead of the feedback currents, aiming at a more conservative restriction. The maximum gain profile for each transfer
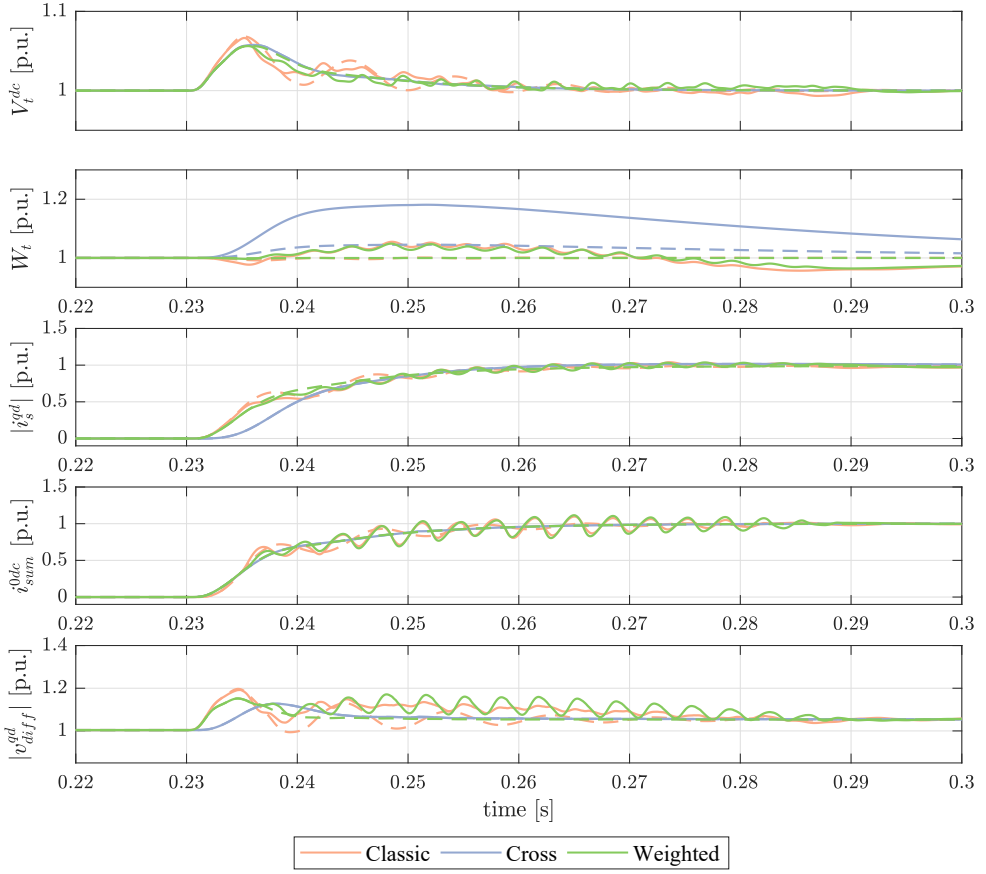
Fig. 5.2: Time-domain simulation of the master MMC system – Internal capacitance impact (dashed: 8 mF, solid: 2 mF)

function from (5.6) is calculated as

$$|G_i(j\omega)| \leq \frac{y_i(0)}{u(0)} \tag{5.7}$$

being $u(0)$ the input disturbance and $y_i(0)$ the corresponding output (considering typical converter limits):

- $u(0) = P_N$

- $y_1(0) = 0.10\ V_N^{\mathrm{dc}}$ (10% overvoltage)

- $y_2(0) = 0.10\ W_t^*$ (10% energy overshoot)

- $y_3(0) = 1.20 \ (P_N/(3V_N^{\text{dc}}))$ (20% $i_{\text{sum}}^{\text{0dc}*}$ overcurrent)

- $y_4(0) = 1.20 \ (\sqrt{2}V_N^{\text{dc}}/(\sqrt{3}U_N))$ (20% i_s^{q*} overcurrent)

The optimisation process will try to keep the gain of the transfer functions (5.6) below the gain limit (5.7).

The optimisation problem to be solved is

$$\min_x \ \max_i (f_i(x)) \qquad (x_{min} < x < x_{max}) \tag{5.8}$$

being x the vector of constants to be tuned (tunable parameters), and f_i the normalized values of the i soft goals (objectives). Limit boundaries for each tunable parameters x_{min} and x_{max} can be optionally included. Functions $f_i(x)$ are obtained as

$$f_i(x) = \|W_{Fi}(s)G_i(s,x)\|_\infty \tag{5.9}$$

being $W_{Fi}(s)$ the frequency weighting functions derived from the maximum gain profile specified, and $G_i(s,x)$ the aforementioned closed-loop transfer functions.

Function `systune` from Matlab has been used to solve the problem. The optimisation algorithm is based on the $\mathcal{H}_\infty$ norm [92]. The following parameters can be set: soft tolerance, minimum decay, and number of random starting points and iterations. The optimiser returns the stable tuning that better accomplishes the optimisation objectives. It has to be noted that this kind of optimisation problem based on the $\mathcal{H}_\infty$ norm is non-smooth and highly non-convex in the controller parameters.

5.4.2 Results and discussion

An extreme case study of a 2 km cable (DC capacitance of 0.16 μF) and a submodule capacitor of 3 mF (total MMC internal capacitance of 45 μF) is considered. An initial stable tuning is necessary in order to warm-start the optimal algorithm. This can be achieved using the weighted control structure and the tuning rules described in Sections 5.3.2 and 5.3.3, multiplying the DC voltage controller parameters by a factor of 6. A first-order rated power disturbance from the other end of the HVDC cable with a settling time of 200 ms is performed at $t = 1$ s.

The original stabilising tuning exhibits a non-linear behaviour, due to the saturation limits of the converter (see Fig. 5.3). Regarding the optimal tuning, the classic structure ($k_2 = k_3 = 0$) leads to an unstable system, suggesting that this structure is not suitable for short link cases, as there is

no possible tuning that meets the requirements. On the other hand, both the cross and weighted structures lead to a stable system with improved performance: the cross structure ($k_1 = k_4 = 0$) shows a smoother response and a higher overshoot of the total energy, whereas the weighted structure ($k_1 = k_2 = k_3 = k_4 = 1$) exhibits a more aggressive response with almost no overshoot, due to the extra degrees of freedom. Looking at the requirements from (5.7), it is shown that the AC current and the energy are below the limits, whereas the DC voltage is slightly exceeded. This is mainly due to the fact that the scenario considered is a very extreme case, and unveils that even with more aggressive tunings, the requirement of maintaining a stiff DC voltage has some limitations with this kind of control if the equivalent capacitance is small. Above all, the selection of the cross control or the weighted control can be understood as a trade-off.
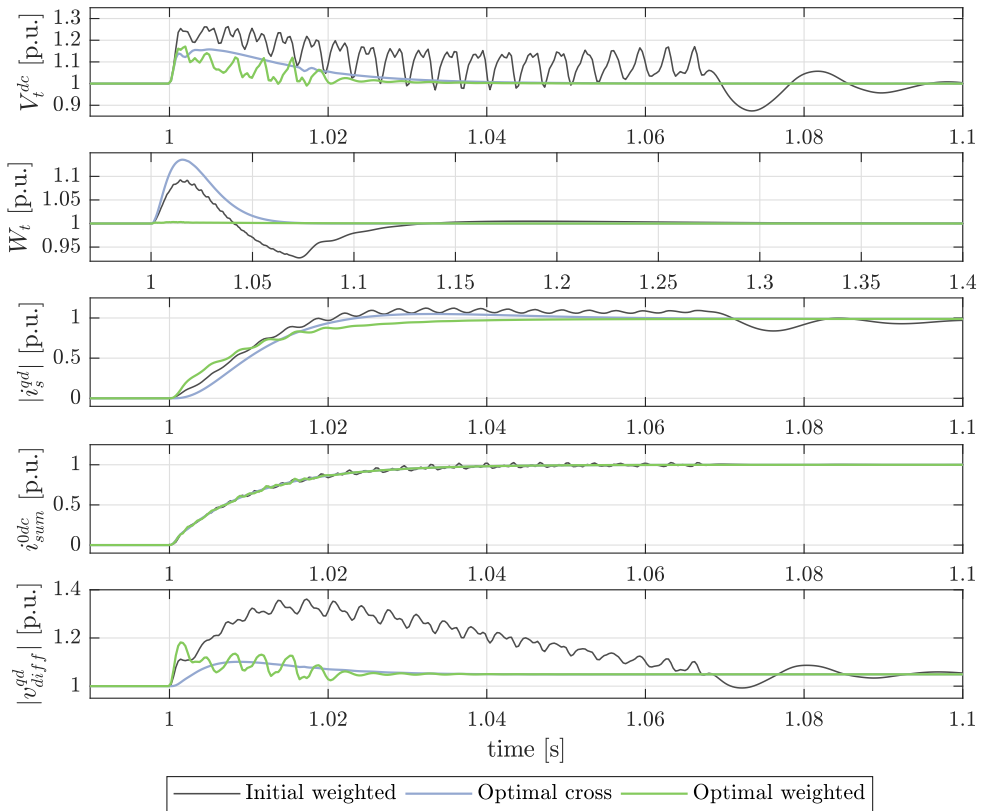
Fig. 5.3: Time-domain simulation of the master MMC system – Initial weighted and optimal cross and weighted tunings

   The Bode gain plots (Fig. 5.4) show that the classic structure, which draws the system unstable, widely exceeds the DC voltage limit and also the current limits. In the cross and weighted structures, the DC voltage limit is still slightly exceeded, meaning that the optimiser has not been able to keep the gain curve below the limit imposed. It is also observed in the $G_2(s)$ plot that the cross structure slightly exceeds the total energy requirement. To conclude, it can be stated that both the cross and weighted structures are suitable candidates to optimally tune an MMC in DC voltage control mode. Different dynamic results might be obtained depending on the requirements and the parameters of the optimisation.
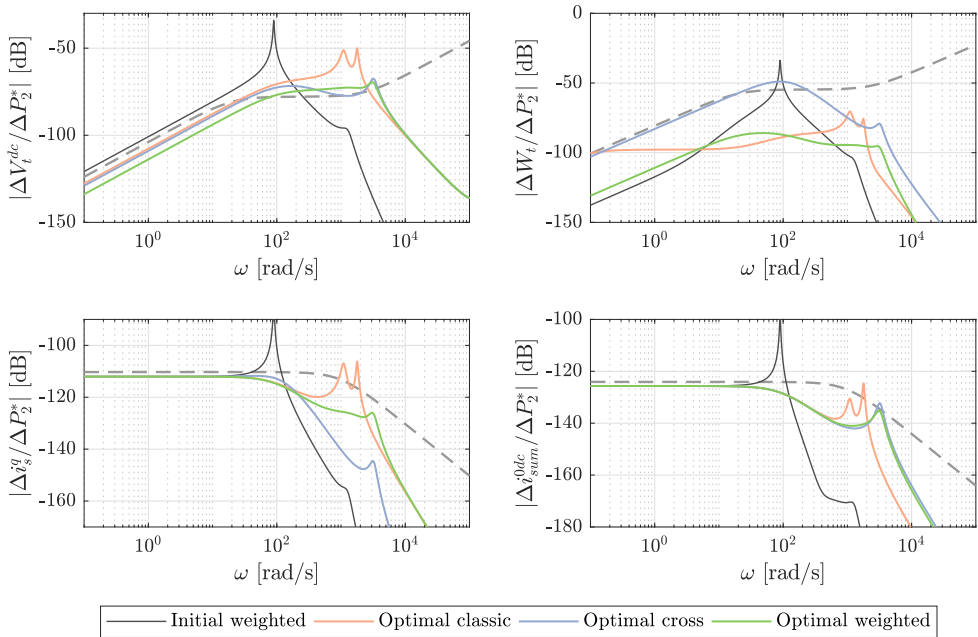
Fig. 5.4: Bode gain plots of the master MMC system (5.6) – Initial weighted and optimal classic, cross and weighted tunings

   The tuning values are summarised in Fig. 5.5. Note that $k_1 = 1$ and $k_4 = 1$ are fixed, as they are redundant with the PI gains. On one hand, it is noticeable that the cross control optimal parameters do not change drastically as compared to initial weighted tuning. On the other hand, some of the weighted control optimal gains are increased notably, specially the ones related to the energy, resulting in a flat response in that magnitude as observed in Fig. 5.3.
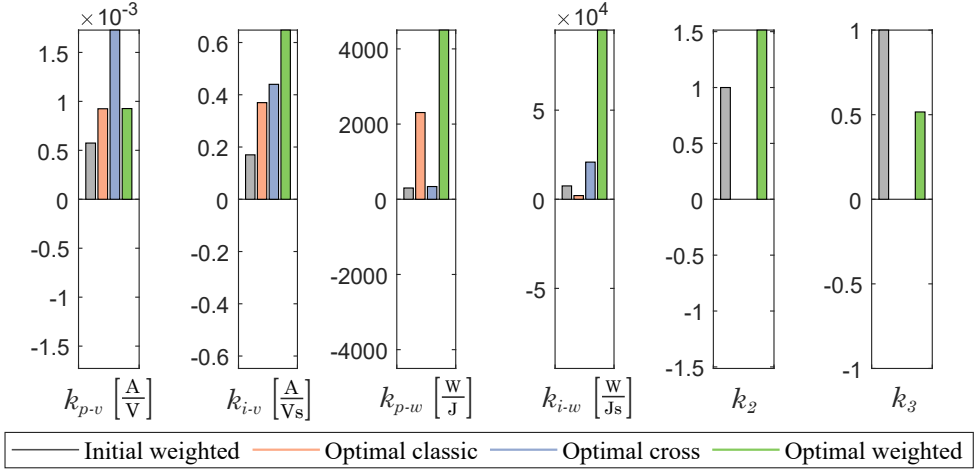
Fig. 5.5: Different controllers $\mathcal{H}_\infty$ tuning results – Parameters k_p and k_i of the weighted initial tuning and the optimal tuning of the classic, cross and weighted control structures (v refers to the DC voltage PI, and w refers to the energy PI)

5.5 Generalised MIMO control structure

In this section, a generalised multivariable outer control structure that consists of a 2×2 MIMO PI controller (Fig. 2.3) and subsumes the classic, cross, and weighted control structures, is proposed. As in the weighted control, the current references i_s^{q*} and $i_{\text{sum}}^{0\text{dc}*}$ are computed as a combination of the DC voltage (V_t^{dc}) and the total energy (W_t). The difference, however, is that this novel structure offers eight degrees of freedom that can be interpreted as parameters of four independent PI controllers: four $k_p - k_i$ ratios and four scaling gains. Instead, in the case of the weighted control only six degrees of freedom are obtained: two $k_p - k_i$ ratios and four scaling gains (Fig. 5.6). It is worth noting that the order of this new MIMO controller is actually the same as in the previous structures.

5.6 Optimal tuning based on $\mathcal{H}_2$-norm

5.6.1 Linear model remarks

The linear model from Section 5.3.1 is recalled, and the inputs $\Delta V_t^{\text{dc}*}$, ΔQ_{ac}^*, ΔW_t^* and Δv_g^{qd} are not considered as disturbances in the present study, so they are set to zero in the small-signal model. The only disturbance consid-

(a) Weighted control   (b) MIMO control
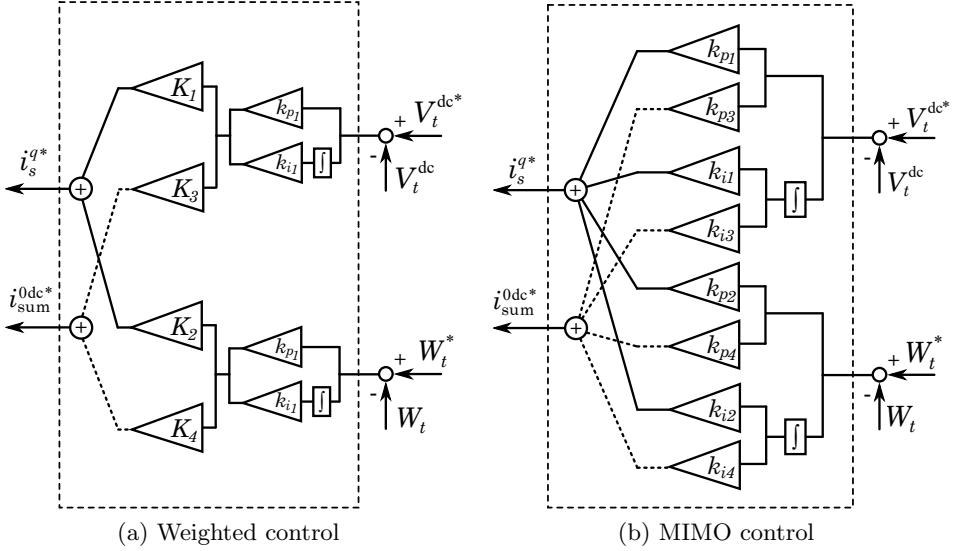
Fig. 5.6: Weighted and MIMO control structures comparison

ered is the AC power reference of the slave converter (ΔP_2^*), which is divided by the nominal voltage V_N^{dc} and, after passing through the first-order filter that emulates the slave converter dynamics, yields the current Δi_2. Then, the closed-loop system can be described by the following equations (see Fig. 5.7)

$$
\begin{cases}
\Delta \dot{x} = \mathbf{A}\Delta x + \mathbf{B}\Delta u + \mathbf{G}\Delta w \\
\Delta u = \mathbf{F}\Delta y \\
\Delta y = \mathbf{C}\Delta x \\
\Delta z = \tilde{\mathbf{C}}\Delta x + \tilde{\mathbf{D}}\Delta u
\end{cases}
, \qquad (5.10)
$$

where $\Delta w \in \mathbb{R}$ denotes the disturbance input accounting for the DC current of the slave converter, $\Delta y \in \mathbb{R}^8$ are the measured outputs to be regulated, $u \in \mathbb{R}^8$ denotes the control inputs, and $\Delta z \in \mathbb{R}^3$ denotes the physical performance output of interest to quantify performance:

$$
\begin{aligned}
&\Delta w = \Delta P_2^*, \\
&\Delta y = (\Delta e_v, \Delta \sigma_v, \Delta e_w, \Delta \kappa_w, \Delta e_v', \Delta \sigma_v', \Delta e_w', \Delta \kappa_w'), \\
&\Delta u = (\Delta i_v^P, \Delta i_v^I, \Delta i_w^P, \Delta i_w^I, \Delta i_v^{P'}, \Delta i_v^{I'}, \Delta i_w^{P'}, \Delta i_w^{I'}), \\
&\Delta z = (\Delta v_{\mathrm{diff}}^q, \Delta W_t, \Delta V_t^{\mathrm{dc}}).
\end{aligned}
$$

The vector Δy contains the DC voltage deviation and its integral, i.e. (Δe_v, $\Delta \sigma_v$, $\Delta e_v'$, $\Delta \sigma_v'$) as well as the deviation of the total energy and its integral (Δe_w, $\Delta \kappa_w$, $\Delta e_w'$, $\Delta \kappa_w'$), and the vector Δu contains the proportional (P) and integral (I) components of the reference currents. The $'$ symbol refers to the control efforts of the second output reference ($i_{\mathrm{sum}}^{\mathrm{0dc*}}$). For clarity of the presentation, only the three most important performance outputs have been selected for the physical performance output vector Δz.
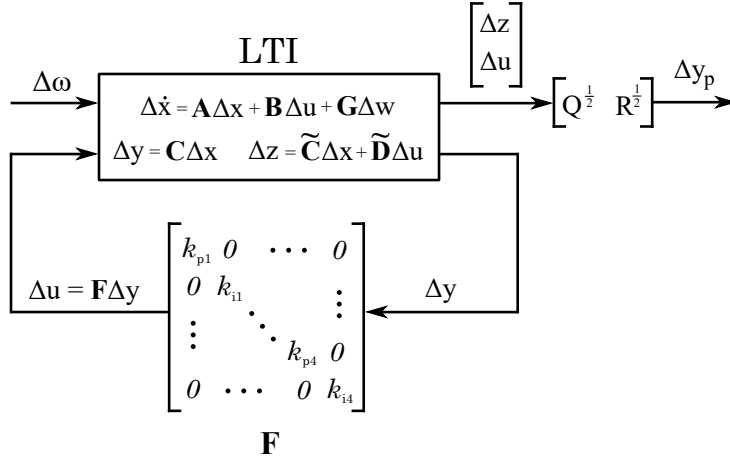
Fig. 5.7: Closed-loop standard form of the overall linear model

5.6.2 Methodology

The control gains of the MIMO control system (i.e. the parameters in the matrix F) are tuned by optimising the $\mathcal{H}_2$-norm [89, 94, 97] of the system. Broadly speaking, the $\mathcal{H}_2$-norm provides a measure of the magnitude of a weighted performance output vector Δy_p in response to a disturbance input vector Δw. The $\mathcal{H}_2$-norm has several (equivalent) interpretations. It captures the energy of the output signals Δy_p in response to impulsive disturbances, it measures the rate of change of the output energy for a step disturbance, and it captures the variance of Δy_p in response to white noise. In a power system this can be interpreted as a line opening/closing (impulse), load-step or loss of a generator (step), and fluctuations of renewable generation (white noise). Moreover, in frequency domain, minimising the $\mathcal{H}_2$-norm corresponds to a minimisation of the area under the magnitude plot of the Bode diagram.

To apply $\mathcal{H}_2$-norm optimisation to the tuning problem at hand, a performance output Δy_p is defined, which contains the outputs of interest (i.e.

Δz) as well as positive (semi)definite matrices $\mathbf{Q}$ and $\mathbf{R}$ that penalise the deviation of the performance outputs Δz and the control effort Δu:

$$\Delta y_p = \mathbf{Q}^{\frac{1}{2}}\tilde{\mathbf{C}}\Delta x + \mathbf{Q}^{\frac{1}{2}}\tilde{\mathbf{D}}\Delta u + \mathbf{R}^{\frac{1}{2}}\Delta u \qquad (5.11)$$

For clarity of the presentation, the weighted performance output Δy_p is defined using the physical performance output Δz, whereas the standard approach in the control literature directly uses $\mathbf{Q}$ and $\mathbf{R}$ to define the output Δz in (5.10). The performance output is used to formulate the cost function:

$$\begin{aligned} J_\infty &= \int_0^\infty y_p^\top y_p \, \mathrm{d}t, \\ &= \int_0^\infty \Delta x^\top \tilde{\mathbf{C}}^\top \mathbf{Q}\tilde{\mathbf{C}}\Delta x + \Delta u^\top (\tilde{\mathbf{D}}^\top \mathbf{Q}\tilde{\mathbf{D}} + \mathbf{R})\Delta u \, \mathrm{d}t \end{aligned}$$

The complete dynamical system $\mathcal{G}$ is obtained by closing the loop via $\Delta u = F\Delta y$ as in Fig. 5.7 and using (5.11):

$$\Delta\dot{x} = (\mathbf{A} + \mathbf{BFC})\Delta x + \mathbf{G}\Delta w = \mathbf{A_{cl}}\Delta x + \mathbf{G}\Delta w$$

$$\Delta y_p = (\mathbf{Q}^{\frac{1}{2}}\tilde{\mathbf{C}} + \mathbf{Q}^{\frac{1}{2}}\tilde{\mathbf{D}}\mathbf{FC} + \mathbf{R}^{\frac{1}{2}}\mathbf{FC})\Delta x = \mathbf{C_{cl}}\Delta x$$

Even though the $\mathcal{H}_2$-norm does not explicitly optimise time-domain criteria (such as the overshoot), it can be used to obtain adequate time-domain performance. The optimisation problem to be solved is defined by [97]

$$\min_F \|\mathcal{G}\|_2^2 \qquad (x_{min} < x < x_{max}) \qquad (5.12)$$

The $\mathcal{H}_2$-norm between the disturbance input Δw and the performance output y_p is given by [94]

$$\|\mathcal{G}\|_2^2 = \operatorname{trace}(\mathbf{G}^\top \mathbf{P_F}\mathbf{G}) \qquad (5.13)$$

where $\mathbf{P_F}$ is the closed-loop observability Gramian obtained as positive definite solution of the Lyapunov equation

$$\mathbf{P A_{cl}} + \mathbf{A_{cl}}^\top \mathbf{P} + \mathbf{C_{cl}}^\top \mathbf{C_{cl}} = 0 \qquad (5.14)$$

for a fixed $\mathbf{F}$. Due to the structure imposed on $\mathbf{F}$ (see Fig. 5.7), the optimisation problem (5.12) is generally non-convex. However, it can be solved efficiently by noting that the gradient of $\|\mathcal{G}\|_2^2$ with respect to the control gains can be computed efficiently. The gradient computation used in [97] cannot be applied here, because $\mathbf{C_{cl}}$ also depends on the control gains. Therefore,

similar steps to the ones in [98] are used to derive an expression for the gradient of $\|\mathcal{G}\|_2^2$ that requires computing the observability Gramian (i.e. (5.14)) and controllability Gramian, i.e. that requires the solution of two Lyapunov equations. The details are omitted for reasons of space. Finally, it is to be remarked that the present approach can be used to optimise the control parameters for multiple operating points by considering the sum of the $\mathcal{H}_2$-norms at different linearisation points (but with the same control parameters) as cost function. However, for the sake of clarity, a single operating point is considered in this study.

5.6.3 Scenario configuration

In this section, the $\mathcal{H}_2$-norm optimisation is applied to tune the control gains of the master converter MIMO control structure. First, the sensitivity of the performance outputs is studied with respect to the penalty parameters. Next, the penalties are iteratively updated to obtain optimal control gains and validate the resulting control performance using the full non-linear model applying an AC power reference change in the slave converter from 0 to 1 p.u. (i.e. flowing from the slave to the master) at $t = 0.2$ s. This relatively large disturbance is a suitable benchmark scenario to verify the effectiveness of the proposed method. Two different scenarios are considered:

- Case 1: Short link of 50 km. Examples of similar real-world projects are Cross-Sound (USA, 40 km, 2002), INELFE (Spain-France, 65 km, 2015), and ElekLink (UK-France, 51 km, to be commissioned in 2020).

- Case 2: Very short link of 5 km. A potential application of a such a short link is the interconnection of neighbouring systems, either at different frequencies or simply non-synchronous. An example of an already existing very short cable project is the Xiamen Island VSC-HVDC demonstrator (China, 10.7 km, 2015).

The $\mathcal{H}_2$-norm approach presented in the previous is implemented in Matlab using the SQP algorithm of `fmincon` and applied to a linear model corresponding to an operating point given by a DC power flow of 1 p.u. from the slave to the master converter. Furthermore, the tuning rules discussed in Chapter 3 are used to obtain an initial guess for the control gains to warm-start the optimisation.

5.6.4 Sensitivity with respect to performance penalties

One of the advantages of using an optimisation method is that it allows for a more intuitive, principled, multivariable, and obviously optimal tuning procedure, i.e. instead of directly tuning the individual gains (eight in total) of SISO controllers, the focus is put on the penalties on the desired performance outputs ($\mathbf{Q}$) and control inputs ($\mathbf{R}$). First, the correlation of the penalties is studied through time-domain performance. To this end, the focus is put on the AC voltage (v_{diff}^q), the total energy (W_t), and the DC voltage (V_t^{dc}) as the most relevant performance outputs that are penalised by the matrix

$$\mathbf{Q} = \mathrm{diag}(q_{v_{\mathrm{ac}}}, q_{w_{\mathrm{t}}}, q_{v_{\mathrm{dc}}}) \tag{5.15}$$

Moreover, the matrix $\mathbf{R}$ penalises the 8 control inputs $\Delta u = \mathbf{F}\Delta y$, where $\mathbf{F}$ contains the tunable static gains.

$$\mathbf{R} = \alpha \, \mathrm{diag}(r_{p_1}, r_{i_1}, \ldots, r_{p_4}, r_{i_4}) \tag{5.16}$$

As the system is normalized to a per unit framework, the initial guess for the penalties $\mathbf{Q}$ and $\mathbf{R}$ is the identity matrix. The effect of different penalties on the dynamics of the outputs of interest is shown in Fig. 5.8 using a cable of 10 km. First, looking at α (the $\mathbf{Q} - \mathbf{R}$ ratio) it can be seen that all magnitudes have low overshoot when this value is low. A value of $\alpha = 0.01$ is fixed for the next cases. Increasing the penalty on v_{diff}^q reduces the overshoot of the AC voltage but at the expense of increasing the overshoot of the total energy. On the other hand, increasing the penalty in W_t shows the opposite effect. Finally, increasing the penalty in V_t^{dc} reduces the overshoot of the DC voltage, even though this magnitude is already at a reasonable level in the previous cases using $\alpha = 0.01$.

The results in Fig. 5.8 highlight how the control gains can be modified through the choice of penalties to achieve the desired performance. Analysing time-domain metrics is a good way to receive feedback from the optimisation, and allows for iterating the penalties until an acceptable result is found.
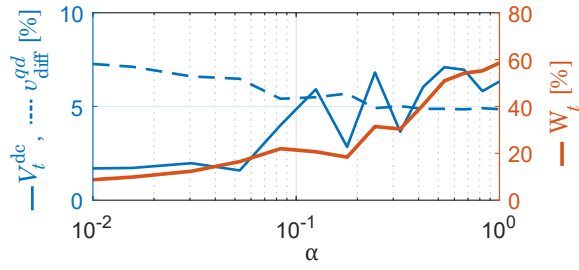
(a) Parametric sweep of α
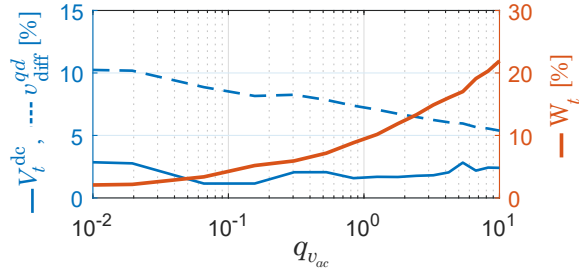
(b) Parametric sweep of $q_{v_{\mathrm{ac}}}$
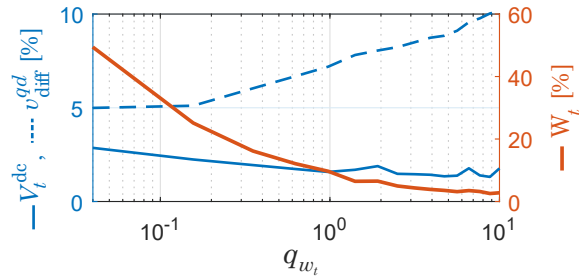
(c) Parametric sweep of q_{w_t}
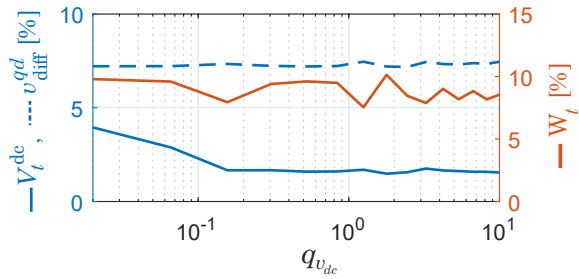
(d) Parametric sweep of $q_{v_{\mathrm{dc}}}$

Fig. 5.8: Effect of different penalties – Overshoot of the DC voltage, AC voltage and total energy, in a 10 km link test case

5.6.5 Results and discussion

Next, the insights on how the penalties affect the resulting performance are used, and the $\mathcal{H}_2$ optimisation is applied to both Case 1 and Case 2. Both penalty matrices $\mathbf{Q}$ and $\mathbf{R}$ are initially set to the identity, and α is set to 0.01. Next, the penalties are modified in two iterations to obtain the desired dynamic performance. The resulting time-domain responses after every iteration are shown in Fig. 5.9. The initial tuning in the 50 km case is equivalent to the weighted control approach with $k_1 = k_2 = k_3 = k_4 = 1$ (see Table 5.1). In the 5 km case, the gains of $\text{PI}_1(s)$ and $\text{PI}_3(s)$ (i.e. the critical controller related to the DC voltage) are multiplied by a factor of 4 to obtain a stabilising initial tuning.

Table 5.1: DC voltage and energy PI controllers initial tuning values

K_1	K_2	K_3	K_4
$-\sqrt{2}V_t^{\text{dc}*}k_1/(\sqrt{3}U_N)$	$-\sqrt{2}k_2/(\sqrt{3}U_N)$	$-k_3/3$	$k_4/(3V_N^{\text{dc}})$

	$\text{PI}_1(s)$	$\text{PI}_2(s)$	$\text{PI}_3(s)$	$\text{PI}_4(s)$
k_p	$K_1\ 2\xi\omega_n C_{\text{dc}}$	$K_2\ 250$	$K_3\ 2\xi\omega_n C_{\text{dc}}$	$K_4\ 250$
k_i	$K_1\ \omega_n^2 C_{\text{dc}}$	$K_2\ 6250$	$K_3\ \omega_n^2 C_{\text{dc}}$	$K_4\ 6250$

The first iteration (i.e. with $\mathbf{Q}$ and $\mathbf{R}$ set to identity) results in a clear improvement of the initial tuning that avoids the converter saturation limits (see the magnitudes v_{diff}^{qd} and V_t^{dc} in Fig. 5.9b). However, the deviation of W_t is relatively big. In order to address this issue, a penalty of $q_{w_\text{t}} = 3$ is used in the second iteration, which shows a significant reduction of the deviation of W_t. However, W_t does not converge back to zero after the disturbance. This can also be seen in the Bode plots of W_t with respect to the input disturbance in Fig. 5.10 that remain at a relatively large value for low frequencies. Moreover, the optimisation results in a very high gain k_{p3} (25 times higher than the initial tuning value in both Cases 1 and 2, see Fig. 5.11) that could compromise the stability of the full original non-linear system, since the operation condition is potentially far from the region where the linearised model is valid. The effects of high gain control can also be observed in the small overshoots of V_t^{dc} in Fig. 5.9 and in the left Bode plots in Fig. 5.10, which show that the curves are pushed down aggressively.

As discussed before (Fig. 5.8a), a lower value in R results in a higher control effort. Therefore, in order to overcome the aforementioned issues, r_{i_2} and r_{i_4} are both reduced to 0.05 (Case 1) and 0.01 (Case 2) to increase the integral

control effort related to the energy, and r_{p_1} and r_{p_3} are both increased to 50 (Case 1) and 100 (Case 2) to reduce the proportional control effort related to the DC voltage, aiming for a less aggressive controller. As a result, after this third iteration of the penalties, the energy reaches its reference value relatively fast, and k_{p_3} is significantly reduced: 5.6 times higher than the initial tuning value in Case 1, and 10 times in Case 2, see Fig. 5.11. Accordingly, Fig. 5.9 shows that the DC voltage overshoot has increased, and the right Bode plots in Fig. 5.10 show that the curves are no longer flat at low frequencies.

While these results have been obtained for a linearisation point corresponding to a DC power flow of 1 p.u. from the slave to the master converter, the resulting control gains result in similar performance characteristics at other operating points (e.g. for a power flow of 1 p.u. from the master to the slave converter).

Based on this challenging case study, it can be observed that:

- The standard tuning rules (based on SISO assumption) used in the MIMO control structure yield acceptable results for long cables (Fig. 5.9a). However, they result in poor performance for shorter links (i.e. a more coupled and stressed system), e.g. resulting in big overshoots in the DC voltage.

- With the proposed method it is possible to automatically obtain an optimal tuning which outperforms the initial one – especially for short cables. Also, the penalties can be tuned in an intuitive way to prioritize the response of some converter outputs over others, depending on the desired specifications of voltages and internal energy.

- Surprisingly, the optimal control gains in the proposed MIMO control structure are negative in some cases (see $PI_4(s)$ in Fig. 5.11). While it may seem counter intuitive from a SISO control point of view, negative control gains can result in improved performance (rather than instability) in a MIMO control structure. More specifically, due to the fact that two different signals participate in each of the control outputs, the combination of positive and negative control efforts can lead to a better solution. Nonetheless, if needed, the control gains can be constrained to positive values in the optimisation routine.

(a) Case 1: 50 km

(b) Case 2: 5 km
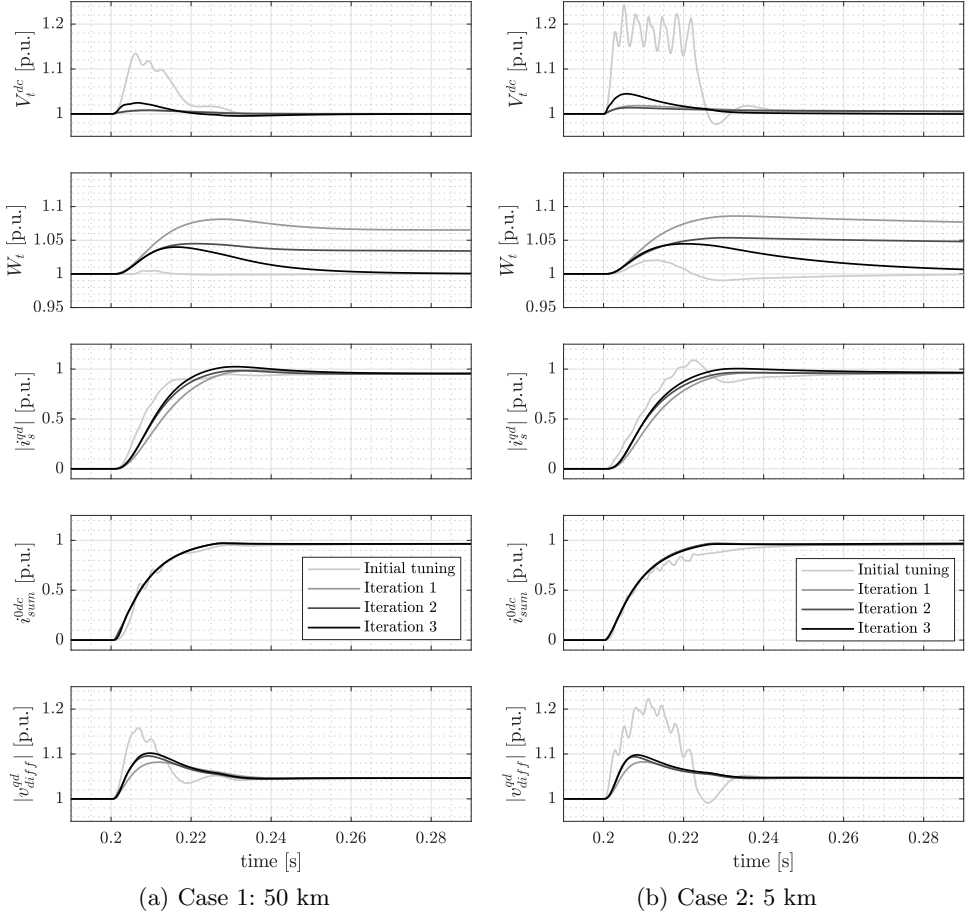
Fig. 5.9: Time-domain simulation of the master MMC system – Initial tuning from Table 5.1, and Iterations 1 to 3 correspond to different penalties in the $\mathcal{H}_2$-norm optimisation.

(a) Case 1: 50 km

(b) Case 2: 5 km
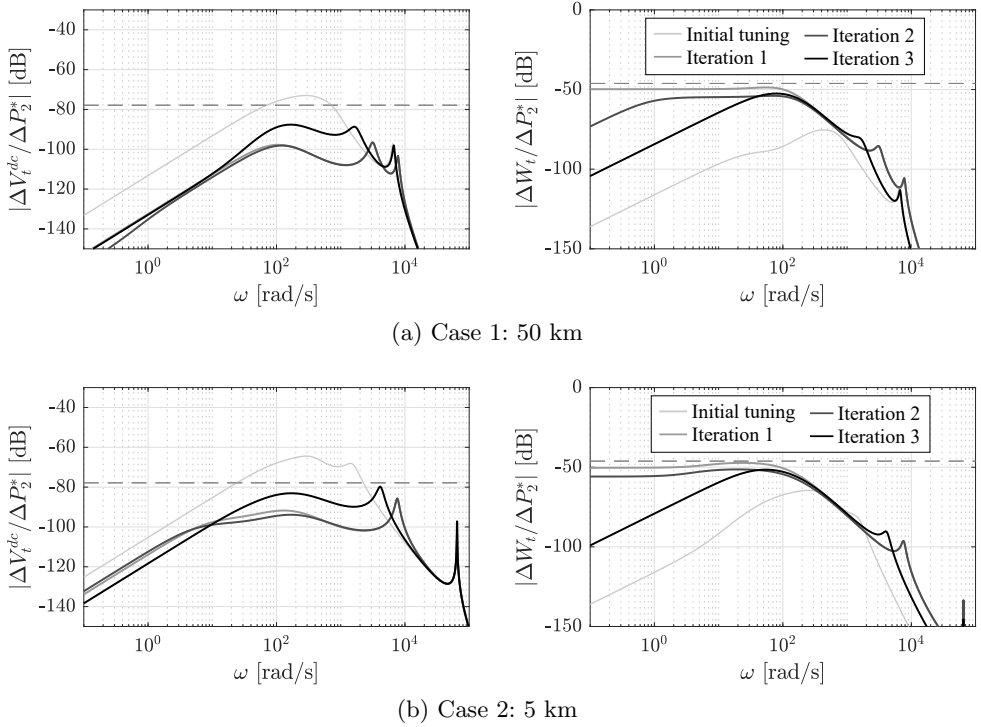
Fig. 5.10: Bode gain plots of the master MMC system – DC voltage and energy of the master MMC, for the initial tuning and the $\mathcal{H}_2$ tuning (three iterations changing the penalties). Horizontal dashed gray line corresponds to a 10% error of the corresponding magnitude
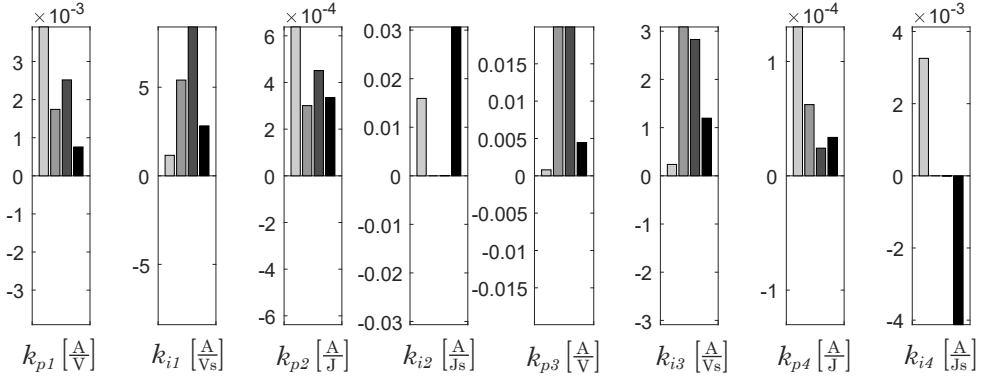
(a) Case 1: 50 km
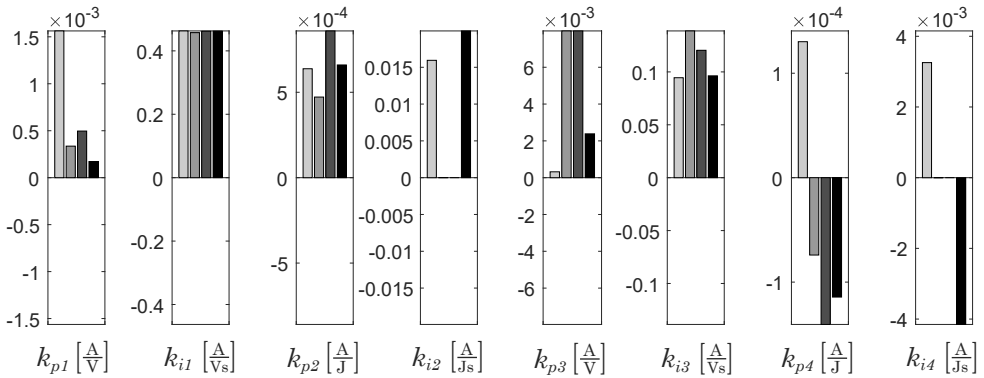
(b) Case 2: 5 km
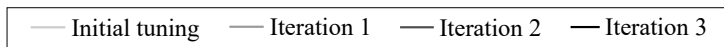
Fig. 5.11: MIMO controller $\mathcal{H}_2$ tuning results – Parameters k_p and k_i of the initial tuning and the optimal tuning (three iterations changing the penalties)

129

5.7 Conclusion

The effect of the DC cable length is a key aspect in terms of dynamic performance of the MMC in DC voltage control mode under an energy-based approach. More specifically, the controllability of the system worsens as the cable length reduces, and the classic control structure does not perform well or even leads to instability. This control challenge has been addressed via an optimal tuning method based on the $\mathcal{H}_\infty$-norm, obtaining an adequate tuning of the DC voltage and the total energy PI controllers under the cross and weighted control structures. On the other hand, the internal capacitance value has a much smaller range of variation due to design reasons (modulation and internal energy), and therefore it does not entail a big challenge in terms of controllability.

Furthermore, a MIMO controller that generalises the weighted structure has been presented. Rather than explicitly tuning the eight control parameters of this controller, which would be complex and non-intuitive, a systematic model-based tuning methodology, based on the $\mathcal{H}_2$-norm, is proposed. This method allows for an intuitive tuning of the controls through penalty factors on performance outputs. An improvement of the overall dynamic performance of the MMC has been obtained, especially in low DC inertia scenarios arising from short and very short HVDC links, in which guidelines for manual control tuning break down. Moreover, as the proposed methodology allows the penalisation of the disturbance response of different performance outputs, as well as the control efforts, it results in a flexible tuning method. In particular, different control objectives such as tight DC voltage regulation, minimisation of internal energy deviations, and the efficient use of control energy can be intuitively combined and different trade-offs are easily established by changing the penalties. This approach resulted in reducing the overshoot of the DC voltage in critically short cable cases, and to iteratively improve the tuning of the integral control action of the controller to ensure that the internal energy reaches the desired steady-state (i.e. zero error) sufficiently fast.

Chapter 6

The MMC in grid-forming operation

This chapter is based on the following publication:

6.1 Introduction

In the upcoming future of power systems, as mentioned in Chapter 1, conventional synchronous generation will experience a progressive reduction, to the benefit of renewable energy generation, such as wind and solar, in order to meet the environmental goals planned for the future [99]. This implies that new power electronics converters will be installed in order to integrate these renewable resources into the system, to the detriment of the large mechanical rotating machines from classic thermal power plants. With such a reduction of rotating mass, some of the aforementioned converters will be responsible of handling the stability and the robustness of the power system by operating in grid-forming mode.

Grid-forming mode is a well-known concept, and several studies for microgrids [100–104] and power system applications [105–107] have been addressed in the literature in the recent years. The two main grid-forming approaches are the Virtual Synchronous Machine (VSM) approach [101] and the frequency-droop approach [108]. In fact, it is shown in [109] that both control approaches are essentially equivalent. Most of these studies deal with 2L-VSCs, focusing on the AC side, whereas only a handful of references are found with respect to grid-forming mode for power system applications using MMCs, as summarised next. Two different controllers in VSC-HVDC interconnectors operating in parallel are compared in [110], and an enhanced control for an offshore wind farm station is discussed in [111]. Despite using MMC models in both articles, they focus on the AC voltage and frequency

control, with no discussion about the internal energy control. In [112], a dynamic protection integrated model predictive control concept is developed and applied to the MMC for grid restoration purposes, focusing on avoiding MMC overcurrents. An AC fault analysis of an islanded grid including MMCs operating in grid-forming mode is presented in [113], also focusing on the AC side control structure. In this case, instead of using an energy-based approach, a circulating current suppressing control (CCSC) scheme is used, meaning that the energy is not explicitly controlled. In [114], a classic grid-forming control scheme together with a full energy-based control is implemented in an MMC and successfully tested in laboratory, discussing the implications of having a storage system on the DC side or inside the MMC submodules. Furthermore, the VSM concept has been recently extrapolated and implemented in the MMC [115, 116].

The buffering capabilities that the MMC offers due to its topology, i.e. due to the internal energy stored in its submodules capacitors, has been a subject of interest within the scientific community over the last years. First of all, the modulation strategy plays a relevant role in the effectiveness of this feature, which in general can be implemented in two ways, namely UCM and CM as explained in Chaper 2. As an example, regarding grid-following MMCs operating in PQ mode, in [46] it is shown how the approach from [51] (UCM) fails to withstand an unbalanced voltage sag, distorting the DC side. Results are notably improved in the case of [49] (CM), and further improved when inner circulating current control loops are included [46].

Regarding unbalanced operation, a control approach aiming to reduce DC side power oscillations is presented in [117], filtering the 100 Hz component out of the zero-sequence additive current, showing the firewall capability of the MMC. A more elaborated approach from the same authors deals with optimal circulating currents reference calculation directly in the *abc* frame [118], that effectively decouples the AC grid conditions from the DC bus, not only in steady-state but also in transient unbalanced conditions in a grid-following MMC, improving and extending results from [53].

Other works deal with control aspects of grid-following MMCs operating in DC voltage control mode. In that case, with a disturbance in the DC grid, a different transient performance on the DC and AC sides is achieved depending on the control structure adopted. A virtual capacitor strategy is proposed in [119], which is able to boost the effective capacitance of the DC side and improve the DC dynamics. In Chapter 3, it was shown that interchanging the AC and DC current control references in an MMC controlling the DC voltage allowed for decoupling the AC and DC sides, avoiding interactions. It can be noted that in terms of the MMC physical limitations, the control

design criteria for grid-forming and grid-following converters can be similar, as these objectives would typically focus in reducing overshoots, avoiding undesired oscillations and obtaining a specific settling time. The fundamental difference, however, is that in grid-following mode the AC power is a control input, whereas in grid-forming mode it is a physical disturbance.

In this context, there is gap in the literature in terms of analysing potential capabilities that the MMC offers in grid-forming mode, for instance in offshore AC wind farms or passive islanded systems. This chapter aims to analyse and provide a comprehensive discussion about the features of this buffering capability in such scenarios. The AC side grid-forming control used in the present work is equivalent to the classic frequency droop used in 2L-VSCs, and the comparison or proposal of new grid-forming controls is not the matter of the present study. However, the extra degree of freedom due to the total internal energy of the MMC can play a relevant role in the dynamic performance of the system. The contribution of this chapter is to analyse different energy control structures, highlighting their differences in transient conditions, and providing control design guidelines to obtain the desired performance. Different case scenarios with one and multiple grid-forming converters are simulated in order to validate the analysis and to highlight the superiority of some of the structures.

6.2 System description

The present study deals with MMCs operating in grid-forming mode. The converter is connected to an HVDC network on the DC side, which provides a stable DC voltage, typically controlled by one or more converters of the HVDC network. On the AC side, the converter controls the amplitude, frequency and angle of the voltage at the point of connection, acting as a slack bus. A list of examples where grid-forming converters can be used in power transmission applications are described below.

- Offshore AC wind farm clusters, where one or more converters impose the AC grid voltage to export the power generated in the offshore wind farm to the mainland grid using HVDC (Fig. 6.1a).

- Passive islanded systems, i.e. islands where the main part or all of the generation needs to be imported from outside, e.g. through one or more HVDC links (Fig. 6.1b).

- Weak grids, i.e. grids with a low short-circuit ratio that need one or more grid-forming converters to stabilise the grid, or to make it robust.
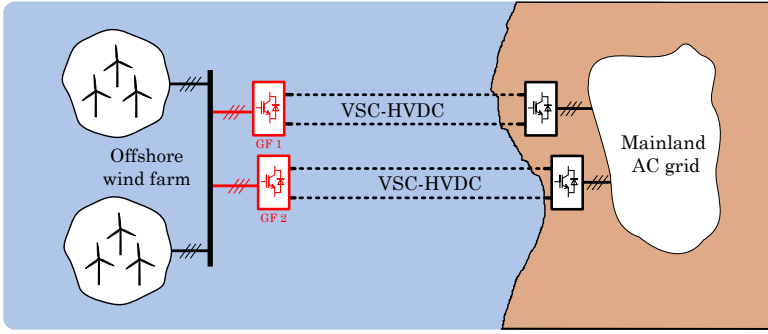
(a) Offshore wind power plant connected to land via HVDC
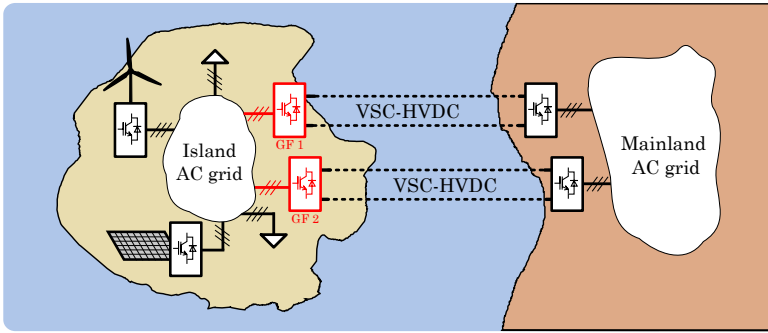
(b) Islanded system connected to main land grid via HVDC

Fig. 6.1: Examples of applications of grid-forming MMCs

In the case of islanded systems, if there is enough synchronous generation, the converter/s that import or export power (GF 1 and GF 2, Fig. 6.1) do not necessarily have to operate in grid-forming mode, and might operate in grid-following mode instead if the AC grid is strong enough. Equivalently, this can be also the case of weak grids. In those cases, the converter can optionally operate in grid-forming mode to support the existing AC grid. However, in other cases such as offshore AC wind farms (Fig. 6.1a) and islanded systems with no synchronous generation (Fig. 6.1b), it is in general necessary that one or more converters operate in grid-forming mode, as there is no AC grid available. As compared to grid-following, grid-forming mode allows the converter to remain in operation after a large or full trip on the AC side, and it can also provide black-start capability. It has to be noted that the AC power acts as a disturbance to the system, instead of as a control input.

6.3 MMC grid-forming control

A classic grid-forming control for VSCs consists of an outer AC voltage vector control plus an inner AC current vector control $(u - i_s)$, both using PI controllers in $qd0$ frame. Also, instead of using a PLL, the angle is generated internally with the desired frequency. Typically, a frequency droop using the active power measurement (see Fig. 2.5b from Chapter 2) is adopted in order to achieve active power sharing in a multiple converter setup. In addition, an optional AC voltage reference droop using the reactive power might be also included, which can be useful to achieve reactive power sharing [106]. In case the droop constant k_u is set to 0, the voltage reference is always constant. This scheme is identical for both 2L-VSCs and MMC-VSCs [113]. Recalling Fig. 2.3, this corresponds to the outer control mode 3, depicted in Fig. 6.2.

It is important to note that typically the output AC filter of an MMC does not include a capacitor, as the modulated voltage sine waves do not require as much filtering as in the 2L-VSC case. Instead, only a coupling RL filter (typically representing a transformer) is present. Therefore, the effective AC capacitance depends on the topology of the AC grid that the MMC is connected to. This implies that the current i_g (optionally used as a feed-forward signal on the AC voltage control in 2L-VSCs) cannot be measured in MMC cases where there is no physical capacitor connected at the grid side of the transformer.
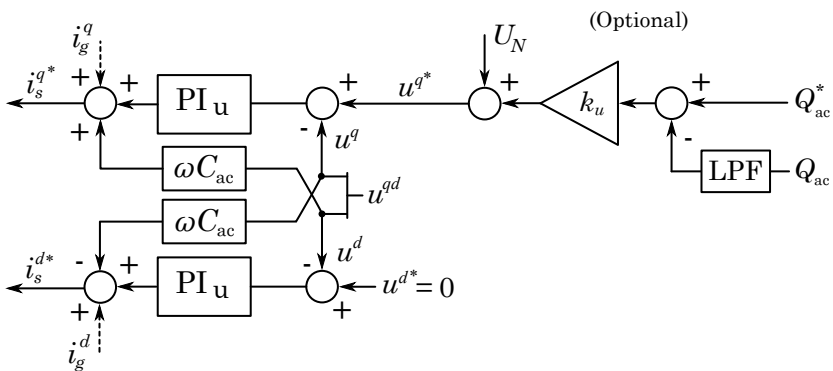
Fig. 6.2: Frequency-droop grid-forming control

6.4 Total energy control structures

In 2L-VSCs, the AC and DC powers are fully coupled, meaning that any disturbance on the AC side will propagate to the DC side, and vice versa. In MMCs, on the contrary, the internal total energy dynamics will have a determining impact on how the AC/DC interaction and disturbance propagation occurs, offering a buffering capability that can be used as desired, depending on the specifications of the converter and its application. When an AC power disturbance occurs, a portion of that power will charge or discharge the MMC internal arm capacitors, and another portion will flow to or from the DC side (Fig. 6.3). The way this power is transiently distributed will depend on what control structure is used and how the tunable control parameters are set.
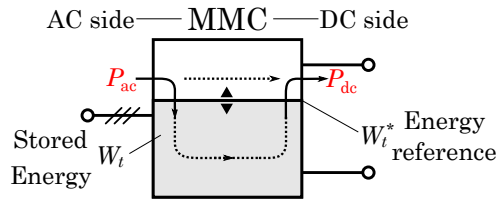
Fig. 6.3: Conceptual representation of how an AC disturbance is partly absorbed by the MMC and partly sent to the DC side

As compared to an MMC controlling the DC voltage, where several control structure combinations might be reasonable (Chapter 3), the structure of the grid-forming MMC control appears to be more evident. On one hand, the classic frequency droop control including a cascaded AC voltage and current vector control used in 2L-VSCs is directly applicable to the MMC, without any difference. On the other hand, it seems to be obvious that the energy controller has to be, therefore, cascaded with the inner additive current, which is the other part of the MMC control. Nevertheless, there are still different alternatives in terms of how to implement the energy control, that will affect the internal MMC and the DC dynamics in different ways.

In order to analyse this mechanism in a comprehensive way, the following assumptions are recalled:

- The DC voltage is constant.

- The zero component circulating current closed loop (i.e. DC component) is simplified to a first-order transfer function with time constant τ_{sum} (faster than the outer loops).

- The AC power is a disturbance of the system.

The dynamics of the DC power and the MMC internal total energy are defined, respectively, in the Laplace domain as

$$P_{\mathrm{dc}}(s) = V_{\mathrm{dc}} I_{\mathrm{dc}}(s) = V_{\mathrm{dc}} \left(3 \frac{I_{\mathrm{sum}}^{0\mathrm{dc}*}(s)}{\tau_{\mathrm{sum}}s + 1} \right) = \frac{P_{\mathrm{dc}}^*(s)}{\tau_{\mathrm{sum}}s + 1} \tag{6.1}$$

$$sW_t(s) = P_{\mathrm{dc}}(s) - P_{\mathrm{ac}}(s) = \frac{P_{\mathrm{dc}}^*(s)}{\tau_{\mathrm{sum}}s + 1} - P_{\mathrm{ac}}(s) \tag{6.2}$$

Both (6.1) and (6.2) depend on the expression of $P_{\mathrm{dc}}^*(s)$, which depends on the control structure adopted, as will be seen next. Also, and for compactness purposes, the control action of the total energy PI controller is defined as

$$G_c(s) = k_p(W_t^*(s) - W_t(s)) + \frac{k_i}{s}(W_t^*(s) - W_t(s)) \tag{6.3}$$

6.4.1 Coupled control approach

A total energy controller with a feed-forward of the active power is a typical structure used in MMCs operating in PQ mode [46, 55, 72, 121], and also in DC voltage control mode [122]. Hereinafter, this structure will be referred to as *coupled* energy control. This structure is somehow a logical extrapolation from the 2L-VSC control, where the AC and DC powers are instantly balanced, as they are physically linked. In the MMC case, using the AC power measurement as a feed-forward signal forces a coupling between both sides. Therefore, it is expected that the dynamics of the MMC under this control scheme will be remarkably similar than those of the 2L-VSC. As will be seen next, the flexibility that this structure offers is quite limited. From (6.4) it is observed that $P_{\mathrm{dc}}(s)$ will react fast to the disturbance $P_{\mathrm{ac}}(s)$. The only limitation to propagate the disturbance to the DC side depends on τ_{sum}, which is relatively small, i.e. the transient is fast. Then, as seen in the first term of the right-hand side of (6.5), the energy is not highly disturbed by $P_{\mathrm{ac}}(s)$, as its coefficient is close to zero. The resulting small deviation of the energy, therefore, will be compensated by the PI controller, which will have a small effect in $P_{\mathrm{dc}}(s)$.

$$P_{\mathrm{dc}}(s) = \frac{P_{\mathrm{ac}}(s)}{\tau_{\mathrm{sum}}s + 1} + \frac{G_c(s)}{\tau_{\mathrm{sum}}s + 1} \tag{6.4}$$

$$sW_t(s) = \left(\frac{P_{\mathrm{ac}}(s)}{\tau_{\mathrm{sum}}s + 1} - P_{\mathrm{ac}}(s) \right) + \frac{G_c(s)}{\tau_{\mathrm{sum}}s + 1} \tag{6.5}$$
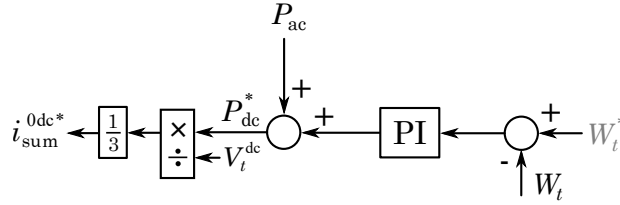
Fig. 6.4: Coupled energy control approach

6.4.2 Power-filtered control approach

Keeping the previous control structure, a low-pass filter (LPF, time constant τ_{g2}) applied to $P_{\text{ac}}(s)$ is proposed. The delay caused by this filter will force the internal energy of the MMC to smoothly increase, thus acting as a buffer between the AC and the DC sides. This structure will be referred to as *power-filtered* energy control. This structure offers extra flexibility as compared to the previous one, thanks to the LPF. In this case, from (6.6) it can be seen that $P_{\text{dc}}(s)$ dynamics will depend on the time constant of the filter τ_{g2} and the DC gain k_{g2}. With a small τ_{g2}, the dynamics will be similar to the coupled case. On the contrary, a high τ_{g2} would lead to a slower propagation of the disturbance to the DC side, and therefore to an increase of the internal energy. Gain k_{g2} will be set to 1 from now on, although this value is potentially tunable.

$$P_{\text{dc}}(s) = \frac{k_{g2} P_{\text{ac}}(s)}{(\tau_{\text{sum}} s + 1)(\tau_{g2} s + 1)} + \frac{G_c(s)}{\tau_{\text{sum}} s + 1} \tag{6.6}$$

$$sW_t(s) = \left(\frac{k_{g2} P_{\text{ac}}(s)}{(\tau_{\text{sum}} s + 1)(\tau_{g2} s + 1)} - P_{\text{ac}}(s) \right) + \frac{G_c(s)}{\tau_{\text{sum}} s + 1} \tag{6.7}$$
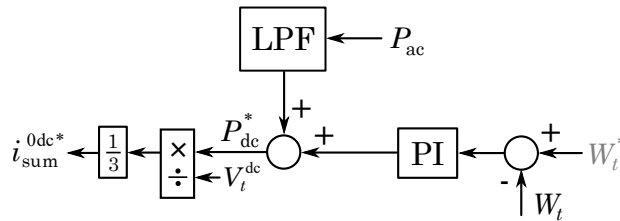
Fig. 6.5: Power-filtered energy control approach

6.4.3 Decoupled control approach

As reported in other studies [56, 76], the energy controller may not include a power feed-forward. In that case, the control effort completely relies on the PI energy controller. In other words, the resulting dynamics of the internal energy and the DC side will completely depend on the PI controller parameters. The more aggressive the controller, the less the energy deviation after a disturbance, and the higher the coupling between the AC and the DC sides. This structure will be referred to as *decoupled* energy control. Then, as in the coupled case, the only tunable part is the PI controller. From (6.8) it is observed that $P_{dc}(s)$ does not depend on $P_{ac}(s)$. Then, the only propagation mechanism relies on the internal energy, i.e. on the PI controller. Looking at (6.9) it is also noticeable that the energy is directly affected by $P_{ac}(s)$. Then, it is the job of the PI controller to reject the disturbance, and the resulting $P_{dc}(s)$ dynamics will depend on that.

$$P_{dc}(s) = \frac{G_c(s)}{\tau_{sum}s + 1} \tag{6.8}$$

$$sW_t(s) = -P_{ac}(s) + \frac{G_c(s)}{\tau_{sum}s + 1} \tag{6.9}$$
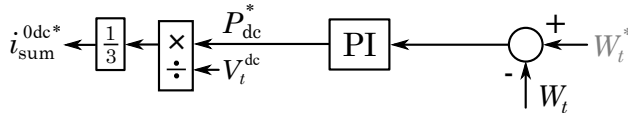
Fig. 6.6: Decoupled energy control approach

6.4.4 Dynamic energy reference control approach

Based on the previous control strategies, the modification of the energy reference signal (W_t^*) is proposed and explored as a new alternative. The energy reference will no longer be a constant value but will be changed dynamically, depending on the AC and DC transient power imbalance. Therefore, when there is a power injection from the AC side to the MMC that increases the energy, the energy reference will be decreased automatically. On the contrary, in case of a load connection that decreases the internal energy, the control will increase the energy reference. The energy-to-power ratio H_c is defined in (3.10), and the parameter k_{g4} adjusts the rate of change of the energy. This structure will be referred to as *dynamic energy reference* control. This

structure also offers more flexibility as the power-filtered case, with an extra tunable parameter. The corresponding P_{dc} and W_t equations are shown in (6.10)-(6.11). In this case, the expressions are more complex, being difficult to make an analytical judgement. Instead, different practical cases will be shown along the next sections.

$$
P_{\text{dc}}(s) = \frac{k_p H_c k_g s + k_i H_c k_g}{\tau_{\text{sum}} s^2 + (k_p H_c k_g + 1)s + k_i H_c k_g} P_{\text{ac}}(s)
$$
$$
+ \frac{s}{\tau_{\text{sum}} s^2 + (k_p H_c k_g + 1)s + k_i H_c k_g} G_c(s) \tag{6.10}
$$

$$
sW_t(s) = \left(1 - \frac{k_p H_c k_{g4} s + k_i H_c k_{g4}}{\tau_{\text{sum}} s^2 + (k_p H_c k_{g4} + 1)s + k_i H_c k_{g4}}\right) P_{\text{ac}}(s)
$$
$$
- \frac{s}{\tau_{\text{sum}} s^2 + (k_p H_c k_{g4} + 1)s + k_i H_c k_{g4}} G_c(s) \tag{6.11}
$$
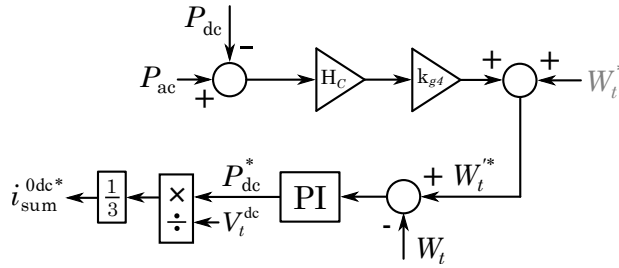
Fig. 6.7: Dynamic energy reference control approach

6.4.5 Summary of the control structures

A simple model based on (6.1)-(6.11) is used to show the transient effect of the AC power disturbance in the DC power and the internal energy of the MMC, summarising the previous energy control structures (Fig. 6.8). The initial control parameters are shown in Table 6.1. The AC power positive direction corresponds to the grid-forming supplying a load. It is shown that the coupled approach rapidly propagates the disturbance to the DC side, as fast as the circulating current control allows for. In the other approaches, the energy fluctuation is much more evident. As an initial example, the parameters τ_{g2} and k_{g4} are changed to show the flexibility that these structures offer. It is noticed that the power-filtered structure is a generic approach that contains

the coupled and the decoupled structures as particular cases (corresponding, respectively, to $\tau_{g2} = 0$ and $\tau_{g2} = \infty$). In Section 6.5, the dynamic behaviour and capabilities of each structure will be further explored.

Table 6.1: Control parameters related to the energy

Parameter	Symbol	Value	Units
Total energy, proportional	k_p	126	W/J
Total energy, integral	k_i	3948	W/(Js)
LPF time constant (pow.-filt.)	τ_{g2}	50	ms
LPF DC gain (dyn. ref.)	k_{g4}	0.05	-
MMC energy-to-power ratio	H_c	49.2	ms

(a) Coupled

(b) Power-filtered

(c) Decoupled

(d) Dynamic W_t^*
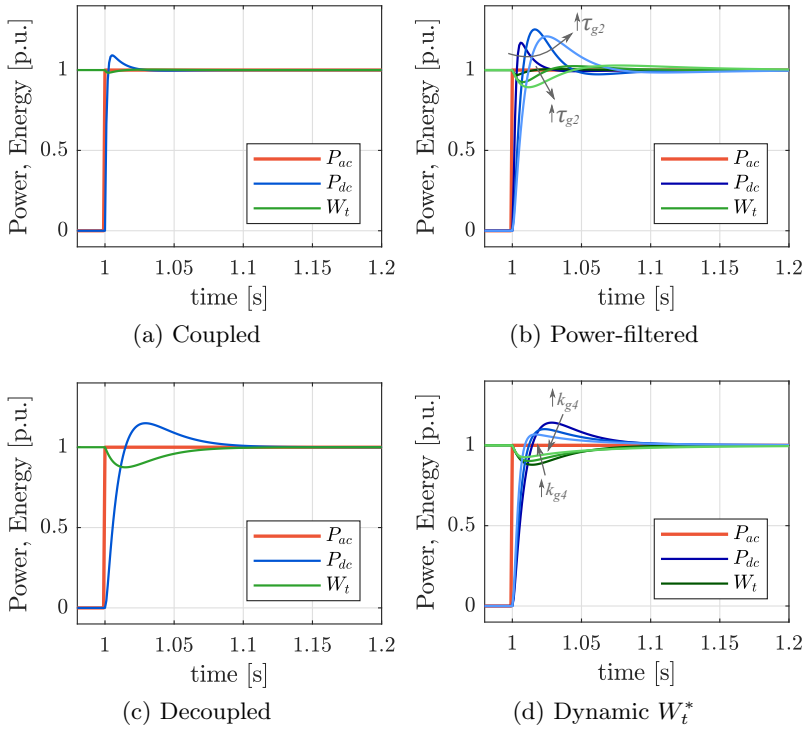
Fig. 6.8: Time-domain plots under a P_{ac} 1 p.u. load step disturbance – Preliminary simplified model (6.1)-(6.11)

6.5 Case study

After presenting the different control structures, a comprehensive analysis evaluating the advantages and drawbacks of each one is addressed in this section using case studies. First of all, an initial case of a single grid-forming MMC is used, for the sake of simplicity in the analysis. Time-domain simulations are carried out using the full non-linear model, consisting of an Average Arm Model (AAM) for the MMC, using the full control scheme from Fig. 2.3, with saturations in the current references and in the modulation indexes.

Then, an eigenvalue analysis using the complete linear model is performed in order to identify potential instabilities related to the proposed energy control structures. After, a straightforward tuning method is presented that allows for a simple way to empirically establish a trade-off between the MMC magnitudes performance (i.e. energy and DC power). Following up on the results obtained, an optimal tuning methodology is used, in order to unveil the full dynamic capabilities of each structure, tuning all the control parameters at once. Finally, a case scenario considering two grid-forming MMCs operating in parallel is considered, showing the results of the suggested control schemes in a bigger and more realistic scenario.

6.5.1 Scenario configuration

In the present study, the frequency droop scheme, which is necessary to achieve active power sharing in a multiple grid-forming setup, is also implemented in the case of a single grid-forming MMC for verification purposes. On the other hand, voltage droop scheme, which is optionally included in some cases for reactive power sharing purposes, is not included for simplicity. System and control parameters related to the AC side are shown in Tables 6.2 and 6.3. Note that τ_{cc} and τ_{sum} are used to calculate the current controllers PI parameters (3.2)-(3.3). The MMC parameters can be found in Table 3.1. The AC side grid-forming control structure and its parameters are adopted from previous studies, and it is not within the scope of this chapter to address that part of the control system.

A constant DC voltage source is used to model the DC side of the MMC, assuming that the HVDC grid is robust and stable. The constant PQ node consists of controllable current sources, as mentioned before, including a PLL that tracks the angle in order to inject the corresponding qd current components. These assumptions, which simplify the models and the analysis, do not compromise the validity of the results, as they do not have a relevant impact in the energy dynamics and the disturbance propagation from the

AC to the DC side.

Table 6.2: AC grid parameters [106]

Parameter	Symbol	Value	Units
AC cable resistance	r_c	0.032	Ω/km
AC cable inductance	l_c	0.4	mH/km
AC cable capacitance	c_c	0.17	μF/km
Cable length	d	25	km

Table 6.3: Control parameters related to the AC side

Parameter	Symbol	Value	Units
AC voltage, proportional	k_{p-u}	0.025	A/V
AC voltage, integral	k_{i-u}	1	A/(Vs)
Frequency droop	k_f	10^{-9}	rad/W
Voltage droop	k_u	0	-
Time constant freq. droop filter	τ_f	40	ms
Time constant AC current control	τ_{cc}	1	ms
Time constant DC current control	τ_{sum}	1	ms

6.5.2 Single grid-forming MMC

A single grid-forming MMC is considered as an initial case scenario, which is depicted in Fig. 6.9. The parameters related to the energy control loop are summarized in Table 6.1. The energy PI controller parameters are selected for a settling time of around 100 ms, based on the decoupled structure, as will be further detailed later on.
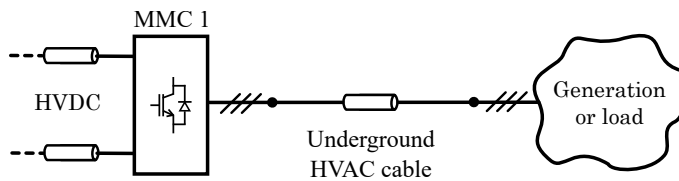
Fig. 6.9: Initial case study consisting of one grid-forming MMC and a PQ node connected through an AC cable

In order to highlight the particular capabilities of grid-forming as compared to grid-following, the converter is simulated as follows. Initially, a ramping

up of the AC voltage (black-start) is performed at $t = 0.2$ s. Then, the PQ node progressively injects active power to the AC grid at $t = 0.4$ s, until it reaches 0.5 p.u. (operating point). A 0.25 p.u. step of generated AC active power is performed at $t = 1$ s (disturbance), reaching an operating point of 0.75 p.u., which corresponds to approximately 1 p.u. of apparent power. Finally, a sudden disconnection of the PQ node occurs at $t = 1.3$ s (large disturbance). Note that the black-start of the voltage and the continuous operation of the converter after a full disconnection on the AC side are not possible in grid-following converters, as they rely on a stable AC grid.

An initial dynamic performance comparison among the different proposed structures, including the case of an equivalent 2L-VSC for completeness, is shown in Fig. 6.10. On one hand, it can be seen that all the AC side magnitudes are unaffected by the MMC control structure used. In the 2L-VSC case, some similarities are observed in terms of the fundamental oscillation component, although some extra oscillatory components as compared to MMC are shown. On the other hand, regarding the DC magnitudes and the energy, clear dynamic differences can be observed, as discussed next.

In the coupled case, DC current and power responses are similar to the 2L-VSC, due to the coupling created by the feed-forward signal. When a low-pass filter is applied to that signal (power-filtered approach), the coupling is reduced, and it is further diminished by eliminating the feed-forward, which corresponds to the decoupled approach. Regarding the dynamic energy reference scheme, the internal energy overshoot is partly compensated, due to the energy reference set point modification during the disturbance. After this initial evaluation, the stability and the performance capabilities of the different structures will be explored in the next subsections.

6.5.3 Linear model remarks

A linearised small-signal model of the previous system with one grid-forming MMC is derived to enable linear analysis and linear control design. Although most of the elements of the system are already described in Chapter 2, some remarks are necessary regarding the constant power node at one end of the AC line.

The constant power node exchanges active and/or reactive power through controllable current sources. On one hand, this can correspond to the offshore wind farm from Fig. 6.1a (power flowing towards the grid-forming MMC), which typically uses power electronics converters synchronized with the offshore AC grid through Phase-Locked Loops (PLL). On the other hand, a scenario such as an islanded system (Fig. 6.1b) would typically involve differ-
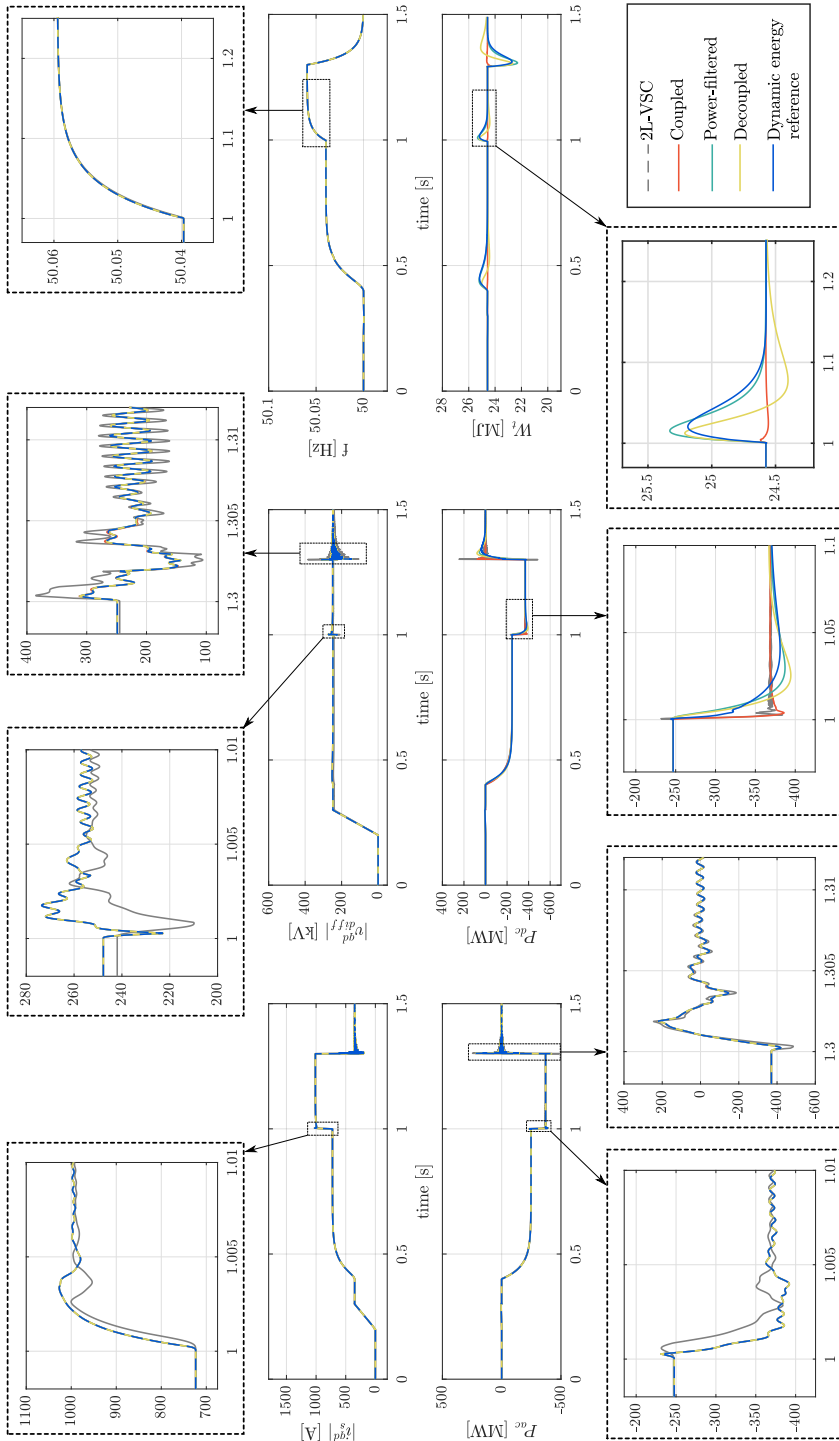
Fig. 6.10: Time-domain simulation of a single grid-forming MMC: ramping up increase of AC voltage (black-start), slow increase to 0.5 p.u. of generation (operating point), sudden increase of 0.25 p.u. of generation (disturbance), and disconnection of the PQ node (large disturbance) – Dynamic performance of the different energy control structures

ent types of loads (constant current, constant impedance and constant power loads), making its dynamic model more complex. However, for convenience in the analysis, the case of a constant power node representing a power electronics interface with a PLL will be considered as well in this second case for simplicity purposes.

Instead of modelling a detailed converter, the power references $\Delta P_l^*(s)$ and $\Delta Q_l^*(s)$ are filtered using first-order transfer functions that emulate the AC power closed-loop response of the converter, with a time constant of τ_p. A PLL (Fig. 2.5a) tracks the voltage angle by means of controlling its d component to zero. Then, according to instantaneous power theory [120], the qd components of the current are calculated as (6.12)-(6.13). An extra first-order filter (time constant of τ_c) is included, representing the dynamics of the current loops (τ_c is typically around 10 times lower than τ_p).

$$\Delta i_l^q(s) = \frac{2}{3}\left(\frac{1}{u_{g0}^q}\frac{\Delta P_l^*(s)}{\tau_p s + 1} - \frac{P_{l0}}{u_{g0}^{q}{}^2}\Delta u_g^q(s)\right)\frac{1}{\tau_c s + 1} \tag{6.12}$$

$$\Delta i_l^d(s) = \frac{2}{3}\left(\frac{1}{u_{g0}^q}\frac{\Delta Q_l^*(s)}{\tau_p s + 1} - \frac{Q_{l0}}{u_{g0}^{q}{}^2}\Delta u_g^q(s)\right)\frac{1}{\tau_c s + 1} \tag{6.13}$$

In order to integrate the different elements into the linear model, a common qd reference frame has to be established. In this case, the reference angle will be the one generated by the grid-forming MMC. The PLL is modelled as a closed-loop with a PI controller that regulates the d component of the measured voltage to zero, as mentioned before. The output of the PI, i.e. the PLL frequency $\Delta\omega_{\mathrm{pll}}$, minus the reference frequency $\Delta\omega_1$ is integrated to obtain $\Delta\Theta$, which is the angle difference between the PQ node and the grid-forming MMC angles. This $\Delta\Theta$ is necessary to transform any qd magnitude from one reference to another. In this case, PQ node magnitudes (qdc) are transformed to the common reference (qd) using (2.34), and vice-versa using (2.35) (see Chapter 2).

A block diagram of the overall linear model, including the control loops and the remaining elements of the system (already covered in Chapter 2) is shown in Fig. 6.11.
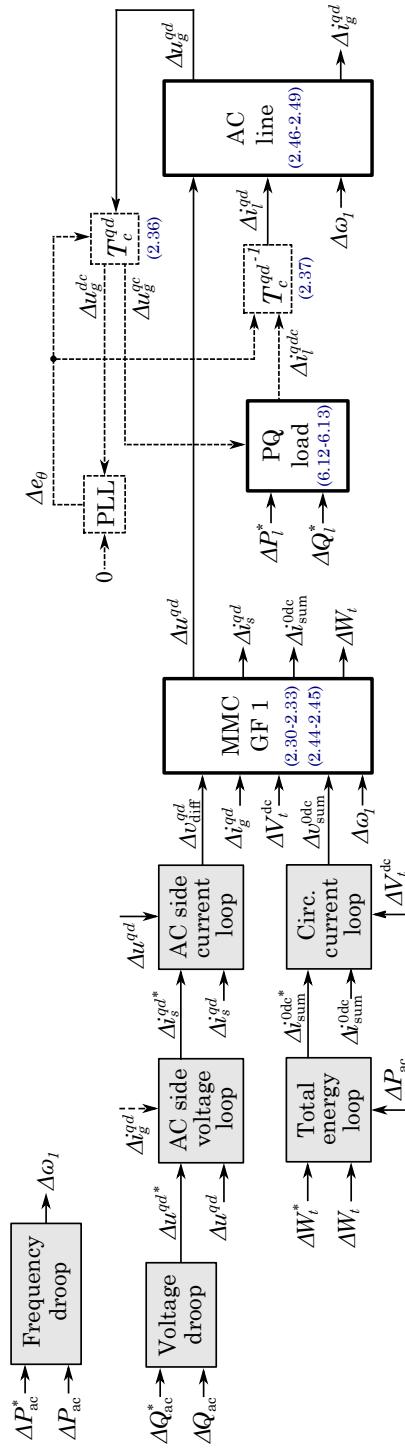
Fig. 6.11: Linear model of an AC line with one grid-forming MMC on one side and one PQ node on the other side

6.5.4 Identification of potential instabilities related to the proposed energy control structures

For a given initial tuning of the energy PI controller, the power-filtered and dynamic energy reference structures offer extra tunable parameters. An eigenvalue analysis of the linear model (Fig. 6.11) using these two approaches is performed in Figs. 6.12 and 6.13, varying these tunable parameters in order to identify potential instabilities: the time constant of the filter (τ_{g2}) in the power-filtered approach, and the DC gain (k_{g4}) in the dynamic energy reference approach. Note that an extra DC gain in the power-filtered approach would affect the transient response but not the state matrix (i.e. the eigenvalues of the system).

Regarding the power-filtered approach, it is observed that τ_{g2} does not cause instability (Fig. 6.12). One real pole approaches the vertical axis when τ_{g2} is increased (a very large value corresponds to the decoupled control approach), but the real part never reaches positive values. On the contrary, when τ_{g2} is reduced (zero value corresponds to the coupled control approach) this pole moves away from the vertical axis.
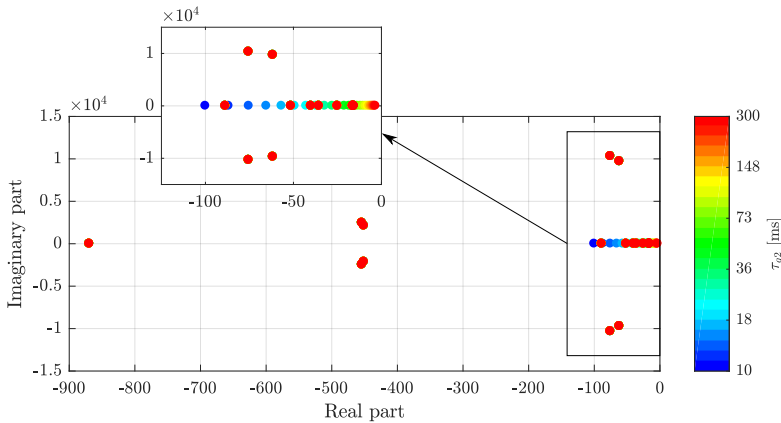
Fig. 6.12: Eigenvalues of the single grid-forming system using the power-filtered approach – Effect of τ_{g2}

With respect to the dynamic energy reference approach, the effect of k_{g4} is shown in Fig. 6.13. A potential instability is detected when this gain is lower than -0.15 (Fig. 6.13b). If k_{g4} is positive and not extremely large, it does not compromise the stability (Fig. 6.13b). However, it will affect the transient performance, as will be explored next.
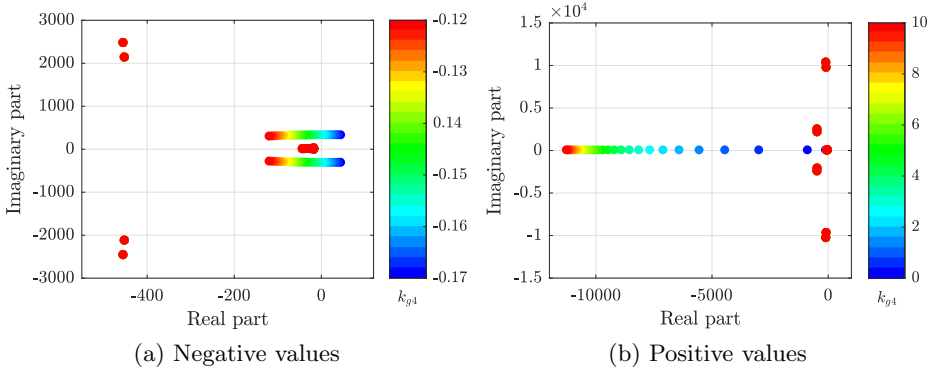
Fig. 6.13: Eigenvalues of the single grid-forming system using the dynamic energy reference approach – Effect of k_{g4}

6.5.5 Empirical tuning

One of the advantages of the power-filtered and dynamic energy reference structures is that, for a given PI controller, they allow to intuitively tune the control system through a single parameter: τ_{g2} and k_{g4}, respectively. This offers some flexibility in terms of establishing a trade-off between the DC power and the energy dynamics.

First, an initial tuning of the energy PI controller has to be established. An initial approximation of the tuning based on reference tracking criteria is adopted, which results in a straightforward approach assuming that the system plant is a single MMC internal equivalent capacitor, which is an acceptable assumption if this controller is several times slower than the inner circulating current controller. The decoupled structure is assumed in this case, and the tuning obtained will be used for all the structures. The closed-loop transfer function of this simplified system is

$$\frac{W_t(s)}{W_t^*(s)} = \frac{k_p s + k_i}{s^2 + k_p s + k_i} \tag{6.14}$$

and k_p and k_i can be defined based on a desired second-order time-domain response, as

$$k_p = 2\xi\omega_n, \quad k_i = \omega_n^2, \tag{6.15}$$

with $\xi = 1$ and $\omega_n = 2\pi(1/0.1)$, to achieve a settling time of around 100 ms (much slower than the current loop) with a critically damped response (i.e. no overshoot). This controller would be typically designed for disturbance

rejection capability. However, an approximate reference tracking criteria has been used instead, that actually resulted in an acceptable disturbance rejection capability as seen in the next plots. The reason for using this tuning is that this is a straightforward way of calculating the controller parameters analytically, whereas for disturbance rejection it is slightly more complex. For simplicity, and because later on an optimal tuning with specific requirements will be explicitly designed, the aforementioned tuning is considered to be sufficient to illustrate the flexibility of the control structures in this section. In Fig. 6.14 it is shown how the power-filtered structure offers a whole range of possibilities through the time constant τ_{g2}, with the coupled and the decoupled structures as extreme cases (i.e. $\tau_{g2} = 0$ and $\tau_{g2} = \infty$, respectively). A trade-off solution between the energy deviation and the DC power smoothness can be selected. The higher energy deviation corresponds to the decoupled structure, whereas the sharpest DC power waveform corresponds to the coupled. Note, however, that for intermediate solutions the DC power overshoot also increases, which might be undesirable.

(a) $P_{\text{dc}}(s)$ response
(b) $W_t(s)$ response
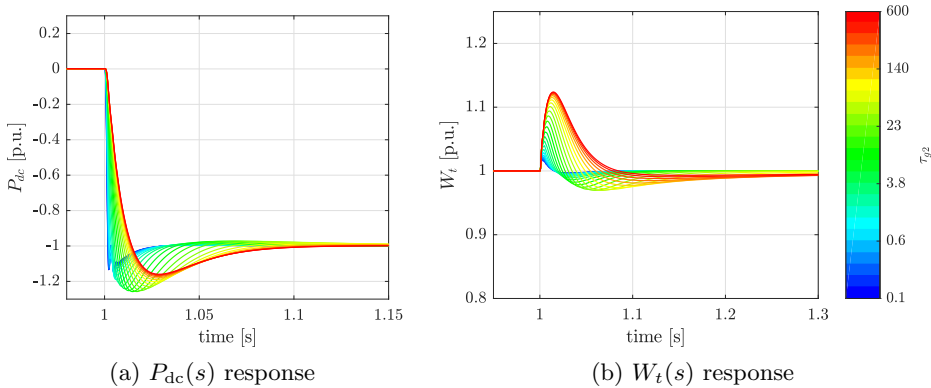
Fig. 6.14: Time-domain simulation of the single grid-forming system using the power-filtered structure – AC power step disturbance, τ_{g2} sweep

In Fig. 6.15, the gain k_{g4} is swept. It can be seen that increasing k_{g4} reduces the energy deviation but a high frequency oscillation appears in the DC power. In this case, $k_{g4} = 0.25$ seems to offer a good trade-off between both specifications.

(a) $P_{\mathrm{dc}}(s)$ response

(b) $W_t(s)$ response
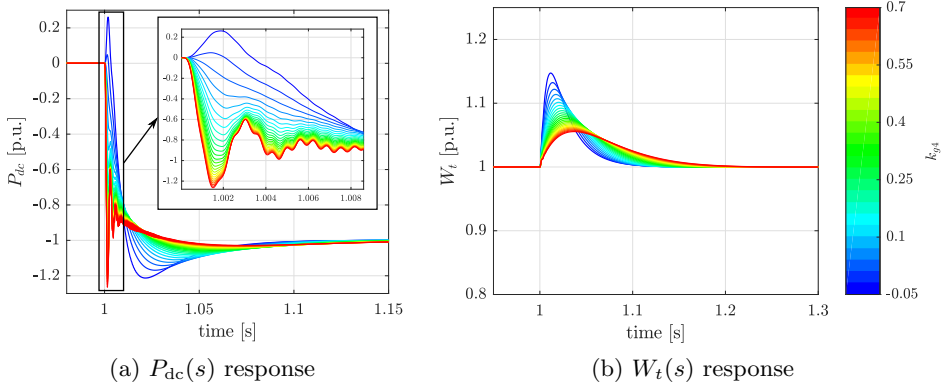
Fig. 6.15: Time-domain simulation of the single grid-forming system using the *textitdynamic energy reference structure* – AC power step disturbance, k_{g4} sweep

6.5.6 Optimal tuning

As seen in the previous subsection, the different trade-offs that can be empirically established suggest carrying out an optimal tuning, in order to achieve a specific dynamic requirements or, furthermore, the best possible dynamic response using the different energy control structures. The control system parameters that are potentially tunable are:

- k_p: proportional part of the total energy PI.

- k_i: integral part of the total energy PI.

- τ_g: time-constant of the low-pass filter (LPF) (only in power-filtered scheme).

- k_g: DC gain of the low-pass filter (only in dynamic energy reference scheme (note that the optimizer might also add a gain in the power-filtered case.).

To understand the potential capabilities of each presented control structure, in this subsection the tunable parameters of the control system will be tuned using optimization tools. The control objectives are specified as follows. First of all, a step disturbance of 1 p.u. of AC power from the PQ node (Fig. 6.9) is considered, so that the system is robust under the worst-case scenario of a sudden disconnection of the generation or the load. Then, the

transfer functions (6.16) are defined (P_g is the active power at the PQ node, and e_{W_t} stands for the error between the total energy reference W_t^* and the total energy W_t, i.e. the energy deviation), which are computed using the complete linear model (Fig. 6.11) and their expressions are not shown for space reasons.

$$G_1(s) = \frac{P_{\mathrm{dc}}(s)}{P_g(s)}, \quad G_2(s) = \frac{e_{W_t}(s)}{P_g(s)} \tag{6.16}$$

Then, the ideal control objectives are defined as follows:

1. DC power (P_{dc}): a smooth response after a step disturbance, i.e. 0% overshoot and mitigation of high frequency oscillations. The corresponding gain limit is imposed in the frequency-domain for $G_1(s)$, with filtering capability at high frequencies.

2. Internal MMC energy (W_t): a maximum overshoot of 10% and relatively fast recovery time. The corresponding gain limit is imposed for $G_2(s)$ in the frequency-domain, reducing the gain for low frequencies to achieve integral action (zero error) in the desired settling time.

These specifications prioritize the DC power over the internal energy, in order to use the MMC as a firewall between the AC and the DC sides. Using robust control techniques for a fixed structure controller, the previous objectives can be specified as constraints for an optimization problem that aims to achieve those objectives [123]. In this case, the algorithm is based on the $\mathcal{H}_\infty$-norm as described in [92]. Starting with a stable initial tuning, the optimizer iterates on the different tunable parameters and aims to satisfy the previous constraints. In order to understand the limits in terms of DC power and energy, three optimal cases corresponding to three different settling times for the energy are analysed. In Figs. 6.16 and 6.17, the results obtained are shown and compared with the initial tuning. Note that these plots are based on the linear model from Fig. 6.11. The initial and the optimized tuning values are summarised in Table 6.4.

First of all, it is shown that the coupled structure is not capable of cancelling the feed-forward effect, and therefore it is not possible to obtain a feasible optimal tuning. This highlights the fact that this structure is not suited to properly enhance the degree of freedom offered by the energy of the MMC. It is shown in Fig. 6.16c that the optimizer is incapable of pushing the Bode plot below the limit. The energy deviation that this structure offers is very low, as the AC power feed-forward mostly bypasses the buffering capability of the MMC.
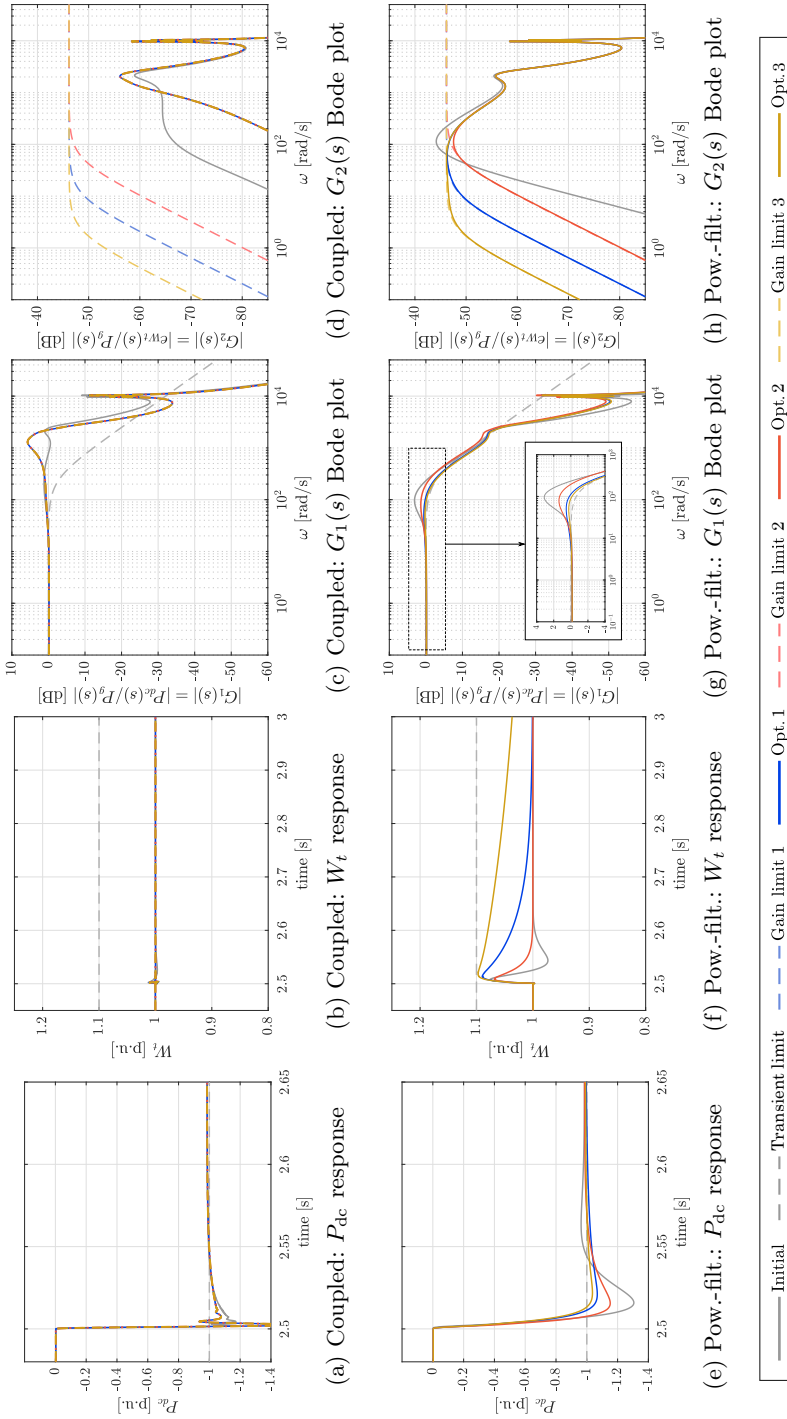
Fig. 6.16: Time-domain simulation and Bode gain plots of the single grid-forming system for the coupled and power-filtered control structures, for the initial and different optimal tunings
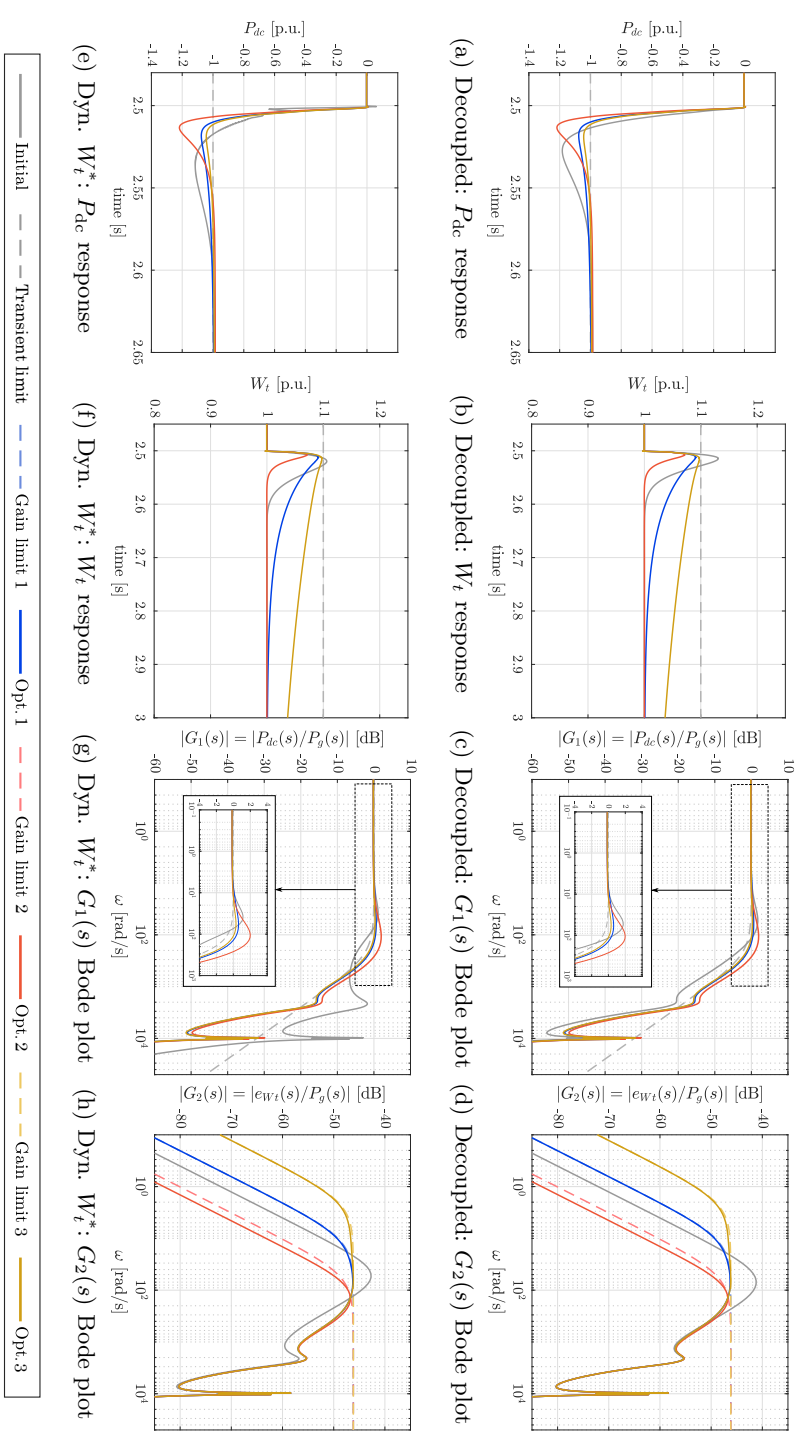
Fig. 6.17: Time-domain simulation and Bode gain plots of the single grid-forming system for the decoupled and dynamic energy reference control structures, for the initial and different optimal tunings

Table 6.4: Initial and optimal tuning parameters

		Initial	Opt. 1	Opt. 2	Opt. 3	Units
Coupled	k_p	126	1854	1854	1854	W/J
	k_i	3948	17	126	4	W/(Js)
Power-filtered	k_p	126	187	224	180	W/J
	k_i	3948	1708	8434	344	W/(Js)
	τ_{g2}	10	0.07	0.07	0.07	ms
	k_{g2}	1	0.143	0.165	0.137	-
Decoupled	k_p	126	219	252	211	W/J
	k_i	3948	1997	14186	400	W/(Js)
Dynamic W_t^*	k_p	126	219	252	211	W/J
	k_i	3948	1998	14215	400	W/(Js)
	k_{g4}	0.1	0.0003	0.0005	0.0003	-

Regarding the other control alternatives, it is noticeable that despite all of them show different dynamics using the initial tuning, the optimal solution tends to be equivalent for the three options. This reveals that, at least for the sort of transient requirements specified, neither the power-filtered nor the dynamic energy reference structures offer a clear advantage when an optimal tuning is computed, meaning that a single PI controller (i.e. decoupled structure) can be seen as the simplest solution to obtain the best possible dynamic response. To better understand and support this statement, the optimal tuning has been performed under three different constraints, namely Opt. 1, Opt. 2 and Opt. 3. In each case, the constraint related to the settling time of the energy (i.e. the cut-off frequency in Figs. 6.16d,h and 6.17d,h) is changed. It can be seen that the optimizer tends to push the Bode plots to the limits in most cases. This unveils that the reduction of the DC power overshoot comes at the expense of a longer settling time of the internal energy. Going to the limit, an overshoot of 0% corresponds to an infinite settling time, i.e. droop control of the internal energy. A DC power overshoot between $3-20\%$ (Figs. 6.16e and 6.16a,d) and an energy settling time of 0.15-1 seconds (Figs. 6.16f and 6.16b,f) are obtained in the different optimal cases.

This highlights that neither the power-filtered nor the dynamic energy reference structures are able to overcome this limitation with their extra parameters nor to outperform the decoupled alternative, concluding that a single PI controller is sufficient. On one hand, in the power-filtered approach, the gain k_{g2} is small in the three cases, and the time constant τ_{g2} is also very small (0.07 ms in all cases), meaning that the filter has almost no effect.

On the other hand, in the dynamic energy reference approach, the gain k_{g4} tends to be almost zero, and the PI parameters are very similar to those of the decoupled structure, meaning that, with an optimal tuning with such requirements, this structure is practically the same as the decoupled one (see Table 6.4).

6.5.7 Multiple grid-forming MMCs

In more realistic power system applications, more than one converter might be required to operate in grid-forming mode. Then, the AC side control must ensure that the active and reactive power flows are properly shared, which is classically carried out through frequency and voltage droop strategies (Fig. 2.3). A case scenario with two grid-forming MMCs (Fig. 6.18) is presented in this final subsection for completeness, where each MMC is using a different energy control structure. This case study represents an offshore wind farm cluster with grid-forming converters exporting power to onshore through two HVDC links.
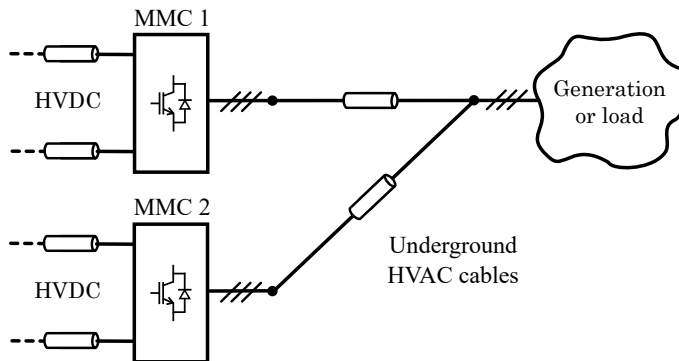
Fig. 6.18: Case study consisting of two grid-forming MMCs and a PQ node connected through AC cables

The system initial operating point is set to 1 p.u. of AC power flowing from the AC side to the converters (each converter is absorbing 0.5 p.u. thanks to the frequency droop control equal power sharing feature). A step of generation coming from the PQ node to the grid-forming MMCs of 0.5 p.u. is performed at $t = 2.5$ s, and a full disconnection of the wind farm is performed at $t = 5$ s. The coupled structure with the initial tuning is used for the first MMC, whereas for the second MMC the power-filtered, decoupled and dynamic energy reference structures using the optimal tuning (Opt. 2) are implemented and compared (Fig. 6.19).

Despite the same AC powers being seen in both MMCs, the performance in terms of DC power and internal energy of each MMC is independent from each other, and it completely depends on the energy control structure used. In the case of the coupled approach (MMC 1), even though the DC power shows a significantly attenuated response with respect to the AC power disturbance, the response is not smooth and some undesired overshoot is observed, specially when the line disconnects (Fig. 6.19b). On the other hand, in MMC 2 the disturbance is completely blocked thanks to the capabilities offered by the power-filtered, decoupled and dynamic energy reference structures under the optimal tuning, which allows for achieving a smooth DC power with barely no overshoot and without compromising the internal energy limits. Also, it is shown that these three structures exhibit practically the same transient characteristics. Some non-linearities are observed in the DC power in Fig. 6.19b, which may be caused by the current saturation of the AC current control and the saturation of the modulation indexes during the transient after the disconnection of the line. Nevertheless, there is no noticeable overshoot in the DC power, and the energy deviates only up to around 6%.

Finally, the same setup is tested under the event of a trip of one of the two converters while feeding a load. In this case, the two grid-forming MMCs are feeding an AC load of 0.8 p.u. of active power. The power is being shared equally by both MMCs (i.e. 0.4 p.u. of active power each). At $t = 2.0$ s, MMC 2 trips, causing a transient and a sudden change of power flow (Fig. 6.20). MMC 1 is able to effectively supply the whole amount of power, keeping the system in operation. It has to be noted that for bigger loads (e.g. 1 p.u. instead of 0.8 p.u.) the current references of MMC 1 reach saturation, causing a much bigger transient in the voltages and currents of the converter and the rest of the system. In those cases, a more detailed fault analysis would be required, considering additional fault ride-through schemes, protecting the converter from overcurrents and overvoltages.

(a) Increase of generation (0.5 p.u.)

(b) Generation disconnection
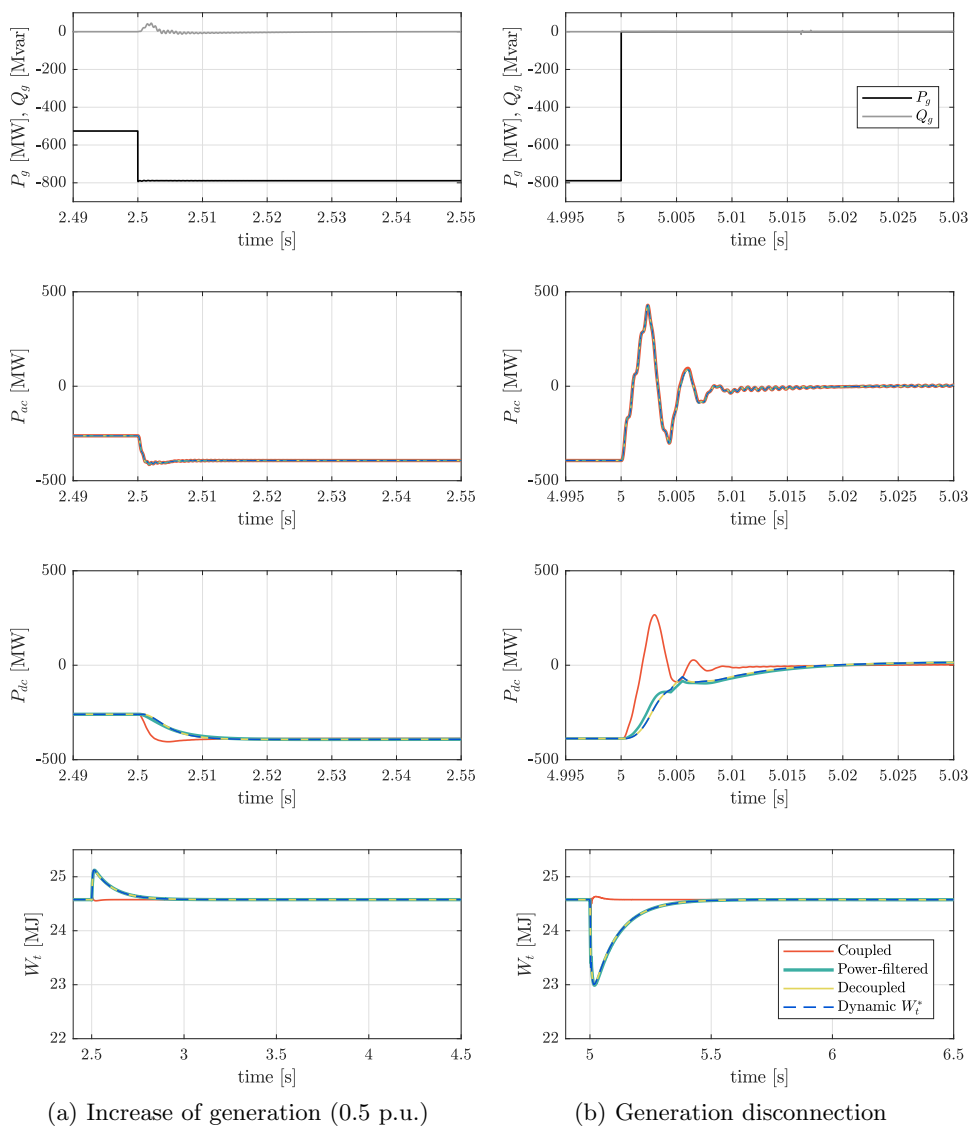
Fig. 6.19: Time-domain simulation of the multiple grid-forming system – Dynamic performance using coupled (MMC 1) and decoupled (MMC 2) control structures after a sudden increase of generation and after a total disconnection
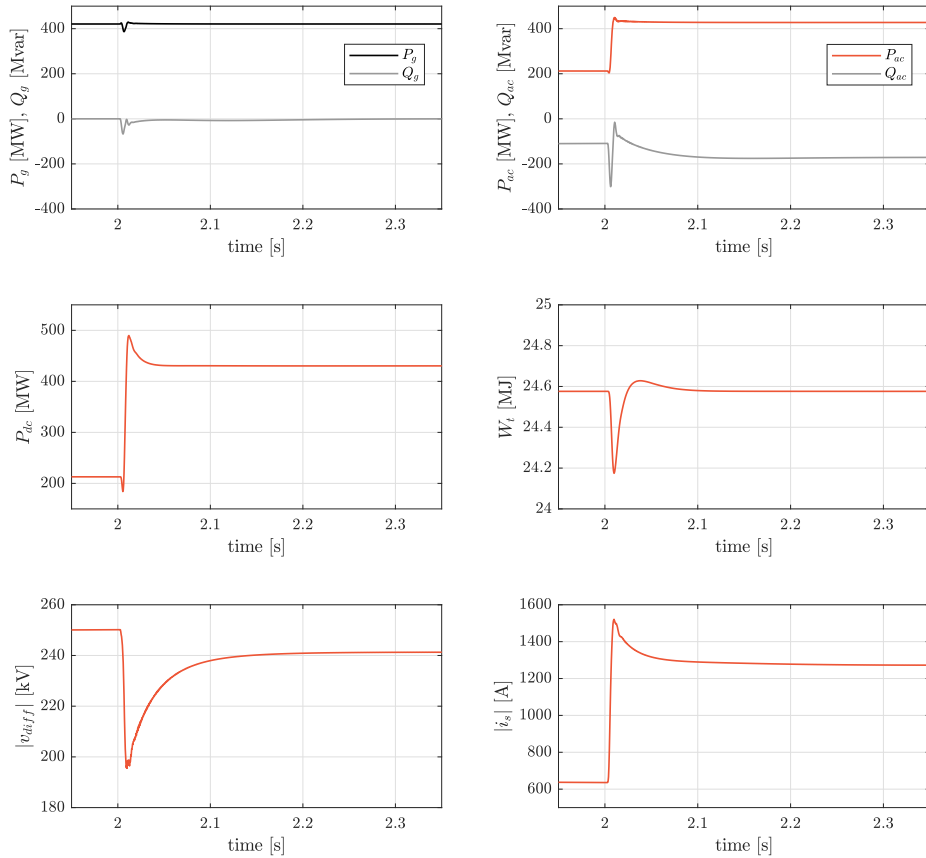
Fig. 6.20: Time-domain simulation of the multiple grid-forming system – Dynamic performance of MMC 1 (coupled control) after a trip of MMC 2

6.6 Conclusion

The buffering feature inherent to the MMC topology can be used to prevent AC side power disturbances to propagate to the DC side when operating in grid-forming mode if an adequate control of its internal energy is performed. As HVDC grids are likely to experience a growth in the upcoming years, this mitigation feature becomes crucial in order to preserve the correct operation of the whole DC system, transiently isolating sudden power changes that may occur in the different AC connection points, specially in the case of large and complex meshed HVDC grids. In this chapter, different control structures for the energy control of the MMC have been explored. On one hand, this degree of freedom related to the energy of the MMC can be effectively exploited with the power-filtered, decoupled and dynamic energy reference structures. The power-filtered and dynamic energy reference options allow for an intuitive and straightforward control tuning through a single parameter. Furthermore, it was demonstrated by optimally tuning the control parameters with highly restrictive requirements that these three structures exhibit equivalent transient performance features. On the other hand, the coupled structure is not recommended, as it does not effectively mitigate the propagation of AC side disturbances to the DC side, bypassing to a greater or lesser extent the energy buffer of the MMC. Ultimately, it can be concluded that the grid-forming MMC under the aforementioned optimal tuning exhibits an appropriate dynamic performance under severe AC power disturbances (i.e. sudden generation increase, sudden disconnection of the generation, and trip of one MMC while feeding a load), with a small deviation of the internal energy and a smooth DC power response with a very small overshoot.

Chapter 7

The MMC in DC voltage droop-controlled MT-HVDC grids

This chapter is based on the following publication:

7.1 Introduction

With the focus on the expansion and evolution of power systems for more renewable energy resources integration in the near future, the idea of multi-terminal (MT) VSC-HVDC grids is becoming more relevant, specially from the point of view of offshore wind farms [27]. Several projects consisting of single HVDC links are already in operation, whereas others are planned to be commissioned soon. This unveils that there is a potential necessity of interconnecting those systems in the future, and also that new projects will be directly planned considering a MT-HVDC setup.

Nowadays, there is a handful of MT VSC-HVDC projects in operation. The world's first project was built in Nan'ao island in Guangdong, China, and was commissioned in 2013. The project consisted of a three-terminal grid, and it was planned in order to safely integrate the high amount of available wind resources in the island to the onshore grid, which was constrained by the existing AC lines, and also looking forward to adding new wind generation in the future [29, 30]. The world's second project was built in the Zhoushan islands, also in China, and was put into service in 2014. The project consists of five terminals, allowing for the integration of the high amount of wind energy from the archipelago reliably, and ensuring the safe operation of the whole system [31, 32]. Another recent project is the four-terminal in Zhangbei, aiming to integrate bulk wind, hydro and solar power resources into Beijing.

Additional terminals are planned to be added, which will expand the MT-HVDC grid in 2021 [37, 38].

The aforementioned projects consist of the integration of distributed bulk clean energy resources into the main power system. Due to the multi-terminal (or meshed) HVDC grid topology, this generated power can flow to the different terminals, even those which are far away from the generation source. This brings flexibility and reliability to the whole system, and allows for a reduction of the non-renewable energy sources overall. Furthermore, the idea of MT-HVDC grids may also include islanded and passive systems (i.e. systems that rely, partially or completely, on external generation). As these systems act as a load, the power can flow in the other direction as compared, for instance, to the offshore wind farm application. This will become relevant in the MT-HVDC grid analysis that will be carried out in this chapter, and extends the range of applications of such grids.

From now on and for simplicity, the acronym MT-HVDC will refer only to VSC-based systems. The control of the DC voltage in a MT-HVDC grid is crucial to ensure the overall grid system stability and adequate performance. The droop control is a well-known solution where usually different converters are responsible for the DC voltage control, which enables a fast regulation of the DC grid and the establishment of power sharing between the different converters [124–126]. Other approaches can be found, such as voltage margin control [127] where only one converter stiffly controls the DC voltage of the MT-HVDC grid. Different implementations or structures of the droop control can be found in the literature. Eight different options either using voltage, current or power for the droop control loop are compared in [128]. Also, some studies include an additional power loop cascaded with the DC voltage droop loop [125], whereas others do not include it [129].

Several studies are focused on the DC grid dynamics, for instance considering its operational limitations [130] or cable dynamics [131]. In [132], AC/DC interactions are considered in the optimisation of the droop control, whereas in [133] a droop design based on a trade-off among power losses, power flow and voltage deviations minimisation is described. In [134], the droop control is addressed considering the complete multi-terminal grid dynamics, including both the linearised DC and AC grid dynamics, the converter controllers and a DC oscillation damping loop. Although the majority of studies in the literature are based on two-level VSCs, some recent droop MT-HVDC studies including the MMC can be found. In [C1], the overall MMC dynamics and a more detailed cable model was included, performing a similar analysis than in [134]. Regarding MMC-based MT-HVDC droop control studies, a control strategy able to ensure grid reliability and stability in case of an

outage of a master station is proposed in [135], whereas in [136] an optimal control design to improve the stability and the dynamic behaviour is applied to a three-terminal grid. A comprehensive modelling of an MMC-based MT-HVDC grid including different energy control approaches to support the DC voltage is presented in [129]. In the co-authored paper [J5], a hierarchical methodology based on a linear model and simulations is proposed to select feasible droop gains.

In this chapter, a detailed, modular and generic MT-(VSC)-HVDC system, useful for applications such as offshore wind integration and islanded systems, is presented. The stability analysis of different control structures for the terminals under DC voltage droop control is addressed, and a joint optimal control tuning of all the droop gains and the energy controllers is detailed and applied to a challenging asymmetrical case study, which contains converters with different power ratings. The results are validated using a complete non-linear model through simulations, under different severe disturbances.

7.2 System description

The system under study is a generic MT-HVDC grid. Such a grid does not only consider the case of offshore wind farm generation to the main land AC grid, but also the connection of islanded or completely passive systems that import power from land or from other stable systems. The system is composed of DC voltage droop controlled terminals and AC grid-forming terminals (Fig. 7.1). On one hand, the AC grid-forming terminals generate a stable AC grid that enables the integration of power generation (e.g. in offshore wind farms) or the supply of power from the HVDC grid (e.g. in islands with a very weak generation or no generation at all). On the other hand, the DC voltage droop controlled terminals (which can be seen as distributed DC grid-forming) are responsible for making the HVDC grid stable and for sharing the power accordingly.

With an adequate definition of the DC voltage droop control gains, power sharing between converters is enabled locally, without communications. However, a slower secondary control [137] with communications could be implemented in order to, for instance, compensate for possible deviations of power or implement an optimisation algorithm that, for instance, minimises the losses [138].
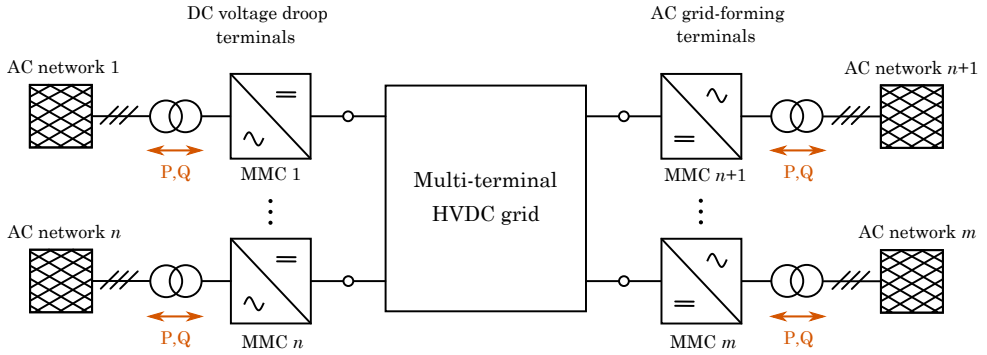
Fig. 7.1: Generic multi-terminal HVDC grid with DC voltage droop controlled terminals and AC grid-forming terminals

7.3 Control approaches

In DC voltage droop controlled MMCs, different control structures are possible, similar to what was presented in Chapter 3. In fact, the control system has to deal mainly with the DC voltage and the total energy through the AC and DC current references. Moreover, an additional power loop can be included, cascaded with the DC voltage control loop. A detailed analysis of the different options will be carried out later on, using a base case study.

The most common control structure, adopted from 2L-VSCs, will be referred to as *droop classic* control, equivalently to Chapter 3. The droop gain k_d amplifies the DC voltage error signal, and yields either the AC current reference i_s^{q*} or the active power reference P_{ac}^* if a power loop is included. On the other hand, the total energy is controlled by means of a PI controller, yielding the zero sequence additive current reference i_{sum}^{0dc*} (i.e. a third of the DC current in a balanced case) after adding a feed-forward based on the measured active power for stability purposes, as mentioned in Chapter 3. Both approaches are depicted in Figs. 7.2 and 7.3.

Another possibility consists of swapping the current references, equivalently referred to as *droop cross* control. The droop gain k_d amplifies the DC voltage error signal, and yields the i_{sum}^{0dc*} reference or the DC power reference P_{dc}^* if a power loop is included. On the other hand, the total energy PI yields either the i_s^{q*} reference or the active power reference P_{ac}^* if a power loop is included. Both approaches are depicted in Fig. 7.4 and 7.5.

These different options will be evaluated in the base case study section, highlighting the potential stabilities that some structures may cause.
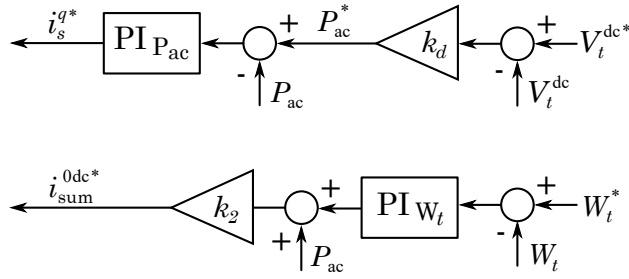
Fig. 7.2: Classic control approach with an additional AC power loop
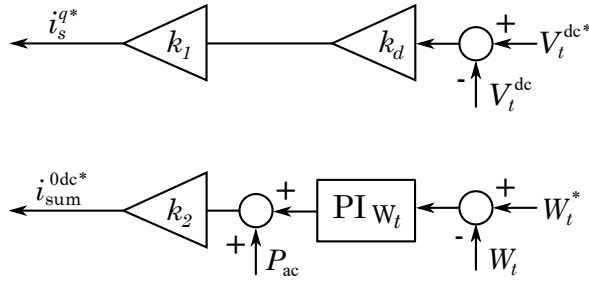
Fig. 7.3: Classic control approach without power loop
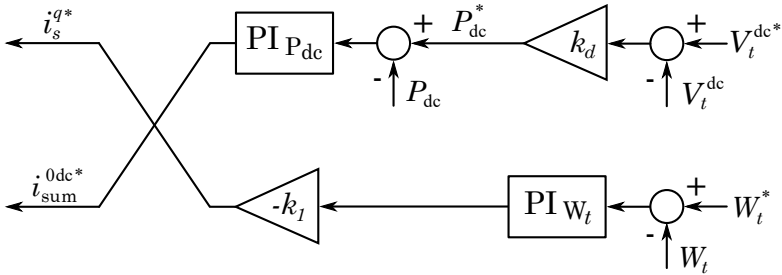
Fig. 7.4: Cross control approach with an additional DC power loop
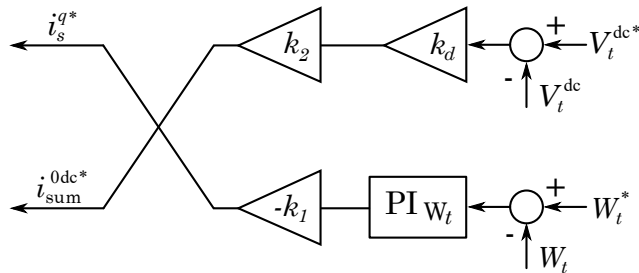
Fig. 7.5: Cross control approach without power loop

7.4 Case study

The analysis and methodology presented in this chapter will be based in the four terminal MT-HVDC grid case study shown in Fig. 7.6, containing droop controlled converters (DCC) 1 and 2, and grid-forming converters (GFC) 3 and 4. However, both the analysis and methodology can be extrapolated to the generic MT-HVDC grid shown in Fig. 7.1. Note that the GFCs are representative of the offshore wind farm case (generation injected into the MT-HVDC grid) as well as feeding loads (e.g. isolated system, island with very weak generation or no generation at all, etc.). As mentioned before, this case study is characterised by its asymmetry, meaning that the rating of the different MMCs and the length of the cables are different. Therefore, the control parameters have to be carefully tuned to ensure its correct operation, specially under severe transient events.
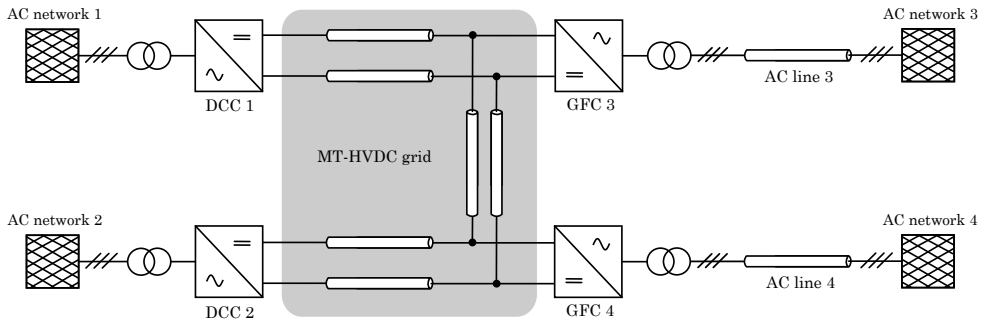
Fig. 7.6: Four terminal MT-HVDC grid with DC voltage droop controlled terminals and AC grid-forming terminals

7.4.1 Scenario configuration

The parameters of all the MMCs can be found in Table 3.1, whereas Table 7.1 shows the rating and the control mode of each MMC. The GFCs are controlled using the decoupled control structure. The values in per-unit from Table 3.1 use the corresponding rated power of each converter (Table 7.1). MMC 1 and 4 are twice the power of MMC 2 and 3, which affects the droop gains calculation. The transient disturbances occurring at AC networks 3 and 4 have to be shared accordingly (both transiently and in steady-state) to avoid the saturation of the MMC with lower power (MMC 2).

The length of the MT-HVDC grid and the parameters corresponding to the AC lines 3 and 4 are shown in Table 7.2. The HVDC cable model consists

Table 7.1: Rating and mode of each MMC

MMC	Mode	Rated power
1	DC voltage droop	1000 MW
2	DC voltage droop	500 MW
3	AC grid-forming	500 MW
4	AC grid-forming	1000 MW

of 3 branches and 1 section, and the parameters can be found in Table 3.2 (Chapter 3). Note that the lengths of the different links are also different, increasing the asymmetry of the system.

Table 7.2: DC and AC lines parameters

Parameter	Symbol	Value	Units
DC line 1-3 length	d_{13}	250	km
DC line 2-4 length	d_{24}	150	km
DC line 3-4 length	d_{34}	100	km
AC line 3 length	d_3	25	km
AC line 4 length	d_3	10	km
AC cable resistance	r_c	0.032	Ω/km
AC cable inductance	l_c	0.4	mH/km
AC cable capacitance	c_c	0.17	μF/km

The droop gains are initially approximated by setting a 10% DC voltage deviation in steady-state for 1 p.u. of power as

$$k_d = \frac{\Delta P}{\Delta V_t^{\mathrm{dc}}} = \frac{1 \text{ p.u.}}{0.1 \text{ p.u.}} = 10 \text{ p.u.} \tag{7.1}$$

The initial tuning for the other controllers is based on the different techniques already mentioned in previous chapters, that will be summarised next. The inner current loops of the MMCs are tuned for a first-order response with time constant 1 ms using IMC (3.2)-(3.3). The PLLs are tuned to track the grid angle within approximately 25 ms (3.4). The energy controller parameters are designed to obtain a second order response (6.15) (Chapter 6), and a slower response is set for the horizontal and vertical balancing energy controllers (note that this tuning is not particularly relevant, as unbalanced faulty scenarios are not considered). Finally, the AC voltage controller parameters are set empirically to a stable value, and frequency droop is not implemented,

as there is only one grid-forming unit in each AC subsystem. The relevant values of the different controllers are shown in Table 7.3. The following scaling factors are used (see Figs. 7.2-7.5):

$$k_1 = \frac{\sqrt{2}}{\sqrt{3}U_N} \ , \ k_2 = \frac{1}{3V_N^{\mathrm{dc}}} \tag{7.2}$$

Table 7.3: Control parameters related to the AC side

Parameter	Symbol	Value	Units
DC voltage droop gain MMC 1	$k_{d,1}$	-15625	W/V
DC voltage droop gain MMC 2	$k_{d,2}$	-7812.5	W/V
Current controls time constant	τ_{cc}	1	ms
PLLs time constant	τ_{pll}	25	ms
Total energy MMC 1-4, proportional	k_{p-w}	126	W/J
Total energy MMC 1-4, integral	k_{i-w}	3948	W/(Js)
AC voltage MMC 3, proportional	$k_{p-u,3}$	0.025	A/V
AC voltage MMC 3, integral	$k_{i-u,3}$	0.500	A/(Vs)
AC voltage MMC 4, proportional	$k_{p-u,4}$	0.020	A/V
AC voltage MMC 4, integral	$k_{i-u,4}$	0.400	A/(Vs)

7.4.2 Linear model

The overall linear model of the 4-terminal system (Fig. 7.7) is built based on the different subsystems presented in previous chapters. Using the droop cross control without power loop, and the decoupled energy control for the total energy in MMCs 3 and 4, the overall system contains 75 states and 20 inputs (AC networks 1 and 2 voltages, controllers references and P and Q references for PQ nodes 3 and 4). The inputs are kept to 0 except for the active power references of PQ nodes 3 and 4, which are the disturbances of the system. Note that the AC grid equations (2.42)-(2.43) are embedded in the MMC DCC blocks, but they do not imply extra states as the Thévenin RL branch is added in series with the MMC AC filter (2.31)-(2.32). The overall linear model is validated against the complete non-linear model (Figs. 7.8-7.9). The operating point is 0.9 p.u. and a step of 1% of the power references of PQ nodes 3 and 4 is performed at $t = 1$ s. Relevant magnitudes of the four MMCs are presented, all of them showing a perfect match with the complete non-linear model.
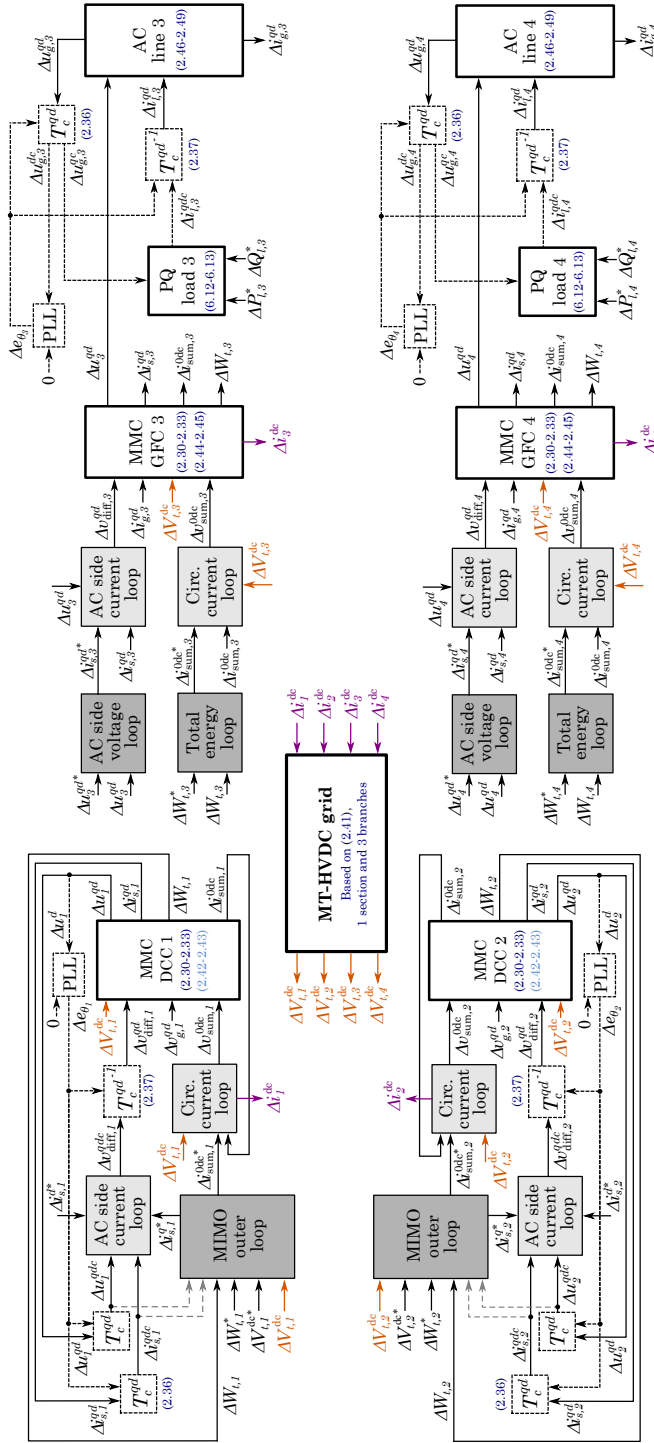
Fig. 7.7: Overall linear model of the 4-terminal HVDC grid
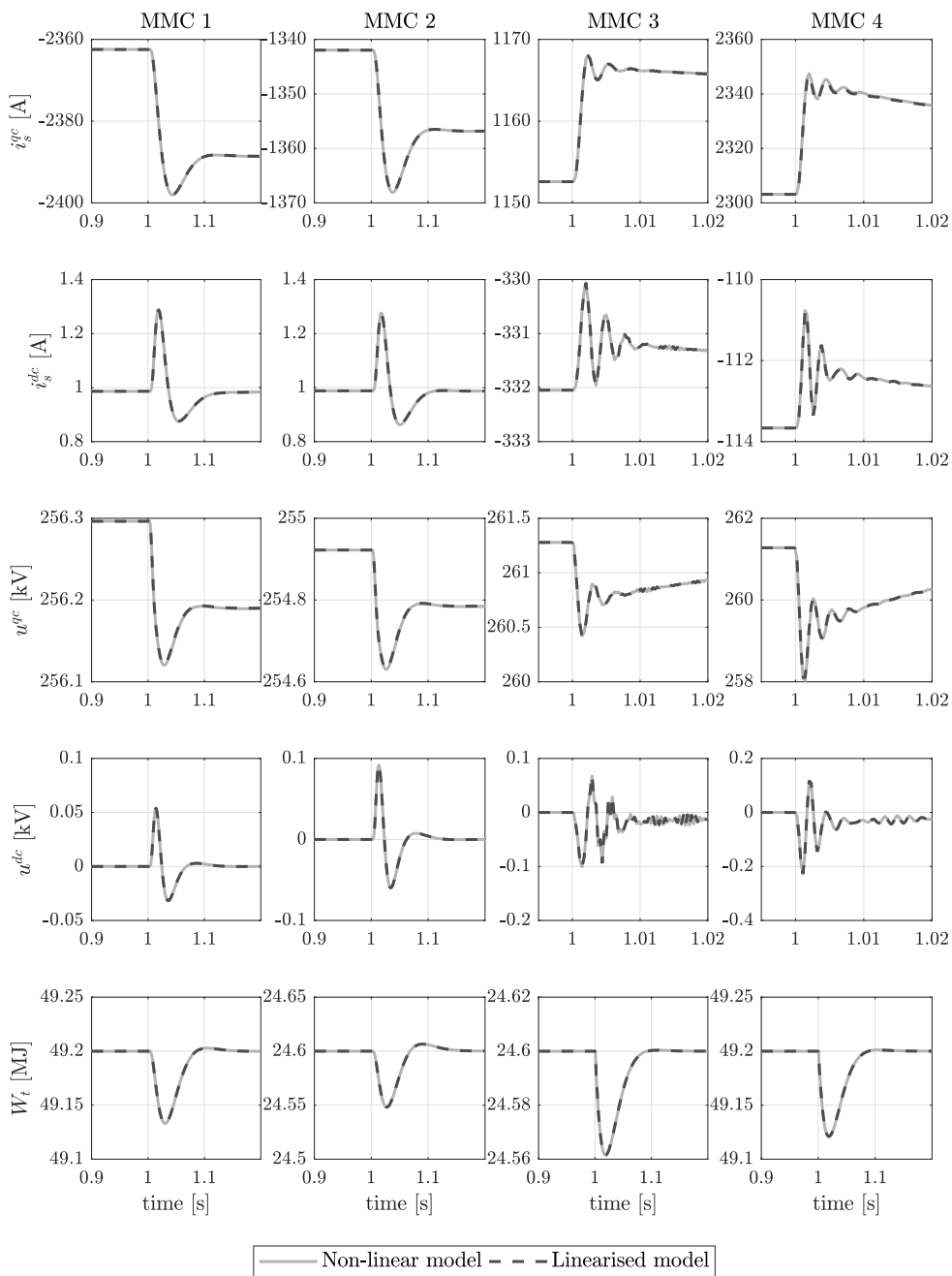
Fig. 7.8: Linear model validation of the 4-terminal HVDC grid linear model – MMC 1 and 2
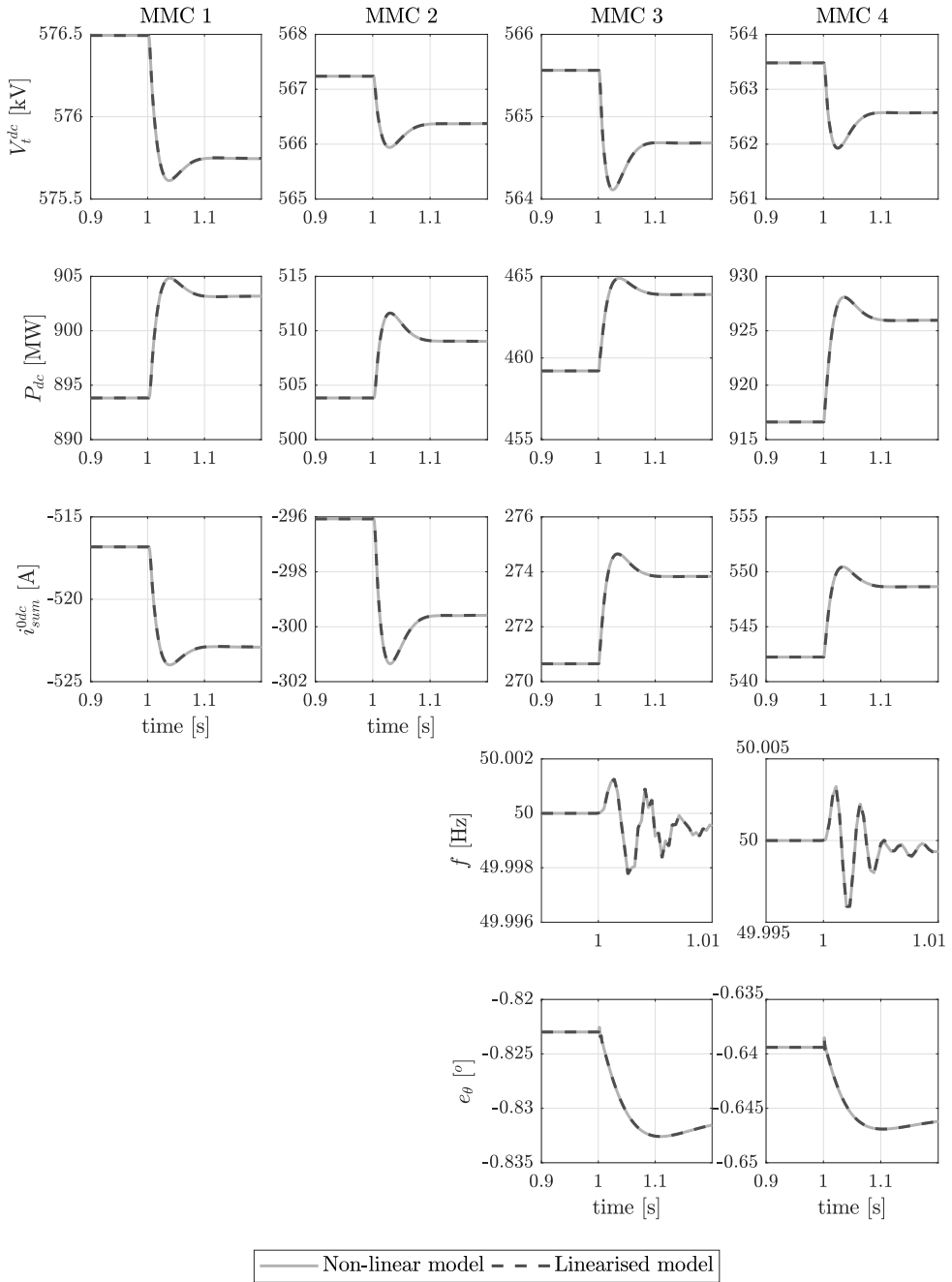
Fig. 7.9: Linear model validation of the 4-terminal HVDC grid linear model – MMC 3 and 4

7.4.3 Stability analysis

After presenting the different control alternatives, a stability analysis is carried out to identify potential instabilities related to the control structures and their parameters. This will be carried out using eigenvalue plots.

Effect of the operating point

The first aspect that needs to be addressed is the identification of the worst operating point in terms of stability. Therefore, the four control structures are investigated in this regard (Figs. 7.10-7.13).

The maximum operating point is defined by the maximum power exchange allowed in the AC networks 3 and 4. When AC networks 3 and 4 inject power (generation), they are allowed to inject up to -1 p.u. (using the respective nominal power of GFCs 3 and 4, Fig. 7.6), as the losses throughout the system will make that AC networks 1 and 2 receive slightly less power and the converters will not saturate. On the other hand, when AC networks 3 and 4 are consuming power (load), this power will be supplied by AC networks 1 and 2. This makes the load case more restrictive, and AC networks 3 and 4 are allowed to have a power demand of up to 0.9 p.u., in order to avoid saturation in DCCs 1 and 2 (Fig. 7.6), as the power from AC networks 1 and 2 will be slightly higher than the one demanded by AC networks 3 and 4.

With the classic control structure (without additional power loop), the system is very close to instability at operating point -0.2 p.u. (Fig. 7.10). If the operating point is further increased, the system becomes unstable for the range of approximately -0.2 p.u. to 0.9 p.u., meaning that this control structure is not recommended.

Adding a power loop to the classic control approach (tuned for an approximate response of 30 ms settling time) highly improves the stability of the system. In this case, the system is able to operate in the whole range (from -1 p.u. to 0.9 p.u.) (Fig. 7.11). However, the system is close to instability at the worst case scenario (0.9 p.u.), which might be dependent on the tuning of this additional power loop (and other controllers). This will be further investigated in the next section, but at first sight it can be stated that this control structure might be a useful alternative.

Regarding the cross control structure, it can be seen that the operating point neither affects the movement of poles significantly nor brings any of them anywhere close to the unstable region (Fig. 7.12). This makes the cross control alternative pretty interesting in the sense that it makes the system minimally sensitive to the operating point.
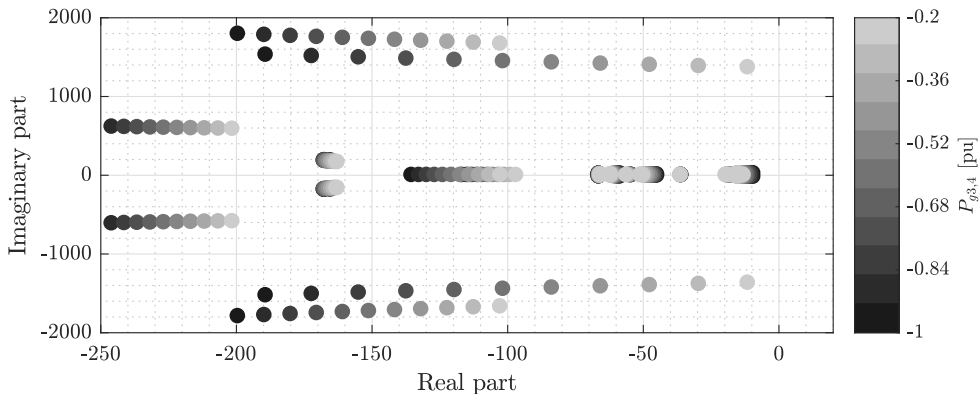
Fig. 7.10: Eigenvalues of the 4-terminal system using droop classic control (without additional power loop) – Operating point sweep
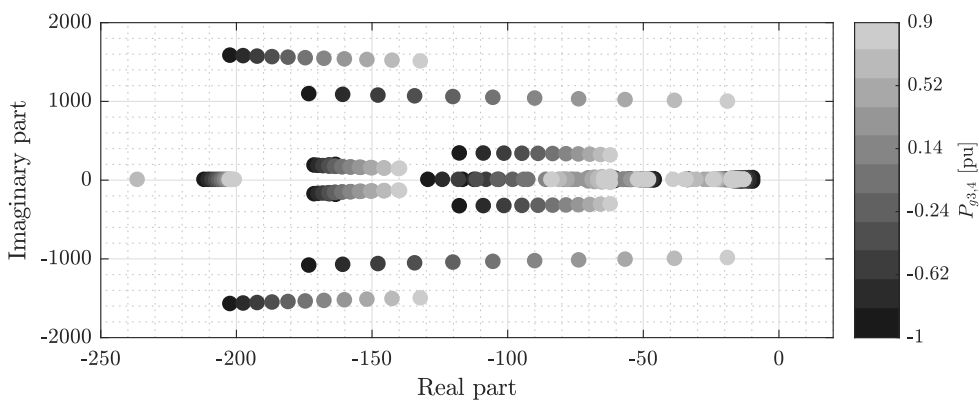
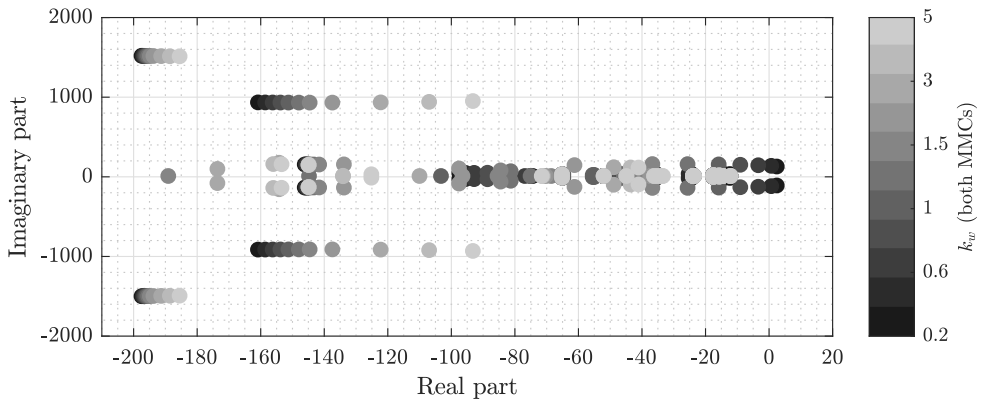Fig. 7.11: Eigenvalues of the 4-terminal system using droop classic + power loop control – Operating point sweep
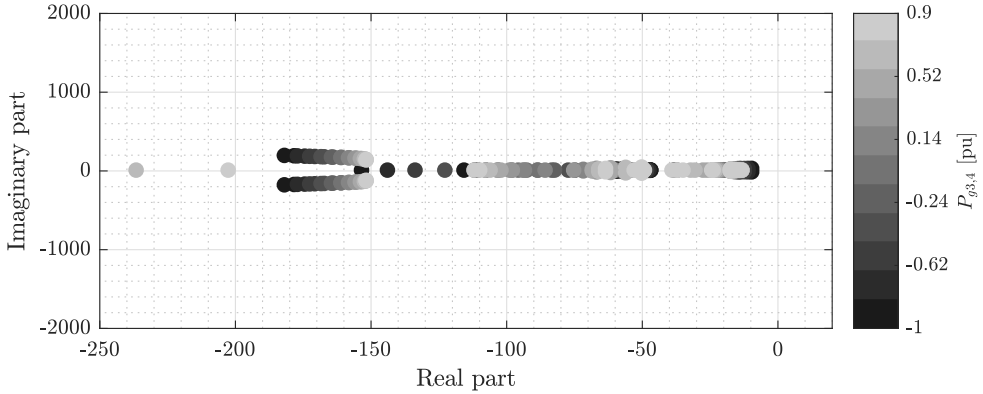
Fig. 7.12: Eigenvalues of the 4-terminal system using droop cross control –
Operating point sweep

Adding a power loop to the cross control approach (tuned for an approx-
imate response of 30 ms settling time) yields the results shown in Fig. 7.13.
It slightly changes the distribution of poles, with no significant difference
compared to the alternative without a power loop. The effect of the power
loop response will be evaluated also in the next section. So far, it can be
concluded that the less stable operating point is 0.9 p.u. of power with the
AC networks 3 and 4 acting as loads. Also, the aforementioned alternatives,
with the exception of the droop classic control without power loop, appear
to be useful approaches for the multi-terminal droop control system.
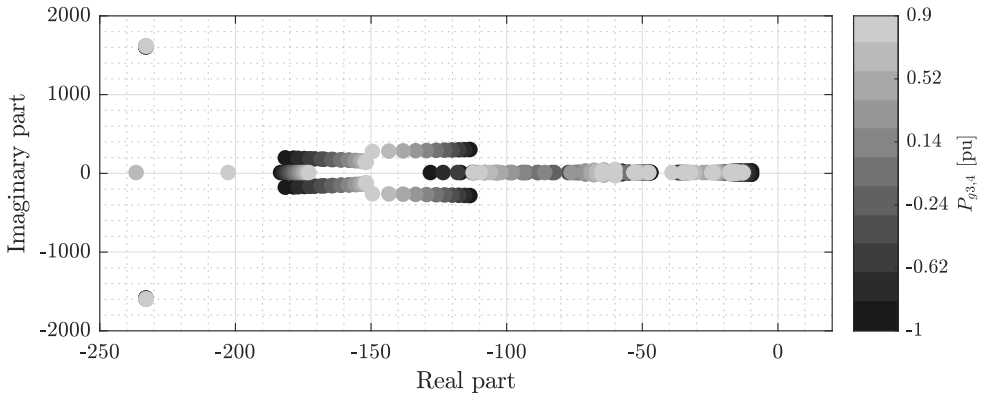
Fig. 7.13: Eigenvalues of the 4-terminal system using droop cross + power
loop control – Operating point sweep

Effect of the additional power loop

The effect of the power loop is explored next. The operating point is set to the worst case scenario (0.9 p.u. in AC networks 3 and 4). A parametric sweep of the settling time of the PI controller (using an independent model of a grid-following MMC controlling the P, and approximately designing a first-order response of the power using the Robust control toolbox from Matlab) of each MMC individually using the classic control is shown in Figs. 7.14a-7.14b. It is shown that a faster power loop brings the system close to the unstable region (in this case, at around 25 ms). The effect of MMC 1 is more evident, moving this pair of poles to the unstable region. On the other hand, a slower power loop moves these poles away from the unstable region. However, there is another set of poles that present opposite characteristic: the slower the power loop, the close they get to the unstable region. This is more obvious when both power loops are changed simultaneously in Fig. 7.14c. In fact, in the present example the system gets unstable at around 300 ms of settling time.

Looking at the cross control, the same parametric sweep is shown in Figs. 7.15a-7.15c. Also, the eigenvalues location of the cross control without power loop is depicted in red. In this case, the individual parametric sweep of MMC 1 and 2 causes a movement of two pairs of poles but the system remains stable without any of the poles approaching the unstable region. However, when both PI controllers are tuned simultaneously in both MMC 1 and 2, the system becomes unstable when the power loops are tuned for a settling time of around 150-200 ms or higher, similarly to what happened in the droop classic case.

After the analysis, the following can be concluded. On one hand, the droop classic control with an additional power loop has a stable range of settling time values (in this example, between 30 and 300 ms). On the other hand, the droop cross control with an additional power loop only presents unstable behaviour when the settling time is sufficiently high (in this example, at around 150-200 ms), with no limitation for faster power loops. It can be concluded that the droop cross control without power loop arises as the most attractive solution, specially for its simplicity in terms of tunable parameters (no additional power loop is required), together with its high stability characteristic.

(a) MMC 1

(b) MMC 2

(c) MMCs 1 and 2
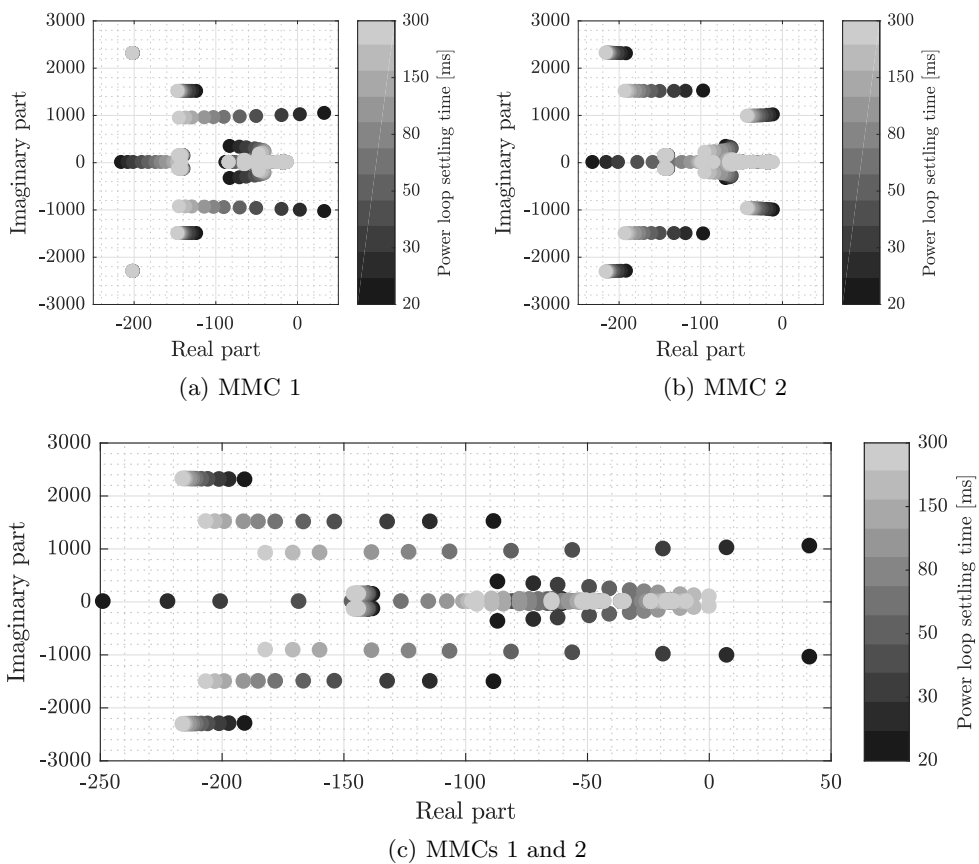
Fig. 7.14: Eigenvalues of the 4-terminal system using droop classic + power loop control – AC power loop settling time sweep

(a) MMC 1

(b) MMC 2

(c) MMCs 1 and 2
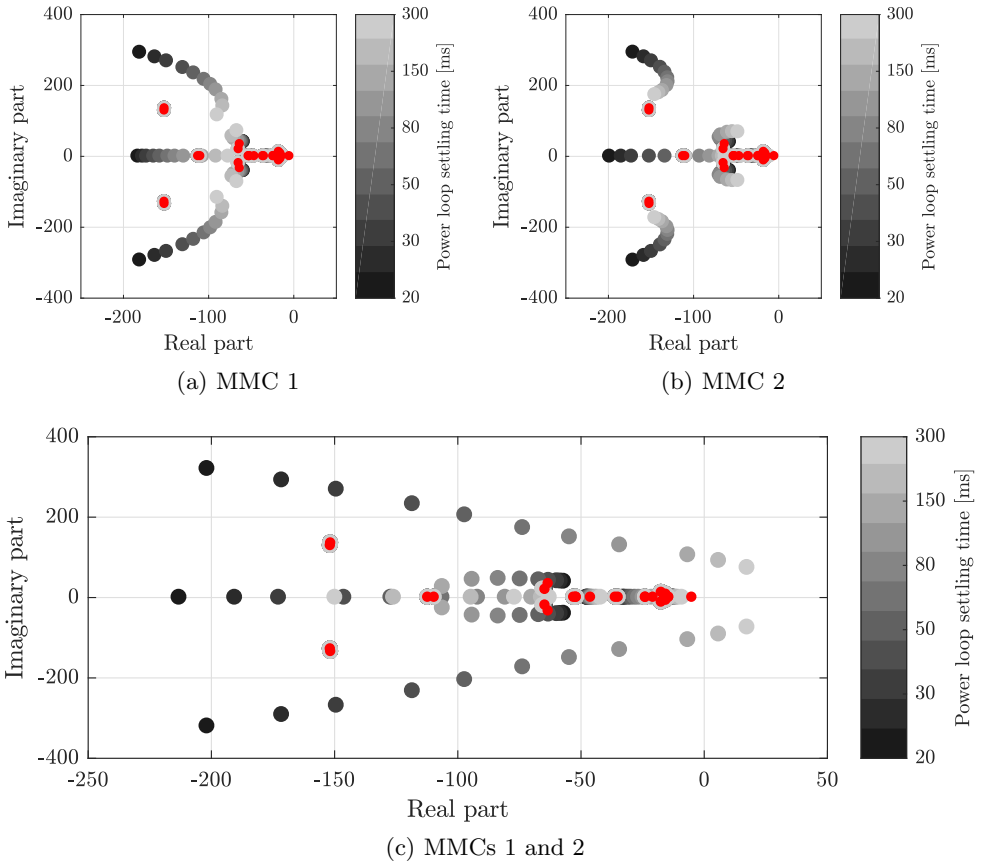
Fig. 7.15: Eigenvalues of the 4-terminal system using droop cross + power loop control – DC power loop settling time sweep (without power loop in red)

Effect of the droop constants

The droop classic with additional power loop and the droop cross structures are selected to evaluate the effect of the DC voltage droop gains. The initial droop parameters (Table 7.3) are multiplied by a gain k_g. The operating point is set to the worst case scenario (0.9 p.u. in AC networks 3 and 4), and the settling time of the droop classic power loop is set to 125 ms, which is a reasonable value within the stable range identified in the previous section. The results show an opposite instability mechanism: with the classic structure, the system becomes unstable when the gains are increased by a factor of approximately 4 (and higher), whereas in the cross structure case the system becomes unstable when the gain is approximately reduced by a factor of 0.12 (or lower) (Figs. 7.16-7.17). This makes the cross structure a more robust approach with respect to the droop gains.
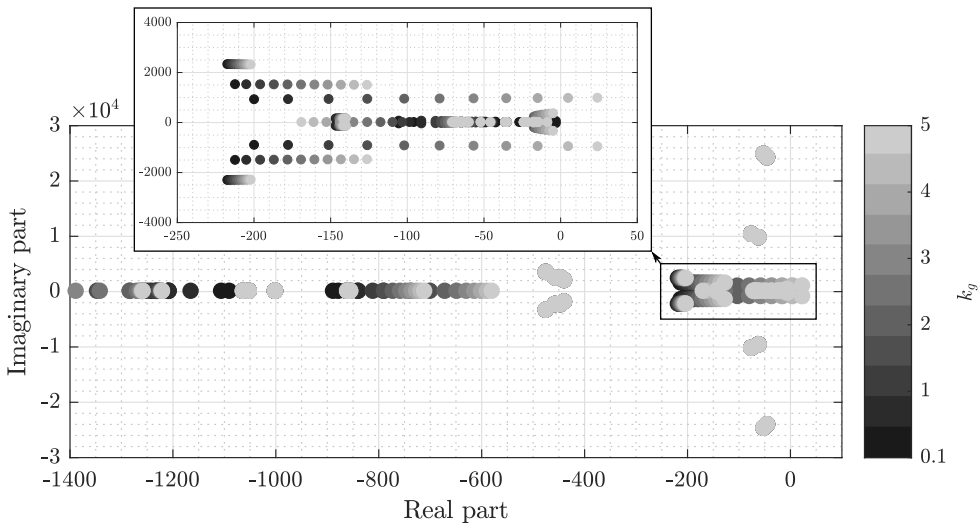
Fig. 7.16: Eigenvalues of the 4-terminal system using droop classic + power loop control – MMCs 1 and 2 droop gains sweep

Effect of the total energy loop

In this last section, the effect of the energy controller is investigated for both the droop classic with additional power loop and the cross structures. A gain k_w is included in both the proportional and the integral constants, in both MMCs at the same time. As in the previous cases, the operating point is set to 0.9 p.u. and the settling time of the droop classic power loop is set to 125
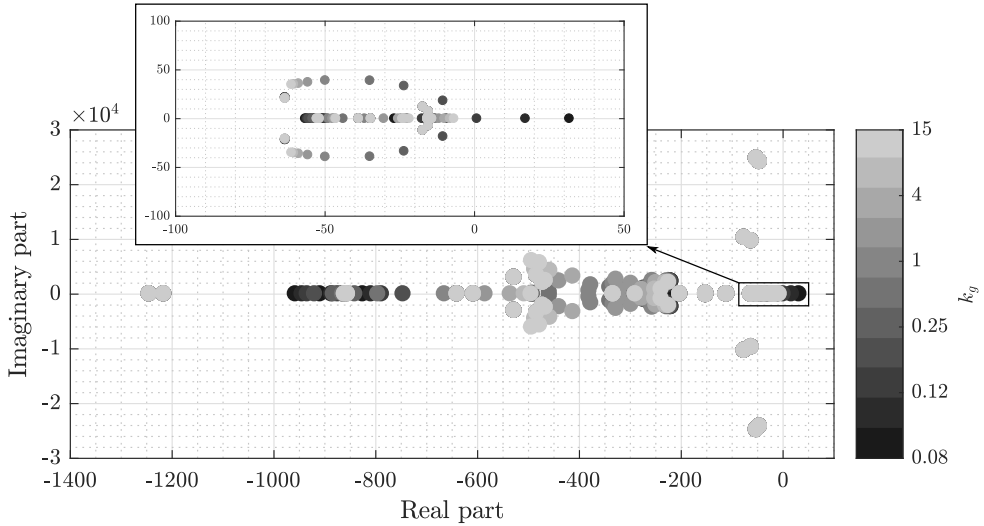
Fig. 7.17: Eigenvalues of the 4-terminal system using droop cross control – MMCs 1 and 2 droop gains sweep

ms. On one hand, when the droop classic with power loop is used, the system becomes unstable when the gain is reduced to approximately 0.4 (Fig. 7.18). On the other hand, the system with the droop cross control becomes unstable when the gain is increased to approximately 4.5 (Fig. 7.19). Therefore, the tuning of the energy PI has to be chosen carefully taking into account which of the two control structures is implemented.

Fig. 7.18: Eigenvalues of the 4-terminal system using droop classic + power loop control – MMCs 1 and 2 energy PI gains sweep

179
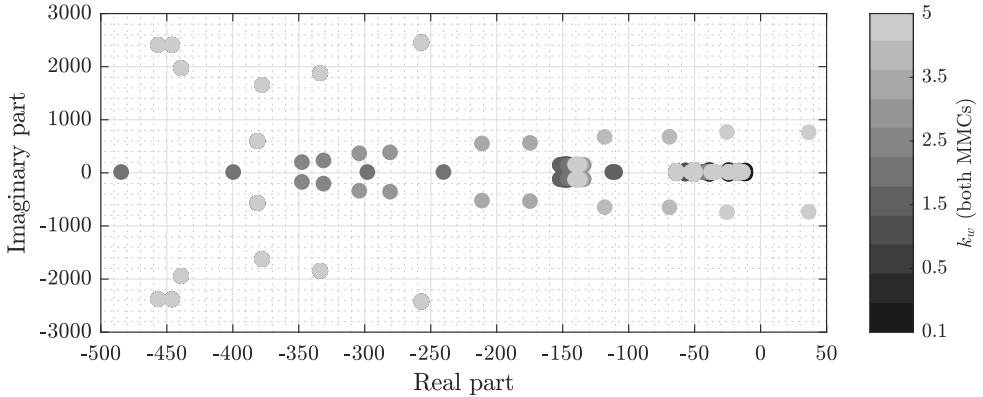
Fig. 7.19: Eigenvalues of the 4-terminal system using droop cross control –
MMCs 1 and 2 energy PI gains sweep

7.4.4 Optimal control design

After the stability analysis presented in the previous section, a joint tuning of
the different controllers of the DCCs (MMCs 1 and 2) is addressed. Based on
the conclusions obtained from the stability analysis, the selected structure is
the droop cross control, due to its stability characteristics and its simplicity,
as it only contains a total of 6 tunable parameters: the droop gains $(k_{d,1}, k_{d,2})$
and the energy PI controllers parameters $(k_{p-w,1}, k_{p-w,2}, k_{i-w,1}, k_{i-w,2})$ of
both MMCs.

What makes this problem challenging is the fact that steady-state require-
ments due to the (proportional) droop control are mixed with transient re-
quirements, specially with such an asymmetric system, where MMC 1 is rated
to twice the power of MMC 2. Although the steady-state operating point will
be adjusted by the TSO, for instance through secondary control, it is desir-
able that the power is approximately shared through the droop control gains,
to avoid large differences after disturbances or power changes.

Using the linear model of the overall system, gain constraints in the fre-
quency domain are set for different transfer functions, equivalently to what
was done in previous chapters using Bode diagrams for SISO systems or sin-
gular values in the case of multi-variable systems. Then, an optimisation
based on $\mathcal{H}_\infty$ (see Chapters 5 and 6) will determine the control parameters.
Note that the system (Fig. 7.6) has to remain stable and within the limits
during different transient phenomena. In this case, the following situations
are considered:

- Avoid overshoots and undershoots in currents, voltages and energy both

in inverter and rectifier modes.

- Stay in operation after a sudden disconnection of the AC lines (3 or 4).

Based on this criteria, the worst case scenarios are defined. Considering the whole operating range (generation and consumption) from AC networks 3 and 4 (disturbances), the following can be stated. On one hand, in the case of generation (offshore wind farms) the disturbances will not be anywhere close to being step changes, as the dynamics of the wind farms are much slower than the dynamics of the MMCs. A disconnection of the wind farm could happen, although it is a very unlikely event. On the other hand, in the case of loads, sudden step changes are likely to happen. However, one cannot consider changes of a large amount of power, which would be rather unrealistic. Instead, positive step changes of 0.2 p.u. (sudden load connection) are considered to be sufficiently restrictive. Also, based on the stability analysis, which showed that the worst operating point is when the DCCs are acting as rectifiers at full power (0.9 p.u. in AC networks 3 and 4), the critical operating point to consider for the application of a 0.2 p.u. step increase is 0.7 p.u., which would bring the system operating point to 0.9 p.u. of power. Furthermore, a sudden disconnection of AC line 4, which is the one with a higher rating, can be considered from that operating point, and the system should remain stable after that disturbance.

The next step is to define the constraints and the disturbances in the linear model, allowing for the tuning of the control parameters afterwards. This problem can be approximated in different ways. One possibility is to consider the largest disturbance (e.g. from 0 to 1 p.u.) with a reasonable time response (e.g. first order response), as it is neither realistic nor feasible to apply it as a step. Then, the constraints are set to the maximum allowed values in absolute terms (i.e. actual voltage and current limits of the converter). Another possibility is to consider a step disturbance (e.g. 0.2 p.u.) and then set the limits of the voltages and the currents proportionally to their maximum allowed values. In this case, it would be a fifth of that value, as the step disturbance has been set as a fifth of the rated power. Bearing in mind the limitations of linear models, the truth is that these methods are still quite useful to obtain an adequate optimal tuning, and it will depend on each case which alternative leads to better results. In order to verify the obtained tunings, the results have to be checked in simulation using the full non-linear model.

In the present case, the first option has resulted to yield adequate results,

as will be seen next. A disturbance of 0.9 p.u.[1] is applied in both AC networks 3 and 4. Then, the constraints are set as follows:

1. Voltage deviation of 12% in DC terminals 3 and 4, as these voltages deviate more than the ones at DC terminals 1 and 2, due to the power flow direction (DCCs in rectifying mode).

2. Total energy deviation of 15% in MMCs 1 and 2.

3. Maximum AC current of 115% in MMCs 1 and 2.

4. Maximum DC current of 115% in MMCs 1 and 2.

5. Maximum DC current difference between MMCs 1 and 2 (in p.u.) of 10% (steady-state constraint).

It is important to remark that these constraints are not exact, as the disturbance is not a small-signal disturbance and the new state after the disturbance is far away from the initial operating point where the linear model is accurate. Moreover, as there are two disturbances in the system, the singular values show the curves for the critical input vector (i.e. the worst combination of inputs that generates the maximum singular values peak). This combination does not have to be necessarily feasible in the real system. For instance, considering that the two input disturbances can be up to 1 p.u., the results of the singular values could correspond, for instance, to the case where one input is 1.3 p.u. and the other one is 0.6 p.u. (i.e. the critical direction). However, it is possible that this combination of inputs is never going to happen in the real system, making the singular values limit tool too restrictive.

The singular values after carrying out the optimisation of the tunable parameters, based on the aforementioned constraints, is shown in Figs. 7.20-7.22. The singular values plots using the initial tuning parameters are also shown as a comparison with the optimal tuning. After several iterations on the constraints, this is the most suitable solution that has been found with the optimiser. It is shown that the optimal tuning plots are pushed down as compared to the initial tuning ones. The steady-state ($\omega = 0$) is below the limit in most cases, whereas the transient slightly exceeds the limit sometimes. It is remarkable that the singular values of MMC 2 (500 MW), which is the most critical converter as it is rated to half the power of MMC 1 (1000 MW), are the ones that are affected the most. Also, the power sharing is improved (Fig. 7.22).

---

[1]First-order response of 100 ms settling time
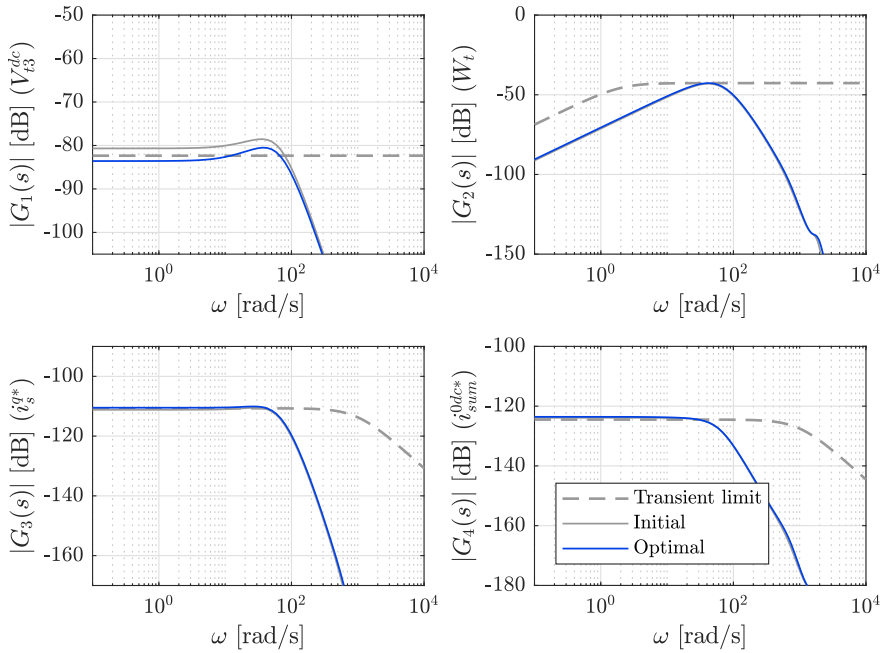
Fig. 7.20: Singular values of the 4-terminal system for the initial and optimal tunings – MMC 1 constraints
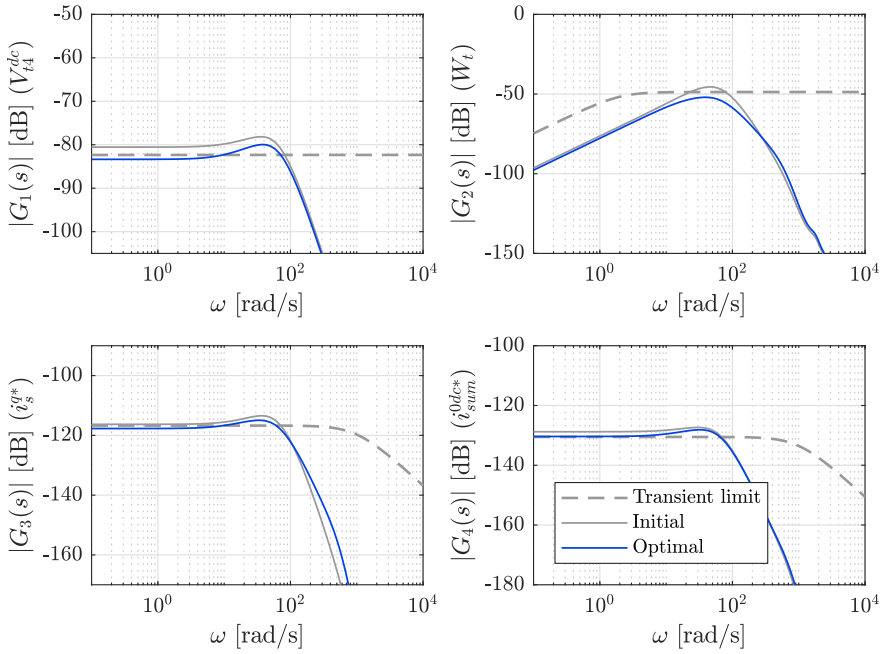
Fig. 7.21: Singular values of the 4-terminal system for the initial and optimal tunings – MMC 2 constraints
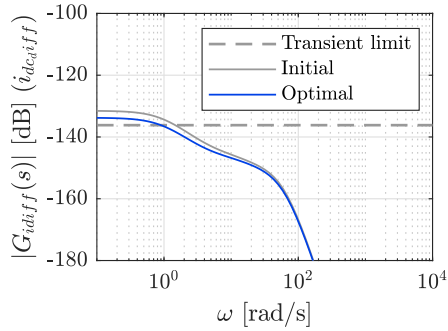
Fig. 7.22: Singular values of the 4-terminal system for the initial and optimal tunings – Power sharing constraint

As the singular values in multi-variable systems might be too restrictive as mentioned before, this can still be an adequate solution to be implemented in the system controllers. The tuning results are shown in Table 7.4. Note that the optimal tuning results in increasing the droop gains, specially the one in MMC 1, which will make this converter respond faster to the disturbances, thus preventing MMC 2 to saturate. Also, the proportional constant of the energy controller of MMC 2 is increased.

Table 7.4: Initial and optimal tuning parameters (MMC 1 and 2)

Parameter	Symbol	Initial	Optimal	Ratio	Units
DC volt. droop (1)	$k_{d,1}$	-15625	-24477	1.567	W/V
DC volt. droop (2)	$k_{d,2}$	-7812.5	-9070	1.161	W/V
Total energy P (1)	$k_{p-w,1}$	126	126	1	W/J
Total energy I (2)	$k_{i-w,1}$	3948	3948	1	W/(Js)
Total energy P (1)	$k_{p-w,2}$	126	259	2.056	W/J
Total energy I (2)	$k_{i-w,2}$	3948	3948	1	W/(Js)

Due to the limitations of the linear model and the singular values constraints mentioned before, the results have to be verified using the complete non-linear model in time-domain simulations in the different worst-case scenarios. The simulation is defined as follows. At $t = 0.05$ s, both AC networks 3 and 4 ramp up their respective powers to 0.7 p.u. (load). At $t = 1$ s, a sudden (step) increase of load is performed in both networks simultaneously, bringing the system to 0.9 p.u. (maximum power). Then, a sudden disconnection of AC line 4 (approximately 1000 MW of power flowing) is performed at $t = 1.6$ s. Based on this scenario, two different options are tested.

With secondary control

In the first case, a secondary control sends new set-points $V_{t,i}^{dc}$ to MMC 1 and 2 in a few hundreds of milliseconds after each change (see Table 7.5). The set-points calculation is based on the power-flow solution (7.3)-(7.6) that constrains the maximum voltage of the MT-HVDC grid to 1 p.u. while keeping the power sharing ratio 2:1. As these set-points depend on the droop gains $(k_{d,i})$, they need to be calculated for a given tuning. Recalling the generic system from Fig. 7.6, the system of equations is composed by $n + m$ node equations, n droop equations, m power balance equations, $n-1$ power sharing equations and 1 maximum voltage requirement equation ($3n + 2m$ equations in total). The unknowns are n voltages references ($V_{t,i}^{dc*}$), $n + m$ voltages

$(V_{t,i}^{\mathrm{dc}})$, and $n + m$ currents (I_i^{dc}).

$$
\begin{bmatrix} I_1^{\mathrm{dc}} \\ I_2^{\mathrm{dc}} \\ I_3^{\mathrm{dc}} \\ I_4^{\mathrm{dc}} \end{bmatrix} = \begin{bmatrix} \frac{1}{R_{13}} & 0 & \frac{-1}{R_{13}} & 0 \\ 0 & \frac{1}{R_{24}} & 0 & \frac{-1}{R_{24}} \\ \frac{1}{R_{13}} & 0 & \frac{1}{R_{13}} + \frac{1}{R_{34}} & \frac{-1}{R_{34}} \\ 0 & \frac{-1}{R_{24}} & \frac{-1}{R_{34}} & \frac{1}{R_{24}} + \frac{1}{R_{34}} \end{bmatrix} \begin{bmatrix} V_{t,1}^{\mathrm{dc}} \\ V_{t,2}^{\mathrm{dc}} \\ V_{t,3}^{\mathrm{dc}} \\ V_{t,4}^{\mathrm{dc}} \end{bmatrix} \tag{7.3}
$$

$$
V_{t,1}^{\mathrm{dc}} I_1^{\mathrm{dc}} = k_{d,1}(V_{t,1}^{\mathrm{dc*}} - V_{t,1}^{\mathrm{dc}}); V_{t,2}^{\mathrm{dc}} I_2^{\mathrm{dc}} = k_{d,2}(V_{t,2}^{\mathrm{dc*}} - V_{t,2}^{\mathrm{dc}}) \tag{7.4}
$$

$$
P_3^{\mathrm{dc}} = V_{t,3}^{\mathrm{dc}} I_3^{\mathrm{dc}}; \quad P_4^{\mathrm{dc}} = V_{t,4}^{\mathrm{dc}} I_4^{\mathrm{dc}} \tag{7.5}
$$

$$
V_{t,1}^{\mathrm{dc}} I_1^{\mathrm{dc}} = 2V_{t,2}^{\mathrm{dc}} I_2^{\mathrm{dc}}; \quad \max(V_{t,i}^{\mathrm{dc}}) = 1 \tag{7.6}
$$

Table 7.5: DC voltage references for the initial and optimal tuning

Time	$v_{t,1}^{\mathrm{dc*}}$ (ini.)	$v_{t,2}^{\mathrm{dc*}}$ (ini.)	$v_{t,1}^{\mathrm{dc*}}$ (opt.)	$v_{t,2}^{\mathrm{dc*}}$ (opt.)
0 s	1.0000 p.u.	1.0000 p.u.	1.0000 p.u.	1.0000 p.u.
0.7 s	1.0724 p.u.	1.0613 p.u.	1.0462 p.u.	1.0512 p.u.
1.3 s	1.0926 p.u.	1.0783 p.u.	1.0591 p.u.	1.0655 p.u.
1.9 s	1.0308 p.u.	1.0282 p.u.	1.0197 p.u.	1.0239 p.u.

The time-domain simulations of the first case are shown in Figs. 7.23-7.25. It can be seen that MMC 1 has a lower DC voltage deviation, and that it takes a slightly larger portion of power. The difference is much more noticeable in MMC 2, which takes a lower amount of power, therefore avoiding saturation in the AC current. It can be seen how the DC voltage reference set-points adjust the power sharing after each disturbance. However, it is remarkable that the optimal tuning already achieves a reasonable power sharing (Fig. 7.25), and the adjustment of the references is small in that case. Also, the energy deviation of MMC 2 is lower than using the initial tuning. Moreover, the system responds well to the disconnection of AC line 4, remaining stable.

Without secondary control

In the second case, the system is tested without a secondary control, i.e. the DC voltage references are set to a constant value of 1 p.u. during the whole simulation, which could represent an eventual loss of communications. The time-domain simulations of the second case are shown in Figs. 7.26-7.28. This case unveils a degraded performance of the system if the initial tuning is
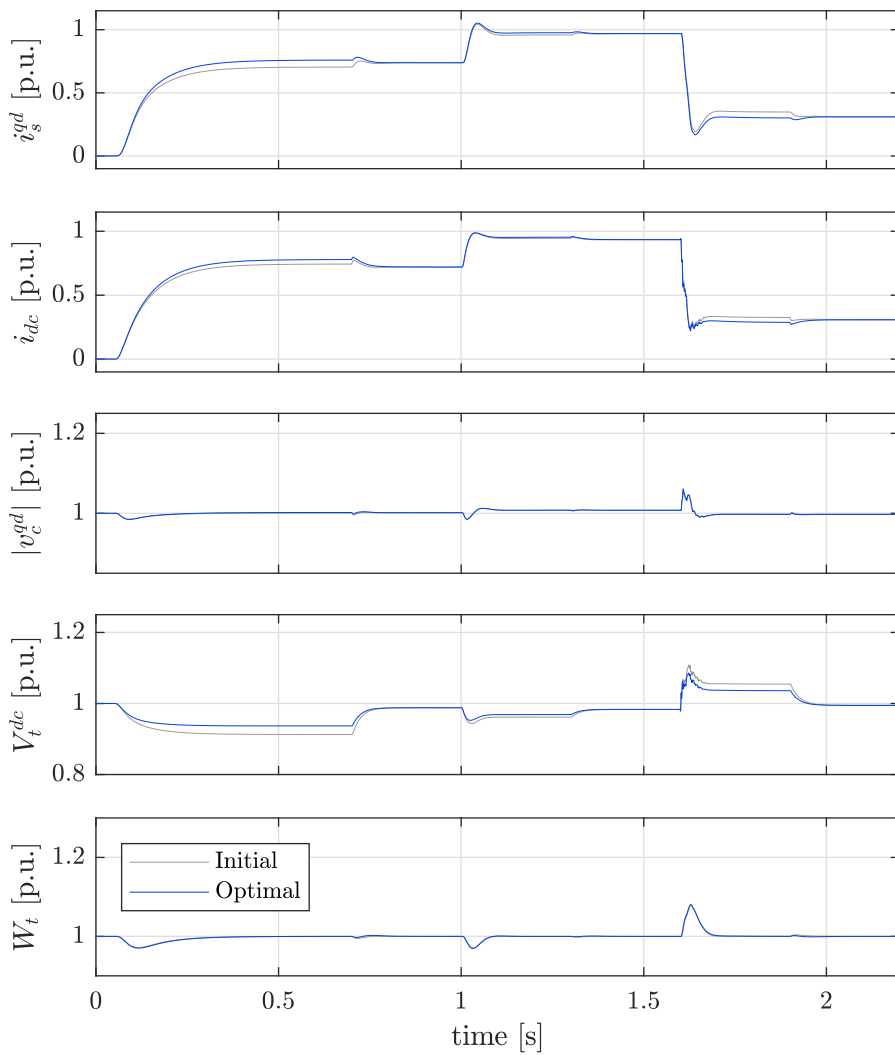
Fig. 7.23: Time-domain simulation of the 4-terminal system for the initial and optimal tunings, with DC voltages references correction – MMC 1 magnitudes (base values of MMC 1, Table 7.1)
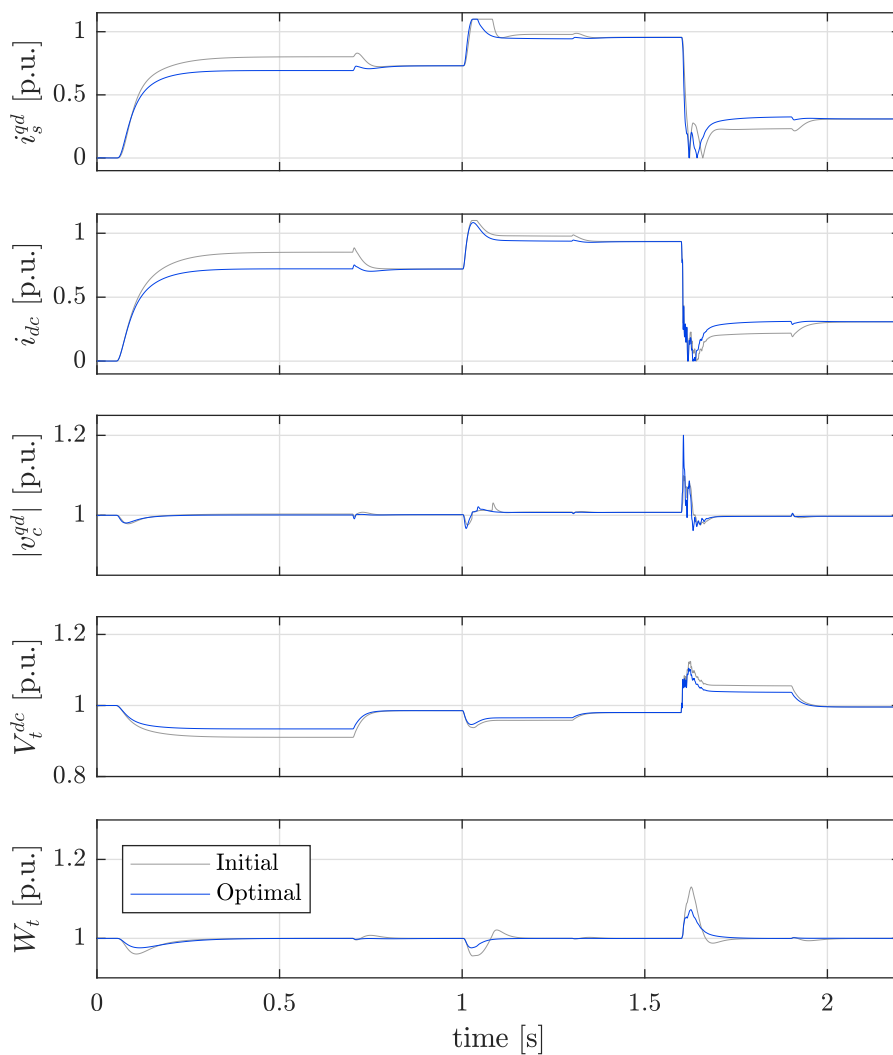
Fig. 7.24: Time-domain simulation of the 4-terminal system for the initial and optimal tunings, with DC voltage references correction – MMC 2 magnitudes (base values of MMC 2, Table 7.1)
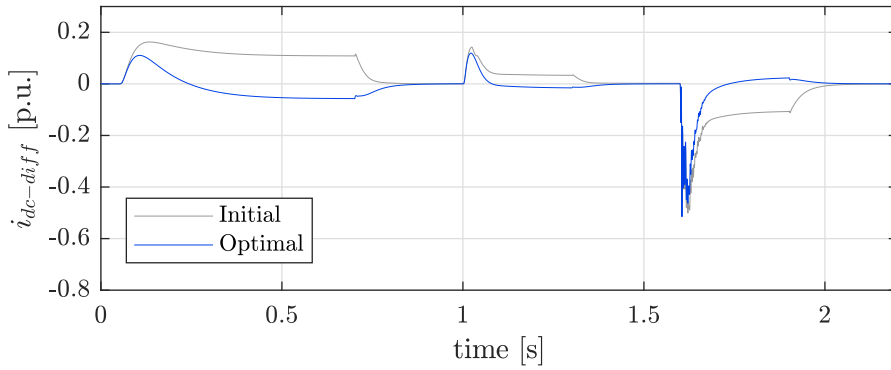
Fig. 7.25: Time-domain simulation of the 4-terminal system for the initial and optimal tunings, with DC voltage references correction – DC current difference

used, because of its poor power sharing features. If this is not corrected by a secondary control as in the first case, when the system is at an operating point with a high degree of load and a disturbance occurs, it will likely bring one or both MMCs to saturation. In this case, the most obvious saturation appears in the DC current in both MMCs. Therefore, in case of an eventual loss of communication, only the optimal tuning guarantees a correct operation of the system.
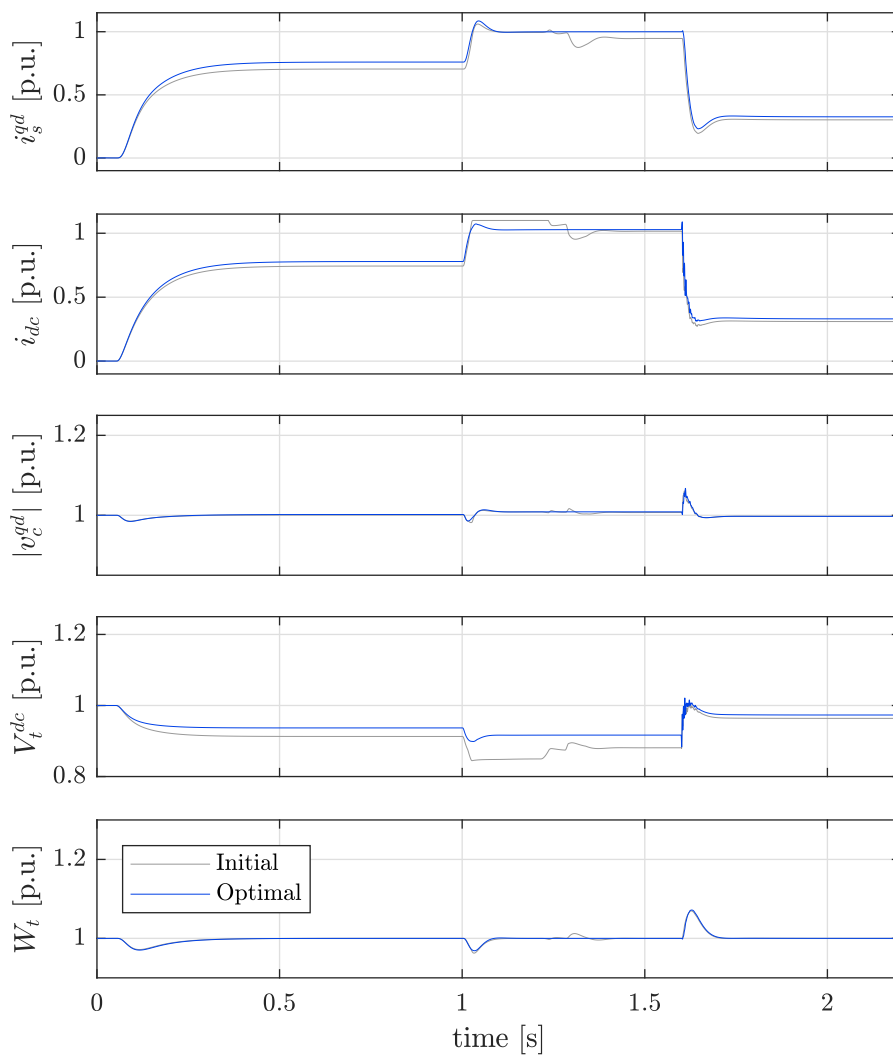
Fig. 7.26: Time-domain simulation of the 4-terminal system for the initial and optimal tunings, with constant DC voltages references – MMC 1 magnitudes (base values of MMC 1, Table 7.1)
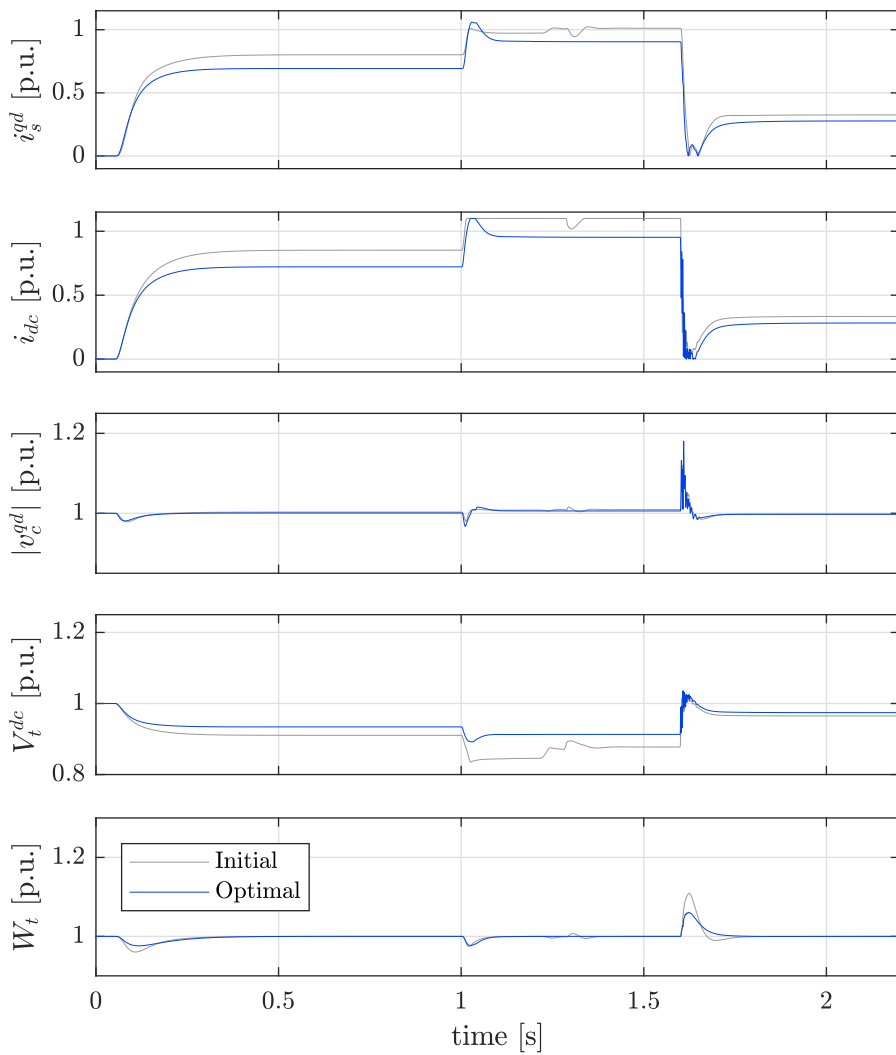
Fig. 7.27: Time-domain simulation of the 4-terminal system for the initial and optimal tunings, with constant DC voltages references – MMC 2 magnitudes (base values of MMC 2, Table 7.1)
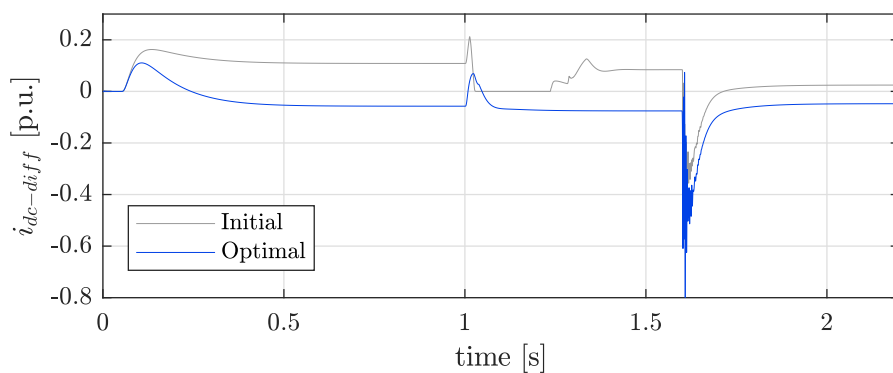
Fig. 7.28: Time-domain simulation of the 4-terminal system for the initial and optimal tunings, with constant DC voltages references – DC current difference

7.5 Conclusion

Due to the potential expansion of HVDC connections in the future power system, the emergence of multi-terminal HVDC grids will gain relevance, and this likely implies multi-terminal grids composed by converters with different power ratings. In this chapter, a control design methodology for a multi-terminal MMC-based HVDC system has been addressed, analysing different control structures. This methodology is valid for a generic multi-terminal HVDC system with several nodes participating in the DC voltage control through a droop control strategy and using an energy-based control approach. Furthermore, aside from the voltage droop controlled converters, the terminals that exchange power have been modelled as detailed grid-forming MMCs as in Chapter 6, and the whole range of operating points (not only generation as in the offshore wind farm case, but also consumption as in an islanded system) has been considered.

It was shown that using the classic control structure the stability of the system can be compromised. Also, the stability was found to be highly dependent on the operating point, being the rectifier mode at rated power the worst case. The options of (i) adding a cascaded power loop with a relatively slow time constant in the classic structure, or (ii) using a cross structure without any additional power loop, have shown to highly improve the system stability. The wider range of stable droop gains and the control structure simplicity make the latter a more attractive option. Furthermore, an automatic tuning procedure based on $\mathcal{H}_\infty$ has been proposed, which yields the droop gains and the total energy controllers parameters that comply with both steady-state and transient requirements under severe power changes. As mentioned before, an asymmetrical case study with converters rated at different powers has been considered. This makes the control system design specially challenging as compared to the case where all the terminals are rated to the same power.

Chapter 8

Conclusions

The integration of power electronics into the power system has increased in the recent years, and it is undeniable that it will keep growing in the near future. In this context, the MMC has been a subject undergoing intense study in the recent years. The present work has mainly focused on the outer control design of the MMC using an energy-based approach, i.e. explicitly controlling the energy balance inside the converter. In this section, the general conclusions, the specific contributions and the main future research lines are presented, as a closure of the doctoral thesis.

8.1 General conclusions

The relatively high complexity of the MMC, as compared to the two-level VSC, poses some control challenges. However, this topology brings extra degrees of freedom that enhance the dynamics and the capabilities of this converter within the power system.

The extra capabilities offered by the MMC can be exploited through the outer control system layer, i.e. the controllers that are on top of the internal currents control. These different controllers are different depending on the application of the converter. The two main applications covered in the present work are the DC voltage control and the AC grid-forming operation modes.

In the case of DC voltage control, four different control structures are investigated and compared, for the case of a master converter in a point-to-point link. It is shown that the classic control used in two-level VSCs can be also applied to the MMC. However, it presents some limitations, specially when the link is not long enough. A cross control structure (swapping the inputs and outputs) is compared to the classic one, and a combination of both is also proposed. Furthermore, an open-loop control is also presented for very short links or back-to-back applications.

Complementarily, a further step is taken on the validation of such a system, setting up an laboratory-scaled experimental platform. The HVDC cable, as

a crucial element of the system, is investigated in terms of how to implement it in a low-voltage platform. The results showed that an improved version of the cascaded π-section can be used not only in linear analysis, but also experimentally, showing a good match between the simulations and the experimental results. However, with such a cable emulator, in order to obtain a higher accuracy it is necessary to increase the cost and the volume of the equipment too much.

Furthermore, a more general multivariable controller is presented. In order to show its full potential, different optimal tuning techniques have been found useful to calculate the parameters of such a controller. Depending on how the different penalties and constraints are set, the desired performance of the system can be obtained, complying with the transient requirements.

In the case of AC grid-forming control, the capabilities of the MMC have been investigated from the point of view of the energy control, using the well-known frequency-droop approach. By slightly changing the structure of the energy control loop, relevant differences have been observed in the AC/DC interactions within the system. Using a decoupled structure allows the MMC to block the AC disturbances, acting as a firewall for the DC side.

Finally, different control structures are also possible in the case of multi-terminal HVDC grids, which strongly affect the stability of the system. A droop cross control without a power loop has demonstrated to yield appropriate results even in asymmetric case scenarios with MMCs of different ratings, exhibiting adequate power-sharing and consistent transient features.

8.2 Contributions

The contributions of this thesis are related to the control of the MMC, in different scenarios and operating modes. More specifically, this thesis has focused on the DC voltage and the internal energy controls using a Compensated Modulation strategy. The major contributions of this thesis are summarised as follows:

- MMCs in DC voltage control mode for point-to-point HVDC links:

  - Analysis and comparison of four different outer control structures (DC voltage, total internal energy) for a DC voltage controlled MMC, highlighting the control challenges of short HVDC links. Proposal of the *weighted* control structure, which combines the *classic* control and the *cross* control, offering more degrees of freedom. Also, proposal of the *constant DC voltage* control structure,

which removes the DC voltage feedback control loop, being suitable for very short links and back-to-back applications, although it requires further analysis to deal with the current limitation (Chapter 3).

– Design and implementation of an HVDC cable emulator, based on the parallel branches model, which accounts for the frequency dependent behaviour of the cable. This cable emulator has been used in the experimental tests of the laboratory-scaled point-to-point HVDC link (Chapter 4).

– Proposal of a generalised MIMO controller (8 degrees of freedom) that generalises the weighted control structure (6 degrees of freedom), and optimal tuning based on the $\mathcal{H}_2$, presenting the details of the methodology and giving insights on the penalties design (Chapter 5).

• MMCs in AC grid forming mode:

– Analysis and qualitative comparison of four different total internal energy control structures, using a frequency droop with vector voltage as AC grid-forming control. Two of the control structures have been proposed, namely *power-filtered* control and *dynamic energy reference* control structures. These structures allow for an intuitive tuning of the energy controller through a single parameter (Chapter 6).

– Demonstration via optimal tuning (based on $\mathcal{H}_\infty$) that the *decoupled* control structure (i.e. using only a PI controller for the energy) is able to achieve the same performance than the two proposed structures. This is also shown in a multiple grid-forming setup simulation (Chapter 6).

• MMCs in DC voltage droop control mode for MT-HVDC grids:

– Stability analysis of different control structures for DC voltage droop controlled MMCs under an energy-based control approach, for the application of multi-terminal HVDC grids (Chapter 7).

– Development of an optimal control design methodology for MMC-based multi-terminal HVDC grids for a generic application, emphasising the case of terminals with different power ratings, which makes the control design more challenging (Chapter 7).

A few additional minor contributions are identified, which are either tools or initial approximations to achieve the major contributions above mentioned:

- Related to the modelling: comprehensive reference guide on the overall control of the MMC using an energy-based approach, and linearisation of all the different subsystems that allow for building an MMC-based system for power electronics based power systems. (Chapter 2).

- Related to the laboratory tests: experimental validation of a laboratory-scaled point-to-point HVDC link, using cross control, and compare it with the corresponding simulated high-voltage system (Chapter 4).

- Related to the MMC operating in DC voltage control: investigation of the performance and controllability limits of the MMC using the classic, cross and weighted control structures, through optimal tuning with high requirements using user-friendly tools offered by commercial software, based on $\mathcal{H}_\infty$ (Chapter 5).

8.3 Future work

The presence of MMCs in the power system is already a reality, and it is currently in a clear growing trend. In the next years, HVDC technology will keep growing, and the complexity of mixed AC/DC power systems will challenge the system stability and reliability. Therefore, further research to improve the state-of-the-art control strategies that ensure robustness and security in bigger and more complex systems with a higher amount of power electronics devices is necessary, and will be continuously developed in the upcoming years.

Focusing on the specific contributions developed in each chapter, the potential future work based on the accomplished achievements of the present thesis is described below:

- Chapter 3:
  - Investigate the effect of the slave MMC control tuning on the master MMC control structure (and the overall system stability), as it has been found that the tuning of the slave MMC energy controller has a relevant impact on the system.
  - Further analyse the use of the constant DC voltage control for back-to-back or very short HVDC connections, as this open-loop

structure might need some additional control features to deal with overcurrents, specially in faulty scenarios.

- Chapter 4:

  - Address a more detailed analysis in terms of how many branches and sections are optimal from the accuracy, the cost and the footprint points of view. Also compare it with the π-section model.

  - Extend the results replacing the DC source for a second MMC prototype operating as a slave, as well as considering different cable lengths and different control structures.

  - Extend the analysis developing a detailed small-signal model of the experimental system in discrete time, in order to provide more solid proofs in terms of the resonance of the cable and a more precise mitigation solution.

- Chapter 5:

  - Based on the $\mathcal{H}_2$-norm section, define an equivalent optimisation problem for the application of the $\mathcal{H}_\infty$-norm in the same conditions (performance indexes, penalties, etc.), allowing for a fair and detailed comparison between both methods. This would allow for drawing more general conclusions on the advantages and downsides of each method.

  - Explore the robustness of such controllers under plant model uncertainty, specially regarding the AC grid and the HVDC cable.

  - Application of the aforementioned methods to other case studies and converter controllers.

- Chapter 6:

  - Explore new forms of grid-forming control that are specific to the MMC topology, for instance using the internal energy to generate the angle or matching the MMC equations to the synchronous generator ones, as already done in the literature for 2-level VSCs.

  - Investigate the grid-forming control interactions among converters and/or synchronous generators when several units are operating in grid-forming mode. This is specially challenging when the system is not symmetrical and using MMCs, as they do not include a capacitor in the AC side, worsening the controllability of the AC voltage using the classic voltage/current vector control. The

aforementioned optimal control tools could be useful to determine the control parameters.

- Chapter 7:
  - Extend the control design methodology to a more general AC/DC power system, considering different operating modes, different potential contingencies and support from one subgrid to another, in order to define the suitable control mode (AC and DC) in each terminal. This is strongly related to the *GridOfGrids* project [J7].

8.4 Related works within the research centre CITCEA-UPC

As a subject of current interest, other research works related to the MMC and to power systems with high penetration of power electronics devices are being carried out at CITCEA-UPC, the research centre where this thesis has been developed. These research lines can be seen as a logical extension of the present thesis, which started at the end of 2015, when the MMC topic was at an initial stage within the research centre know-how. Such ongoing works are summarised below:

- Ongoing PhD thesis entitled "Design of advanced system controllers in HVDC grids", conducted by Mr. Saman Dadjo Tavakoli. This work focuses on the analysis of interactions in MMC-based HVDC systems, such as point-to-point links and multi-terminal grids. This work is a logical extension of the work developed in the present thesis, and the author has actively collaborated in this research as a co-author in [J5], [J6], and other ongoing research.

- Ongoing PhD thesis entitled "Control and design of modular multi-level Converters", conducted by Mr. Daniel Westerman Spier. This work focuses on exploring the degrees of freedom of each MMC arm in unbalanced faults, considering each individual arm and the MMC capabilities in such scenarios.

- Ongoing PhD thesis related to the project "Control of a grid composed by AC and DC subgrids interconnected through power converters", conducted by Mr. Josep Arévalo-Soler. This research aims to analyse and design the control of the different MMCs, defining their roles and the most adequate control structure for the correct operation of the overall grid. The author actively participates in this PhD thesis.

Appendix A

Publications

This section presents a list of the author's journal, conference and other publications. Some of them are directly related to the chapters of this thesis, whereas others correspond to other related works that have been done in collaboration with other researchers.

Journal papers

Published - Included in the thesis

J1 E. Sánchez-Sánchez, E. Prieto-Araujo, A. Junyent-Ferré and O. Gomis-Bellmunt, "Analysis of MMC energy-based control structures for VSC-HVDC links", *IEEE Journal of Emerging and Selected Topics in Power Electronics*, vol. 6, no. 3, pp. 1065-1076, September 2018.

J2 E. Sánchez-Sánchez, D. Groß, E. Prieto-Araujo, Florian Dörfler and O. Gomis-Bellmunt, "Optimal multivariable MMC energy-based control for DC voltage regulation in HVDC applications", *IEEE Transactions on Power Delivery*, vol. 35, no. 2, pp. 999-1009, April 2020.

J3 E. Sánchez-Sánchez, E. Prieto-Araujo and O. Gomis-Bellmunt, "The Role of the Internal Energy in MMCs Operating in Grid-Forming Mode", *IEEE Journal of Emerging and Selected Topics in Power Electronics*, vol. 8, no. 2, pp. 949-962, June 2020.

Published - Not included in the thesis

J4 D. Heredero-Peris, C. Chillón-Antón, E. Sánchez-Sánchez and D. Montesinos-Miracle, "Fractional proportional-resonant current controllers for voltage source converters", *Electric Power Systems Research*, vol. 168, pp. 20-45, November 2018.

J5 S. Dadjo-Tavakoli, E. Sánchez-Sánchez, E. Prieto-Araujo and O. Gomis-Bellmunt,"DC Voltage Droop Control Design for MMC-Based Multi-terminal HVDC Grids", *IEEE Transactions on Power Delivery*, vol. 35, no. 5, pp. 2414-2424, October 2020.

J6 S. Dadjo-Tavakoli, E. Prieto-Araujo, E. Sánchez-Sánchez and O. Gomis-Bellmunt, "Interaction Assessment and Stability Analysis of the MMC-Based VSC-HVDC Link", *Energies* 2020, 13, 2075.

J7 O. Gomis-Bellmunt, E. Sánchez-Sánchez, J. Arévalo-Soler, and E. Prieto-Araujo, "Principles of operation of grids of DC and AC subgrids interconnected by power converters", *IEEE Transactions on Power Delivery*, Early Access, 2020.

Submitted

S-J8 E. Sánchez-Sánchez, E. Prieto-Araujo, O. Gomis-Bellmunt, and S. Galceran-Arellano, "Systematic design of optimal controllers for droop-controlled MMCs in MT-HVDC networks", under revision in *IEEE Transactions on Power Delivery*.

Conferences

Published papers - Included in the thesis

C1 E. Sánchez-Sánchez, E. Prieto-Araujo and O. Gomis-Bellmunt, "Multi-terminal HVDC voltage droop control design considering DC grid, AC grid and MMC dynamics", in *13th IET Int. Conf. on AC and DC Power Transmission*, Manchester, United Kingdom, Feb. 2017.

C2 E. Sánchez-Sánchez, E. Prieto-Araujo and O. Gomis-Bellmunt, "On the performance of the energy-controlled MMC: impact of the internal and the DC capacitances in HVDC applications", in *15th IET Int. Conf. on AC and DC Power Transmission*, Coventry, United Kingdom, Feb. 2019.

C3 E. Sánchez-Sánchez, A. Junyent-Ferré, Prieto-Araujo, O. Gomis-Bellmunt and T. Green, "Modelling and experimental validation of a laboratory-scaled HVDC cable emulator tested in an MMC-based platform", in *22nd European Conference on Power Electronics and Applications (EPE '20 ECCE Europe)*, Lyon, France, Sept. 2020.

Published papers - Not included in the thesis

C4 E. Sánchez-Sánchez, D. Heredero-Peris and D. Montesinos-Miracle, "Stability analysis of current and voltage resonant controllers for Voltage Source Converters", in *17th European Conference on Power Electronics and Applications (EPE'15 ECCE Europe)*, Geneva, Switzerland, September 2015.

C5 D. Heredero-Peris, E. Sánchez-Sánchez, C. Chillón-Antón and D. Montesinos-Miracle, "A novel fractional proportional-resonant current controller for voltage source converters", in *18th European Conference on Power Electronics and Applications (EPE'16 ECCE Europe)*, Karlsruhe, Germany, September 2016.

C6 E. Prieto-Araujo, D. Bodgan-Bolboceanu, E. Sánchez-Sánchez and O. Gomis-Bellmunt, "Design methodology of the primary droop voltage control for DC microgrids", in *IEEE 2nd International Conference on DC Microgrids (ICDCM)*, Berlin, Germany, June 2017.

C7 E. Prieto-Araujo, E. Sánchez-Sánchez, S. Galceran-Arellano and O. Gomis-Bellmunt, "Interaction Analysis between MMC-Based VSC-HVDC Links and DFIG-Based WPPs within the AC Network", in *16th Wind Integration Workshop*, Berlin, Germany, October 2017.

C8 C. Collados-Rodríguez, M. Cheah-Mañé, E. Prieto-Araujo, R. Ferrer-San-José, E. Sánchez-Sánchez and O. Gomis-Bellmunt, "Stability and interaction analysis in islanded power systems including VSC-HVDC and LCC-HVDC power converters", in *2018 CIGRE-Session Papers and Proceedings*, 2018.

Presentations in other events

P-C1 Presentation of "Multi-terminal HVDC voltage droop control design considering dc grid, ac grid and MMC dynamics", in *8th HVDC Doctoral Colloquium*, Cardiff, United Kingdom, September 2017.

P-C2 Presentation of "Control of multi-terminal HVDC grids", in *MSc EIT InnoEnergy SENSE and Smart Cities Workshop*, Barcelona, Spain, October 2017.

P-C3 Presentation of "The Modular Multilevel Converter: insights and applications in High Voltage Direct Current systems", in *IfA Coffee Talks, ETH Zürich*, Zürich, Switzerland, March 2018.

P-C4 Presentation of "Analysis of MMC energy-based control structures for VSC-HVDC links", in *IRPWind workshop at IREQ - Grid Integration of High Power Density Modular Multilevel Converter*, Barcelona, Spain, April 2018.

P-C5 Presentation of "Analysis of MMC energy-based control structures for VSC-HVDC links", in *9th HVDC Doctoral Colloquium*, Barcelona, Spain, September 2018.

Other Contributions

O1 F. García Martínez, FUTURED - Plataforma Española de Redes Eléctricas, "La electrónica de potencia en España: situación y potencial", 2019. [Online]: https://www.futured.es/documentos/documentos-search /download-info/electronica-de-potencia-futured/

Appendix B

Mathematical transformations

Throughout the thesis, different mathematical transformations are used, mainly for control design purposes. As some of these transformations can be defined in different ways, and several versions can be found in the literature, this appendix lists the specific ones used in the present work.

B.1 Clarke transformation

Clarke transformation (B.1) consists of a change in the orientation of the abc stationary frame axes into the so-called $\alpha\beta0$ axes. This is useful in terms of representing a balanced three-phase system with only two variables ($\alpha\beta$), and it can be also useful to isolate the 0 (zero-sequence) component of any system. As seen in (2.22)-(2.23) in Chapter 2, Clarke transform can be even useful to obtain simplified expressions in cases where it may not seem intuitive to be applied. The inverse Clarke transformation is obtained as in (B.2).

$$\underline{\Theta}^{\alpha\beta0} \triangleq \mathbf{C}\underline{\Theta}^{abc} = \frac{1}{3} \begin{bmatrix} 2 & -1 & -1 \\ 0 & -\sqrt{3} & \sqrt{3} \\ 1 & 1 & 1 \end{bmatrix} \underline{\Theta}^{abc} \tag{B.1}$$

$$\underline{\Theta}^{abc} \triangleq \mathbf{C}^{-1}\underline{\Theta}^{\alpha\beta0} = \frac{1}{2} \begin{bmatrix} 1 & 0 & 2 \\ -1 & -\sqrt{3} & 2 \\ -1 & \sqrt{3} & 2 \end{bmatrix} \underline{\Theta}^{\alpha\beta0} \tag{B.2}$$

B.2 Park transformation

Park transformation (B.3) consists of a change from the abc stationary frame to a synchronous reference frame at the fundamental frequency of the abc system. Additional synchronous reference frames for subsequent harmonic components can be similarly implemented. In the present work, the $qd0$ notation is used, based on the work on electrical machines from Krause [64],

and to be consistent with previous research from the supervisors of this thesis. The inverse Park transformation is obtained as in (B.4).

$$
\underline{\Theta}^{qd0} \triangleq \mathbf{P}\underline{\Theta}^{abc} = \frac{2}{3}
\begin{bmatrix}
\cos(\theta) & \cos(\theta - \frac{2\pi}{3}) & \cos(\theta + \frac{2\pi}{3}) \\
\sin(\theta) & \sin(\theta - \frac{2\pi}{3}) & \sin(\theta + \frac{2\pi}{3}) \\
\frac{1}{2} & \frac{1}{2} & \frac{1}{2}
\end{bmatrix}
\underline{\Theta}^{abc}
\tag{B.3}
$$

$$
\underline{\Theta}^{abc} \triangleq \mathbf{P}^{-1}\underline{\Theta}^{qd0} =
\begin{bmatrix}
\cos(\theta) & \sin(\theta) & 1 \\
\cos(\theta - \frac{2\pi}{3}) & \sin(\theta - \frac{2\pi}{3}) & 1 \\
\cos(\theta + \frac{2\pi}{3}) & \sin(\theta + \frac{2\pi}{3}) & 1
\end{bmatrix}
\underline{\Theta}^{qd0}
\tag{B.4}
$$

B.3 Fortescue transformation

According to the symmetrical components theory, any three-phase system can be expressed as the linear combination of three independent subsystems, namely direct-sequence, inverse-sequence and zero-sequence. The direct-sequence component corresponds to a purely balanced positive sequence three-phase system, the inverse-sequence component corresponds to a purely balanced negative sequence three-phase system, and the zero-sequence corresponds to a three-phase system with all the phasors in phase.

This system obviously presents the same number of degrees of freedom (six) than the system in the *abc* frame. However, the system expressed in symmetrical components presents two independent balanced systems and one pure zero-sequence system. Defining $\underline{p} = e^{j\frac{2\pi}{3}}$, the Fortescue transformation is expressed as (B.5), whereas the inverse Fortescue transformation is derived as (B.6).

$$
\underline{\Theta}^{+-0} \triangleq \mathbf{F}\underline{\Theta}^{abc} = \frac{1}{3}
\begin{bmatrix}
1 & \underline{p} & \underline{p}^2 \\
1 & \underline{p}^2 & \underline{p} \\
1 & 1 & 1
\end{bmatrix}
\underline{\Theta}^{abc}
\tag{B.5}
$$

$$
\underline{\Theta}^{abc} \triangleq \mathbf{F}^{-1}\underline{\Theta}^{+-} = \frac{1}{3}
\begin{bmatrix}
1 & 1 & 1 \\
\underline{p}^2 & \underline{p} & 1 \\
\underline{p} & \underline{p}^2 & 1
\end{bmatrix}
\underline{\Theta}^{+-0}
\tag{B.6}
$$

Appendix C

Small-signal analysis

Small-signal stability analysis has been used in power systems over the last decades. In classic power systems, this is defined as the ability of the power system to maintain synchronism when subjected to small disturbances [139]. In general, small-signal analysis considers a small disturbance applied to a system around an operating point. In terms of the state-space representation of a system, it analyses the state matrix $\mathbf{A}$ (C.1). If the system is not linear (i.e. it contains non-linear differential equations) it has to be previously linearised in order to derive the state-space representation of it.

$$
\begin{aligned}
\dot{x} &= \mathbf{A}x + \mathbf{B}u \\
y &= \mathbf{C}x + \mathbf{D}u
\end{aligned}
\tag{C.1}
$$

Then, the eigenvalues of the matrix $\mathbf{A}$, i.e. the roots of the characteristic equation (C.2), can be computed ($\lambda = \lambda_1, \lambda_2, ...\lambda_n$). These eigenvalues can be real or complex, and if $\mathbf{A}$ is real, complex eigenvalues always appear in conjugate pairs. Similar matrices have identical eigenvalues. The eigenvalues of a matrix are given by the values of the scalar parameter λ for which non-trivial solutions to (C.3) exist.

$$
\det(\mathbf{A} - \lambda I) = 0
\tag{C.2}
$$

$$
\mathbf{A}\phi = \lambda\phi
\tag{C.3}
$$

The stability of a linear dynamic system is independent from the inputs. In fact, it is determined by the eigenvalues by the Lyapunov's first method [140] as follows:

- All eigenvalues with negative real parts: system asymptotically stable.

- At least one eigenvalue with positive real part: system unstable.

- Some eigenvalues with real parts equal to zero: undetermined in general.

Also, each eigenvalue is related to a system mode, and these modes are determined as follows:

- A real eigenvalue corresponds to a non-oscillatory mode. A negative eigenvalue represents a decaying mode, and the larger its magnitude, the faster the decay. A positive eigenvalue represents aperiodic instability.

- Complex eigenvalues occur in conjugate pairs, and each pair corresponds to an oscillatory mode. Given a complex pair of eigenvalues (C.4), the frequency and the damping of such oscillatory mode are given by (C.5) and (C.6).

$$\lambda = \sigma \pm j\omega \tag{C.4}$$

$$f = \frac{\omega}{2\pi} \tag{C.5}$$

$$\zeta = \frac{-\sigma}{\sqrt{\sigma^2 + \omega^2}} \tag{C.6}$$

For any eigenvalue λ_i, the n-column vector ϕ_i which satisfies (C.7) is called the right eigenvector of $\mathbf{A}$ associated with the eigenvalue λ_i. The same occurs in the case of the left eigenvector (C.8).

$$\mathbf{A}\phi_i = \lambda_i\phi_i \tag{C.7}$$

$$\psi_i\mathbf{A} = \lambda_i\psi_i \tag{C.8}$$

It can be demonstrated [139] that the right eigenvector gives the relative activity of the state variables when a particular mode is excited. The magnitude of the elements of ϕ_i give the extents of the activities of the n state variables in the ith mode, whereas the angles give phase displacements of the state variables with regard to the mode. Moreover, the left eigenvector ψ_i identifies which combination of the original state variables displays only the ith mode. Thus, the kth element of the right eigenvector ϕ_i measures the activity of the variable x_k in the ith mode, and the kth element of the left eigenvector ψ_i weighs the contribution of this activity to the ith mode.

One problem in using these vectors individually for identifying relationships between states and modes is the dependence on units and scaling. Participation factors matrix (C.9) is proposed as a solution, which measures the net participation (dimensionless):

$$\boldsymbol{P} = [\boldsymbol{p_1} \ \boldsymbol{p_2} \ ... \ \boldsymbol{p_n}] \tag{C.9}$$

$$\boldsymbol{p_i} = [\phi_{1i}\psi_{i1} \ \phi_{2i}\psi_{i2} \ ... \ \phi_{ni}\psi_{in}]^T \tag{C.10}$$

Appendix D

Transformer parameters determination

An elevator star-delta transformer is used to couple the MMC to the AC grid. On one hand, in the real system the primary (p) of the transformer is connected to the 400 kV transmission network, whereas the secondary (s) side is connected to the MMC, with a voltage of 320 kV. On the other hand, the primary side of the MMC prototype transformer is connected to 340 V, and the secondary side to 780 V (Table 4.2). Due to laboratory constraints, the primary side voltage is much lower than the secondary side, and the transformer was designed to elevate that voltage to the rated MMC AC voltage.

The parameters of the transformer have to be properly characterised, as they are used in the MMC prototype inner controller design, and also in the detailed simulation model. The equivalent single-phase circuit of the transformer is depicted in Fig. D.1.
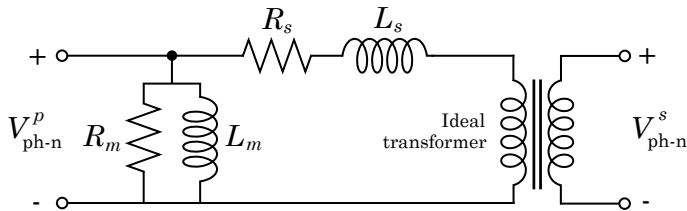
Fig. D.1: Equivalent single-phase circuit of a three-phase transformer

D.1 Open-circuit test

The open-circuit test consists of the application of the rated voltage in one side while the other side is in open-circuit. In this case, two phase-to-neutral voltages, two line currents and two active powers are measured (Fig. D.2). The input power corresponds to the iron losses of the transformer. The parameters R_m and L_m of the equivalent single-phase circuit of the transformer

(Fig. D.1) can be calculated as

$$R_m = \frac{V_{\text{ph-n}}^{p\;2}}{P_{\text{ph}}} \tag{D.1}$$

$$L_m = \frac{V_{\text{ph-n}}^{p\;2}}{2\pi 50 \sqrt{I^{p2} - \left(\dfrac{P_{\text{ph}}}{V_{\text{ph-n}}^{p}}\right)^2}} \tag{D.2}$$
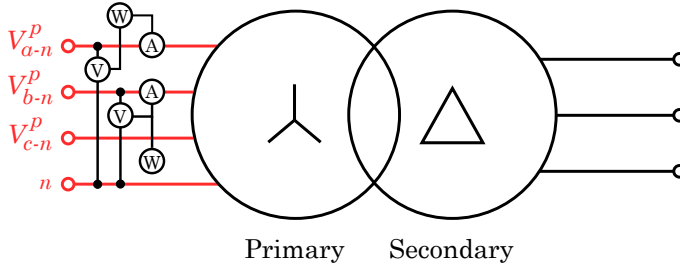
Fig. D.2: Transformer open-circuit test setup

Note that ph refers to phase, ph-n refers to phase-to-neutral and ph-ph refers to phase-to-phase. The collected data is summarised in Table D.1. Note that the values shown correspond to the average of phases a and b. Steps of approximately 20% of the input phase-neutral voltage in the primary side of the transformer are applied.

Table D.1: Data from the transformer open-circuit test

$V_{\text{ph-n}}^{p}$ [V]	I^p [A]	W_{ph} [W]
41.2	0.073	2.19
80.2	0.104	6.60
119.3	0.130	12.75
157.4	0.158	20.65
226.1	0.239	41.45

D.2 Short-circuit test

The short-circuit test consists of the application of a reduced voltage in one side using a variac, whereas in the other side the three phases are short-

circuited. In this case, two phase-to-phase voltages, two line currents and two active powers are measured (Fig. D.2). The applied voltage is increased until the rated current is reached. Usually, the short-circuit side corresponds to the lower voltage side (the primary side in this case). Note that as the secondary winding is in delta configuration, the phase-to-neutral voltages cannot be measured. This implies that the instantaneous measured active power given by the oscilloscope is a projection of the single phase active power, which is taken into account when calculating (D.5). The input power corresponds to the copper losses of the transformer. The parameters R_s and L_s of the equivalent single-phase circuit of the transformer (Fig. D.1) can be calculated as

$$R_s = \frac{U^s_{\text{ph-ph}}}{\sqrt{3}I^s \cos\phi}, \tag{D.3}$$

$$L_s = \frac{1}{2\pi 50} \frac{U^s_{\text{ph-ph}}}{\sqrt{3}I^s} \sqrt{1 - \cos^2\phi}, \tag{D.4}$$
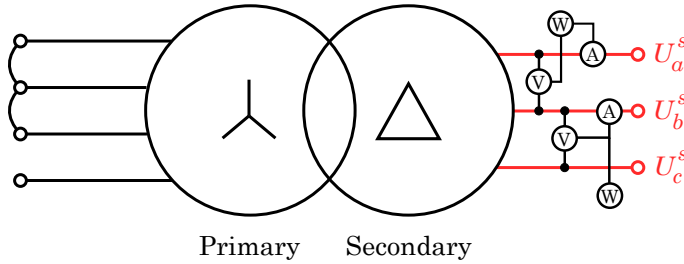
Fig. D.3: Transformer short-circuit test setup

where $\cos\phi$ is calculated as

$$\cos\phi = \cos\left(\cos^{-1}\left(\frac{P_{ph}}{U^s_{\text{ph-ph}}I^s}\right) - \frac{\pi}{6}\right) \tag{D.5}$$

The collected data is summarised in Table D.2. Note that the values shown correspond to the average of the voltage measurements U_{ab} and U_{ac}. Note that the maximum voltage applied to the secondary side, which corresponds to almost the rated current, is around 3% of the rated voltage.

Finally, the parameters of the transformer are summarised in Table D.3. The turns ratio of the transformer has been calculated experimentally applying voltages in the primary side and measuring them in the secondary side (D.6). With respect to the series and shunt impedances of the single-phase

transformer equivalent, they are referred to the primary side.

$$r_t = \frac{U^p_{\text{avg}}}{U^s_{\text{avg}}} = \frac{N_p}{N_s} \tag{D.6}$$

Table D.2: Data from the transformer short-circuit test

$U^s_{\text{ph-ph}}$ [V]	I^s [A]	W^s_{ph} [W]
27.25	9.40	172.2
21.35	7.30	106.4
15.27	5.16	53.7
10.46	3.42	24.5
5.37	1.61	5.9

Table D.3: Parameters of the transformer

Parameter	Symbol	Value	Units
Turns ratio	r_t	0.418	-
Rated primary voltage	U^p_{rms}	520	V
Rated secondary voltage	U^s_{rms}	1250	V
Rated power	S_t	20	kVA
Turns ratio	r_t	0.4178	-
Winding losses[1]	R_s	1.6150	Ω
Leakage inductance[1]	L_s	1.5960	mH
Iron losses[1]	R_m	6776.6	Ω
Magnetising inductance[1]	L_m	29.634	H

---

[1]Referred to the secondary side (MMC AC side)

List of Figures

List of Tables

Bibliography

[1] European Network of Transmission System Operators for Electricity, "ENTSO-E annual report 2018," Tech. Rep. May, 2019. 1

[2] D. Van Hertem, O. Gomis-Bellmunt, and J. Liang, *HVDC grids: for offshore and supergrid of the future.* Hoboken, NJ: Wiley, 2016. 1, 10

[3] Red Eléctrica de España, "Rómulo: interconexión eléctrica península-Baleares," Tech. Rep., 2011. 1

[4] ——, "Interconexión eléctrica por los Pirineos catalanes," Tech. Rep., 2011. 1

[5] P. L. Francos, S. S. Verdugo, H. F. Alvarez, S. Guyomarch, and J. Loncle, "INELFE Europe's first integrated onshore HVDC interconnection," in *IEEE Power and Energy Society General Meeting*, 2012. 1, 8

[6] Red Eléctrica de España, "Spain-France electricity interconection across the Bay of Biscay," Tech. Rep., 2018. 2

[7] "INELFE (Interconexión Eléctrica Francia-España)." [Online]. Available: https://www.inelfe.eu/ 2, 215

[8] Wind Europe, "Wind energy in Europe: Outlook to 2023," Tech. Rep. October, 2019. 2, 3, 215

[9] ——, "Our Energy, our Future. How offshore wind will help Europe go carbon-neutral," Tech. Rep. November, 2019. 2

[10] Friends of Sustainable Grids, "Interconnecting electricity for Europe's sustainable future." [Online]. Available: https://supergrid.brussels/ 2, 4, 215

[11] GWEC, "Global Wind Report 2018," Tech. Rep. April, 2019. 4

[12] P. Fairley, "A grid as big as China," *IEEE Spectrum*, vol. 56, no. 3, pp. 36–41, 2019. 4, 5, 6, 215

[13] EU Horizon 2020 (H2020), "PROgress on Meshed HVDC Offshore Transmission Networks (PROMOTioN)," 2015. [Online]. Available: https://www.promotion-offshore.net/ 5

[14] M. Barnes and A. Beddard, "Voltage source converter HVDC links - The state of the art and issues going forward," in *Energy Procedia*, vol. 24, 2012, pp. 108–122. 5, 6

[15] M. P. Bahrman and B. K. Johnson, "The ABCs of HVDC transmission technologies," *IEEE Power and Energy Magazine*, vol. 5, no. 2, pp. 32–44, 2007. 6

[16] R. Adapa, "High-Wire Act. HVdc technology: The State of the Art," *IEEE Power and Energy Magazine*, pp. 18–29, 2012. 6, 10, 22

[17] A. Lesnicar and R. Marquardt, "An innovative modular multilevel converter topology suitable for a wide power range," in *IEEE Bologna Power Tech Conference*, vol. 3, 2003. 6, 22

[18] K. Johannesson, A. Gustafsson, J. Karlstrand, and M. Jeroense, "HVDC Light Cables for long distance grid connection," in *European Offshore Wind Conference*, 2009. 6

[19] N. Mahimkar, G. Persson, and C. Westerlind, "HVDC Technology for Large Scale Offshore Wind Connections," in *Smartelec 2013*, 2013. 8

[20] Siemens AG, "HVDC – High-voltage direct current transmission: An overview of worldwide LCC and VSC references," Tech. Rep., 2017. 8

[21] TenneT, "Taking power further - Offshore projects Germany." [Online]. Available: https://www.tennet.eu/our-grid/offshore-projects-germany/offshore-projects-germany/ 8

[22] T. Westerweller, K. Friedrich, U. Armonies, A. Orini, D. Parquet, and S. Wehn, "Trans Bay Cable - World's first HVDC system using multilevel voltage-sourced converter," in *43rd International Conference on Large High Voltage Electric Systems, CIGRE*, 2010. 8

[23] TenneT and Energinet.dk, "COBRAcable – From concept to connection," 2019. 8

[24] O. Vestergaard and P. Lundberg, "Maritime link the first bipolar VSC HVDC with overhead line," *AEIT HVDC International Conference*, pp. 2–5, 2019. 8

[25] "NordLink - Statnett." [Online]. Available: https://www.statnett.no/en/our-projects/interconnectors/nordlink/ 8

[26] "Eleclink." [Online]. Available: http://www.eleclink.co.uk/ 8

[27] O. Gomis-Bellmunt, J. Liang, J. Ekanayake, R. King, and N. Jenkins, "Topologies of multiterminal HVDC-VSC transmission for large offshore wind farms," *Electric Power Systems Research*, vol. 81, no. 2, pp. 271–281, 2011. 10, 161

[28] G. Buigues, V. Valverde, A. Etxegarai, P. Eguía, and E. Torres, "Present and future multiterminal HVDC systems: Current status and forthcoming developments," *Renewable Energy and Power Quality Journal*, vol. 1, no. 15, pp. 83–88, 2017. 10

[29] X. Li, Z. Yuan, J. Fu, Y. Wang, T. Liu, and Z. Zhu, "Nanao multi-terminal VSC-HVDC project for integrating large-scale wind generation," *IEEE Power and Energy Society General Meeting*, no. October, 2014. 10, 161

[30] G. Bathurst and P. Bordignan, "Delivery of the Nan'ao Multi -terminal VSC-HVDC System," in *11th IET International Conference on AC and DC Power Transmission*, 2015. 10, 161

[31] G. Tang, Z. He, H. Pang, X. Huang, and X.-p. Zhang, "Basic topology and key devices of the five-terminal DC grid," *CSEE Journal of Power and Energy Systems*, vol. 1, no. 2, pp. 22–35, 2015. 10, 161

[32] Y. Pipelzadeh, B. Chaudhuri, and T. C. Green, "Modelling and Dynamic Operation of the Zhoushan DC Grid: Worlds First Five-Terminal VSC-HVDC Project," in *International High Voltage Direct Current Conference*, 2015, pp. 87–95. 10, 161

[33] H. Rao and Y. Zhou, "Key technologies of ultra-high voltage hybrid LCC-VSC MTDC systems," *CSEE Journal of Power and Energy Systems*, vol. 5, no. 3, pp. 365–373, 2019. 10

[34] H. Rao, Y. Zhou, and Z. Zhu, "Research and development of Ultra-High-Voltage VSC for the multi-terminal hybrid ±800kV HVDC project in China Southern Power Grid," Tech. Rep., 2018. 10

[35] "The North Sea Wind Power Hub (NSWPH)." [Online]. Available: https://northseawindpowerhub.eu/vision/ 11

[36] NSCOGI, "The North Seas Countries' Offshore Grid Initiative." [Online]. Available: https://www.msp-platform.eu/practices/north-seas-countries-offshore-grid-initiative-nscogi 11

[37] G. Tang, H. Pang, Z. He, and X. Wei, "Research on Key Technology and Equipment for Zhangbei 500kV DC Grid," in *The International Power Electronics Conference.* IEEJ Industry Application Society, 2018. 11, 162

[38] NR Electric, "Case Study: NR's VSC-HVDC Solution, ±500kV Zhangbei DC Grid for boosting large scale hybrid renewables penetration," Tech. Rep., 2019. [Online]. Available: http://www.nrec.com/en/web/upload/2019/05/14/15578229444108hgcuh.pdf 11, 162

[39] J. Arrillaga, Y. H. Liu, and N. R. Watson, *Flexible Power Transmission*, 2007. 11

[40] W. Leterme, P. Tielens, S. De Boeck, and D. Van Hertem, "Overview of grounding and configuration options for meshed HVDC grids," *IEEE Transactions on Power Delivery*, vol. 29, no. 6, pp. 2467–2475, 2014. 11, 12

[41] W. G. B4-57, "Guide for the Development of Models for HVDC Converters in a HVDC Grid," *CIGRE Technical Brochure*, vol. 604, 2014. 21

[42] L. Harnefors, A. Antonopoulos, S. Norrga, L. Angquist, and H. P. Nee, "Dynamic analysis of modular multilevel converters," *IEEE Transactions on Industrial Electronics*, vol. 60, no. 7, pp. 2526–2537, 2013. 21, 30, 49, 53

[43] H. Saad, X. Guillaud, J. Mahseredjian, S. Dennetière, and S. Nguefeu, "MMC Capacitor Voltage Decoupling and Balancing Controls," *IEEE Transactions on Power Delivery*, vol. 30, no. 2, pp. 704–712, 2015. 21

[44] S. Rohner, J. Weber, and S. Bernet, "Continuous model of modular multilevel converter with experimental verification," in *IEEE Energy Conversion Congress and Exposition.* IEEE, 2011, pp. 4021–4028. 21

[45] H. Saad, S. Dennetiere, J. Mahseredjian, P. Delarue, X. Guillaud, J. Peralta, and S. Nguefeu, "Modular multilevel converter models for electromagnetic transients," *IEEE Transactions on Power Delivery*, vol. 29, no. 3, pp. 1481–1489, 2014. 25

[46] E. Prieto-Araujo, A. Junyent-Ferré, C. Collados-Rodríguez, G. Clariana-Colet, and O. Gomis-Bellmunt, "Control design of Modular Multilevel Converters in normal and AC fault conditions for HVDC grids," *Electric Power Systems Research*, vol. 152, pp. 424–437, 2017. 26, 30, 33, 34, 57, 60, 76, 132, 137, 223

[47] K. Sharifabadi, L. Harnefors, H. P. Nee, S. Norrga, and Teodorescu, *Design, control and application of modular multilevel converters for HVDC transmission systems.* Hoboken, NJ: Wiley, 2016. 29, 30, 49

[48] G. Bergna, J. A. Suul, and S. D'Arco, "State-space modelling of modular multilevel converters for constant variables in steady-state," in *IEEE 17th Workshop on Control and Modeling for Power Electronics (COMPEL)*, 2016. 29, 49

[49] A. Antonopoulos, L. Angquist, and H.-P. Nee, "On dynamics and voltage control of the Modular Multilevel Converter," in *13th European Conference on Power Electronics and Applications*, 2009. 29, 132

[50] L. Angquist, A. Antonopoulos, D. Siemaszko, K. Ilves, M. Vasiladiotis, and H.-P. Nee, "Open-loop control of modular multilevel converters using estimation of stored energy," *IEEE Transactions on Industry Applications*, vol. 47, no. 6, pp. 2516–2524, 2011. 29, 49

[51] Q. Tu, Z. Xu, and L. Xu, "Reduced Switching-frequency modulation and circulating current suppression for modular multilevel converters," *IEEE Transactions on Power Delivery*, vol. 26, no. 3, pp. 2009–2017, 2011. 30, 49, 132

[52] J. Peralta, H. Saad, S. Dennetière, J. Mahseredjian, and S. Nguefeu, "Detailed and averaged models for a 401-level MMC-HVDC system," *IEEE Transactions on Power Delivery*, vol. 27, no. 3, pp. 1501–1508, 2012. 30

[53] G. Bergna, J. A. Suul, E. Berne, J. C. Vannier, and M. Molinas, "MMC circulating current reference calculation in ABC frame by means of Lagrange Multipliers for ensuring constant DC power under unbalanced grid conditions," in *16th European Conference on Power Electronics and Applications, EPE-ECCE Europe.* IEEE, 2014. 30, 132

[54] N. R. Chaudhuri, R. Oliveira, and A. Yazdani, "Stability Analysis of Vector-Controlled Modular Multilevel Converters in Linear

Time-Periodic Framework," *IEEE Transactions on Power Electronics*, vol. 31, no. 7, pp. 5255–5269, 2016. 30

[55] J. Freytes, G. Bergna, J. A. Suul, S. D'Arco, F. Gruson, F. Colas, H. Saad, and X. Guillaud, "Improving Small-Signal Stability of an MMC with CCSC by Control of the Internally Stored Energy," *IEEE Transactions on Power Delivery*, vol. 33, no. 1, pp. 429–439, 2018. 30, 50, 51, 137

[56] G. Bergna Diaz, J. A. Suul, and S. D'Arco, "Small-signal state-space modeling of modular multilevel converters for system stability analysis," in *IEEE Energy Conversion Congress and Exposition (ECCE)*, 2015, pp. 5822–5829. 30, 38, 49, 50, 51, 139

[57] A. Egea-Álvarez, A. Junyent-Ferré, and O. Gomis-Bellmunt, "Active and Reactive Power Control of Grid Connected Distributed Generation Systems," in *Modeling and Control of Sustainable Power Systems*. Berlin: Springer-Verlag, 2012, pp. 47–81. 30, 57

[58] S. K. Chung, "A phase tracking system for three phase utility interface inverters," *IEEE Transactions on Power Electronics*, vol. 15, no. 3, pp. 431–438, 2000. 32

[59] E. Prieto-Araujo, A. Junyent-Ferre, G. Clariana-Colet, and O. Gomis-Bellmunt, "Control of modular multilevel converters under singular unbalanced voltage conditions with equal positive and negative sequence components," *IEEE Transactions on Power Systems*, vol. 32, no. 3, pp. 2131–2141, 2017. 34, 58

[60] J. Freytes, "Small-signal stability analysis of Modular Multilevel Converters and application to MMC-based Multi-Terminal DC grids," Ph.D. dissertation, École Centrale de Lille, 2017. 38, 60, 223

[61] G. Bergna-Diaz, J. Freytes, X. Guillaud, S. D'Arco, and J. A. Suul, "Generalized Voltage-based State-Space Modelling of Modular Multilevel Converters with Constant Equilibrium in Steady-State," *IEEE Journal of Emerging and Selected Topics in Power Electronics*, vol. 6, no. 2, pp. 707–725, 2018. 38

[62] G. Bergna-Diaz, J. A. Suul, and S. D'Arco, "Energy-Based State-Space Representation of Modular Multilevel Converters with a Constant Equilibrium Point in Steady-State Operation," *IEEE Transactions on Power Electronics*, vol. 33, no. 6, pp. 4832–4851, 2018. 38

[63] A. Junyent-Ferré, P. Clemow, M. M. C. Merlin, and T. C. Green, "Operation of HVDC modular multilevel converters under DC pole imbalances," *16th European Conference on Power Electronics and Applications (EPE-ECCE)*, 2014. 38

[64] P. C. Krause, O. Wasynczuk, and S. D. Sudhoff, *Analysis of Electric Machinery and Drive Systems.* Hoboken, NJ: Wiley, 2002. 39, 205

[65] C. E. Ugalde-Loo, E. Acha, and E. Licéaga-Castro, "Multi-machine power system state-space modelling for small-signal stability assessments," *Applied Mathematical Modelling*, vol. 37, no. 24, pp. 10 141–10 161, 2013. 39

[66] L. Zhang, "Modeling and Control of VSC-HVDC Links Connected to Weak AC Systems," Ph.D. dissertation, Royal Institute of Technology, 2010. 40

[67] A. Morched, B. Gustavsen, and M. Tartibi, "A universal model for accurate calculation of electromagnetic transients on overhead lines and underground cables," *IEEE Transactions on Power Delivery*, vol. 14, no. 3, pp. 1032–1038, 1999. 41, 75

[68] W. Leterme, N. Ahmed, J. Beerten, L. Ängquist, D. Van Hertem, and S. Norrga, "A new HVDC grid test system for HVDC grid dynamics and protection studies in EMT-type software," in *11th IET International Conference on AC and DC Power Transmission*, 2015. 41, 78, 79

[69] C. E. Ugalde-Loo, O. D. Adeuyi, S. Eang, N. Jenkins, S. Ceballos, M. Santos, I. Vidaurrazaga, S. D'Arco, G. Bergna, M. Barenys, M. Parker, S. Finney, A. Gatti, A. Pitto, M. Rapizza, D. Cirio, P. Lund, A. Castro, and I. Azpiri, "Open access simulation toolbox for the grid connection of offshore wind farms using multi-terminal HVDC networks," in *13th IET International Conference on AC and DC Power Transmission*, 2017. 41, 79, 84

[70] J. Beerten, S. D'Arco, and J. A. Suul, "Frequency-dependent cable modelling for small-signal stability analysis of VSC-HVDC systems," *IET Generation, Transmission & Distribution*, vol. 10, no. 6, pp. 1370–1381, 2016. 41, 50, 75, 77, 78

[71] S. Akkari, E. Prieto-Araujo, J. Dai, O. Gomis-Bellmunt, and X. Guillaud, "Impact of the DC cable models on the SVD analysis of a Multi-

Terminal HVDC system," in *19th Power Systems Computation Conference (PSCC)*, 2016. 41, 42, 49

[72] J. Freytes, S. Akkari, J. Dai, F. Gruson, P. Rault, and X. Guillaud, "Small-signal state-space modeling of an HVDC link with modular multilevel converters," in *IEEE 17th Workshop on Control and Modeling for Power Electronics (COMPEL)*, 2016. 42, 49, 137

[73] A. J. Far and D. Jovcic, "Small-Signal Dynamic DQ Model of Modular Multilevel Converter for System Studies," *IEEE Transactions on Power Delivery*, vol. 31, no. 1, pp. 191–199, 2016. 49

[74] G. Bergna, J. A. Suul, and S. D'Arco, "Impact on small-signal dynamics of using circulating currents instead of AC-currents to control the DC voltage in MMC HVDC terminals," in *IEEE Energy Conversion Congress and Exposition (ECCE)*, 2016. 50

[75] H. Saad, Y. Fillion, S. Deschanvres, Y. Vernay, and S. Dennetiere, "On Resonances and Harmonics in HVDC-MMC Station Connected to AC grid," *IEEE Transactions on Power Delivery*, vol. 32, no. 3, pp. 1565–1573, 2017. 51, 57

[76] J. Beerten, G. B. Diaz, S. D'Arco, and J. A. Suul, "Comparison of small-signal dynamics in MMC and two-level VSC HVDC transmission schemes," *IEEE International Energy Conference (ENERGYCON)*, 2016. 51, 139

[77] S. Debnath, J. Qin, B. Bahrani, M. Saeedifard, and P. Barbosa, "Operation, Control, and Applications of the Modular Multilevel Converter: A Review," *IEEE Transactions on Power Electronics*, vol. 30, no. 1, pp. 37–53, 2014. 56

[78] A. Yazdani and R. Iravani, *Voltage-Sourced Converters in Power Systems: Modeling, Control and Applications.* Hoboken, NJ: John Wiley and Sons, 2010. 58

[79] A. Egea-Alvarez, F. Bianchi, A. Junyent-Ferre, G. Gross, and O. Gomis-Bellmunt, "Voltage control of multiterminal VSC-HVDC transmission systems for offshore wind power plants: Design and implementation in a scaled platform," *IEEE Transactions on Industrial Electronics*, vol. 60, no. 6, pp. 2381–2391, 2013. 75

[80] S. A. Amamra, F. Colas, X. Guillaud, P. Rault, and S. Nguefeu, "Laboratory Demonstration of a Multiterminal VSC-HVDC Power Grid," *IEEE Transactions on Power Delivery*, vol. 32, no. 5, pp. 2339–2349, 2017. 75

[81] B. Gustavsen and A. Semlyen, "Rational approximation of frequency domain responses by vector fitting," *Advances in Mathematics*, vol. 14, no. 3, pp. 1052–1061, 1999. 77, 78

[82] B. Gustavsen, "The Vector Fitting Website." [Online]. Available: https://www.sintef.no/projectweb/vectorfitting/ 79

[83] M. Cheah-Mane, O. D. Adeuyi, J. Liang, and N. Jenkins, "A scaling method for a multi-terminal DC experimental test rig," in *2015 17th European Conference on Power Electronics and Applications, EPE-ECCE Europe 2015*. Jointly owned by EPE Association and IEEE PELS, 2015. 84

[84] P. Clemow, P. Judge, G. Chaffey, M. Merlin, T. Luth, and T. C. Green, "Lab-scale experimental multilevel modular HVDC converter with temperature controlled cells," in *16th European Conference on Power Electronics and Applications, EPE-ECCE Europe*. IEEE, 2014. 86

[85] S. D. Arco, J. A. Suul, J. Beerten, and S. Member, "Configuration and model order selection of frequency-dependent π -models for representing dc-cables in small-signal eigenvalue analysis of HVDC transmission systems," *IEEE Journal of Emerging and Selected Topics in Power Electronics*, vol. PP, p. 1, 2020. 88

[86] M. M. C. Merlin, "Hybrid multi-level HVDC converter and Multi-Terminal DC networks," Ph.D. dissertation, 2013. 94, 95

[87] P. D. Judge, "Power converter design for HVDC applications," Ph.D. dissertation, 2016. 94, 95

[88] P. Münch, D. Görges, M. Izák, and S. Liu, "Integrated current control, energy control and energy balancing of Modular Multilevel Converters," *IECON 2010 - 36th Annual Conference on IEEE Industrial Electronics Society*, pp. 150–155, 2010. 95

[89] S. Skogestad and I. Postlethwaite, *Multivariable feedback control: analysis and design*. Chichester, West Sussex: Wiley, 2005. 108, 120

[90] J. C. Doyle, "Guaranteed Margins for LQG Regulators," *IEEE Transactions on Automatic Control*, vol. AC-23, no. 4, pp. 756–757, 1978. 108

[91] J. C. Doyle and B. A. Francis, "State-Space Solutions to Standard $\mathcal{H}_2$ and $\mathcal{H}_\infty$ Control Problems," *IEEE Transactions on Automatic Control*, vol. 34, no. 8, pp. 831–847, 1989. 108

[92] P. Apkarian and D. Noll, "Nonsmooth $\mathcal{H}_\infty$ synthesis," *IEEE Transactions on Automatic Control*, vol. 51, no. 1, pp. 71–86, 2006. 109, 115, 152

[93] N. Bruinsma and M. Steinbuch, "A fast algorithm to compute the $\mathcal{H}_\infty$-norm of a transfer function matrix," *Systems & Control Letters*, vol. 14, pp. 287–293, 1990. 109

[94] K. Zhou, J. C. Doyle, and K. Glover, *Robust and Optimal Control*. Upper Saddle River, NJ: Prentice Hall, 1996. 109, 120, 121

[95] D. Groß, S. Bolognani, B. K. Poolla, and F. Dörfler, "Increasing the Resilience of Low-inertia Power Systems by Virtual Inertia and Damping," in *IREP Bulk Power Systems Dynamics and Control Symposium*, 2017. 109

[96] V. Blondel and J. N. Tsitsiklis, "NP-hardness of some linear control design problems," *SIAM Journal on Control and Optimization*, vol. 35, no. 6, pp. 2118–2127, 1997. 110

[97] B. K. Poolla, D. Groß, and F. Dörfler, "Placement and Implementation of Grid-Forming and Grid-Following Virtual Inertia and Fast Frequency Response," *IEEE Transactions on Power Systems*, vol. 34, no. 4, pp. 3035–3046, 2019. 120, 121

[98] A. Ademola-Idowu and B. Zhang, "Optimal Design of Virtual Inertia and Damping Coefficients for Virtual Synchronous Machines," in *IEEE Power and Energy Society General Meeting*, 2018. 122

[99] P. Fragkos, N. Tasios, L. Paroussos, P. Capros, and S. Tsani, "Energy system impacts and policy implications of the European Intended Nationally Determined Contribution and low-carbon pathway to 2050," *Energy Policy*, vol. 100, pp. 216–226, 2017. 131

[100] N. Pogaku and M. Prodanovic, "Inverter-based microgrids: Small-signal modelling and testing," in *The 3rd International Conference on Power Electronics, Machines and Drives*, 2006, pp. 499–504. 131

[101] S. D'Arco and J. A. Suul, "Virtual synchronous machines - Classification of implementations and analysis of equivalence to droop controllers for microgrids," in *IEEE Grenoble Conference PowerTech*, 2013. 131

[102] Z. Li, S. Member, C. Zang, P. Zeng, and H. Yu, "Control of A Grid-Forming Inverter Based on Sliding Mode and Mixed $\mathcal{H}_2$ / $\mathcal{H}_\infty$ Control," *IEEE Transactions on Industrial Electronics*, vol. 64, no. 5, pp. 3862–3872, 2017. 131

[103] A. Navarro-Rodríguez, P. García, J. M. Cano, and M. Sumner, "Limits, Stability and Disturbance Rejection Analysis of Voltage Control Loop Strategies for Grid Forming Converters in DC and AC Microgrids with High Penetration of Constant Power Loads," in *19th European Conference on Power Electronics and Applications, EPE-ECCE Europe*, 2017. 131

[104] L. Antonio De Souza Ribeiro, F. D. Freijedo, F. De Bosio, M. Soares Lima, J. M. Guerrero, and M. Pastorelli, "Full Discrete Modeling, Controller Design, and Sensitivity Analysis for High-Performance Grid-Forming Converters in Islanded Microgrids," *IEEE Transactions on Industry Applications*, vol. 54, no. 6, pp. 6267–6278, 2018. 131

[105] L. Zeni, B. Hesselbaek, P. E. Sorensen, A. D. Hansen, and P. C. Kjaer, "Control of VSC-HVDC in offshore AC islands with wind power plants: Comparison of two alternatives," *IEEE Eindhoven PowerTech*, 2015. 131

[106] M. Raza, E. Prieto-Araujo, and O. Gomis-Bellmunt, "Small-Signal Stability Analysis of Offshore AC Network Having Multiple VSC-HVDC Systems," *IEEE Transactions on Power Delivery*, vol. 33, no. 2, pp. 830–839, 2018. 131, 135, 143, 223

[107] G. Denis, T. Prevost, M.-S. Debry, F. Xavier, X. Guillaud, and A. Menze, "The Migrate project: the challenges of operating a transmission grid with only inverter-based generation. A grid-forming control improvement with transient current-limiting control," *IET Renewable Power Generation*, vol. 12, no. 5, pp. 523–529, 2018. 131

[108] J. Rocabert, A. Luna, F. Blaabjerg, and P. Rodríguez, "Control of power converters in AC microgrids," *IEEE Transactions on Power Electronics*, vol. 27, no. 11, pp. 4734–4749, 2012. 131

[109] S. D'Arco and J. A. Suul, "Equivalence of virtual synchronous machines and frequency-droops for converter-based Microgrids," *IEEE Transactions on Smart Grid*, vol. 5, no. 1, pp. 394–395, 2014. 131

[110] S. I. Nanou and S. A. Papathanassiou, "Evaluation of Control Schemes for Island VSC-HVDC Links Operating in Parallel with AC Interconnectors," in *IEEE Manchester PowerTech*, 2017. 131

[111] Y. Jing, R. Li, L. Xu, and Y. Wang, "Enhanced AC voltage and frequency control on offshore MMC station for wind farm," *The Journal of Engineering*, vol. 2017, no. 13, pp. 1264–1268, 2017. 131

[112] F. Mahr and J. Jaeger, "Advanced Grid-Forming Control of HVDC Systems for Reliable Grid Restoration," in *IEEE Power and Energy Society General Meeting*. IEEE, 2018. 132

[113] H. Saad, S. Dennetière, and P. Rault, "AC Fault dynamic studies of islanded grid including HVDC links operating in VF-control," in *15th IET International Conference on AC and DC Power Transmission*, 2019. 132, 135

[114] S. Henninger, M. Schroeder, and J. Jaeger, "Grid-Forming Droop Control of a Modular Multilevel Converter in Laboratory," in *IEEE Power and Energy Society General Meeting*, 2018. 132

[115] S. D'Arco, G. Guidi, and J. A. Suul, "Operation of a Modular Multilevel Converter Controlled as a Virtual Synchronous Machine," *2018 International Power Electronics Conference, IPEC-Niigata - ECCE Asia 2018*, pp. 782–789, 2018. 132

[116] Z. Lv and Q. C. Zhong, "Control of modular multilevel converters as virtual synchronous machines," *IEEE Power and Energy Society General Meeting*, 2018. 132

[117] G. Bergna, J. A. Suul, E. Berne, P. Egrot, P. Lefranc, J. C. Vannier, and M. Molinas, "Mitigating DC-side power oscillations and negative sequence load currents in Modular Multilevel Converters under unbalanced faults-First approach using resonant PI," in *38th Annual Conference on IEEE Industrial Electronics Society (IECON)*, 2012, pp. 537–542. 132

[118] G. Bergna-Díaz, J. A. Suul, E. Berne, J. C. Vannier, and M. Molinas, "Optimal Shaping of the MMC Circulating Currents for Preventing AC-Side Power Oscillations from Propagating into HVdc Grids," *IEEE Journal of Emerging and Selected Topics in Power Electronics*, vol. 7, no. 2, pp. 1015–1030, 2019. 132

[119] K. Shinoda, A. Benchaib, J. Dai, and X. Guillaud, "Virtual Capacitor Control: Mitigation of DC Voltage Fluctuations in MMC-Based HVdc Systems," *IEEE Transactions on Power Delivery*, vol. 33, no. 1, pp. 455–465, 2018. 132

[120] H. Akagi, E. H. Watanabe, and M. Aredes, *Instantaneous power theory and Applications to power conditioning.* Hoboken, NJ: Wiley, 2007. 146

[121] K. Shinoda, J. Freytes, A. Benchaib, J. Dai, H. Saad, and X. Guillaud, "Energy Difference Controllers for MMC without DC Current Perturbations," in *The 2nd International Conference on HVDC, Shanghai, China*, 2016. 137

[122] J. Freytes, P. Rault, F. Gruson, F. Colas, and X. Guillaud, "Dynamic impact of MMC controllers on DC voltage droop controlled MTDC grids," *18th European Conference on Power Electronics and Applications, EPE ECCE Europe*, 2016. 137

[123] P. Apkarian, P. Gahinet, and C. Buhr, "Multi-model, multi-objective tuning of fixed-structure controllers," *European Control Conference, ECC*, pp. 856–861, 2014. 152

[124] L. Xu and L. Yao, "DC voltage control and power dispatch of a multi-terminal HVDC system for integrating large offshore wind farms," *IET Renewable Power Generation*, vol. 5, no. 3, pp. 223–233, 2011. 162

[125] CIGRE, "The CIGRE B4 DC Grid Test System," *Working groups B4-57 and B4-58*, 2013. 162

[126] J. Beerten, S. Cole, and R. Belmans, "Modeling of multi-terminal vsc hvdc systems with distributed dc voltage control," *IEEE Transactions on Power Systems*, vol. 29, no. 1, pp. 34–42, 2014. 162

[127] V. Mier, P. G. Casielles, J. Coto, and L. Zeni, "Voltage margin control for offshore multi-use platform integration," in *Renewable Energy and Power Quality (ICREPQ'12)*, 2012. 162

[128] F. Thams, R. Eriksson, and M. Molinas, "Interaction of Droop Control Structures and Its Inherent Effect on the Power Transfer Limits in Multiterminal VSC-HVDC," *IEEE Transactions on Power Delivery*, vol. 32, no. 1, pp. 182–192, 2017. 162

[129] J. Freytes, S. Akkari, P. Rault, M. M. Belhaouane, F. Gruson, F. Colas, and X. Guillaud, "Dynamic Analysis of MMC-Based MTDC Grids: Use of MMC Energy to Improve Voltage Behavior," *IEEE Transactions on Power Delivery*, vol. 34, no. 1, pp. 137–148, 2019. 162, 163

[130] E. Prieto-Araujo, F. D. Bianchi, A. Junyent-Ferré, and O. Gomis-Bellmunt, "Methodology for droop control dynamic analysis of multiterminal VSC-HVDC grids for offshore wind farms," *IEEE Transactions on Power Delivery*, vol. 26, no. 4, pp. 2476–2485, 2011. 162

[131] X. Zhao and K. Li, "Droop setting design for multi-terminal HVDC grids considering voltage deviation impacts," *Electric Power Systems Research*, vol. 123, pp. 67–75, 2015. 162

[132] R. Eriksson, J. Beerten, M. Ghandhari, and R. Belmans, "Optimizing DC voltage droop settings for AC/DC system interactions," *IEEE Transactions on Power Delivery*, vol. 29, no. 1, pp. 362–369, 2014. 162

[133] X. Zhao and K. Li, "Adaptive backstepping droop controller design for multi-terminal high-voltage direct current systems," *IET Generation, Transmission and Distribution*, vol. 9, pp. 975–983, 2015. 162

[134] E. Prieto-Araujo, A. Egea-Alvarez, S. Fekriasl, and O. Gomis-Bellmunt, "DC voltage droop control design for multi-terminal HVDC systems considering AC and DC grid dynamics," *IEEE Transactions on Power Delivery*, vol. 31, no. 2, pp. 575–585, 2016. 162

[135] C. E. Spallarossa, T. C. Green, C. Lin, and X. Wu, "A DC voltage control strategy for MMC MTDC grids incorporating multiple master stations," in *IEEE PES T&D Conference and Exposition*, 2014. 163

[136] M. M. Belhaouane, J. Freytes, M. Ayari, F. Colas, F. Gruson, N. B. Braiek, and X. Guillaud, "Optimal control design for Modular Multilevel Converters operating on multi-terminal DC Grid," in *Power Systems Computation Conference (PSCC)*. IEEE, 2016. 163

[137] A. Egea-Alvarez, J. Beerten, D. Van Hertem, and O. Gomis-Bellmunt, "Primary and secondary power control of multiterminal HVDC grids," in *IET Conference Publications*, 2012. 163

[138] M. Aragüés-Peñalba, A. Egea-Àlvarez, O. Gomis-Bellmunt, and A. Sumper, "Optimum voltage control for loss minimization in HVDC multi-terminal transmission systems for large offshore wind farms," *Electric Power Systems Research*, vol. 89, pp. 54–63, 2012. 163

[139] P. Kundur, *Power system stability and control.* New York, NY: McGraw-Hill Education, 1994. 207, 208

[140] A. M. Lyapunov, "Stability of motion: general problem," *International Journal of Control*, vol. 55, no. 3, pp. 767–772, 1992. 207